Inelastic Collisions of Atomic Antimony, Aluminum, Erbium and Thulium below 1 K

Dissertation advisor

John Morrissey Doyle

Author

Colin Bryant Connolly

Inelastic collisions of atomic antimony, aluminum, erbium and thulium below 1 K

Abstract

Inelastic collision processes driven by anisotropic interactions are investigated below 1 K. Three distinct experiments are presented. First, for the atomic species antimony (Sb), rapid relaxation is observed in collisions with ^{4}He. We identify the relatively large spin-orbit coupling as the primary mechanism which distorts the electrostatic potential to introduce significant anisotropy to the ground $^4S_{3/2}$ state. The collisions are too rapid for the experiment to fix a specific value, but an upper bound is determined, with the elastic-to-inelastic collision ratio $\gamma \leq 9.1 \times 10^2$. In the second experiment, inelastic m_J-changing and J-changing transition rates of aluminum (Al) are measured for collisions with ^{3}He. The experiment employs a clean method using a single pump/probe laser to measure the steady-state magnetic sublevel population resulting from the competition of optical pumping and inelastic collisions. The collision ratio γ is measured for both m_J- and J-changing processes as a function of magnetic field and found to be in agreement with the theoretically calculated dependence, giving support to the theory of suppressed Zeeman relaxation in spherical $^2P_{1/2}$ states [1]. In the third experiment, very rapid atom–atom relaxation is observed for the trapped lanthanide rare-earth atoms erbium (Er) and thulium (Tm). Both are nominally nonspherical ($L \neq 0$) atoms that were previously observed to have strongly suppressed electronic interaction anisotropy in collisions with helium ($\gamma > 10^4$–10^5, [2, 3]). No suppression is observed in collisions between these atoms ($\gamma \lesssim 10$), which likely implies that evaporative cooling them

in a magnetic trap will be impossible. Taken together, these studies reveal more of the role of electrostatic anisotropy in cold atomic collisions.

Contents

List of Figures

List of Tables

To my wife, daughter and parents,

whose support has never flickered

Citations to Previously Published Work

Portions of this thesis have appeared previously in the following paper:

> "Large spin relaxation rates in trapped submerged-shell atoms," Colin B. Connolly, Yat Shan Au, S. Charles Doret, Wolfgang Ketterle, and John M. Doyle, *Phys. Rev. A* **81**, 010702(R) (2010). [4]

Acknowledgements

This thesis was completed with a wealth of assistance. I would like to acknowledge some of those contributions, in no particular order.

First, I thank my thesis advisor John Doyle for his guidance, encouragement and support through the many phases of my time in his lab. From my arrival at Harvard, I was happy to have a healthy student-mentor relationship and I have become keenly aware of its benefits to all. I have also been grateful for his focus on the big picture, which has helped me to view my work better in relation to the field and to think critically about future directions. On the practical side, his rational and reliable approach to providing adequate resources to attack experimental challenges has been not only a benefit to the experiments themselves, but a relief to his students. I did not leave stones unturned for lack of liquid helium or lasers.

I have been grateful to have a second mentor in Wolfgang Ketterle, the co-PI of this work. His input has been invaluable, and his distinct approach and experience provides welcome diversity to our discussions. With John and Wolfgang, I always feel that I have two mentors rather than two bosses. I also acknowledge the role of the Harvard-MIT Center for Ultracold Atoms in facilitating this collaboration.

My research partners Charlie Doret, Yat Shan Au and Eunmi Chae have made countless contributions to this research. Charlie helped to build and/or install much of the apparatus, and he was a model senior student during the helium BEC work. I learned a great deal working alongside him and enjoyed his friendship through our years parked in front of twin computers at the experiment. After Charlie's departure, Yat was instrumental in all the work that followed, especially his stellar work with a dizzying array of laser systems that include all those described in this thesis. I am grateful for his efforts. I also appreciate Eunmi's contributions amid her classes and other projects. Her assistance with the aluminum

simulations was especially helpful when we struggled to understand a new experimental method and atomic system.

The theoretical contributions from Timur Tscherbul and Alexei Buchachenko has greatly strengthened the science and given me a much clearer view of the physics underlying my research. That collaboration has been very valuable and enabled the experiments to go further than they otherwise would have.

The entire Doyle Lab has been a great source of assistance and camaraderie, and it is a joy to work among its members. Dave Patterson, Amar Vutha, Nathan Brahms and Matthew Wright have frequently devoted hours to solving problems in my experiment and offered critical insight. I also appreciate the efforts of Wes Campbell, Edem Tsikata, Matt Hummon and Hsin-I Lu, not only in blazing the trail with NH and nitrogen, but for leaving excellent notes, advice, ideas and equipment behind them. I would also like to give credit to those who wrote excellent and thoroughly useful Ph.D. theses, especially Jonathan Weinstein, Nathan, Charlie and Wes, to whose work I referred many times and used as a model for my own.

Stan Cotreau in the Physics Machine Shop and Jim MacArthur in the Electronic Instrument Design Lab have given me a great deal of excellent technical advice and friendly company while I labored to do the most minor tasks in their respective specialties. They are priceless and irreplaceable resources at Harvard.

Finally, I am grateful for the enthusiastic support of my wife and family. Nathalie has given much of herself toward my own success and deserves much of the credit. The support of my parents, as well, has always been clear. I appreciate their efforts to understand the esoteric details of my work, including reading my papers dense with jargon such as "electronic interaction anisotropy." Last, I am fortunate to have little Chloé in my life, and grateful for the healthy perspective that her presence gives me—and the demands of efficiency that it brings.

Chapter 1

Introduction

1.1 Physics with cold atoms

The last two decades have seen fantastic progress in methods for cooling, trapping and manipulating atoms, which has fueled an explosion of applications for cold atoms that range from precision measurement and quantum information processing to quantum simulation of complex systems.

Early progress with ultracold atoms focused primarily on the alkali metals, which can be readily produced at high vapor densities with ovens or getters and whose simple single-electron valence structures lead to the closed electronic transitions and highly elastic collisions that allow laser cooling and evaporative cooling to be very effective. Alkali atom experiments have now created Bose-Einstein condensates of over 10^8 atoms [5], reached equilibrated temperatures of 300 pK [6], observed quantum phase transitions in an optical lattice with single-atom resolution [7], and constructed atomic clocks with relative frequency accuracy of $\approx 10^{-16}$ [8].

Indeed, the great achievements with alkali atoms has led researchers to explore the pe-

riodic table more fully to make use of the wide array of atomic properties available there. Ultracold alkaline-earth and alkaline-earth-like atoms and ions have been used for improved clocks operating at optical frequencies [9], and highly magnetic atoms have been used to create dipolar quantum gases [10, 11]. This expansion of cold atomic physics into new systems has been facilitated by the increasing availability of inexpensive and reliable solid-state laser systems in a widening spectrum of optical, infrared and ultraviolet wavelengths.

More recently, focus has increasingly shifted towards cold molecules. Many diatomic molecules have significant electric dipole moments and can be fully polarized in laboratory electric fields, giving rise to a long-range ($\propto 1/r^3$) dipole-dipole interaction. The prospect of an ultracold ensemble of strongly-interacting dipoles has inspired a number of proposals to study exotic phase transitions [12–17] and quantum computing schemes [18, 19]. The energy levels of certain molecules have been shown to be highly sensitive to New Physics beyond the Standard Model, and several experiments are underway using molecules to measure the electric dipole moment of the electron [20–22]. The variety of molecules greatly exceeds that of atoms, and such diversity brings myriad opportunities; however, not all molecules are currently accessible for low-temperature experiments. There have thus far been only a small handful of polar molecules cooled to the ultracold regime ($\lesssim$1 mK), limited to alkali dimers. Since the primary route to producing these ultracold molecules has been magnetoassociation or photoassociation from ultracold atoms, the desire for new ultracold molecules has driven interest in expanding the range of atom cooling techniques to widen the available pool of component species [23–25].

More than half of the naturally-occurring neutral atomic species in the periodic table have now been cooled to below 5 K in the lab rest frame (see, for example, [26–28] and references therein), with over a dozen species further cooled to quantum degeneracy. There remain open questions, however, that continue to fuel study of novel systems. Atomic collisions, in

particular, not only provide a tool for probing electronic structure, but also are in many cases a path to lower temperatures through sympathetic or evaporative cooling. The experiments described in this thesis expand the boundaries of cold atomic physics to new species, using collisions to map out some of the diversity of interactions found across the periodic table.

1.2 Buffer-gas cooling and trapping

Over half of the atomic species studied at low temperatures have been cooled using the technique of buffer-gas cooling, in which a warm or hot source of atoms or molecules is cooled by elastic collisions with a cold inert buffer gas (usually helium or neon). The success of the method is in large part due to its simplicity and generality: nearly any atomic species and a large number of molecular species[1] can be cooled with an appropriate buffer gas density and temperature. Additionally, large volumes ($\gg$1 cm^3) and densities ($\gtrsim 10^{12}$ cm^{-3}) can be cooled in nearly all degrees of freedom,[2] resulting in large phase space densities and high collision rates for trapped ensembles.

One limitation of buffer-gas cooling is that it is limited to temperatures high enough for the buffer gas to remain in the gas phase, setting a lower limit of about 200 mK (using helium-3) [28, 30]. Additional cooling methods are therefore required to reach the ultracold regime starting from buffer-gas cooled ensembles. Fortunately, the large atom numbers that can be achieved leave room for losses along the approach to lower temperatures, as was demonstrated by the creation of a Bose-Einstein condensate of buffer-gas cooled metastable

[1]Over two dozen molecular species have been cooled below 10 K and there is evidence to suggest that most small molecules of $N \lesssim 10$ can be buffer-gas cooled without cluster formation [28, 29].

[2]Vibrational cooling of molecules has been observed to be less efficient using the buffer-gas technique than cooling of rotational and translational degrees of freedom [28].

helium-4 atoms, which were evaporatively cooled by over five orders of magnitude from ∼500 mK [31]. Further cooling of buffer-gas cooled and trapped ensembles has also been demonstrated with chromium [32], molybdenum [33] and dysprosium [34].

Further cooling requires thermal isolation of the species of interest from the buffer gas. Without the buffer gas, however, and in the absence of some other confinement, the cooled species will immediately expand and freeze to the walls of the cryogenic environment. Hence experiments that seek further collisional cooling below ∼1 K have generally employed very deep (≈4 T) superconducting magnetic traps, the only technology currently available to produce kelvin-scale trap depths for neutral species. Alternative methods include the use of laser cooling to further reduce the temperature to a range where other trapping methods can be used [35], an approach that uses the phase space density enhancement of the initial buffer-gas cooling step to relax the requirements of laser cooling—namely, the number of photons that must be scattered to bring the particles to rest. Nevertheless, as with laser cooling of hot atoms, this method is limited to species for which narrow-line, high-power lasers are available. Furthermore, the need to scatter $\gtrsim 10^4$ photons makes the method impractical for species which lack a sufficiently small and closed set of optical transitions, as is the case with most molecules outside of a special subset [36, 37].

The majority of atomic and molecular species are paramagnetic. As a result, the generality of magnetic trapping—along with the high trap depth, large trap volume and excellent stability it can provide—has made the method a workhorse of the field, including for many non-alkali species [2, 33, 38–41]. It is particularly well-suited to buffer-gas cooled species, of which over a dozen have been trapped [28]. The fundamental drawback to magnetic trapping, however, is that only magnetic field minima, and not maxima, can be created in free space [42], so that only low-field-seeking states can be trapped with static fields. This leaves the trapped particles vulnerable to inelastic collisions that cause transitions to lower-

energy untrapped states. Such collisions impose lifetime and density limits that can hinder experiments, especially those that rely on collisional processes such as evaporative cooling.

1.3 Inelastic collisions

From a technical perspective, inelastic collisions are more often bane than boon to experiments with cold atoms and molecules. Elastic collisions—those that preserve the internal state of the colliding particles—are used to thermalize trapped ensembles during evaporative cooling. They are also used to bring two ensembles into equilibrium during sympathetic cooling, as with buffer-gas cooling. Inelastic collisions, in contrast, act to equilibrate all degrees of freedom, which is undesirable when the fully-equilibrated state is not the goal (*e.g.*, magnetic trapping).[3] There are important exceptions to this perspective. Collisional quenching of the rotational state distribution in buffer-gas cooled molecules greatly increases population in the lowest rotational levels, enhancing phase space density. Looking instead to higher energies, collisional excitation in discharges is used to rapidly transfer population to metastable states, such as the $^3S_1$ state of helium. Thus inelastic collisions can also act as a tool for engineering a desired state distribution.

In addition to technical interest, there is significant scientific interest in inelastic collisions and what they reveal about the structure and interactions of the colliding partners. During a collision between two atoms, the energy levels are perturbed by the interparticle interaction. Inelastic transitions can result from the mixing of different states in the collision, and hence the collision rates provide a window to the energy levels and their couplings. This can be

[3]In fact, the fully-equilibrated state is virtually never the goal for experiments with cold atoms, as all ultracold gases are in a metastable phase—in true equilibrium, the atoms form a solid. Inelastic collisions are the only route to equilibrium and determine the window of metastability for cold gases.

dramatically displayed by resonant behavior, in which the temperature or magnetic field is tuned such that the collision energy is nearly resonant with a bound molecular state, at which point the cross section may diverge or vanish [43–45].

The behavior of the inelastic cross section as a function of temperature or applied field can also reveal a great deal about the mechanism behind inelastic transitions, be it the electric [46] or magnetic [47] dipole-dipole interaction, or electrostatic interaction anisotropy [48]. A complete understanding of these processes in a given colliding system allows for improved predictions in new, more complex systems, and may potentially inspire new methods for experiments to control or exploit inelastic collisions. For this reason, and because collisions remain a crucial tool for cooling and state preparation, collision measurements are a critical element of the expansion of cold atomic and molecular physics into unexplored territory.

1.3.1 Measuring cold inelastic collisions

Inelastic collision rates can be observed and measured in several different ways. Perhaps the simplest is to bombard a target atom or molecule with a known flux of collision partners and directly detect the collision product states [47], which in the case of an inelastic collision will differ from the initial state. Chemical reaction rates were first measured in this manner several decades ago [49]. For small inelastic rates, however, the product states are limited in density and may not be observable. Also, molecular beam collision experiments generally operate far from the ultracold limit, and while the beam may be narrow in its energy distribution, the forward velocity is often quite high [50].

Another approach to measuring inelastic collisions is to observe a system move towards equilibrium. This can be done by introducing atoms from a highly energetic distribution, such as an oven source or an ablation plume, and allowing inelastic collisions to thermalize the internal state distribution to a low-temperature bath. This method is employed in the

experiment with antimony described in Chapter 2 of this thesis, and in the experiment with erbium and thulium in Chapter 4. Alternatively, an equilibrated ensemble can be driven out of equilibrium, *e.g.* by rapidly turning on a trapping field or resonant laser light, and then allowed to relax. In both cases, the dynamical return to equilibrium can provide a direct measurement of inelastic collisions.

Yet another method is to apply a continuous perturbation to the system and measure its steady-state response. The population of an optically pumped ground state, for example, is determined by the competition between the pumping rate and the rate at which inelastic collisions repopulate the state. The "stiffness" of the system can be explored by varying the perturbation strength, and the collision rate determined from this response. This technique is used in the aluminum experiment described in Chapter 3.

For any given colliding system, the degree of collisional inelasticity can be quantified by the ratio

$$\gamma = k_{\mathrm{el}}/k_{\mathrm{in}}, \tag{1.1}$$

where k_{el} and k_{in} are the elastic and inelastic rate coefficients, respectively, given by

$$k_X = \int \sigma_X(E) v(E) f(E)\, dv, \tag{1.2}$$

where $\sigma_X(E)$ is the appropriate energy-dependent cross section, $v = (2E/m)^{-1/2}$ is the collision velocity, and $f(E)$ is the Maxwell-Boltzmann velocity distribution. When considering elastic collisions in a thermalized ensemble, experiments are often not sensitive to the total elastic cross section, but rather the momentum transfer cross section, defined as [51]

$$\sigma_{\mathrm{d}} = \int [1 - \cos(\theta)]\, \sigma_{\mathrm{el}}(\theta) \sin(\theta)\, d\theta. \tag{1.3}$$

The effect of the integral is to weaken the contribution from forward-peaked ($\theta \sim 0^\circ$) scattering that does not significantly change the particle velocities. Velocity randomization is

integral to particle diffusion and thermalization, and hence it is the momentum transfer collision rate k_{d} that is extracted from measurements of those processes. For the remainder of this thesis, the definition

$$\gamma = k_{\mathrm{d}}/k_{\mathrm{in}} \tag{1.4}$$

will be used.

Chapter 2

Antimony–^{4}He collisions

2.1 Pnictogen collisions

In addition to their fundamental importance to chemistry and biology, nitrogen and the other pnictogens (Group 15 atoms) are experimentally promising and theoretically interesting from the perspective of atomic and molecular physics. Atomic nitrogen, in particular, has a low polarizability and a highly isotropic electronic distribution, both of which contribute to robust elasticity in collisions with other atoms and molecules, often limited only by modest magnetic dipole-dipole interactions [52, 53]. For this reason, nitrogen has been identified as a promising sympathetic coolant for molecular species, including NH [53–55]. Based on theoretical calculations, it is also reasonable to expect that evaporative cooling of nitrogen to the ultracold regime in a magnetic trap will be efficient [52], and hence a quantum degenerate nitrogen gas may be achievable in a magnetic trap. Such developments would make nitrogen a potential component of novel and physically unique ultracold diatomic species.

A significant technical drawback to experiments using nitrogen atoms is that the lowest-energy E1 transition from the ground state is at 121 nm, a difficult vacuum ultraviolet

(UV) wavelength that precludes the use of traditional laser cooling techniques that have been so successful in atoms such as the alkali metals. Despite this impediment, very large trapped ensembles of cold atomic nitrogen have been achieved by means of buffer-gas cooling [52]; nitrogen has also been co-trapped with NH molecules, a critical first step towards sympathetic cooling of the molecules [54]. Lacking a 121-nm laser, these experiments have detected nitrogen using two-photon absorption laser induced fluorescence (TALIF) with a pulsed 207-nm laser. This method has been satisfactory thus far, but limitations imposed by the shot-to-shot variation, linewidth, and calibration difficulties inherent to this method are an impediment to rapid experimental progress.

To this end, the other pnictogens are appealing from a technical perspective as potential stand-ins for nitrogen. With each step down in the Group 15 column, the optical transition frequencies are reduced [56], simplifying detection. However, there potentially are significant challenges to replacing nitrogen with a heavier pnictogen. Atomic polarizability grows with mass, as does spin-orbit coupling strength. The latter was shown theoretically in the case of the bismuth to result in severe deformation of the ground $^4S_{3/2}$ electronic structure, resulting in rapid inelastic bismuth–helium collisions which were observed experimentally [57]. Since bismuth is the heaviest stable atom with a half-filled p shell, it is not surprising that its structure—nominally equivalent to that of nitrogen—is significantly affected by relativistic distortions.

2.1.1 The importance of antimony

Between the extreme cases of nitrogen and bismuth, cold collisions of the other pnictogens have heretofore not been investigated, and it has remained an open question of how the strong anisotropy observed in bismuth develops through the group. In fact, even in the case of bismuth the theoretically calculated inelastic collision rates are well beyond the

experimentally accessible parameter space, leaving a wide gap between predictions and experimental bounds. It has also remained unclear whether there exists a good compromise between technical feasibility and collisional robustness among the pnictogens, which could lead to important advancement.

In general, many relativistic effects in atoms are strong functions of the atomic mass. Hence, it is reasonable to suppose that the inelasticity in bismuth collisions would be significantly reduced in collisions instead involving the next-lightest pnictogen, antimony. Antimony is also the lightest pnictogen for which single-photon excitation is straightforward with standard narrow-band laser technology, a critical hurdle overcome towards experimental simplicity. For these reasons, antimony appears well-positioned to be a useful compromise.

This chapter describes experiments investigating Zeeman relaxation of antimony in a magnetic field due to collisions with helium-4. These inelastic collisions are unfortunately found to be too rapid to allow for buffer-gas loading of a magnetic trap. However, the antimony–helium system allows for a more fruitful comparison between experimental and theoretical results than that which was achievable for the bismuth–helium system. This comparison supports our understanding of the critical role of spin-orbit coupling in driving the inelastic transitions [57] and provides a constraint to the antimony–helium interaction potential. Furthermore, the exploration of this important regime in the pnictogen series informs the possibilities for future experiments with these atoms.

2.2 Experimental design

2.2.1 Experimental cell

The experiments investigating antimony–helium inelastic collisions were performed in an experimental cell modeled in part on the cell used to evaporatively cool metastable helium

atoms to create a Bose-Einstein condensate [31, 58]. The success of that cell in maintaining excellent vacuum within seconds of buffer-gas trap loading made it an attractive model for extending such methods to cool molecular species. The new cell was constructed with the primary goal of trapping of molecular NH and sympathetic cooling with atomic nitrogen (see Section A.5). In addition to the antimony experiment described here, it was also used for the aluminum experiment described in Chapter 3.

As with the metastable helium cell, the antimony cell consists of two concentric G-10 CR fiberglass-epoxy composite tubes[1] with a jacket of superfluid helium filling the space between them (Figure 2.1). The superfluid provides excellent thermal conductivity without electrical conductivity, minimizing eddy current heating when the magnetic field is reduced to implement evaporative cooling. The superfluid jacket space extends through a flexible bellows to a copper heat exchanger bolted to the mixing chamber of a dilution refrigerator[2]. Sintered silver powder attached to copper fins mounted in the heat exchanger minimize the Kapitza resistance [59] between metal and superfluid so that the thermal contact between the refrigerator and cell is limited by the narrow bellows section. The cell's power curve is shown in Figure 2.2, from which the flexible link's thermal conductivity at temperature T is computed to be $\kappa = (0.47\,T^3)$ W/K^4, in good agreement with calculations from Equation 2.13 of [59].

Sealing the cell at its base is a wedged window made of uncoated UV-grade fused silica. At the top of the cell is a deep-UV aluminum mirror for reflecting a probe laser, as well as several solid ablation targets attached with Stycast 2850FT black epoxy. There is no line of sight between the ablation targets and mirror surface to avoid coating the mirror with ablated material. A small impedance separates the cell from a buffer gas reservoir

[1]Spaulding Composites, Inc., Rochester, NH.

[2]Model MNK126-500, Leiden Cryogenics b.v., Leiden, the Netherlands.

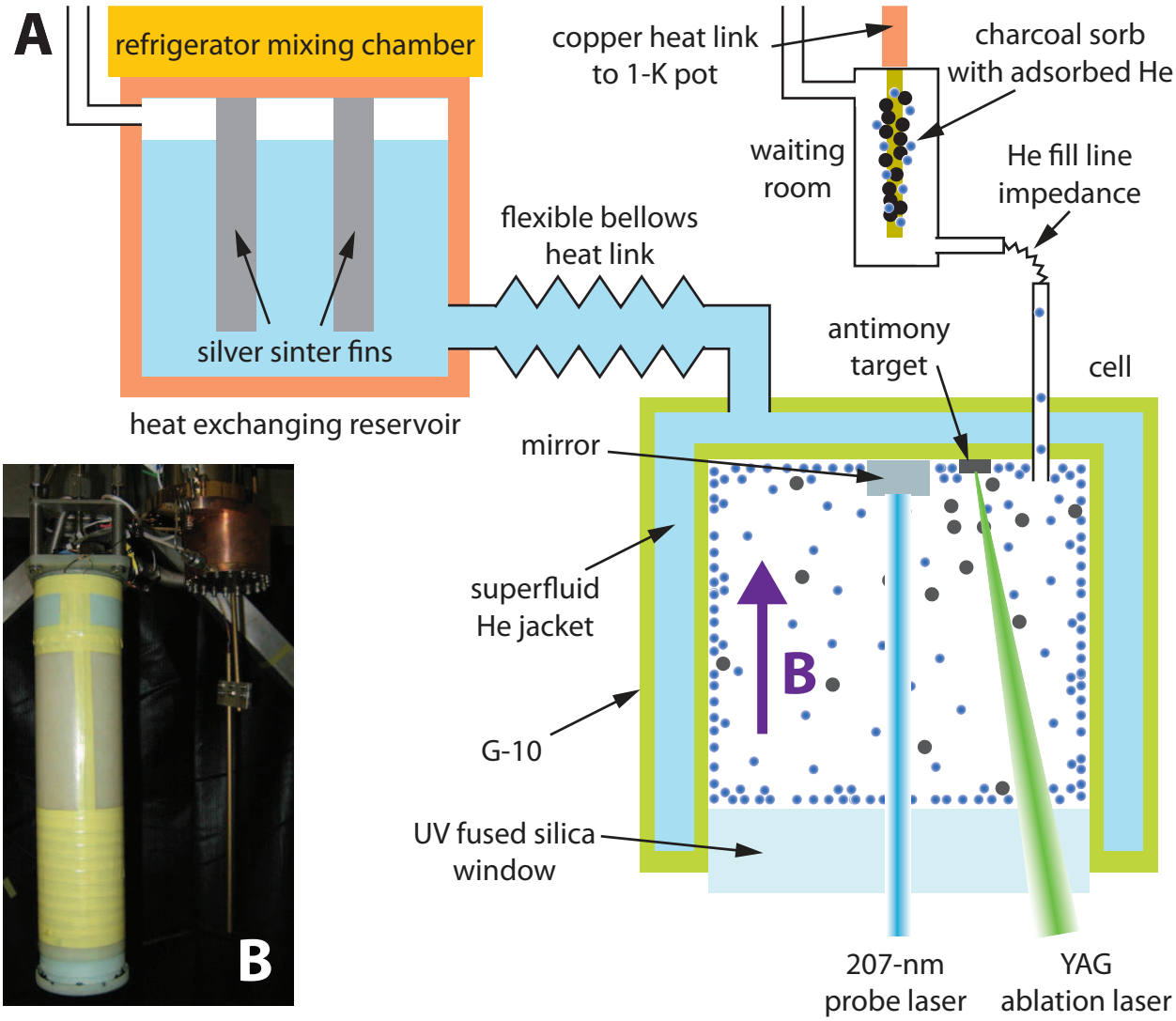

Figure 2.1: (A) Schematic of the G-10 superfluid-jacketed cell; (B) photo of the cell installed in the apparatus. The magnet that surrounds the cell is not shown.

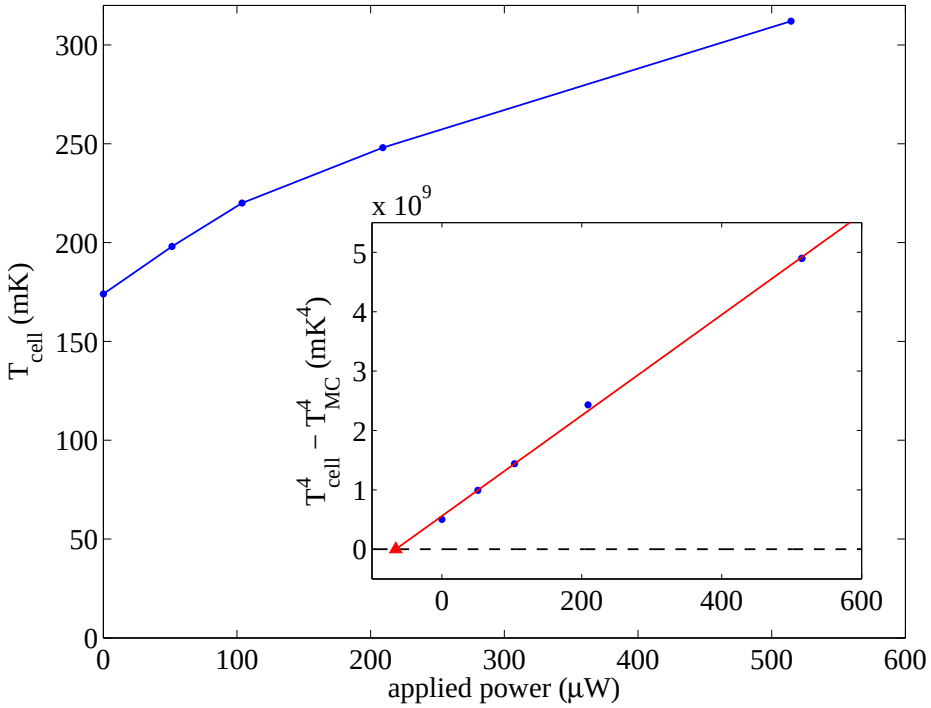

Figure 2.2: Measured power curve of the G-10 superfluid-jacketed cell. The inset shows the conductivity calibration of the flexible thermal link, with the difference of the fourth powers of the cell and mixing chamber temperature plotted against the same horizontal axis. The inset data are fit to the function expected based upon the T^3 dependence of the superfluid helium thermal conductivity [59]. Extrapolating the fit to zero thermal gradient and taking the absolute value yields an estimate of the base heat load on the cell of 66 μW (red triangle).

called the "waiting room" [60]. Inside the waiting room is ≈0.5 cm^3 (0.1 g) of activated coconut charcoal sorb attached to a brass post with Stycast 2850FT black epoxy, which is thermally anchored to the refrigerator's 1-K pot. Applying current through a resistive wire wound on the post rapidly warms the charcoal to >10 K, releasing adsorbed helium atoms and pressurizing the waiting room. The cell is filled with buffer gas by applying a 1-s heating pulse of 0.1–0.4 J to the sorb heater, after which it cools below 2 K within 30 s and cryopumps the waiting room space back to low pressure. The time for buffer gas in the cell to be pumped back to the waiting room through the impedance is much longer, allowing for many ablation cycles at relatively constant buffer gas density.

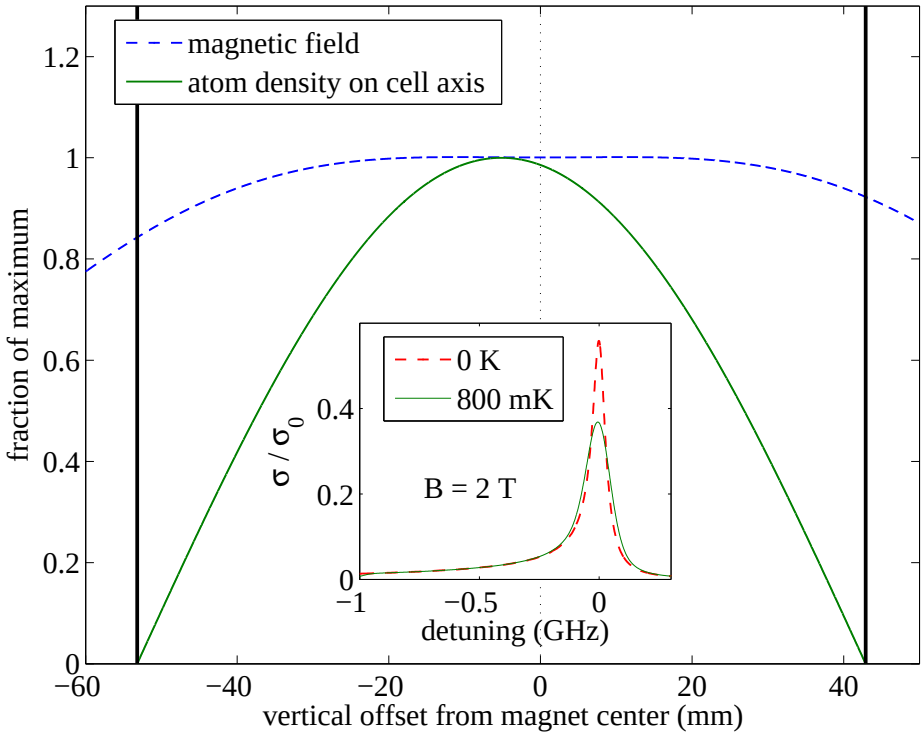

Figure 2.3: Calculated Helmholtz magnetic field profile overlayed with the expected atomic density distribution (Equation 2.3). The solid vertical lines are the cell boundaries. The inset shows the calculated Zeeman-broadened lineshape (for a line with positive Zeeman shift) that results from the convolution of the magnetic field and density profiles.

The cell sits within the bore of a superconducting magnet ("Mark IV" [61]) consisting of a pair of Helmholtz coils in a titanium alloy cask. With the same current in both coils, a magnetic field of up to 6 T is produced.[3] The magnetic field is homogeneous to better than 0.1% in a region 30 mm long on the magnet axis, and drops outside of that region, so that spectral lines are generally narrow with a weak, broad pedestal on one side (see Figure 2.3). In practice, the Zeeman broadening is increased somewhat by the field distortion induced by ferromagnetic ablation targets at the cell top, which become magnetized. This field

[3]The maximum achievable Helmholtz field is likely near 6.9 T, as estimated from simulations of the magnetic field and from the maximum field achievable with the magnet in the anti-Helmholtz coil configuration (5.1 T at the magnet bore surface).

contribution is not known precisely, and may depend on the magnetic field history.

2.2.2 Antimony production and cooling

Atomic antimony is produced by focusing a <10-ns, 1–5-mJ ablation pulse from a 532-nm doubled Nd:YAG laser onto a ≈3-mm lump of pure antimony metal. Ablation yields are typically excellent ($>10^{13}$ atoms), even for low ablation energies, perhaps due in part to a combination of the moderate melting point and low thermal conductivity of antimony metal that allows for localized vaporization [62]. Good ablation yield is a boon to the experiment, not only in terms of detection, but because cold antimony gas can be obtained with minimal heating of the cryogenic environment.

The cell temperature is held fixed near 800 mK to ensure adequate helium-4 vapor pressure. Lower-temperature buffer-gas cooling is possible with helium-4, however the helium density is more stable at higher temperatures where the cell heat capacity is larger. Since ablation heating inevitably causes the cell to heat and cool, it is prudent when the helium density is critical to the experiment—as is the case when measuring collision rates of atoms with helium—to operate in a warmer, more density-stable regime whenever possible. After ablation, the atoms cool to within 0.1 K of the pre-ablation cell temperature within 20 ms (Figure 2.4).

After ablation and cooling, the atoms diffuse through the buffer gas to the cell walls, where they freeze. This diffusive transport is governed by the diffusion equation [51],

$$\frac{\partial}{\partial t} n(\boldsymbol{r}, t) = D\, \nabla^2 n(\boldsymbol{r}, t), \tag{2.1}$$

$$D = \frac{3\pi}{32} \frac{\bar{v}}{n_{\mathrm{b}} \sigma_{\mathrm{d}}}, \tag{2.2}$$

where D is the diffusion constant, n and n_{b} are the antimony and buffer gas densities, respectively, $\bar{v} = \sqrt{8 k_{\mathrm{B}} T / \pi \mu}$ is the mean inter-species velocity with reduced mass μ, and σ_{d}

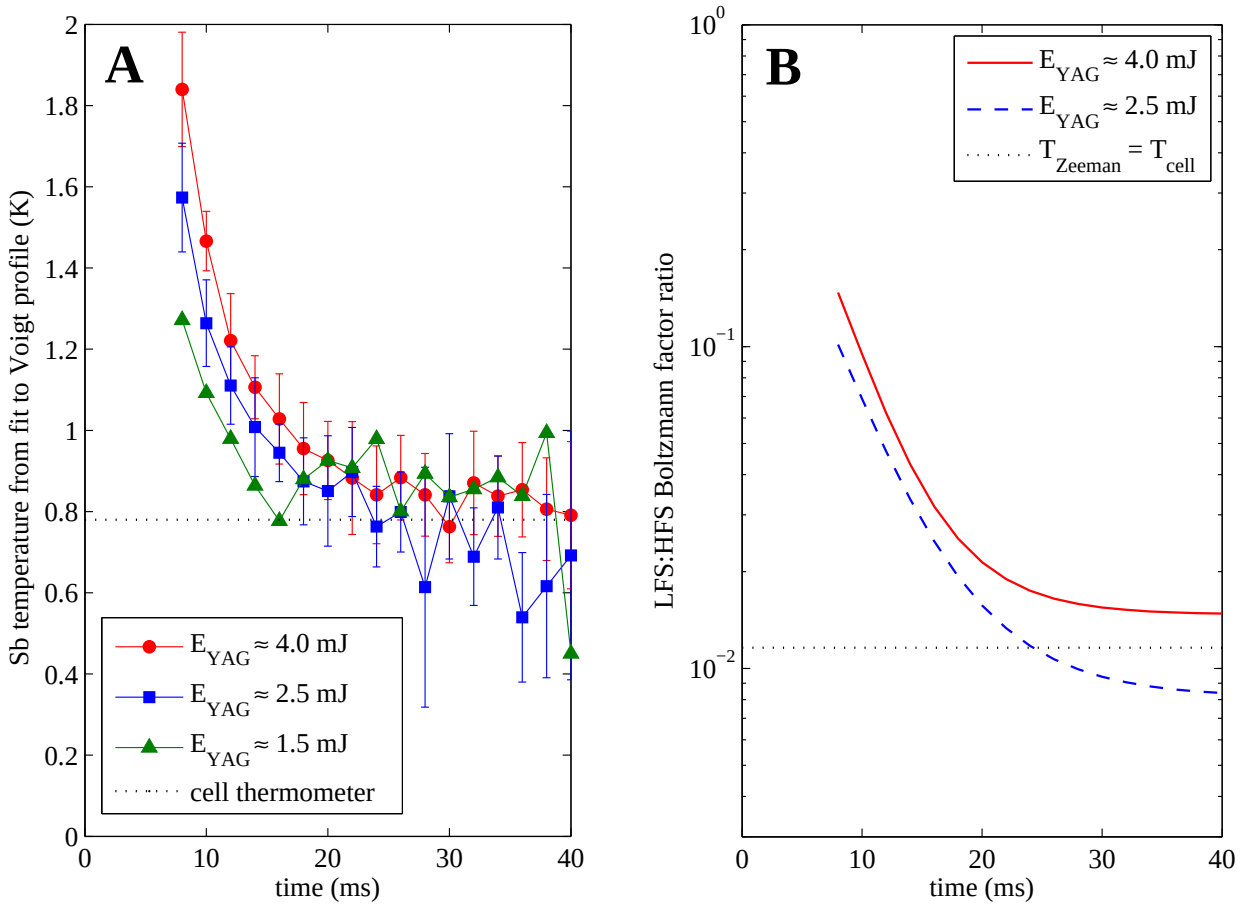

Figure 2.4: (A) Cooling profile of antimony atoms after ablation, as extracted from Voigt profile fits to data at zero field; (B) thermal equilibrium ratio of the Boltzmann factors of the $m_J = J$ and $-J$ states at a field of 0.86 T, using exponential fits to the temperature data in (A). The dotted lines in (A) and (B) are the temperature measured by the cell thermometer and the corresponding Boltzmann factor ratio, respectively.

is the thermally averaged momentum transfer cross section (Equation 1.3). For a cylindrically symmetric cell of radius R and length L, the solution to Equation 2.1 is a sum of diffusion modes, of which the longest lived is the lowest-order mode,

$$n(\vec{r},t) = n_0 J_0\left(\frac{j_{01} r}{R}\right)\cos\left(\frac{\pi z}{L}\right) e^{-t/\tau_{\rm d}}. \tag{2.3}$$

This lowest mode's lifetime, $\tau_{\rm d}$, also called the diffusion time, is given by

$$\tau_{\rm d} = \frac{1}{DG} = \frac{32}{3\pi}\frac{n_{\rm b}\sigma_{\rm d}}{\bar{v}\,G}, \tag{2.4}$$

$$G = \frac{j_{01}^2}{R^2} + \frac{\pi^2}{L^2}. \tag{2.5}$$

$J_0(x)$ is the zeroth-order Bessel function of the first kind and j_{01} is its first zero. For $L \sim 2R$, higher-order modes decay at least several times faster than the lowest mode and can be safely ignored after waiting 1–3 diffusion times. The applied magnetic field is largely homogeneous across the cell and does not significantly affect the diffusive motion.

2.2.3 Thermal dynamics of Zeeman relaxation

Antimony atoms are produced at a temperature much higher than the energy splitting $\Delta E = \mu B/J$ between magnetic sublevels, where $\mu = 3\mu_\mathrm{B}$ is the ground state magnetic moment. Hence, the atoms initially populate all sublevels equally. We define the Zeeman temperature from the sublevel distribution in a magnetic field B such that the ratio of populations in the stretched low- and high-field-seeking (LFS and HFS) states are given by

$$\frac{N_{m_J=J}}{N_{m_J=-J}} = \exp\left(-\frac{2\mu B}{k_\mathrm{B}T}\right). \tag{2.6}$$

As the atoms cool by colliding with the buffer gas, the Zeeman temperature equilibrates to the translational temperature only *via* inelastic collisions (Zeeman relaxation). For sufficiently large values of the antimony–helium elastic-to-inelastic collision ratio γ (introduced in Section 1.3.1, Equation 1.4), the translational temperature will drop and stabilize while the Zeeman temperature remains high. Under these circumstances, the difference between the lifetimes of different sublevels reveals the inelastic collision rate.

In the other extreme of $\gamma \approx 1$, where inelastic and elastic collisions occur at similar rates, the Zeeman distribution remains in equilibrium with the translational temperature. The lifetimes of the sublevels will then be determined by the temporal and spatial cooling profile in the first milliseconds after ablation. Measuring low values of γ by watching the Zeeman temperature fall to equilibrium after ablation is quite difficult, as it requires decon-

volving relaxation from the imprecisely-known cooling profile. In general, this presents an intractable experimental challenge for measuring $\gamma \lesssim 1{,}000$ in this manner, and the method can only produce an upper bound for the inelastic collision rate [57, 63, 64]. As discussed in Section 1.3.1, there are other ways to measure faster rates of inelastic collisions, such as the optical pumping method described in Chapter 3. However, other methods may not be technically feasible in all systems. The discussion here will focus on observing equilibration of the Zeeman and translational temperatures after ablation into the buffer gas.

The difficulty in observing low values of γ after ablation depends on the ablation energy and heat capacity of the cell. A large heat capacity—achieved either with a large cell or a high temperature—will cause the cell temperature to remain stable after ablation. In practice, the temperature must be kept low enough to achieve a significant Boltzmann factor between magnetic sublevels with the available magnetic field. In addition, the Zeeman relaxation rate will in general change with temperature and field, and it is better not to technically constrain these parameters more than necessary. Using as an example the initial temperature of 1 K and the measured specific heats [59], one finds that a cell built of 100 cm^3 of copper will heat by approximately 10% and 70% upon absorbing energies of 1 and 10 mJ, respectively. In comparison, with only 10 cm^3 of superfluid helium-4 (the material used to cool the cell for the antimony experiments described here) the temperature rise is <10% for 10 mJ. The latter's heat capacity is sufficient for a stable mean temperature over the entire cell. However, the thermal conduction time across the cell can place an additional limit on the stability of the buffer gas temperature, as described in the following section.

2.2.4 Thermal dynamics in G-10 cells

There is reason to expect that the challenge of separating Zeeman relaxation from equilibrated cooling is particularly acute in experimental cells constructed from G-10 rather than

a material of high thermal conductivity such as copper. Specifically, a thermal barrier at the cell wall—such as low-conductivity G-10—that obstructs diffusion of heat into the bulk of the cell will cause the internal cell surface to temporarily remain at an elevated temperature, even with high total cell heat capacity. This effect extends the cooling time of the buffer gas and forces the experiment to allow more collisions to occur while waiting for the translational temperature to stabilize enough to measure Zeeman relaxation. The minimum observable γ is thus raised.

For a more quantitative description, we can estimate the cooling timescales. The thermal time constant to cool a solid from one end over a length L is given by [65]

$$\tau_{\mathrm{th}} = A \left(\frac{c_V}{\kappa} \right) L^2, \tag{2.7}$$

where c_V and κ are the specific heat per unit volume and thermal conductivity of the material and A is a dimensionless geometric factor.[4] Using Equation 2.7 with $L = 1$ mm and $T = 1$ K gives $\tau_{\mathrm{th}} \approx 0.4$ μs for copper (RRR = 100) and ≈6 ms for G-10. The G-10 cooling time rises to ≈25 ms at 0.3 K. Comparing the two materials at 1 K, heat can diffuse within a few milliseconds through ∼10 cm of copper, but barely penetrate a minimal-thickness G-10 wall. As a result, after this time the much larger available copper heat capacity will ensure a colder cell wall than in the G-10 cell (see Figure 2.5). If a superfluid helium jacket lies behind the G-10, then the relevant heat capacity surges once enough time has passed to reach the superfluid, but there will be a finite and significant delay.

The implication for measurement of Zeeman relaxation is that the experiment will be "blind" for the time it takes for the falling translational temperature to diverge from the Zeeman temperature. For the cell in this experiment, the blinded time is at minimum 10 ms. To ensure that the diffusion time τ_{d} exceeds this minimal cooling time, at least

[4] $A = 4/\pi^2$ for a rod of length L and constant cross section.

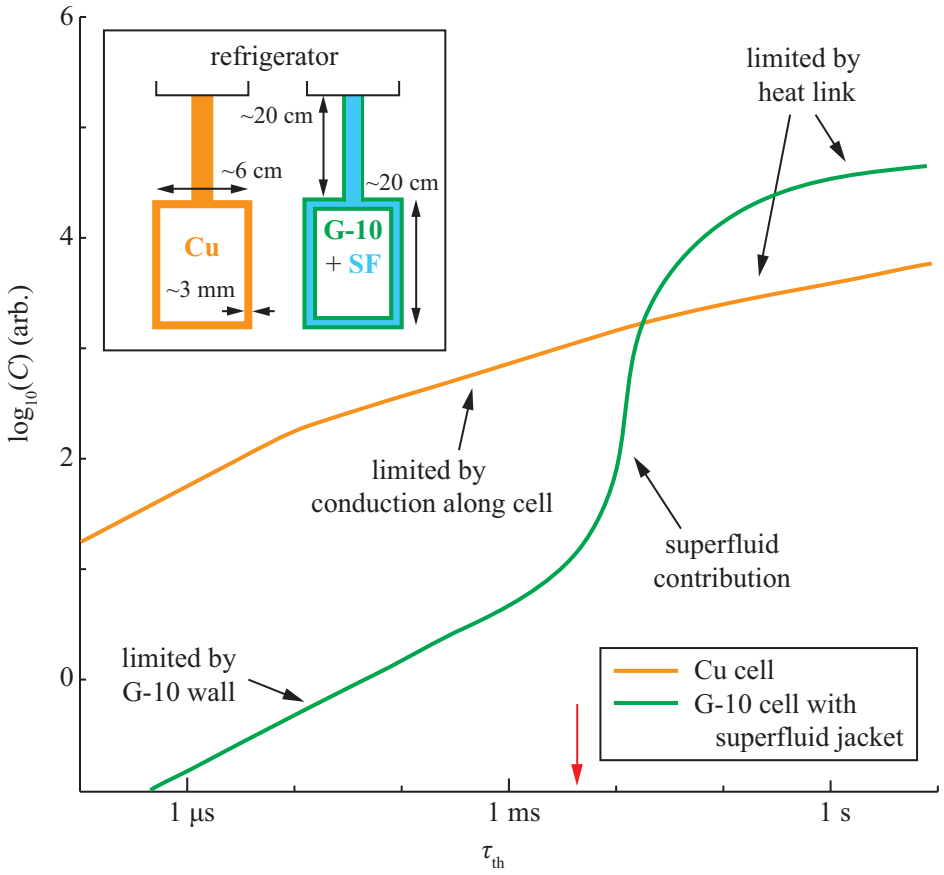

Figure 2.5: Sketch of thermal behavior of copper *vs.* superfluid-jacketed G-10 cells for a simplified model cell with some dimensions shown. The heat capacity C available to absorb energy (such as that used for ablation production of Sb) is given as a function of the time necessary for diffusing heat to reach that heat capacity. A larger value of C implies a cooler temperature. Over short timescales, heat can reach only the inner wall of the cell, but over long times the entire cell, heat link and refrigerator contribute. The low thermal conductivity of G-10 implies a low C for timescales $\lesssim$10 ms. However, the very large conductivity and specific heat of superfluid helium dramatically changes the behavior beyond this time. The red arrow indicates the average ballistic cell transit time of Sb at 800 mK. This diagram is approximate and highly dependent on temperature and geometry. The effects of the cell window and other "hot spots" have been ignored.

$\sim$1,000 collisions are required, *i.e.*, a minimum observable $\gamma \gtrsim 1{,}000$. The contrast in thermal behavior of superfluid-jacketed G-10 cells has further implications for buffer-gas trapping, especially for marginally-trappable species with γ of 10^4–10^5. Sections 4.2.2 and A.3.4 describe this behavior in relation to specific experiments.

2.2.5 Absorption spectroscopy detection system

Ground state optical detection of the lighter pnictogens is difficult due to the short-wavelength UV lasers required for single-photon excitation. Antimony is the lightest of the group for which this wavelength is greater than 205 nm, the lower limit for single harmonic generation (SHG) in beta barium borate (BBO) nonlinear crystals [66]. Narrow-band continuous wave (CW) lasers can be created at shorter wavelengths [67, 68], but the process is significantly more difficult [69], and experimental implementation of such laser systems can be hindered by limited availability of optical elements such as low-absorption windows.

The antimony level diagram is shown in Figure 2.6. Ground $^4S_{3/2}$ state excitation to the ^4P fine structure manifold is possible with wavelengths of 231.2 nm, 217.6 nm or 206.9 nm to excite to the $J = 1/2$, $3/2$ or $5/2$ state, respectively. The latter ($^4S_{3/2} \rightarrow {}^4P_{5/2}$) is used in this work for two primary reasons: first, the transition strength from the $m_J = J$ ground state sublevel is strongest for a $J \rightarrow J + 1$ transition; second, high-power diode lasers are commercially available near 413.8 nm, the fundamental wavelength for SHG.

A schematic diagram and photographs of the 206.9-nm laser system are shown in Figures 2.7 and 2.8. The system consists of three parts optically coupled by single-mode fibers: a grating-stabilized diode master laser at 413.8 nm, a slave diode laser injection locked to the master, and a delta-configuration doubling cavity for SHG in BBO to 206.9 nm. The power outputs of the master and slave lasers are $\approx$5 mW and $\approx$80 mW, respectively. The slave laser power is lower than desired for maximum SHG conversion efficiency, limiting the CW

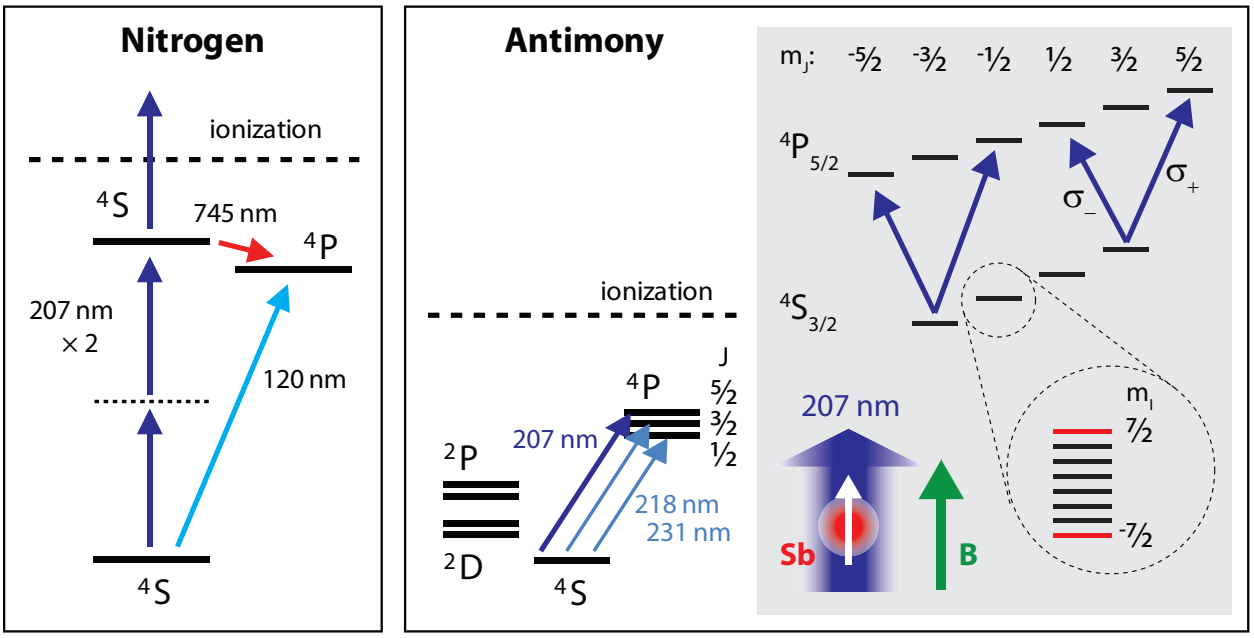

Figure 2.6: Relevant energy levels Sb, with those of N shown for comparison, and in-field Sb magnetic sublevels. The vertical spacing of levels outside the gray box are drawn roughly to scale. The hyperfine states drawn in red exist for ^{123}Sb, but not ^{121}Sb. As the field is parallel to the laser propagation, only $\Delta m_J = \pm 1$ transitions can be driven with $\sigma_\pm$-polarized light. Note that the excited state of N used for 2-photon excitation does not exist in Sb below the ionization energy.

power of the output UV to ≈100 nW. In addition, the doubling cavity and controller are designed to run with higher fundamental power, so the cavity lock is not particularly good, which leads to large intensity fluctuations and PID feedback loop oscillations. When the cavity is scanned, its transmission reaches a peak several times higher than the mean value when locked, suggesting that perfecting the cavity lock could gain an order of magnitude in UV power.

Both the slave laser injection lock and the doubling cavity lock are sensitive to attempts to tune the laser frequency. Rapid scanning of a range spanning more than a few GHz at scan rate $\gtrsim$ 30 Hz causes the cavity lock to fail. Since the Zeeman relaxation timescales are typically below 30 ms, scanned spectra thus cannot be used for the relaxation measurement.

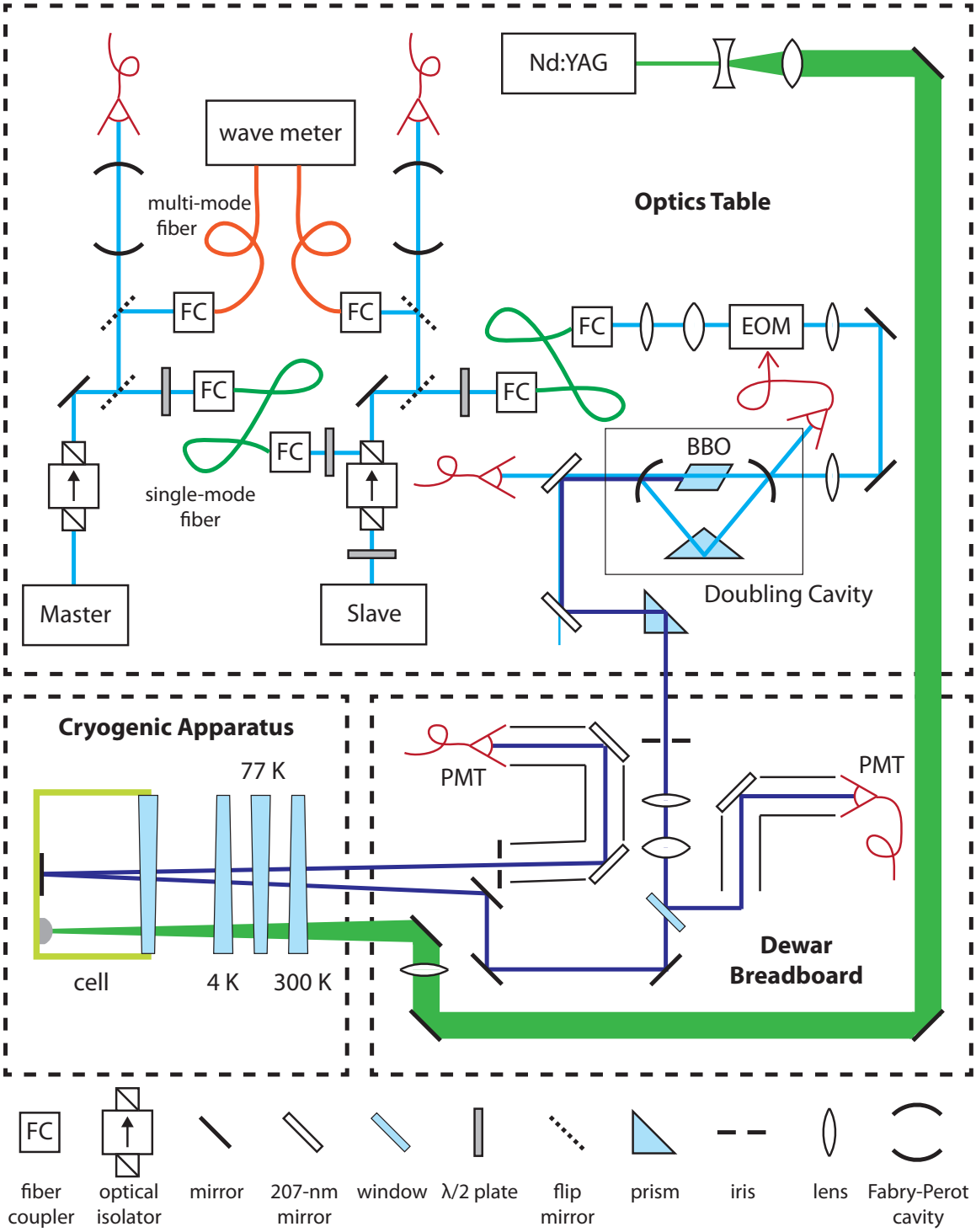

Figure 2.7: Schematic of 414 → 207-nm laser system and optics layout for Sb absorption spectroscopy. Some steering mirrors are not shown.

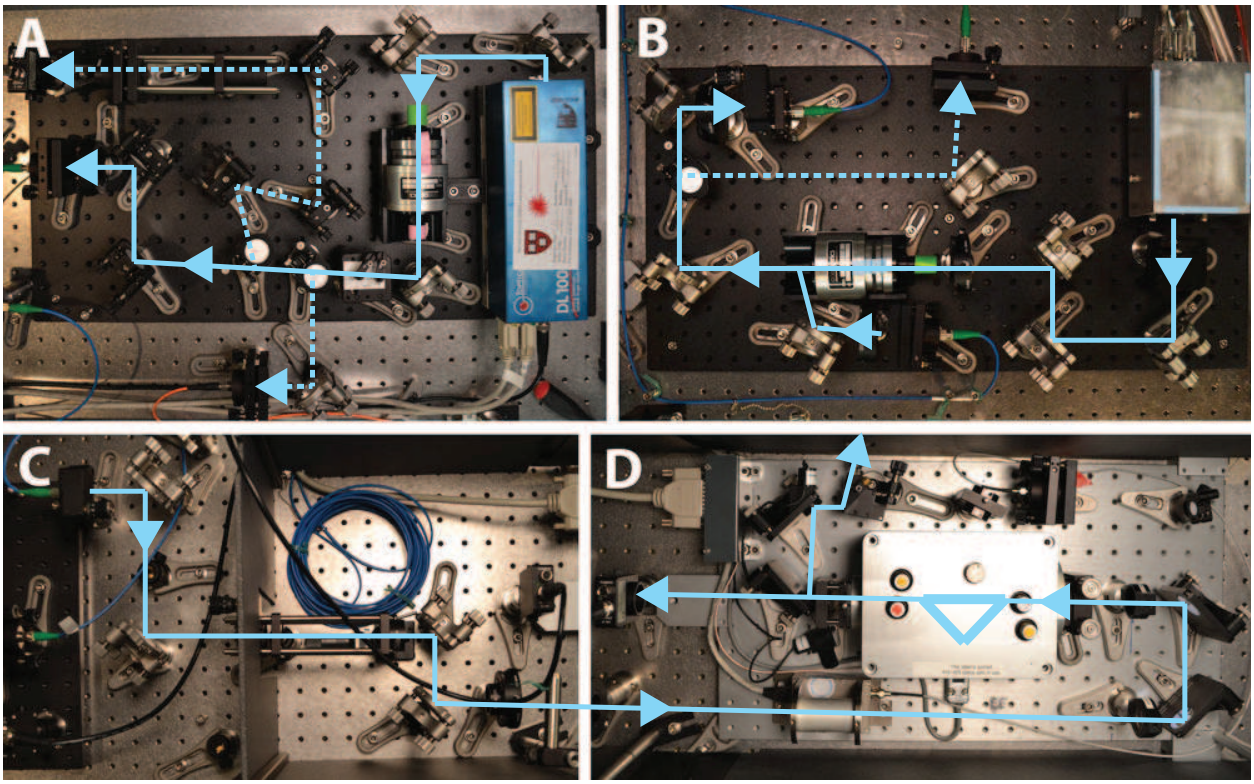

Figure 2.8: Photographs of the laser system used for SHG to 207 nm. (A) Master and (B) slave diode lasers; (C) mode shaping optics for insertion into (D) the Δ-configuration doubling cavity (covered). Dashed lines indicate optional beam paths from flip mirrors.

Larger frequency tuning that requires changing the lasing mode of the master diode causes the injection lock to fail, and the 1–10 minutes necessary to reestablish it makes it impractical to rely on broad tuning for measurements in rapid succession.

The UV beam is free-space coupled over ∼10 m to the cryogenic dewar. A small fraction is sampled as an intensity reference for balanced absorption spectroscopy. The remainder of the probe beam reflects from the cell mirror, passing twice through the atomic ensemble. Both the probe and the reference beam intensities are monitored by gated photomultiplier tube (PMT) modules, which are gated off for ablation. Since optical filters are hard to find for this wavelength, rejection of unwanted light was accomplished by a combination of spatial and reflective filtering using right-angle reflection from dielectric mirrors in long lens tubes.

Each mirror, coated for >99% reflectivity at 207 nm, reflects ≈4% of out-of-band light on average. In addition, the dewar is shrouded in black tarp and the room lights are turned off. The signal-to-noise of absorption measurements is then limited by beam motion relative to the cell and to the PMTs, likely caused by vibrations of the dewar and cell relative to the optics tables that contain the doubling cavity and routing optics.

2.3 Experimental procedure

2.3.1 Momentum transfer cross section comparison

The antimony–helium-4 momentum transfer cross section σ_d can be determined from Equation 2.2 by observation of antimony diffusion if the helium density n_b is known. In practice, absolute measurement of n_b at low temperatures is complicated by the effects of transpiration and adsorption of helium onto cold surfaces, and it is not directly measured in this experiment. Under carefully controlled conditions in previous experiments, however, the density was measured and used to calibrate σ_d for certain benchmark atoms and molecules in the range of 1 K [70, 71]. It is thus possible to calibrate the cross sections of other atoms by comparing their diffusive motion to that of a benchmark species in the same (unknown) buffer gas density. Manganese is a second-order benchmark species, the cross section $\sigma_{\mathrm{d,Mn–^3He}}$ having been calibrated against that of the first-order benchmark species chromium [58]. In the case of chromium, n_b was determined by adding a known quantity of helium-3 in gas phase to a cell of known volume, after saturating the available surface area.

The comparison of σ_d between antimony and manganese is conducted as follows. The cell is filled to an unknown but relatively high density of helium-4 buffer gas (σ_d for manganese was calibrated using helium-3, and so this is an imperfect comparison). Two separate YAG lasers of equal pulse energy are aligned to the antimony and manganese targets, respectively.

One of the targets is ablated and the atomic diffusion measured, and several repetitions are made over about 3 min before switching to ablate the other target. The probe lasers are also interchanged with a flip-mounted mirror, and share the same beam path through the dewar and to the same PMTs. Manganese is detected on the $^6S_{5/2} \rightarrow {}^6P_{7/2}$ transition at 403.2 nm using a diode laser. The weak reflections of the manganese probe from the deep UV optical coatings of the reflective filters described in Section 2.2.5 are sufficient for good signal-to-noise in measuring absorption.

Diffusion lifetime comparisons of manganese and antimony are shown in Figure 2.9. The helium-4 density decays during the experiment, so that the lifetimes steadily decrease. The lifetimes for manganese diffusion are fit to a decaying exponential, and then the set of antimony lifetimes is scaled to minimize the sum of squares of the residuals from this fit. The resulting scale factor yields the cross section ratio

$$\frac{\sigma_{\mathrm{d,Mn–^4He}}}{\sigma_{\mathrm{d,Sb–^4He}}} = \sqrt{\frac{\mu_{\mathrm{Sb}}}{\mu_{\mathrm{Mn}}}} \left(\frac{\tau_{\mathrm{d,Mn}}}{\tau_{\mathrm{d,Sb}}} \right), \tag{2.8}$$

where μ_X is the reduced mass of the colliding X–^{4}He system.

The experiment was conducted twice, using two different quantities of filled helium-4. For the larger fill, the helium density was observed to decay more quickly. The two values obtained for the cross section ratio are 1.94 after the smaller fill and 1.56 after the larger fill. The discrepancy may reflect an ablation-induced difference in the buffer gas density, since the two species are produced using separate YAG beams, only one of which is used at a time. Helium-4 adsorbed to cell surfaces heated by ablation may temporarily increase the buffer gas density. For this reason, it is preferable to ablate both targets simultaneously each time, as is done for the calibration of $\sigma_{\mathrm{d,Al–^3He}}$ described in Section 3.4.4. Since this was not the procedure used for the antimony-manganese comparison, the cross section ratio is taken to be the geometric mean of the two observed ratios, with their discrepancy added as systematic error in quadrature with measurement error, to yield $\tau_{\mathrm{d,Sb}}/\tau_{\mathrm{d,Mn}} = 0.57(7)$. The resulting

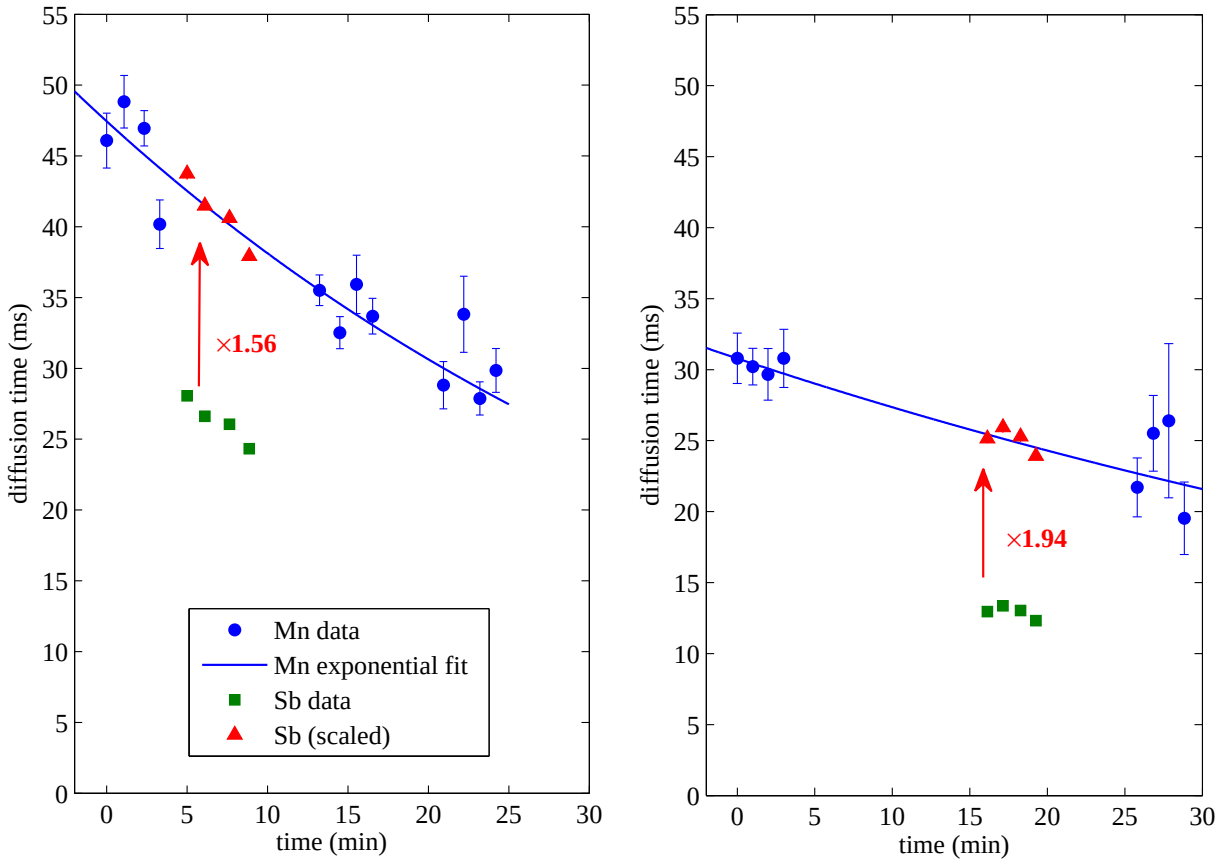

Figure 2.9: Comparison of momentum transfer cross sections $\sigma_{\mathrm{d,Sb\text{–}^4He}}$ and $\sigma_{\mathrm{d,Mn\text{–}^4He}}$. The cell is filled with ^{4}He, which decays on a ≈1-hour timescale. We observe diffusion of Mn before and after measuring Sb diffusion. The scaling factor required to minimize χ^2 for the Sb data with respect to the exponential fit to the Mn data is equal to the cross section ratio $\sigma_{\mathrm{d,Mn\text{–}^4He}}/\sigma_{\mathrm{d,Sb\text{–}^4He}}$. The two figures present two realizations of the experiment with different ^{4}He filling amounts. The discrepancy between the two scaling factors is likely due to variations in the amount of ^{4}He desorbed from the cell walls by the two ablation lasers.

cross section calibration is $\sigma_{\mathrm{d,Sb\text{–}^4He}} = 5.7(7) \times 10^{-15}$ cm^2, assuming $\sigma_{\mathrm{d,Mn\text{–}^4He}} = \sigma_{\mathrm{d,Mn\text{–}^3He}}$.

2.3.2 Zeeman relaxation model

Zeeman relaxation in antimony–helium collisions is investigated by monitoring the lifetime of the $m_J = J = 3/2$ sublevel of the ground state as a function of buffer gas density. The time constant for relaxation to lower-energy states is found by summing the contributions of transitions to all other ground state sublevels,

$$\tau_{\mathrm{R}} = \frac{1}{n_{\mathrm{b}} k_{\mathrm{R}}}, \tag{2.9}$$

$$k_{\mathrm{R}} = \sum_{m'_J \neq J} k_{\mathrm{R},m_J \to m'_J}, \tag{2.10}$$

where k_{R} is the total Zeeman relaxation rate coefficient. At zero temperature, the $m_J = J$ state decays under the combined effects of diffusion and relaxation. However, at finite temperature there are two important modifications to the time dependence. First, atoms with $m_J < J$ will also experience m_J-changing collisions, and the collision energy will occasionally be sufficient to promote an atom to a state of higher m_J, thus re-populating the stretched state [64, 72]. These thermal excitations will slow the relaxation to equilibrium, an effect that is amplified at higher temperatures and in cases of atoms with many closely-spaced sublevels, such as the lanthanide rare-earth atoms studied in Chapter 4. This effect is numerically modeled for the specific experimental conditions used to study antimony, using the thermal excitation model described in [64]. Two extreme cases were chosen as bounds: (1) Zeeman relaxation transitions can only occur for $\Delta m_J = \pm 1$; and (2) transitions can occur to any sublevel. The numerical simulation suggests that thermal excitations introduce an τ_{R} overestimate of <20% for $B > 0.7$ T at a temperature of 800 mK (Figure 2.10).

The second modification to the $m_J = J$ state lifetime is due to the thermal population that remains even at equilibrium. The time dependence of the $m_J = J$ state population N_J,

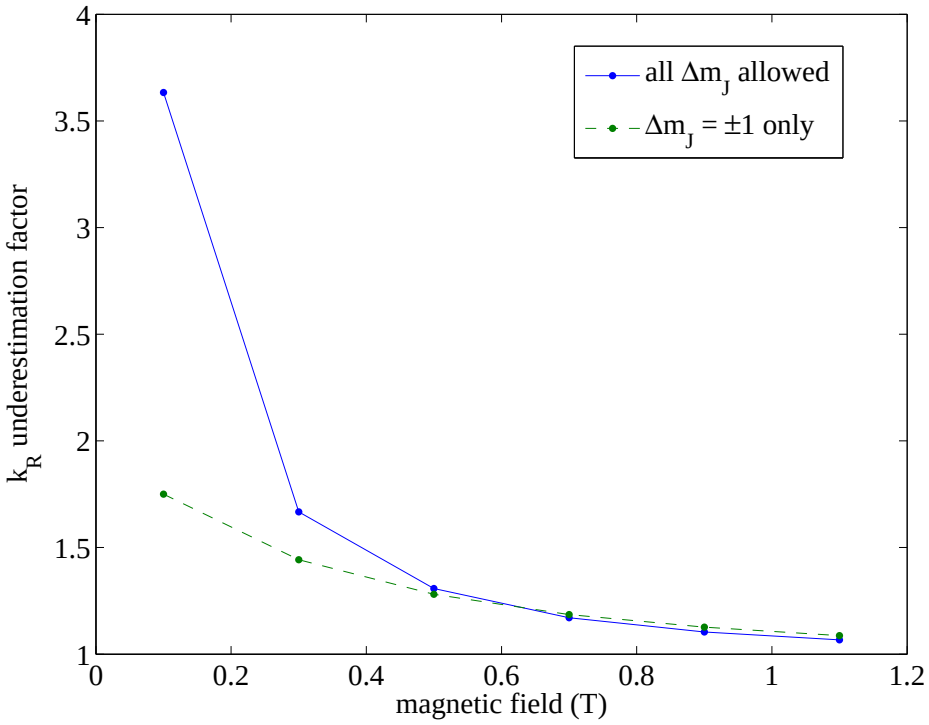

Figure 2.10: Simulation of Sb relaxation dynamics including thermal excitations at $T = 800$ mK. The two cases plotted are opposite selection rule extremes, with relaxation transitions occurring either only to neighboring states or to all states. The vertical axis is the factor by which the decay of the $m_J = J$ state decay appears slower than the true Zeeman relaxation rate.

neglecting thermal excitations, is

$$N_J(t) = N_0 e^{-t/\tau_{\rm d}} \left(f_{\rm eq} + (1 - f_{\rm eq}) e^{-t/\tau_{\rm R}} \right), \tag{2.11}$$

where N_0 is the initial state population and

$$f_{\rm eq} = \frac{\exp\left[-\dfrac{g_J J \mu_B B}{k_B T}\right]}{\sum_{m_J} \exp\left[-\dfrac{g_J m_J \mu_B B}{k_B T}\right]} \tag{2.12}$$

is the thermal equilibrium fraction of the total population that occupies the $m_J = J$ state at temperature T and magnetic field B, for ground state Landé g-factor g_J. Note that at zero temperature, $f_{\rm eq} = 0$ and Equation 2.11 simplifies to the appropriate simple exponential

decay.

Combining Equations 2.4 and 2.9 allows the relaxation lifetime to be expressed as

$$\begin{aligned} \tau_{\mathrm{R}} &= \frac{32}{3\pi}\left(\frac{1}{\bar{v}^2 G}\right)\left(\frac{1}{\tau_{\mathrm{d}}}\right)\left(\frac{k_{\mathrm{d}}}{k_{\mathrm{R}}}\right) \\ &= \frac{32}{3\pi}\left(\frac{\gamma}{\bar{v}^2 G}\right)\left(\frac{1}{\tau_{\mathrm{d}}}\right), \end{aligned} \tag{2.13}$$

where $\bar{v}$ is the mean inter-species velocity and G is a geometric factor defined in Equation 2.5. The second equality has made use of the elastic-to-inelastic collision ratio γ (Equation 1.4). Equation 2.13 conveniently has no explicit dependence on the helium density and varies only with τ_{d}. Therefore measurement of both the relaxation and diffusion lifetimes (along with the cell geometry and temperature) is sufficient to determine γ without the influence of uncertainty in the buffer gas density or momentum transfer cross section calibration.

While it is in principle possible to extract γ from a single measurement, many measurements are made while varying the helium density in order to confirm that τ_{R} varies inversely proportionally to τ_{d}. This provides a check against systematic error. In particular, there may be other processes contributing to or dominating the decay of the $m_J = J$ state—such as molecule formation [73]—which will exhibit a different dependence on buffer gas density.

2.3.3 Lifetime measurements

Extracting τ_{R} from fits to Equation 2.11 is more reliable if τ_{d} can be independently determined and eliminated as a free parameter, especially at low temperatures where f_{eq} is small. Ideally, the lifetime of the $m_J = J$ state is measured at finite B and at $B = 0$ under identical conditions. However, since it takes 10–100 s to ramp the magnetic field, and also since doing so induces some measure of eddy-current heating, this comparison risks systematic error. Instead, the lifetimes of the $m_J = J$ and $-J$ states are compared at very similar finite values of B, which can be switched more rapidly with little heating. The $m_J = -J$ state has the

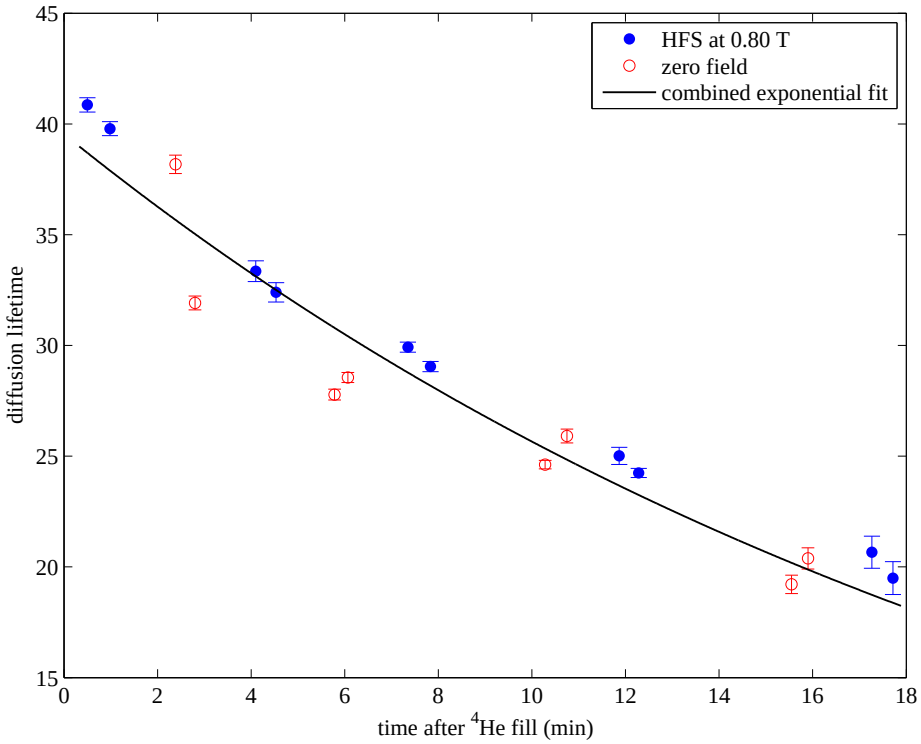

Figure 2.11: Comparison of Sb diffusion times of the $m_F = 4$ state of ^{121}Sb measured at zero magnetic field and of the $m_J = -J$ state at $B = 0.80$ T. No difference is observed, confirming that in-field decay is an accurate measure of the field-free diffusion time given by Equation 2.4.

highest thermal fraction of all sublevels, such that its diffusive decay can still be observed after the Zeeman temperature has reached equilibrium in order to determine τ_d. In order to ensure that the $m_J = -J$ state decay at late times is not influenced by the magnetic field, we compare the in-field state lifetime to that of zero-field diffusion by alternately ramping the magnetic field on and off over a long period of time, slowly enough to avoid significant disturbance of the buffer gas density and temperature. As shown in Figure 2.11, no field dependence is observed, confirming that the $m_J = -J$ state lifetime is an accurate yardstick for τ_d.

As mentioned in Section 2.2.5, tuning the detection laser system over more than a few GHz cannot be reliably accomplished quickly. Hence it is impractical to compare different

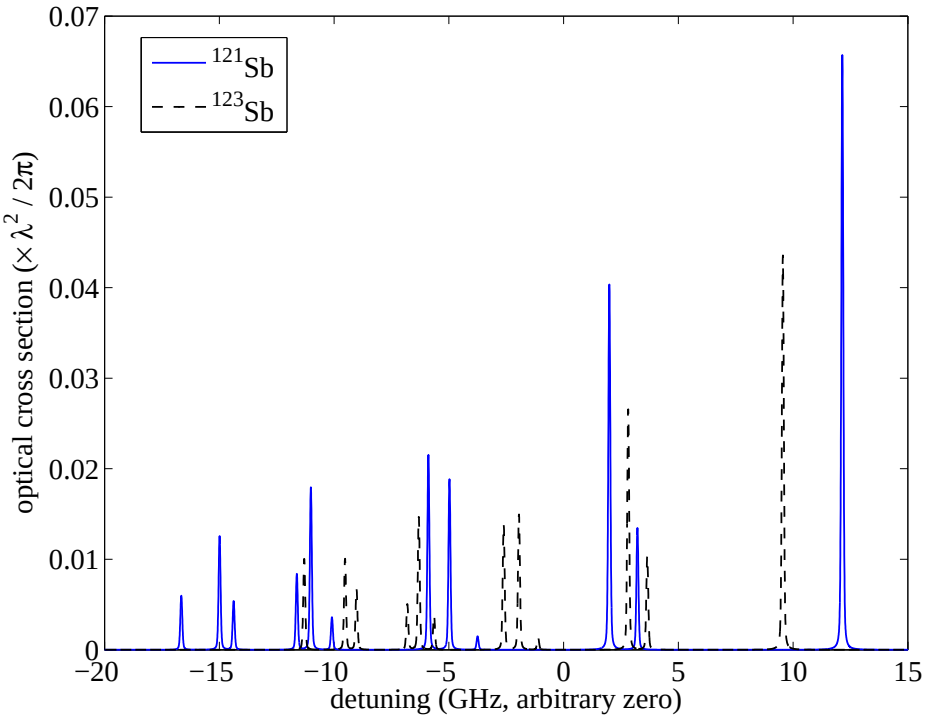

Figure 2.12: Simulated zero-field hyperfine spectrum of Sb at 800 mK.

state lifetimes unless the states have optical transitions that are closely spaced in energy. An additional complication in the case of the $^4S_{3/2} \rightarrow {}^4P_{5/2}$ transition of antimony is that the hyperfine spectrum is quite broad and dense, with 24 lines spanning about 30 GHz at zero field, splitting into 112 lines in a large magnetic field (Figures 2.12 and 2.13). These many lines behave differently in the magnetic field, leading to many crossings, and there is significant overlap in the Doppler- and Zeeman-broadened spectrum. This threatens the possibility of inaccurately identifying spectral features, especially when the laser detuning and magnitude of the magnetic field are not known with absolute precision.

To address both the issue of spectral confusion and the need for closely-spaced lines from opposite sublevels, simulated spectra are constructed from known hyperfine parameters and the isotope shift determined from zero-field spectra ($\Delta\nu_{123\text{–}121} = 273(10)$ MHz; see Figure 2.14). We identify spectral locations where two strong lines, one from each of the

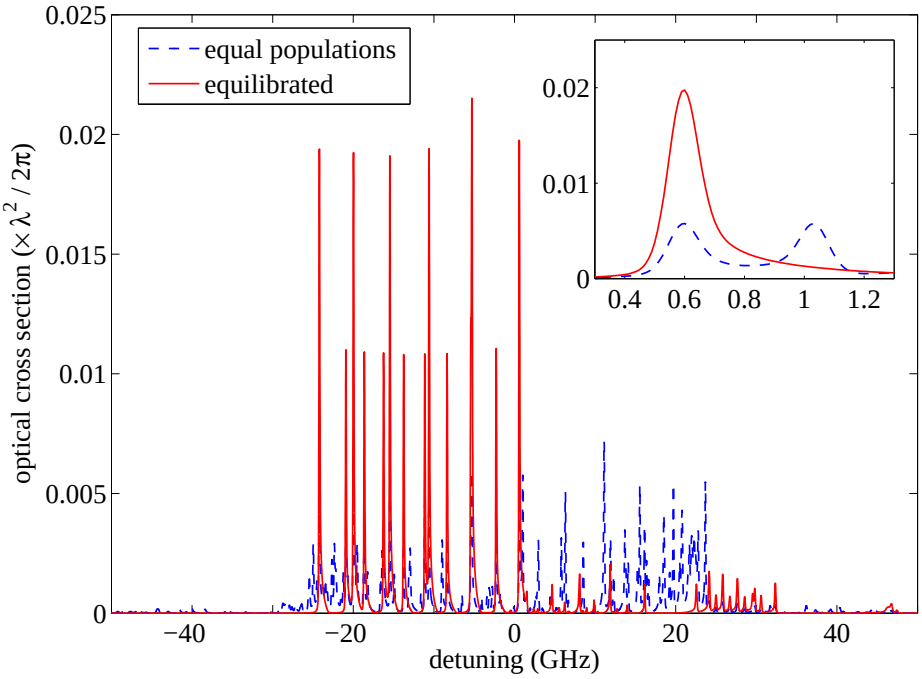

Figure 2.13: Simulated spectrum of Sb in a $B = 0.9$-T Helmholtz field for the cases of infinite T_{Zeeman} (dashed blue) and $T_{\text{Zeeman}} = 800$ mK (solid red). The calculated magnetic field inhomogeneity has been used to generate the asymmetric lineshape, which is then convolved with a Gaussian with 0.2% standard deviation to simulate the effect of further Zeeman broadening due to magnetized ablation targets. Doppler broadening is also included. The inset zooms in on the pair of lines from the $m_J = \pm J$ states which are used to look for Zeeman relaxation. The zero of the detuning axis is the same as in Figure 2.12.

$m_J = J$ and $-J$ states, cross at a certain magnetic field in a relatively sparse region of the spectrum. Such crossings can then be located experimentally, providing a calibration of the detuning and magnetic field as well as a opportunity for rapid comparison of state lifetimes. One of these crossings is shown in Figure 2.15.

Once an appropriate pair of spectral lines is identified, the experiment proceeds as follows. The cell is filled with helium-4 to some density, which then begins to decay. The laser frequency is held fixed to minimize detection noise, and the $m_J = J$ or $-J$ state is brought into resonance by slight adjustment (≈10%) of the magnetic field. After ablation, the optical density ($OD = \int n\,\sigma\; dz$) of the atomic ensemble is measured, and this process is repeated

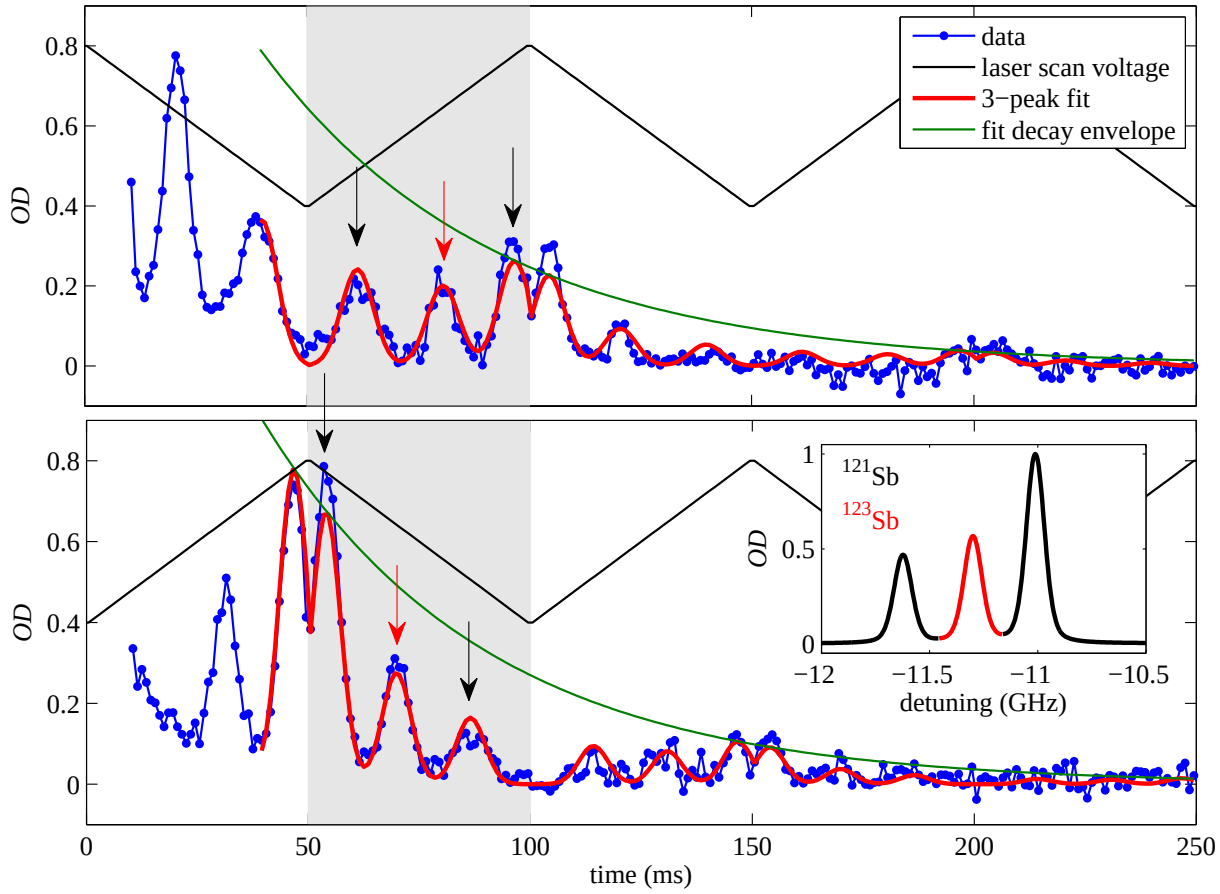

Figure 2.14: Measurement of the Sb $^4S_{3/2} \rightarrow {}^4P_{5/2}$ isotope shift. The laser is scanned over 3 peaks (a single scan is highlighted in gray), which simulation of the hyperfine spectrum identifies as the $m_F = 2 \rightarrow 3$ and $3 \rightarrow 3$ transitions of ^{121}Sb (black arrows) and the $m_F = 2 \rightarrow 1$ transition of ^{123}Sb (red arrow). The laser can only be stably scanned over this range at $\leq$10 Hz, so there is significant spectral distortion due to diffusive decay ($\tau_\mathrm{d} \approx$ 50-ms). The scanned data trace is fit to a 3-peak spectrum (inset) repeated at the scan rate within a decaying exponential envelope (dashed green). To mitigate nonlinearity in the laser scan, the measurement is repeated with the scan phase shifted by 180°. The two results bound the measurement confidence interval and are averaged to give a final value of $\Delta\nu_{123\text{–}121} = 273(10)$ MHz.

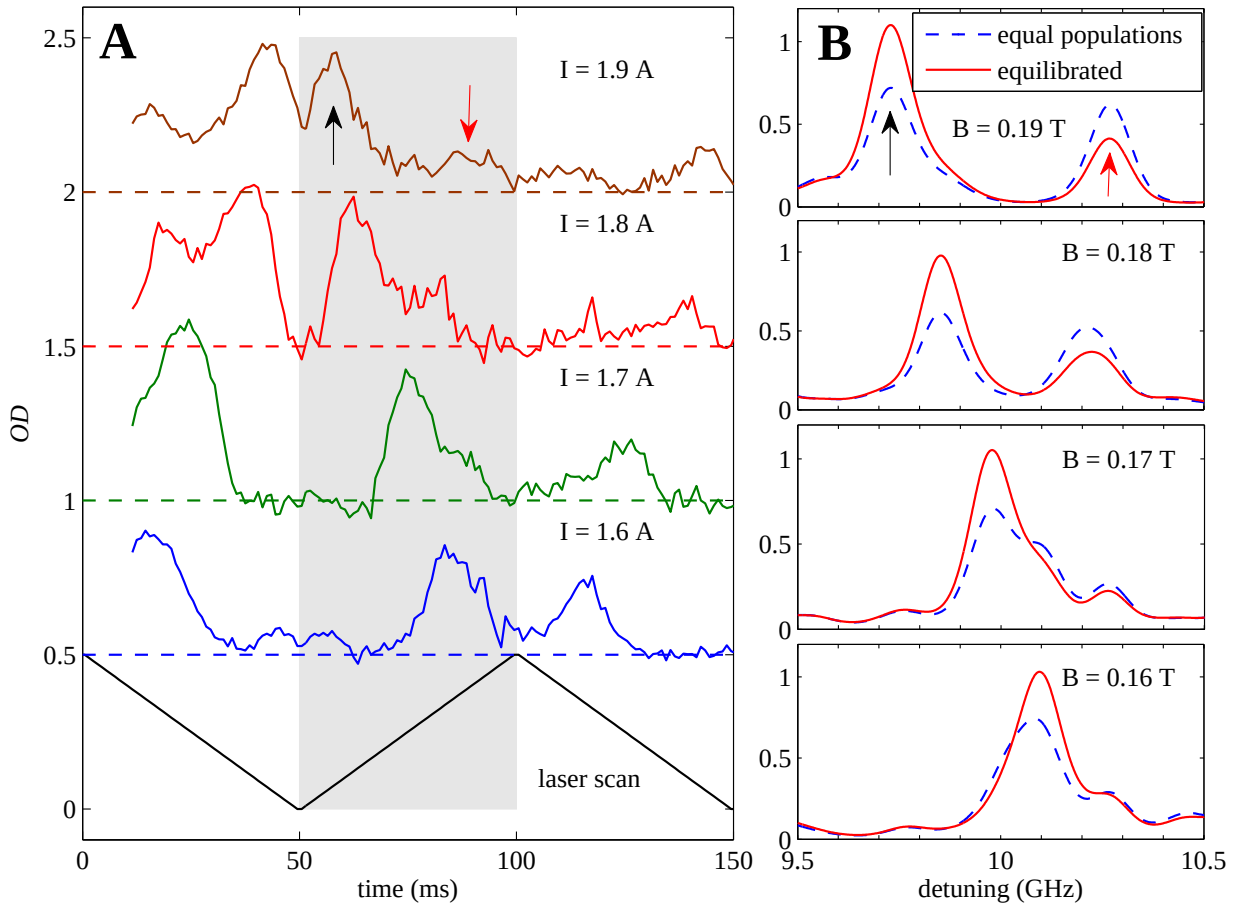

Figure 2.15: Calibration of simulated spectra by observing the crossing of two Zeeman-shifted lines, in this case from the $|m_J, m_I\rangle = |-3/2, +5/2\rangle$ state of ^{121}Sb (black arrows) and the $|+3/2, +5/2\rangle$ state of ^{123}Sb (red arrows). (A) The ≈800-mK data at different magnet currents are compared to (B) the simulations to determine the magnetic field and laser detuning, and the crossing provides positive identification of the two primary peaks as high- and low-field-seeking states. The traces in (A) have been offset vertically for clarity; the dashed lines are $OD = 0$ for each trace. The dashed blue and solid red traces in (B) simulate the spectrum for infinite T_{Zeeman} and $T_{\text{Zeeman}} = 1$ K, respectively, showing the population transfer to lower m_J with cooling. The single data scan highlighted in gray is consistent with T_{Zeeman} having equilibrated to the cell temperature.

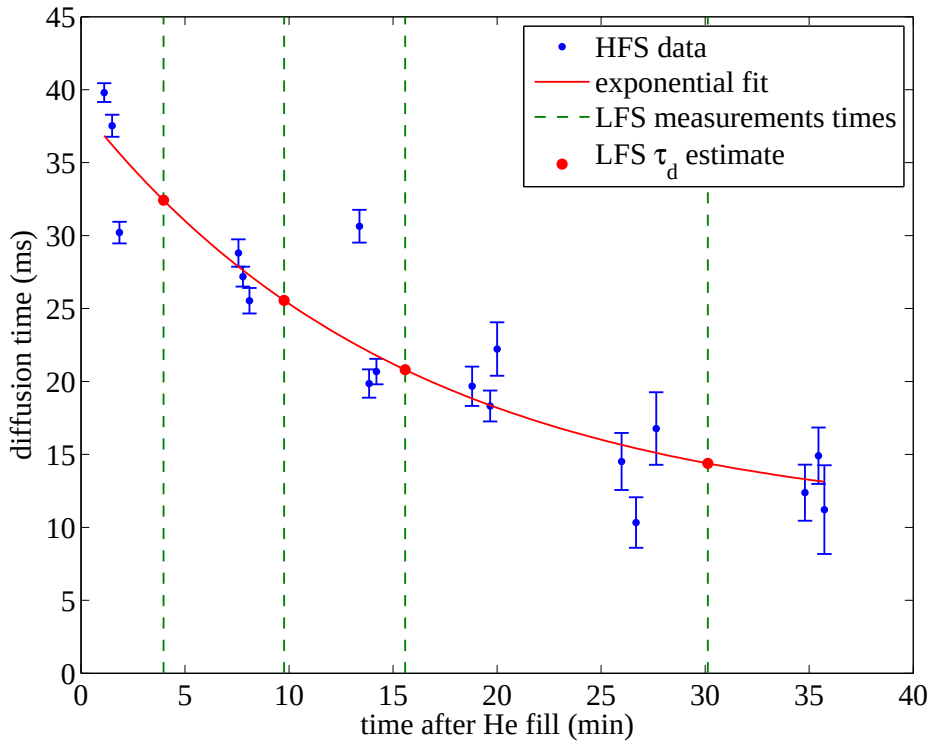

Figure 2.16: Measurements of HFS ($m_J = -J$) diffusion used to estimate the diffusion time at the moments of LFS ($m_J = J$) decay measurements.

several times, alternating between the two states about every 2 min. For each measurement of the $m_J = -J$ state, the data are fit to exponential decay, with the fit restricted to times after which the Zeeman temperature has reached equilibrium. The results from all fits are subsequently fit to the model function

$$n_\mathrm{b} \propto \tau_\mathrm{d} = a\, e^{-t/b} + c, \tag{2.14}$$

which approximates the buffer gas decay profile very well within measurement error. The additional positive fit parameter c is necessary for good fits, suggesting that the helium decay is not well described by a single exponential, as could be the case if a significant quantity of the added helium temporarily adsorbs to the walls. The fit is used to interpolate the values of τ_d for the times corresponding to $m_J = J$ LFS state decay measurements (see Figure 2.16),

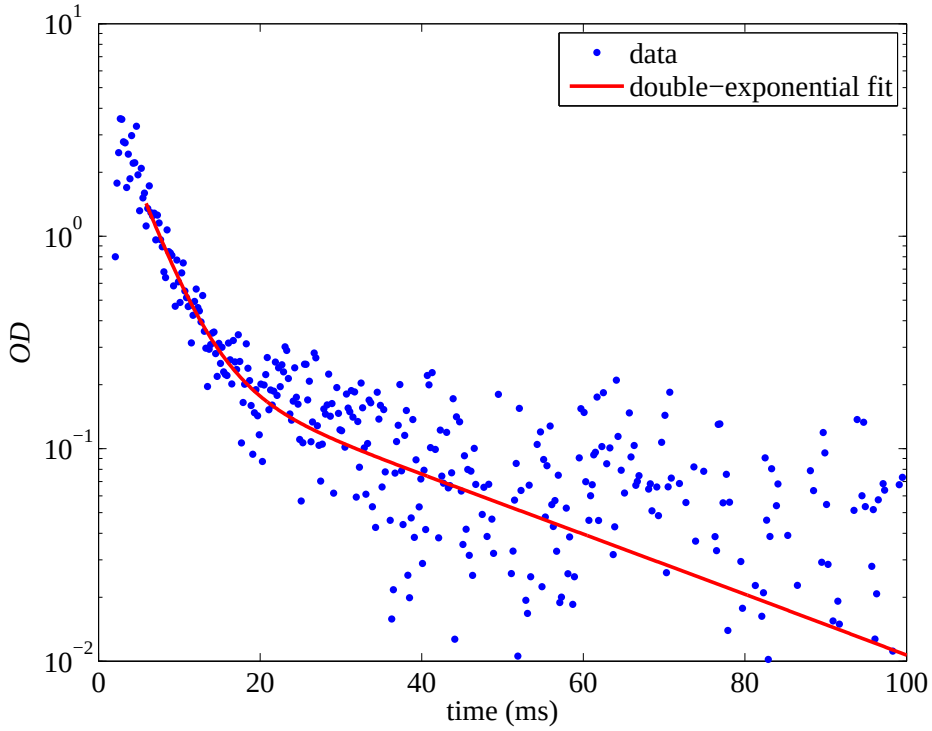

Figure 2.17: Decay of the $|m_J, m_I\rangle = |+3/2, -5/2\rangle$ state of ^{121}Sb at $B = 0.86$ T and $T_{\text{cell}} = 800$ mK, along with the fit to Equation 2.11. The rapid decay before $t = 20$ ms is likely influenced by cooling and not a reliable indicator of the Zeeman relaxation rate.

which are then used to constrain the fits of those data to Equation 2.11.

2.4 Results and discussion

2.4.1 Upper bound on Zeeman relaxation rate

An example of $m_J = J$ state decay at $B = 0.86$ T is shown in Figure 2.17, along with the bimodal decay fit to Equation 2.11. The results of many such fits over a range of buffer gas densities are plotted in Figure 2.18. There is no statistically significant dependence of τ_{R} on τ_{d}, meaning that the apparent relaxation time is independent of buffer gas density. Therefore, the decay of the stretched LFS state is not due to spin relaxation.

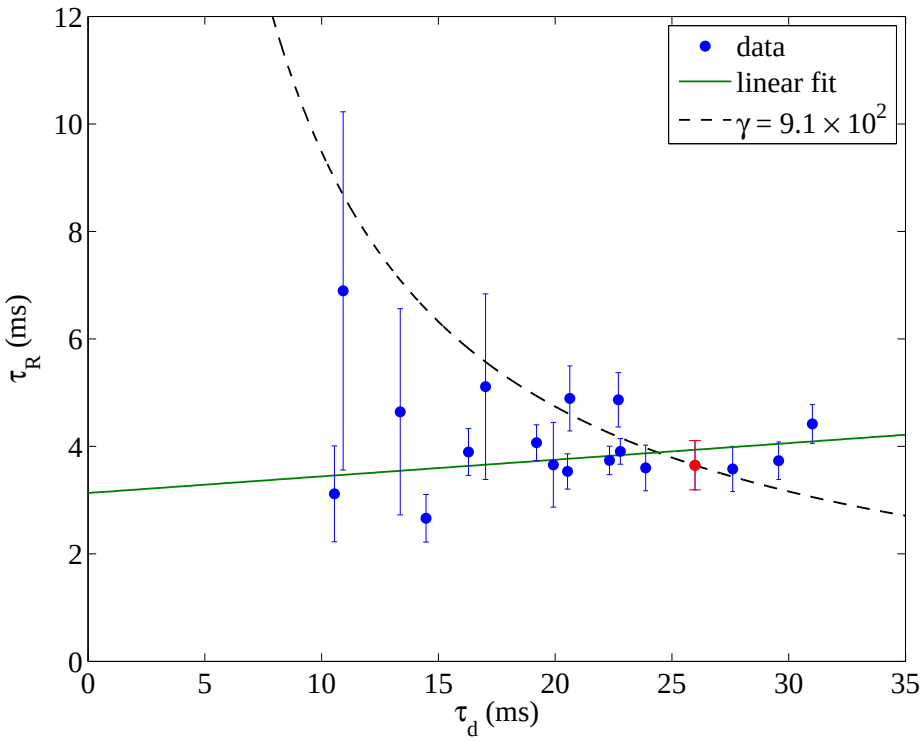

Figure 2.18: Apparent Zeeman relaxation lifetime τ_{R} *vs.* diffusion time τ_{d}. The data do not follow the expected trend (Equation 2.13, dashed black line) and a linear fit (green line) yields a slope that is statistically consistent with zero. Hence the observed τ_{R} is likely due to cooling and is therefore greater than the true Zeeman relaxation lifetime. The red point is used to set the plotted bound of $\gamma \leq 9.1 \times 10^2$. The data with lower diffusion times may be systematically biased to low τ_{R} by variations in buffer gas density caused by ablation (see discussion in Section 2.4.1).

Most likely, the early decay in Figure 2.17 is due to cooling of the buffer gas and cell during this time, with rapid Zeeman relaxation ensuring that the Zeeman temperature remains close to equilibrium with the translational temperature. Figure 2.4 gives the zero-field cooling profile measured from fits to a Voigt profile. This profile is fit to exponential decay and the result is used to compute the instantaneous equilibrium fraction f_{eq} as a function of time. For very rapid Zeeman relaxation for which $\gamma \approx 1$, the stretched LFS state population will closely track f_{eq} and strongly resemble the decay profile in Figure 2.17. If early-time decay of the LFS state is due to slow cooling, then the extracted τ_{R} values are likely to monotonically

increase with $\tau_{\rm d}$ at higher buffer gas densities. This behavior is due to slower heat diffusion in the buffer gas, which increases the cooling time constant. Such a trend is suggested in Figure 2.18, although it is not statistically significant.

Without complete knowledge of the temporal and spatial cooling profile it is not possible to extract the Zeeman relaxation rate from the observed decay of the stretched LFS state. However, the observation of equilibrated Zeeman and translational temperatures allows for the establishment of an upper bound for γ. To establish this bound, data are selected from the $B = 0.86$ T experimental run. At this field, the thermal equilibrium fraction in the stretched LFS state is minimal, but detectable, which aids in suppression of systematic errors.

For the data taken at low buffer gas densities, the helium desorbed from the walls by the ablation pulse may significantly increase the buffer gas density for a short period of time before being re-adsorbed after the cell walls cool. In such a situation, diffusion times measured after this period will underestimate the density during the time that Zeeman relaxation was occurring. This would introduce a systematic bias to lower Zeeman lifetimes, and hence lower values of γ. To avoid this, spectra in which $\tau_{\rm d} \approx 25$ ms (where the signal and lifetime are large enough for careful study) are analyzed and the decay after $t = 5$ ms is found to be consistent with a constant helium density. Hence only data for which $\tau_{\rm d} > 25$ ms are considered. The strictest bound is found by using the data point highlighted in red in Figure 2.18 and inverting Equation 2.13 to yield

$$\begin{aligned} \gamma &\leq \frac{3\pi}{32}\left(\bar{v}^2 G \tau_{\rm d} \tau_{\rm R}\right) \\ \gamma &\leq 9.1 \times 10^2. \end{aligned} \tag{2.15}$$

The bound of γ is the most accurate experimental quantity for comparison to theoretical calculations, since Equation 2.15 is not sensitive to precise knowledge of the buffer gas density.

2.4.2 Theory of spin-orbit induced Zeeman relaxation

The Hamiltonian for the system of antimony or other pnictogen atoms interacting with helium is

$$\hat{H} = -\frac{\hbar^2}{2\mu R}\frac{\partial^2}{\partial R^2}\,R + \frac{\hat{\ell}^2}{2\mu R^2} + \hat{V}_{\rm nr} + \hat{V}_{\rm SO} + \hat{V}_{\rm B}, \tag{2.16}$$

where μ is the reduced mass, R is the interatomic distance, $\hat{\ell}$ is the rotational angular momentum of the nuclei, and $\hat{V}_{\rm nr}$, $\hat{V}_{\rm SO}$ and $\hat{V}_{\rm B}$ are operators describing the nonrelativistic electrostatic interaction, spin-orbit interaction, and interaction with the magnetic field, respectively. The operator $\hat{V}_{\rm SO}$ comes about through the relativistic motional magnetic field generated by electrons moving through the electric field generated by the nucleus. For a single electron around a nuclear charge Z,

$$\hat{V}_{\rm SO} = -\boldsymbol{\mu}\cdot\left[\frac{\boldsymbol{v}}{c^2}\times\boldsymbol{\mathcal{E}}_{\rm nuc}\right] = -\boldsymbol{\mu}\cdot\left[\frac{\boldsymbol{v}}{c^2}\times\left(\frac{Z}{4\pi\epsilon_0 r^2}\,\hat{\boldsymbol{r}}\right)\right], \tag{2.17}$$

from which it follows that $\hat{V}_{\rm SO}\propto Z/c^2r^3$. Using $\langle r\rangle\propto a_0/Z$, where a_0 is the Bohr radius, the approximation can be made that $\langle\hat{V}_{\rm SO}\rangle\propto Z^4$. Consideration of additional electrons will not significantly alter this result, both because it is dominated by small-orbit contributions that are not screened by other electrons, and also because the contributions from the interaction of $\boldsymbol{\mu}$ with the orbits of other electrons will lack the Z-enhancement and in general add destructively. This strong Z-dependence of $\hat{V}_{\rm SO}$ leads to a wide variation in spin-orbit induced anisotropy as one looks from top to bottom in the periodic table.

The spin-orbit interaction couples the $^4S_{3/2}$ ground state to excited anisotropic ^2P and ^2D states, through which inelastic transitions occur during collisions with helium. To lowest nonzero order, the anisotropy is given by [57],

$$\Delta E(R) = \frac{2}{3}\frac{B_{SP}^2}{E_P^2}\left[V_{P\Pi}(R) - V_{P\Sigma}(R)\right], \tag{2.18}$$

where B_{SP} is the spin-orbit coupling matrix element between the ^4S and ^2P states, E_P is

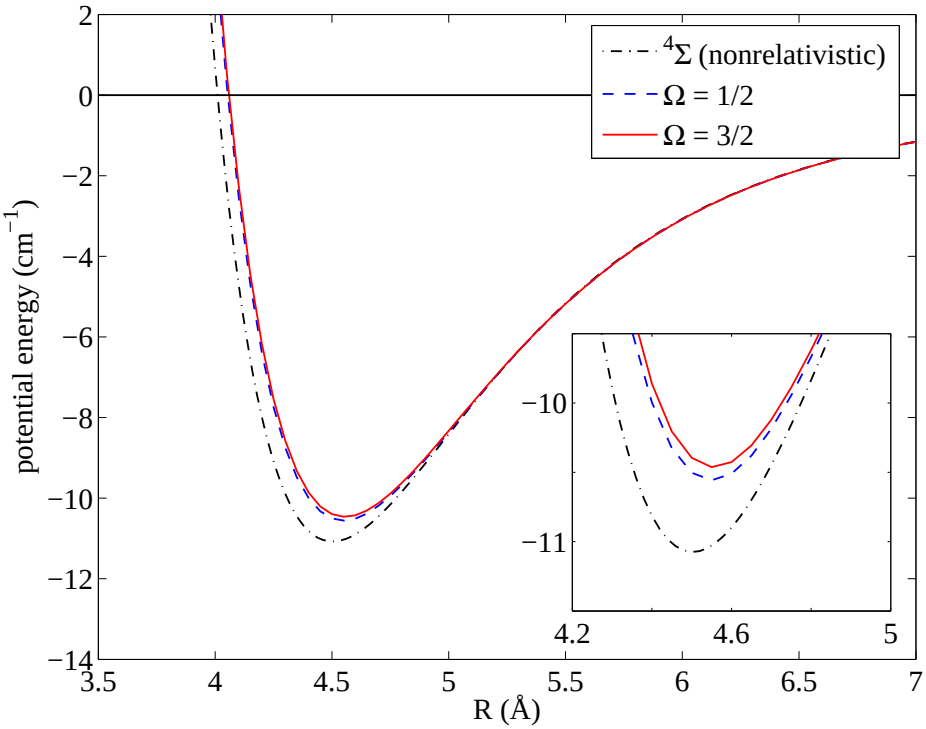

Figure 2.19: Lowest nonrelativistic and spin-orbit-coupled interaction potentials for the Sb–He system, calculated by Buchachenko [74].

the energy of the ^2P state, and $V_{P\Pi}$ and $V_{P\Sigma}$ are the nonrelativistic interaction potentials of the pnictogen atom (^2P) and helium.

2.4.3 Sb–^{4}He calculations

The *ab initio* antimony–helium interaction potentials are computed by Alexei Buchachenko. Figure 2.19 shows the potentials for the lowest states, including both the nonrelativistic case and the spin-orbit-coupled case. The anisotropy $\Delta E(R)$ due to the spin-orbit splitting of the coupled potentials is plotted in Figure 2.20, where it is shown to be an order of magnitude smaller than in the bismuth–helium system.

To calculate collision cross sections, Tscherbul numerically integrated the Schrödinger equation using Equation 2.16 and the *ab initio* potentials [76]. Calculation of the momentum

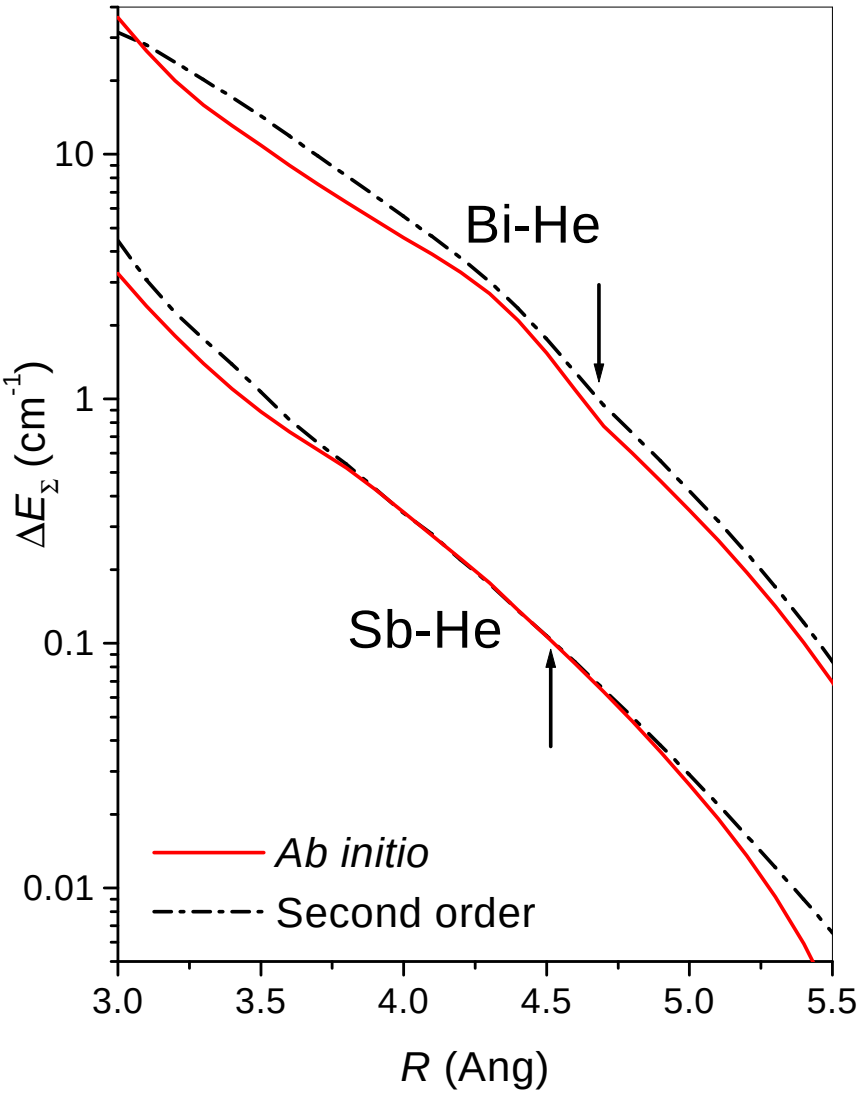

Figure 2.20: Spin-orbit-induced anisotropy $\Delta E(R)$ of the lowest Sb–He and Bi–He interaction potentials. Shown are calculations both from the *ab-initio* potentials as well as from the nonrelativistic potentials using Equation 2.18. The Sb–He system exhibits an order of magnitude smaller anisotropy than the Bi–He system. The arrows indicate the ground state equilibrium distances. Figure courtesy of Alexei Buchachenko [75].

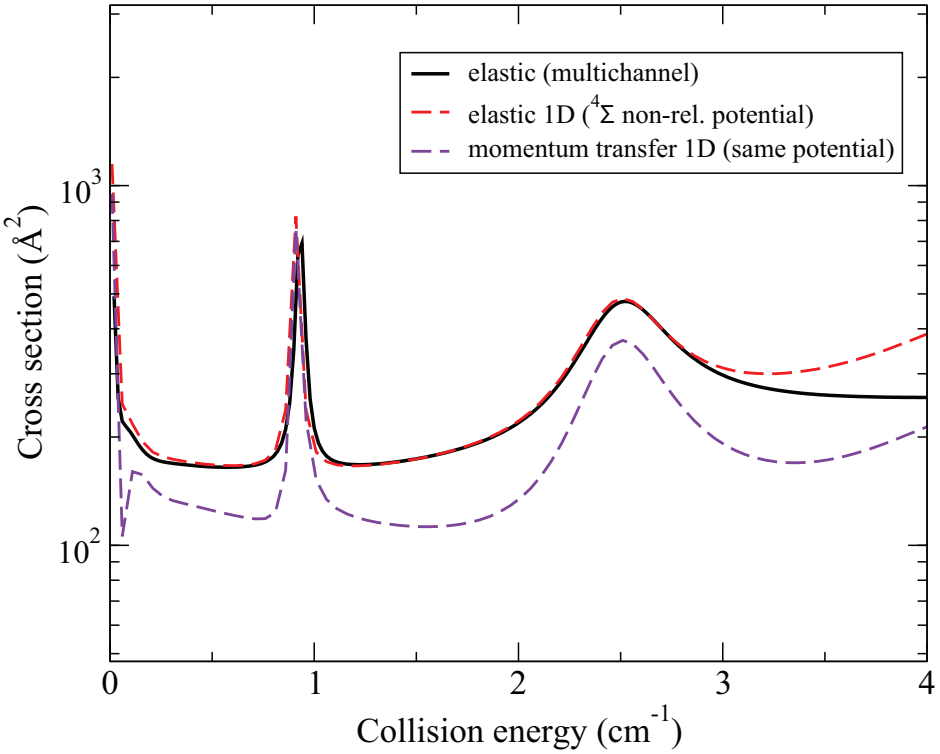

Figure 2.21: Calculated Sb–He total elastic and momentum transfer cross sections. The solid curve is an exact multichannel calculation and the dashed curves are calculated using a 1D approximation that includes only the lowest nonrelativistic adiabatic potential. The excellent agreement between the two calculations of the total elastic cross section (black and red curves) implies that this is a good approximation in this range. Figure courtesy of Timur Tscherbul [76].

transfer cross section (Equation 1.3) is computationally intensive, and so a 1D approximation using only the lowest nonrelativistic adiabatic potential is used for simplicity. This procedure is validated by calculating the total elastic cross section σ_{el} in the same manner and comparing it to the full multichannel calculation. The two methods differ by less than 10% over the temperature range 0.1–3 K, as shown in Figure 2.21. In this range the momentum transfer cross section is ∼30% smaller than the elastic cross section.

Integration over the Maxwell-Boltzmann distribution provides rate coefficients for comparison with the experiment. The ratio γ of the momentum transfer rate to the Zeeman

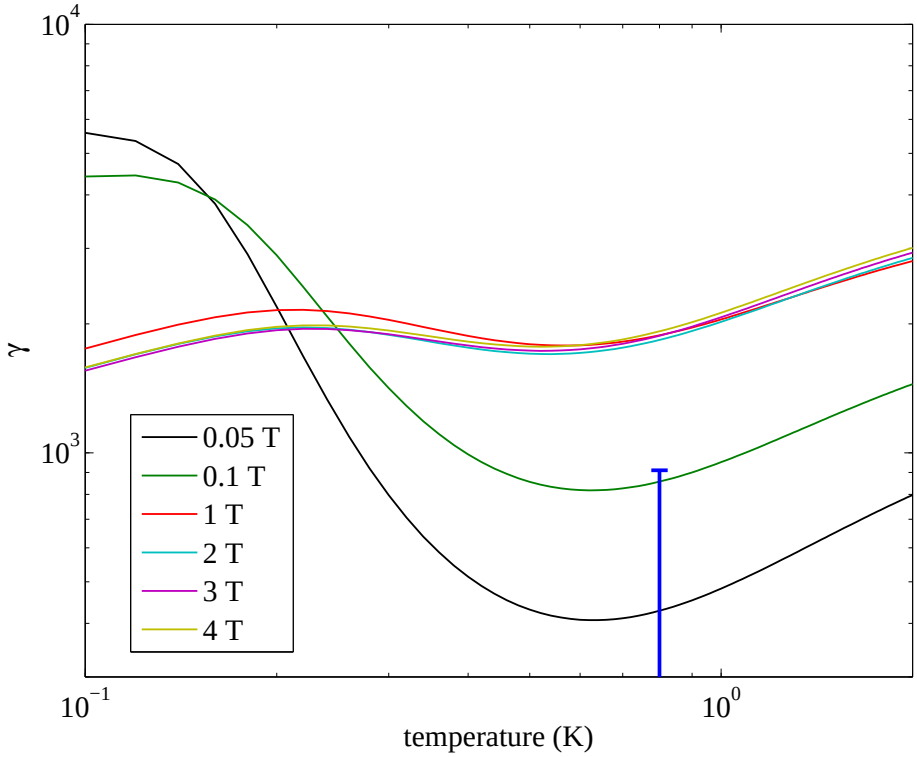

Figure 2.22: Theoretical calculations of the Sb–^{4}He elastic-to-inelastic collision rate ratio γ by Tscherbul [76] using *ab initio* potentials of Buchachenko [74]. The cross sections have been thermally averaged (Equation 1.2). The experimental bound obtained at $T = 800$ mK and $B = 0.86$ T is also shown (thick blue line).

relaxation rate is plotted in Figure 2.22. The calculated $\gamma = 1.88 \times 10^3$ at $T = 800$ mK is not consistent with the experimental bound of $\gamma \leq 9.1 \times 10^2$. To address this discrepancy, the calculation was repeated with the interaction potential scaled by a factor λ between 0.9 and 1.1. The resulting function $\gamma(\lambda)$ is monotonically decreasing with increasing λ over nearly the entire calculated range, such that the calculation comes into agreement with the experiment at $\lambda = 1.1$ (Figure 2.23). This level of inaccuracy is not unreasonable for the *ab initio* calculation [1], and the experimental constraint provides useful feedback to inform similar calculations in the future.

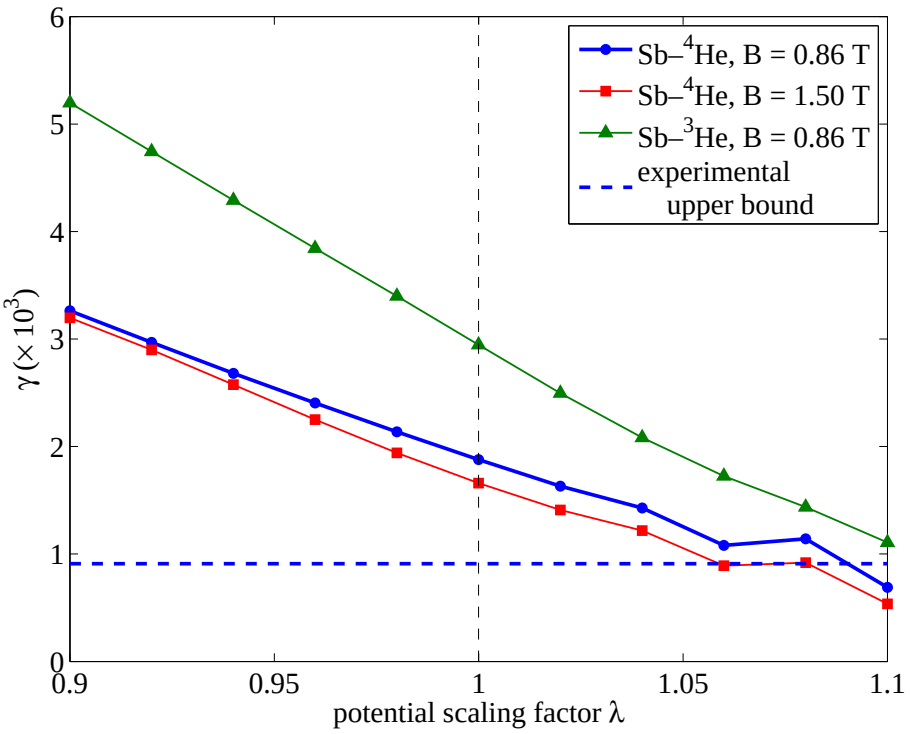

Figure 2.23: Calculations by Tscherbul [76] of the elastic-to-inelastic collision rate ratio γ after scaling the interaction potentials [74] by λ. The blue circles are those corresponding to the experimental parameters. The experimental bound (dashed line) is in agreement with theory for $\lambda = 1.1$. Also shown (green triangles) are calculated results for the Sb–^{3}He system, for which the inelasticity is reduced due the absence of a collision resonance near 1 K.

2.4.4 Summary and future outlook

The results presented here for Zeeman relaxation of antimony in collisions with helium provide a valuable window into the onset of spin-orbit induced anisotropy in pnictogen atoms. The order of magnitude smaller anisotropy in the antimony–helium system compared to bismuth–helium leads to a similar reduction in the calculated Zeeman relaxation rate. However, inelastic transitions are still too rapid for the experiment to measure directly, and γ is far below the value of $\sim 10^4$ necessary for buffer-gas loading of a magnetic trap. As a result, buffer-gas loaded antimony does not present an attractive path to ultracold temperatures, nor is it expected to be a practical alternative to nitrogen as a sympathetic

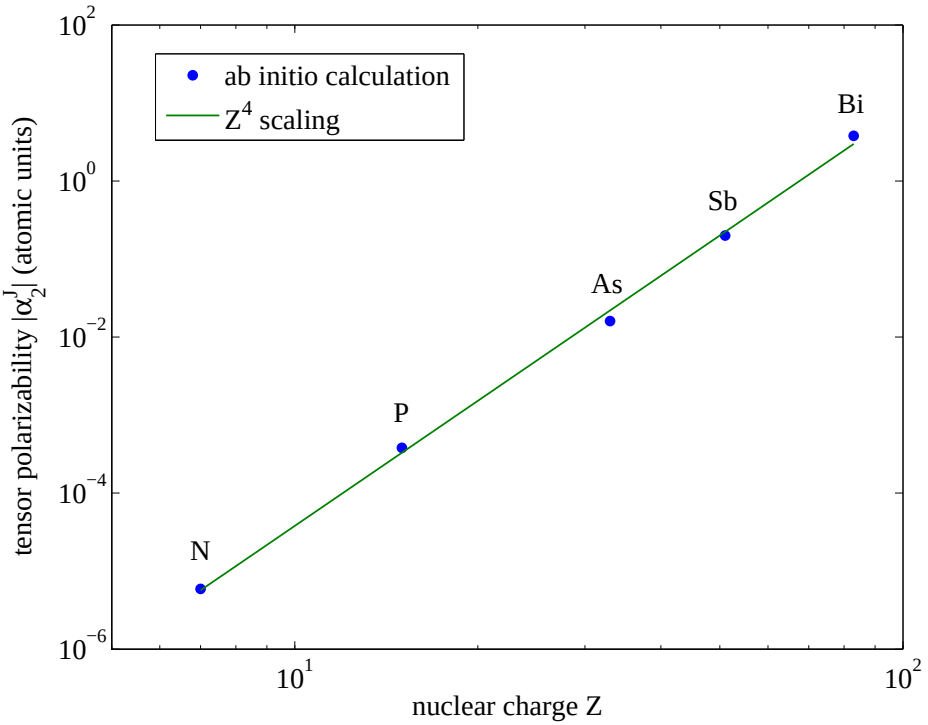

Figure 2.24: Calculated tensor polarizabilities of pnictogen atoms, from [77], along with Z^4 scaling predicted for spin-orbit coupling (see Equation 2.17).

coolant for molecules.

A natural extension of this work is to look further up the pnictogen column to arsenic and phosphorus. The required laser wavelengths are shorter than 200 nm, which is a significant complication to the experiments. There has, however, recently been theoretical effort by Buchachenko to build a qualitative understanding of how spin-orbit effects are manifest from nitrogen to bismuth [77]. Figure 2.24 shows *ab initio* calculations for all pnictogen atoms of the anisotropic tensor polarizability α_2^J, one of the simplest expressions of atomic anisotropy. The calculated values of $|\alpha_2^J|$ closely follow the Z^4 spin-orbit scaling implied by Equation 2.17. Buchachenko specifically cautions against drawing quantitative conclusions from these values, especially for the high-Z atoms, due to convergence issues with the calculations; however, the trend clearly aligns with the expectation of anisotropy induced by

spin-orbit coupling. In addition, the full scattering calculations by Tscherbul *et al.* [57, 76] give values of γ for antimony–helium and bismuth–helium that are separated by about an order of magnitude, similar to the corresponding values of $|\alpha_2^J|$.

If we extend the comparison, the calculation in Figure 2.24 suggests that arsenic will relax significantly more slowly than antimony in collisions with helium, but still quickly enough to make the species marginal for trapping and further cooling. It would then seem that nitrogen is the best candidate for further efforts toward evaporative cooling and toward sympathetic cooling of molecules; a conclusion that is based both on its excellent collisional properties and on the lack of an alternative pnictogen that preserves these properties while offering a more practical optical transition.

Chapter 3

Aluminum–^{3}He collisions

3.1 Properties and prospects of ^2P atoms

The previous chapter described a mechanism for Zeeman relaxation in the pnictogens that arises from perturbation of the spherical symmetry of the ground S-states by nonspherical excited states. In that case, the larger the contribution of $L \neq 0$ states, the larger the probability of an inelastic transition. Yet while electronic orbital angular momentum can introduce the anisotropy that drives these transitions, it is not necessarily the case that non-S state atoms will have rapid inelastic collisions. The next two chapters focus on $L \neq 0$ atoms for which inelastic collisions with helium are largely suppressed, although the mechanisms at play in the two cases are quite distinct.

This chapter describes experiments measuring inelastic collision rates in the aluminum–helium system. The ground $^2P_{1/2}$ state of aluminum and other Group 13 atoms is, perhaps counterintuitively, spherical (see Section 3.2). As a result, Zeeman relaxation is suppressed. Like S-state atoms, inelastic transitions at low temperature occur through collisional mixing

of an excited state,[1] in this case the other state in the fine-structure doublet, the $^2P_{3/2}$ state. The Zeeman relaxation rate for gallium and indium collisions with helium has been shown to be very low [1], and the same may be true for collisions of these atoms with other S-state atoms if the interaction is sufficiently weak, allowing for sympathetic cooling in a magnetic trap. This could open a new class of atoms for study at ultracold temperatures. Laser cooling of Group 13 atoms has already been demonstrated for aluminum [79], gallium [80] and indium [27], and a scheme for laser cooling of thallium has been proposed [81]. Much of the interest in laser cooling these atoms has been to produce controlled, narrow atomic beams for use in creating patterned nanostructures [82]. In addition, there are proposals for microwave lattice clocks [83] and precision measurement of atomic electric dipole moments (EDMs) [81, 84]. Until very recently [22], the best limit for the electron EDM was long set by an experiment using thallium atoms [85]; the sensitivity of such experiments may be improved by using cold atoms to reduce the influence of $\boldsymbol{E} \times \boldsymbol{v}$ systematic effects [86]. The unique ground state electronic structure of Group 13 and halogen atoms also presents new opportunities for cold chemistry [87] and for association of ultracold molecules of novel electronic structure.

3.1.1 Improved study of $X(^2P_{1/2})$–He Zeeman relaxation

The experiments with aluminum described here build upon earlier theory by Tscherbul *et al.* and experiments by Lu *et al.* that demonstrated low inelasticity in collisions of gallium and indium with helium [1]. The mechanism of Zeeman relaxation was shown theoretically to be collisional mixing of the upper $^2P_{3/2}$ state into the ground $^2P_{1/2}$ state. The upper state is highly anisotropic and will readily reorient its magnetic moment in collisions—

[1] Inelastic transitions can also occur due to nuclear spin exchange during collisions with helium-3, however this interaction is quite weak [78].

Table 3.1: Fine-structure splittings Δ and calculated elastic-to-inelastic collision ratios γ for Group 13 and halogen atoms colliding with ^{3}He at $T = 0.5$ K and $B = 0.5$ T, taken from reference [1]. The fine-structure splitting for Tl has been added; it was not included in the calculations.

		γ	
Atom	Δ (cm^{-1})	$J = 1/2$	$J = 3/2$
F	404.14	1.9×10^2	4.7
Cl	882.35	5.0×10^4	2.7
Br	3,685.24	1.3×10^8	3.0
I	7,603.15	1.6×10^9	3.0
Al	112.06	7.0×10^3	2.4
Ga	826.19	4.1×10^6	33.0
In	2,212.60	4.6×10^7	15.1
Tl	7,792.7	—	

the norm for P-states [88]. The Zeeman relaxation rate in the spherical ground state is therefore determined by the degree to which the upper state is mixed, and therefore is strongly dependent on the fine-structure splitting Δ. Table 3.1 gives the values of Δ for several Group 13 atoms, as well as calculated values of γ from reference [1]. Also included are halogen atoms, which have the same pair of lowest-energy fine-structure states with energies inverted such that the metastable $^2P_{1/2}$ lies above the ground $^2P_{3/2}$ state. Table 3.2 presents theoretical and experimental results at low field for the gallium–helium and indium–helium systems, broken down into the three component inelastic processes.

The calculated values of γ for the $J = 1/2$ state shown in Table 3.1 clearly show the expected trend, climbing monotonically with the energy gap as inelastic transitions are suppressed. The experimental results in Table 3.2, however, are inconclusive on this point. Measuring very slow inelastic transition rates within the finite timescale of the experiment can be difficult, and in this case the experiment was able only to provide a lower bound on

Table 3.2: Results of previous work with ^{69}Ga–^{4}He and ^{115}In–^{4}He collisions, taken from reference [1]. Rate coefficients at 5 K and 3 G are given in units of 10^{-17} cm^3 s^{-1} and refer to inelastic transitions *from* the $|J = 1/2, F = J + I, m = F\rangle$ state in the case of m_J-changing collisions and *to* this state for F- and J-changing collisions. The theoretical values in parentheses are calculated for a factor of 1.2 increase in the interaction anisotropy, which is found to give better qualitative agreement with the experiment. The ratios γ have added the contributions for all three inelastic processes.

Atom	Ga		In	
rate coefficient	Expt.	Theory	Expt.	Theory
k_m	< 300	0.8 (2.3)	< 50	3.8
k_F	5.3 ± 1.3	2.3 (6.6)	$< 2.3 \pm 1.4$	0.1
k_J	1.0 ± 0.3	0.03 (1.3)	< 8	0.0004
γ	$> 4.2 \times 10^4$	(2.6×10^6)	$> 3.0 \times 10^5$	6.7×10^6

those rates.[2] Nevertheless, the bounds for γ above 10^4 or 10^5 demonstrated the dramatic suppression of inelasticity in the $^2P_{1/2}$ state.

In order to provide a more definitive and quantitative test of theory in this system, the experiment described here differs in two important ways. First, it is focused on the aluminum atom, for which the fine-structure splitting is only a few times larger than the interaction energy. Second, inelastic collision rates are measured over more than an order of magnitude variation in a strong magnetic field, an important additional parameter axis that reduces the measurement's susceptibility to "accidental" resonances.

In addition to establishing a bound on γ for the ground state, the earlier experiment with gallium directly measured the rate coefficients for F- and J-changing collisions of the $^2P_{3/2}$ state in collisions with helium. These inelastic transitions are also greatly suppressed,

[2]Unlike the antimony experiment described in the previous chapter, in this case the inelastic collisions were too *slow* to be observed. When magnetic trapping can be employed, much slower atom–helium inelastic collision rates are experimentally accessible (see, for example, [2, 32, 63, 89])

despite the absence of an energy barrier. This is in contrast to rapid fine-structure changing collision rates (spin-orbit relaxation) in other systems. For example, fine-structure-changing collisions between ultracold metastable $^3P_2$ ytterbium atoms were observed to be very rapid [90]; theoretical calculations for $^3P_0$ and $^3P_1$ oxygen atoms colliding with helium at both zero magnetic field and $B = 1$ T showed the same below ∼1 K [88, 91].[3] The aluminum–helium system bridges an important gap between these extremes due to its intermediate balance between fine-structure splitting and interaction energy. Hence it is an important test bed to explore spin-orbit relaxation in a nontrivial regime.

3.2 Theory of Zeeman relaxation in $^2P_{1/2}$ atoms

Theoretical calculations of Group 13 and halogen atom collisions with helium were performed by Tscherbul *et al.* [1] by expanding the quantum-scattering formalism developed by Krems and Dalgarno [91] to ^2P atoms with nonzero nuclear spin. Their procedure is summarized here along with new and more detailed calculations for the aluminum–helium system.

The Hamiltonian of the colliding aluminum(^2P)–helium complex is written as a modified version of the parameterization in Equation 2.16:

$$\hat{H} = -\frac{\hbar^2}{2\mu R}\frac{\partial^2}{\partial R^2}R + \frac{\hat{\ell}^2}{2\mu R^2} + \hat{V}(\boldsymbol{R}, \boldsymbol{r}) + \hat{H}_{\mathrm{Al}}, \tag{3.1}$$

where again μ is the reduced mass, $\boldsymbol{R}$ is the interatomic distance, $\boldsymbol{r}$ is the electronic coordinates, and $\hat{\ell}$ is the rotational angular momentum of the nuclei; the operator $\hat{V}(\boldsymbol{R}, \boldsymbol{r})$ is the aluminum–helium interaction potential and the operator

$$\hat{H}_{\mathrm{Al}} = A_{\mathrm{SO}}\,\hat{L}\cdot\hat{S} + \mu_{\mathrm{B}}B\left(\hat{L}_z + 2\hat{S}_z\right) + \hat{H}_I, \tag{3.2}$$

[3]Experimental and theoretical work with titanium–helium collisions also observed suppression of inelasticity [92, 93], and attributed this to the submerged-shell nature of titanium (see Section 4.1).

is the Hamiltonian of the isolated aluminum atom in a magnetic field $\boldsymbol{B}$. $A_{\mathrm{SO}} = 2\Delta/3$ is the spin-orbit constant of the aluminum atom, $\hat{L}_z$ and $\hat{S}_z$ are the projections of the electronic orbital angular momentum and spin operators $\hat{L}$ and $\hat{S}$ onto the field axis, and $\hat{H}_I$ is the hyperfine Hamiltonian.

The fully uncoupled basis $|Jm_J\rangle|Im_I\rangle|\ell m_\ell\rangle$ is used, where m_J, m_I and m_ℓ are the projections of $\boldsymbol{J}$, $\boldsymbol{I}$ and $\boldsymbol{\ell}$ onto the field axis. Following [91], the matrix elements of the interaction potential $\hat{V}(\boldsymbol{R}, \boldsymbol{r})$ are

$$\begin{aligned}
&\langle Jm_J|\langle Im_I|\langle \ell m_\ell|\hat{V}(\boldsymbol{R},\boldsymbol{r})|J'm'_J\rangle|I'm'_I\rangle|\ell' m'_\ell\rangle \\
&\quad = \delta_{m_I m'_I}(-)^{S+J+J'-m_J-m'_\ell} \\
&\qquad \times \left[(2L+1)^2(2J+1)(2J'+1)(2\ell+1)(2\ell'+1)\right]^{1/2} \\
&\qquad \times \sum_{\lambda=0,2} V_\lambda(R) \begin{Bmatrix} L & J & S \\ J' & L & \lambda \end{Bmatrix} \begin{pmatrix} J & \lambda & J' \\ -m_J & m_J - m'_J & m'_J \end{pmatrix} \qquad (3.3) \\
&\qquad \times \begin{pmatrix} \ell & \lambda & \ell \\ -m_\ell & m_\ell - m'_\ell & m'_\ell \end{pmatrix} \begin{pmatrix} L & \lambda & L \\ 0 & 0 & 0 \end{pmatrix} \begin{pmatrix} \ell & \lambda & \ell' \\ 0 & 0 & 0 \end{pmatrix}, \qquad (3.4)
\end{aligned}$$

where the symbols in parenthesis and curly braces are 3-j and 6-j symbols, respectively. V_0 and V_2 are the isotropic and anisotropic parts of the interaction potential, respectively.

Highly accurate *ab initio* aluminum–helium interaction potentials of Σ- and Π-symmetry are obtained from [94] and fitted to analytic functions with proper long-range behavior. Expanding the wave function in the uncoupled basis given above and inserting it into the Schrödinger equation with the Hamiltonian in Equation 2.16 gives a system of close-coupled differential equations. These equations are solved to yield the probabilities for J- and m_J-changing transitions during the collision. In addition, the momentum transfer cross section is calculated from a 1D approximation using the lowest spin-orbit-coupled potential $V_{1/2,1/2}(R)$, similar to the method described in Section 2.4.3. The calculated values of the collision rate

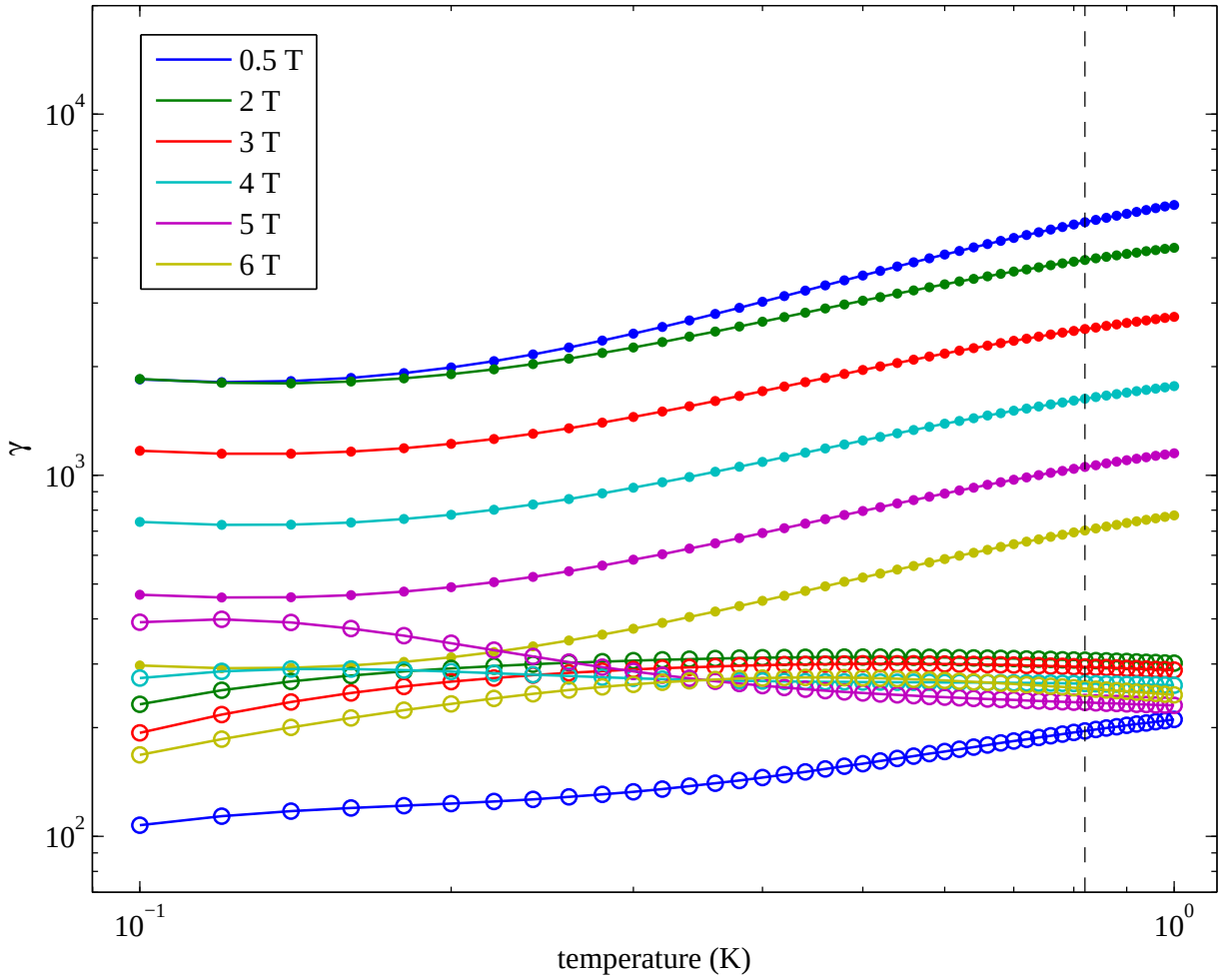

Figure 3.1: Theoretical calculations of the Al–^{3}He collision rate ratios for $^2P_{1/2}$ state m_J-changing (•) and $^2P_{3/2}$ state J-changing collisions (○) by Tscherbul [95]. Both values of γ reflect the ratios of the *ground-state* momentum transfer rate coefficient to the respective inelastic collision rate coefficients. The dashed line is the experimental temperature.

ratio γ are shown in Figure 3.1.

The general behavior of suppressed inelasticity in $^2P_{1/2}$ systems is apparent from analysis of Equation 3.3. Specifically, the first 3-j symbol vanishes for $J = J' = 1/2$, meaning that Zeeman relaxation cannot occur in the $^2P_{1/2}$ manifold at first order. This is the manifestation of the spherical symmetry of the ground state electron distribution. In contrast, the different magnetic sublevels of the upper $^2P_{3/2}$ manifold are directly coupled by the $\lambda = 2$ term in

Equation 3.3, hence Zeeman relaxation proceeds rapidly in this state. As such, Zeeman relaxation of the ground state proceeds through second-order coupling to the $^2P_{3/2}$ state, at a rate suppressed by the state splitting.

The spherical symmetry of the $^2P_{1/2}$ state can be shown directly by expressing the electronic wave function $|\psi\rangle = |J = 1/2, m_J = 1/2\rangle$ in the $|L, m_L\rangle|S, m_S\rangle$ basis:

$$|\psi\rangle = \sqrt{\frac{2}{3}}\,|1,1\rangle|1/2,-1/2\rangle - \sqrt{\frac{1}{3}}\,|1,0\rangle|1/2,+1/2\rangle \tag{3.5}$$

$$= \sqrt{\frac{1}{4\pi}}\left[\sin(\theta)\,e^{i\phi}\,|\downarrow\rangle - \cos(\theta)|\uparrow\rangle\right], \tag{3.6}$$

where the second line makes use of the spherical harmonics $Y_1^1(\theta,\phi)$ and $Y_1^0(\theta,\phi)$ and defines $|\uparrow\rangle$ and $|\downarrow\rangle$ to be the $m_S = \pm 1/2$ electronic spin wave functions. For any function $f(\theta,\phi) = \sum_{\ell m} C_{\ell m}\, Y_\ell^m(\theta,\phi)$, the expectation value is equal to

$$\begin{aligned}\langle\psi|f|\psi\rangle &= \frac{1}{4\pi}\int d\Omega\, f(\theta,\phi)\left[\sin^2(\theta) + \cos^2(\theta)\right] \\ &= \frac{1}{4\pi}\int d\Omega \sum_{\ell m} C_{\ell m}\, Y_\ell^m(\theta,\phi) \\ &= C_{00},\end{aligned} \tag{3.7}$$

i.e., the nonspherical contribution is zero. The nature of the $^2P_{1/2}$ state demonstrates the incompleteness of the argument that $L \neq 0$ atoms are in general not spherical; spin-orbit coupling can produce spherical P-states. As was demonstrated first in [1] and now further investigated in the case of aluminum, these states are correspondingly protected by the spin-orbit splitting from Zeeman relaxation in collisions with helium.

3.3 Optical pumping

Inelastic aluminum–helium collisions are measured by observing the response of the colliding system to perturbation by optical pumping. Both J-changing and m_J-changing collision rates

can be simultaneously extracted using a clean method that employs a single pump/probe laser. This method has advantages compared to observing relaxation to equilibrium after ablation (the method used for antimony in Chapter 2), especially for low-γ systems. First, the measurement occurs at times well after ablation, when the buffer gas density and temperature are stable. Second, the experiment is not critically dependent on a large Boltzmann factor, and so the experimental parameters of magnetic field and temperature are decoupled. For the aluminum experiment described here, this allows for measurement of inelastic collisions over a range of magnetic fields at a single temperature.

Briefly, the experimental procedure consists of optical pumping of one ground state magnetic sublevel while observing the pump laser absorption to determine the rate of collisional refilling of the pumped sublevel. The energy level diagram with relevant state-changing processes is shown in Figure 3.2. The laser is tuned to the $^2P_{1/2} \rightarrow {}^2S_{1/2}$ transition at 394.5 nm. One magnetic sublevel of the ground state $^2P_{1/2}$ manifold is addressed to pump the system out of equilibrium. Simultaneously, the sublevel population is probed by monitoring the fraction of pump light absorbed. Inelastic collisions push the state distribution back towards equilibrium, competing with optical pumping to produce a steady-state population. This population is observed as a steady-state *OD* which varies with pump laser power. The inelastic collision rates are revealed by probing this steady-state as a function of pump power to determine the "stiffness" of the system. Through measurements of this response over a range of helium densities, and by making separate measurements addressing each magnetic sublevel, the effects of J-changing and m_J-changing collisions can be separated and systematic errors can be controlled.

The finite spatial width of the pump laser beam introduces another process to compete with optical pumping: diffusion of atoms into and out of the laser beam. At low helium density, the mean free path is long and atoms pumped to other states will rapidly diffuse

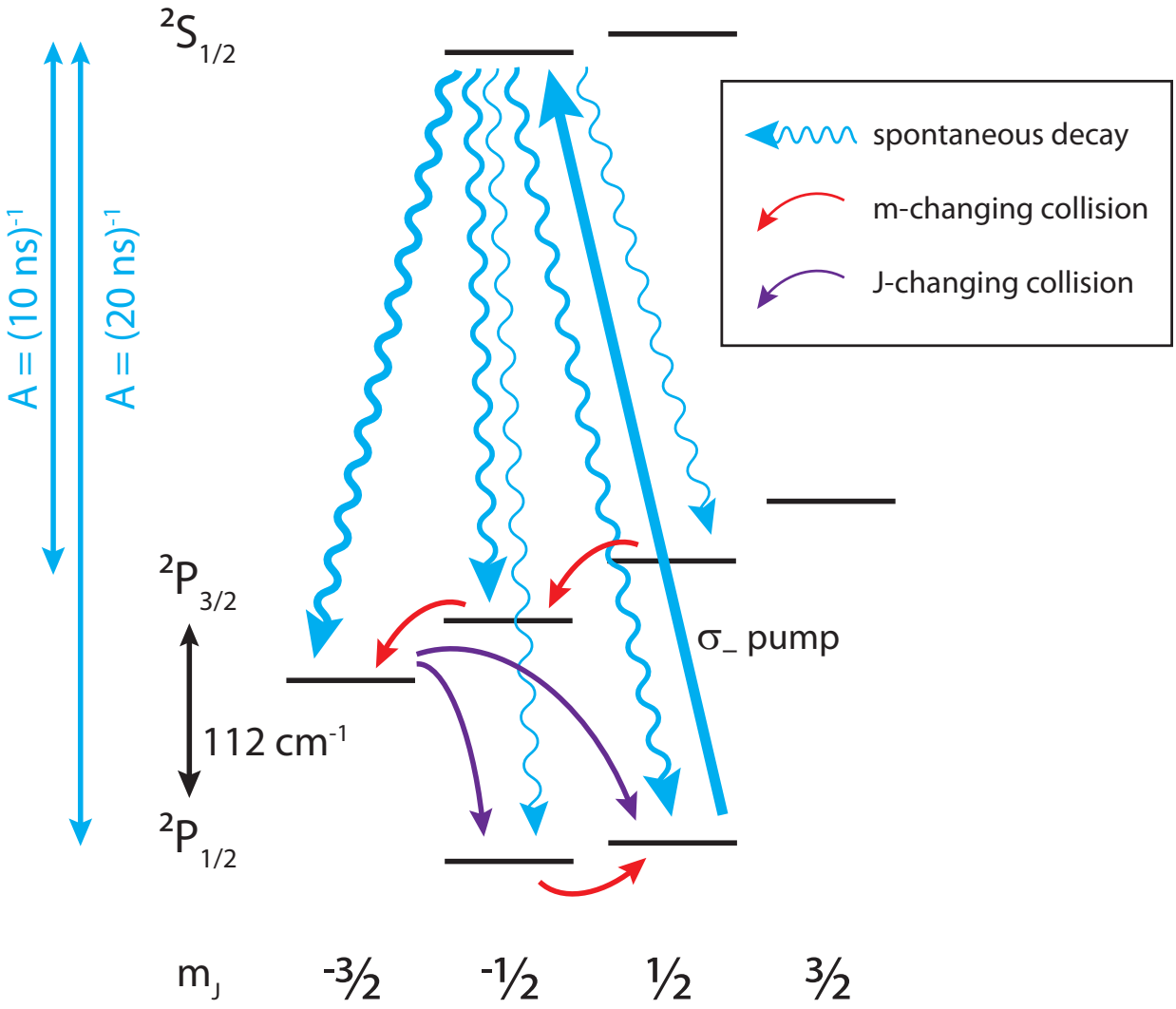

Figure 3.2: Energy level diagram of Al with relevant state-changing processes for the case of optical pumping of the $m_J = +1/2$ LFS state.

out of the beam and be replaced with "unpumped" atoms diffusing into it. This effectively increases the reservoir of resonant atoms to include those near to the beam, blunting the impact of optical pumping and increasing the observed *OD*.

The effect of diffusion can be understood through two limiting cases. In the limit of high helium density the atoms are unable to diffuse a significant distance before an inelastic collision occurs, and so the *OD* is unaffected by diffusion. In this limit the *OD* rises with

increasing helium density as collisions become more rapid. At the other extreme, of low density, inelastic collisions are rare and the *OD* is determined by the number of atoms that can diffuse into the beam to replenish those that are pumped. In this limit the *OD* rises with *decreasing* helium density, as the diffusion becomes more rapid and a larger volume of atoms participate in the competition between diffusion and optical pumping. The actual behavior in this limit is somewhat more subtle than this simple description, and will be addressed more completely in Section 3.3.2.

Between these two limits, which are hereafter referred to as the *relaxation regime* and the *diffusive regime*, respectively, we expect to find a minimum in *OD* as the helium density is varied. Since the two regimes behave in fundamentally different ways with respect to many experimental parameters, this minimum provides a sensitive diagnostic tool.

3.3.1 Quantitative model

As shown in Figure 3.2, optical pumping to the $^2S_{1/2}$ state results in spontaneous decay to a number of sublevels of both ^2P fine-structure states. The majority (66% [96]) decay to the upper state, from which they only reach the lower state via J-changing collisions with helium. The optically pumped $^2P_{1/2}$ sublevel is replenished by these collisions, as well as by m_J-changing collisions from the other $^2P_{1/2}$ sublevel. Atoms in $^2P_{3/2}$ sublevels will also undergo m_J-changing transitions; due to the large anisotropy of this state, these collisions will be very rapid (Table 3.1) compared to other timescales. We therefore assume thermal equilibrium in the $^2P_{3/2}$ state. Under this condition $\gtrsim$88% of atoms occupy the lowest $m_J = -3/2$ sublevel under all experimental conditions except those with the lowest field ($B = 0.5$ T), for which the fraction is $\approx$50%. Possible systematic error due to this simplification is discussed in Section 3.5.3.

A quantitative model is constructed to predict the state populations N_+, N_- and $N_{3/2}$—

each a function of space and time—using the rate equations below. The subscript indices $+$, $-$, and $3/2$ refer to the $m_J = +1/2$ and $m_J = -1/2$ states of the $^2P_{1/2}$ manifold and to the $m_J = -3/2$ state of the $^2P_{3/2}$ manifold, respectively. For simplicity, we take the pump to be resonant with the $m_J = +1/2$ state of the ground manifold; the result is similar for addressing the $m_J = -1/2$ state.

$$\dot{N}_+ = -\Gamma_\mathrm{p}(1 - C_+)N_+ + \Gamma_m(\kappa N_- - N_+) + f_+\Gamma_J N_{3/2} + D\,\nabla^2 N_+ \tag{3.8}$$

$$\dot{N}_- = \Gamma_\mathrm{p} C_- N_+ - \Gamma_m(\kappa N_- - N_+) + f_-\Gamma_J N_{3/2} + D\,\nabla^2 N_- \tag{3.9}$$

$$\dot{N}_{3/2} = \Gamma_\mathrm{p} C_{3/2} N_+ - \Gamma_J N_{3/2} + D\,\nabla^2 N_{3/2} \tag{3.10}$$

where Γ_p, Γ_m and Γ_J are the rates of optical pumping, m_J-changing collisions and J-changing collisions, respectively, and D is the diffusion constant (Equation 2.2). The coefficients C_X and f_X are the branching fractions into state X for spontaneous emission from the $^2S_{1/2}$ state and for J-changing collisional transitions from the $^2P_{3/2}$ state, respectively. The Boltzmann factor $\kappa = \exp(-g_J\mu_B B/k_B T)$ suppresses inelastic transitions to higher-energy magnetic sublevels, where $g_J = 2/3$ is the Landé g-factor. Thermal excitation from the ground state to the $^2P_{3/2}$ state is negligible. As discussed above, the $^2P_{3/2}$ manifold is assumed to be in thermal equilibrium and the $m_J > -3/2$ states are neglected.

The only unknown parameters in Equations 3.8–3.10 are Γ_m, Γ_J and the branching ratio f_+/f_-. Due to the spatial dependence of the diffusive terms, there is in general no analytic solution to Equations 3.8–3.10. However, in the relaxation regime at high helium density, D is small and these terms can be neglected. More precisely, the beam-averaged instantaneous rate of diffusion of resonant atoms into and out of the beam can be defined as $\Gamma_\mathrm{d,b} = \langle (D\,\nabla^2 N_+)/N_+ \rangle_\mathrm{beam}$. The relaxation regime is thus defined by $\Gamma_\mathrm{d,b} \ll \Gamma_m, \Gamma_J$, for which the analytic steady-state solution corresponding to $\dot{N}_+ = \dot{N}_- = \dot{N}_{3/2} = 0$ can be

obtained:

$$N_+ = \frac{\kappa}{1+\kappa}\left[\frac{1}{1+\frac{1}{2(1+\kappa)}\frac{\Gamma_\mathrm{p}}{\Gamma_\mathrm{m}}\left(1-C_-+C_++C_{3/2}\left(\Delta f+2\kappa\frac{\Gamma_\mathrm{m}}{\Gamma_\mathrm{J}}\right)\right)}\right] \tag{3.11}$$

$$N_- = \frac{1}{1+\kappa}\left[\frac{1+\frac{1}{2}\frac{\Gamma_\mathrm{p}}{\Gamma_\mathrm{m}}\left(1-C_-+C_++C_{3/2}\Delta f\right)}{1+\frac{1}{2(1+\kappa)}\frac{\Gamma_\mathrm{p}}{\Gamma_\mathrm{m}}\left(1-C_-+C_++C_{3/2}\left(\Delta f+2\kappa\frac{\Gamma_\mathrm{m}}{\Gamma_\mathrm{J}}\right)\right)}\right] \tag{3.12}$$

$$N_{3/2} = f_{3/2}\frac{\Gamma_\mathrm{p}}{\Gamma_\mathrm{J}}\left[\frac{\kappa}{1+\frac{1}{2(1+\kappa)}\frac{\Gamma_\mathrm{p}}{\Gamma_\mathrm{m}}\left(1-C_-+C_++C_{3/2}\left(\Delta f+2\kappa\frac{\Gamma_\mathrm{m}}{\Gamma_\mathrm{J}}\right)\right)}\right], \tag{3.13}$$

where $\Delta f = f_+ - f_-$.

Equation 3.11 has the form

$$N = \frac{N_0}{1+bP}, \tag{3.14}$$

where N_0 is the population without optical pumping, b is a constant, and the dependence on the power P arises through the optical pumping rate Γ_p. The solution retains this simple form when spontaneous decay to additional states is included—such as decay to the other $^2P_{3/2}$ sublevels. By measuring *OD* while varying pump power, the N *vs.* P curve can be mapped out and normalized to yield the coefficient b, which describes the stiffness of the system's response to the optical pumping perturbation. This method allows for a power-independent comparison of the response across experimental parameters such as helium density.

It is clear from Equation 3.11 that for increasing helium densities (increasing Γ_m and Γ_J), the coefficient b decreases, increasing N and *OD*. Hence there will be a positive slope of *OD vs.* helium density in the relaxation regime.

3.3.2 Diffusion into and out of the beam

The opposite limit of low helium density and high D is the diffusive regime, satisfying the condition $\Gamma_\mathrm{d,b} \gg \Gamma_m, \Gamma_J$. A qualitatively description follows below of the behavior in this regime and its transition to the mixed regime of intermediate helium density. For the

conditions considered here, we also impose the additional constraint that the mean free path of aluminum atoms is much smaller than the beam diameter d_b, such that the motion remains diffusive on the scale of d_b.

For a very large volume ($R, L \gg d_\mathrm{b}$), we can ignore the slow diffusion of atoms to the walls and consider the initial atom distribution to be uniform near the region illuminated by the pump beam. As atoms are optically pumped out of the resonant state, the pumped atoms (those now in different states) diffuse out of the beam and unpumped atoms (those in the resonant state) diffuse into the beam from the dark region of the cell. Initially, this happens rapidly, at a rate $\Gamma_\mathrm{d,b} \sim (d_\mathrm{b}/R)^2/\tau_\mathrm{d}$, where τ_d is the cell diffusion time given in Equation 2.4.

Soon, however, the region just outside of the pump laser becomes depleted of atoms in the resonant state. Hence the rate of resonant atoms diffusing into the beam decreases, shifting the balance of competition between optical pumping and diffusion to be more and more in favor of optical pumping. The steady state solution is thus the trivial one: complete pumping ($N_+ = 0$). For nonnegligible values of Γ_m and Γ_J, however, the pumped atoms that diffuse far from the beam eventually collide inelastically to return to the resonant state, replenishing the reservoir. The inelastic collision rate sets an average radius beyond which the resonant state is not significantly depleted, and the system evolves to a steady state in which resonant atoms have been depleted within this radius.

For given values of the J- and m_J-changing collision cross sections, the radius of the steady-state depletion zone shrinks with increasing helium density, due both to slower diffusive transport and faster inelastic transitions. The smaller depletion zone has correspondingly fewer atoms experiencing inelastic collisions. At steady-state with fixed pump laser power, this necessarily corresponds to a reduced density of resonant atoms being optically pumped, *i.e.*, a lower resonant atom density and lower OD. Therefore, the diffusive regime is char-

acterized by a negative slope of *OD vs.* helium density. As the helium density continues to rise, an increasing number of inelastic collisions occur within the beam region. Eventually these collisions are sufficient to compete with optical pumping without the enhancement of the diffusion-expanded resonant reservoir. Near this density, between the diffusive and relaxation regimes, the *OD* takes its minimum value.

While the quasi-steady-state solution to Equations 3.8–3.10 is complicated, the numerical solution (described in Section 3.5.2) closely resembles the simple form of Equation 3.14 for the range of *OD* used in the experiment. Hence it is a good approximation to describe the system with a single stiffness coefficient b in all helium density regimes of the experiment. The following two sections, however, describe important effects that modify this response.

3.3.3 Doppler broadening

The frequency of the optical pumping laser is kept constant, resonant with one of the two ground state sublevels. At temperatures above ≈50 mK, the Doppler width exceeds the natural linewidth of the transition, leaving fast-moving atoms only weakly resonant with the pump laser. These nonresonant atoms do not stay nonresonant for long, however; elastic collisions with helium atoms fully remix the velocity distribution after about M/m collisions, where M and m are the masses of aluminum and helium, respectively. As long as all other relevant dynamics (inelastic collisions, diffusion over the scale of d_b, etc.) are much slower than this remixing time $\tau_\mathrm{remix} = \tau_\mathrm{c} \times (M/m) = M/(m n_\mathrm{b} \sigma_\mathrm{D} \bar{v})$, then there will be no significant distortion, or "bleaching," of the velocity distribution.

If this condition is met, then the only remaining effect of Doppler broadening is that the optical pumping rate Γ_p is reduced compared to the case of $T = 0$; fewer atoms are resonant at a given time, so fewer will be pumped. The reduction factor, F_D, is easily computed by taking the ratio of the absorption cross sections calculated for $T = 0$ and for finite T.

3.3.4 Zeeman broadening

In addition to Doppler broadening, the spectral line is also Zeeman broadened due to inhomogeneity of the magnetic field (the field distribution and spectral profile are discussed in Section 2.2.1). Zeeman broadening presents a particular challenge to the aluminum optical pumping measurement because the distribution of atoms with different Zeeman detunings implies a distribution of optical pumping rates. The issue is similar to Doppler broadening, except that the Zeeman distribution does not remix. For the Zeeman detuning of an invididual atom to change, either the magnetic field at that position must vary or the atom must travel to a location with a different magnetic field. The inductance ($\approx$7 H) and size (inner diameter = 8.2 cm) of the magnetic field coils are large enough that it is highly unlikely for temporal or spatial field variation to be large enough for an atom to sample significantly different Zeeman detunings within the experimental timescale. It is thus appropriate to treat each atom as fixed at a certain magnetic field, and the distribution of Zeeman detunings to be static.

Since aluminum–aluminum collisions are very rare on the time scale of the experiment, each aluminum atom illuminated by the pump laser has an independent contribution to the observed OD. Likewise, each atom has an independent probability of occupying the resonant state, depending on the global system parameters (Γ_m, Γ_J and D) and the value of Γ_p specific to the local Zeeman detuning. As a result, the OD dependence on pump laser power has the form of a sum over all atoms,

$$OD = \sum_i \frac{OD_{0,i}}{(1 + b_i P)}, \tag{3.15}$$

using the simple model introduced in Equation 3.14. The coefficient b_i contains the effect of Zeeman detuning for optical pumping of the i^{th} atom, whose absorption contribution is $OD_{0,i}$ in the limit of vanishing laser power. In general, Equation 3.15 cannot be expressed

as a single term and the optical pumping effect cannot be simply characterized by a single b coefficient.

3.4 Experimental procedure

3.4.1 Aluminum production

The same cell is used for the measurement of aluminum–helium inelastic collisions as was used for the antimony experiment described in Chapter 2. Aluminum is produced by ablating an aluminum nitride ceramic target into helium-3 buffer gas. Originally intended as a nitrogen ablation source for NH production, aluminum nitride is likely not the ideal ablation precursor for atomic aluminum. While the aluminum yield is excellent, since NH production using the same material was also quite good (see Appendix A), we must assume that atomic nitrogen is produced in similar or greater quantities. It is possible that aluminum–nitrogen collisions could cause inelastic transitions that confuse analysis of the aluminum–helium system. For an interspecies inelastic cross section of 10^{-14} cm^2, such collisions would be likely to occur within the aluminum diffusion lifetime at nitrogen densities above 10^{11} cm^{-3}. However, even with very high ablation yield of $>10^{14}$ N atoms, such a density would exist only for a short time before decaying due to diffusion. The aluminum measurement is performed only after waiting multiple diffusion lifetimes, and so nitrogen–aluminum collisions are unlikely to play a role.

To increase confidence that these collisions can be ignored, it would be ideal to directly probe the nitrogen density *via* 207-nm two-photon absorption laser-induced fluorescence (see Figure 2.6). Unfortunately, a UV-absorbing film accumulated on the outer surface of the 77-K window between the antimony and aluminum experiments, precluding this direct approach. Instead, the nitrogen density was indirectly probed by searching for a dependence

on aluminum density in the system's response to optical pumping. It is safe to assume that atomic nitrogen will decay on a timescale not very different from that of aluminum in the same cell, since momentum transfer cross sections for collisions of different atoms with helium are generally quite similar [32, 71, 97]. Therefore, a significant change in aluminum density will be accompanied by a similar change in nitrogen density. By observing no density variation in the power dependence of OD, we can conclude that neither aluminum–nitrogen nor aluminum–aluminum inelastic collisions affect the measurement.

3.4.2 Pump/probe laser system

Aluminum is detected by absorption spectroscopy on the 394.5-nm $^2P_{1/2} \rightarrow {}^2S_{1/2}$ transition using the diode laser system outlined in Figure 3.3. Aluminum has a single isotope with nuclear spin $I = 5/2$ and a simple optical spectrum both at zero (Figure 3.4) and large (Figure 3.5) magnetic field. For the $\geq$0.5 T fields used in inelastic collision measurements described here the states are >99% pure in the J-basis. The zero-field spectrum is fit to a Voigt profile to confirm that the aluminum temperature is stable and in equilibrium with the cell walls. A Fabry-Pérot cavity is used to calibrate the diode laser scan range and linearity. Hyperfine a coefficients of the ground and excited states are taken from [98].

The energy level diagram of aluminum is shown in Figure 3.2, along with the relevant state-changing processes. Atoms are pumped with right(left)-circular polarization from the $m_J = -1/2$ $(+1/2)$ state. The lifetime of the excited state is 6.74 ns, with 66% of atoms decaying to the $^2P_{3/2}$ manifold, 11% to the opposite sublevel of the ground manifold and 22% back to the original sublevel [96]. The laser intensity used here is far from saturation ($s_0 < 0.1\%$), so the steady-state $^2S_{1/2}$ population is negligible.

The beam is spatially filtered with an iris after expansion with a telescope, producing a rather flat, circular intensity profile immediately following the iris. This profile evolves

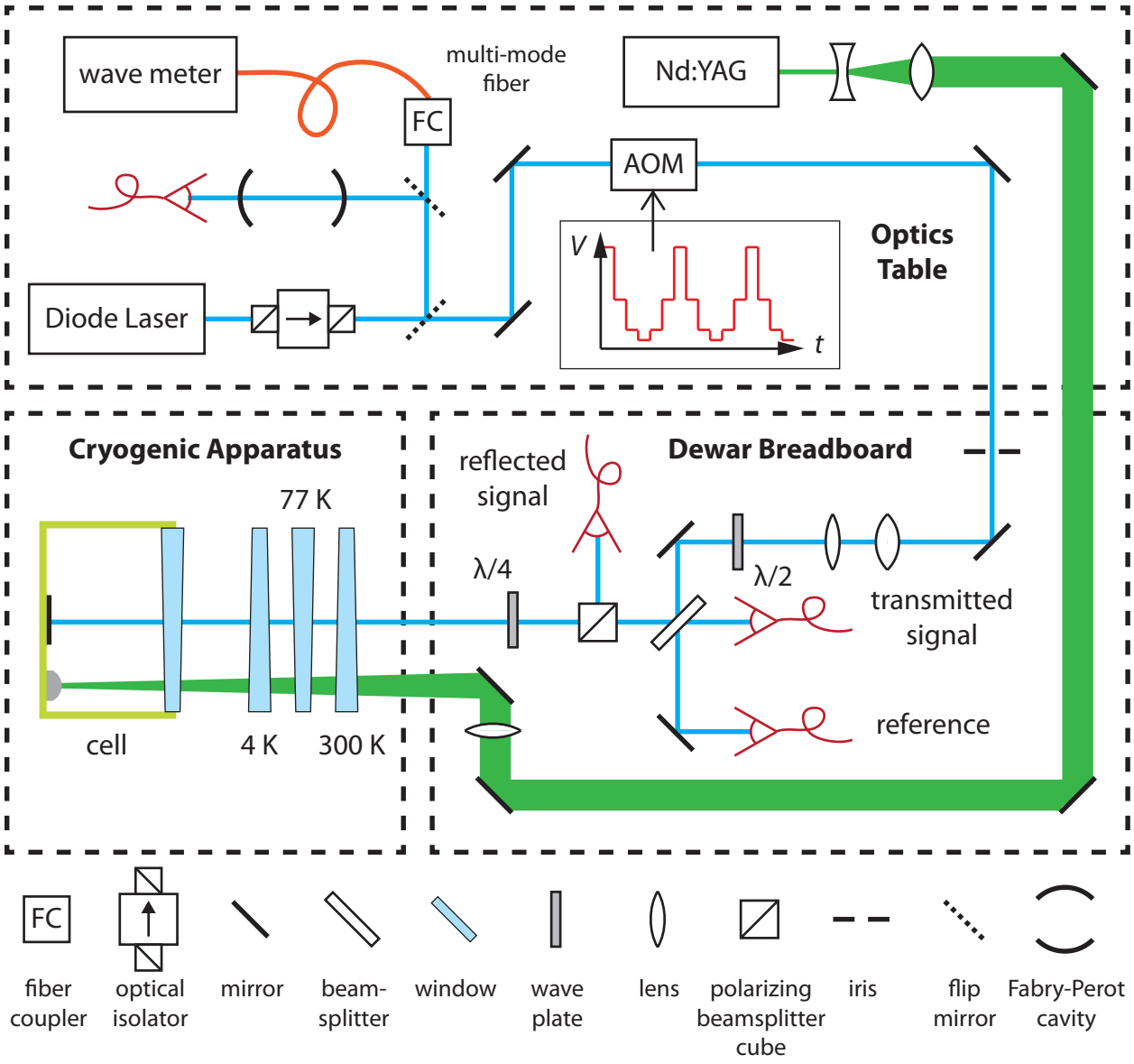

Figure 3.3: Schematic of 394.5-nm diode laser system and optics layout for Al optical pumping experiment. The signal photodiode monitoring the polarizing beamsplitter cube reflection is the primary signal detector; the transmitted channel is used for diagnostic purposes. Some steering mirrors are not shown.

due to diffraction as it propagates to the experiment, resulting in the fringed downstream images shown in Figure 3.6. It is not necessary for the experiment to have a flat intensity profile at the atoms, however the beam profile there must be known. To that end, the beam

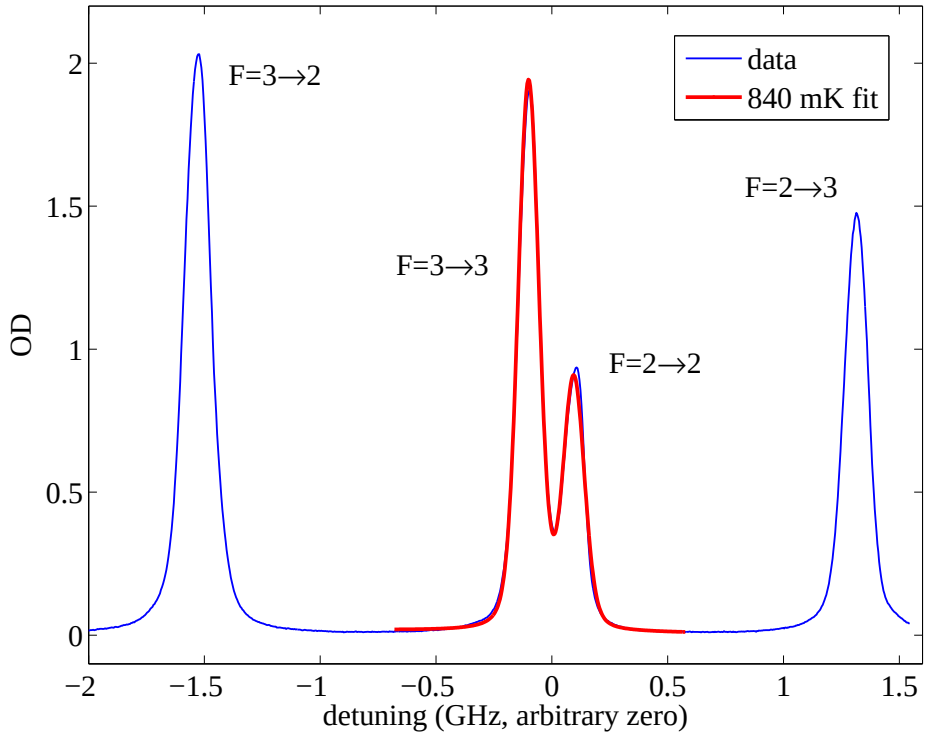

Figure 3.4: Zero-field hyperfine spectrum of Al at 394.5 nm. The pair of closely-spaced peaks at the center are fit with a Voigt lineshape.

diffraction is simulated by numerically integrating the Green's function. The simulated intensity profiles are checked against the images, and then a simulated image is generated for the point downstream corresponding to the cell mirror location. Since the beam evolves for 10 cm both before and after this point, all the while interacting with the atoms, this is an imperfect procedure. The optical pumping measurement is not limited by this uncertainty, however, and it is sufficient to have approximate knowledge of the fringe period and depth.

To determine the stiffness of the system to the optical pumping perturbation, it is necessary to compare the *OD* observed while pumping to that of the weak-probe limit of vanishing laser intensity. Without separate knowledge of the aluminum density distribution, this limit can only be extrapolated from measurements with low laser power. We measure the steady-state *OD* over a range of powers, with each cooled ensemble of aluminum atoms individually

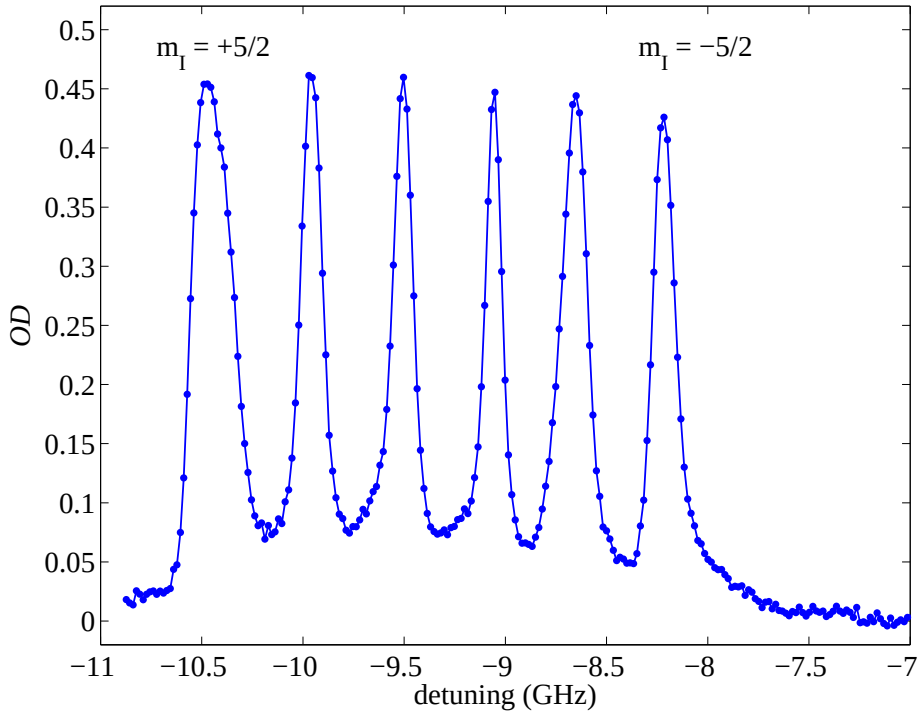

Figure 3.5: Hyperfine spectrum of $\Delta m_J = -1$ transitions from the $m_J = +1/2$ manifold of nuclear spin states at $B = 0.5$ T. A very similar manifold of $\Delta m_J = +1$ lines from $m_J = -1/2$ states is found at opposite detuning. The alignment of the magnetic field with the laser propagation direction largely suppresses $\Delta m_J = 0$ transitions. Some distortion of the lineshape is caused by nonlinearity in the laser frequency sweep due to the rapid 200-Hz diode grating scan.

probed several times within the diffusion lifetime. This approach controls for variation in ablation yield and buffer gas density between separate realizations of the expeirment. We modulate the laser power with an acousto-optical modulator (AOM), stepping between four logarithmically-spaced levels in the pattern shown in Figure 3.7. The power is held constant for 3 ms at each power level, the first 1.5 ms of which are used to allow the system to reach steady-state and which are ignored in the data analysis. The steady-state *OD vs.* power data are fit to a model function, which is then extrapolated to zero power. Details of this fitting procedure are discussed in Section 3.5.

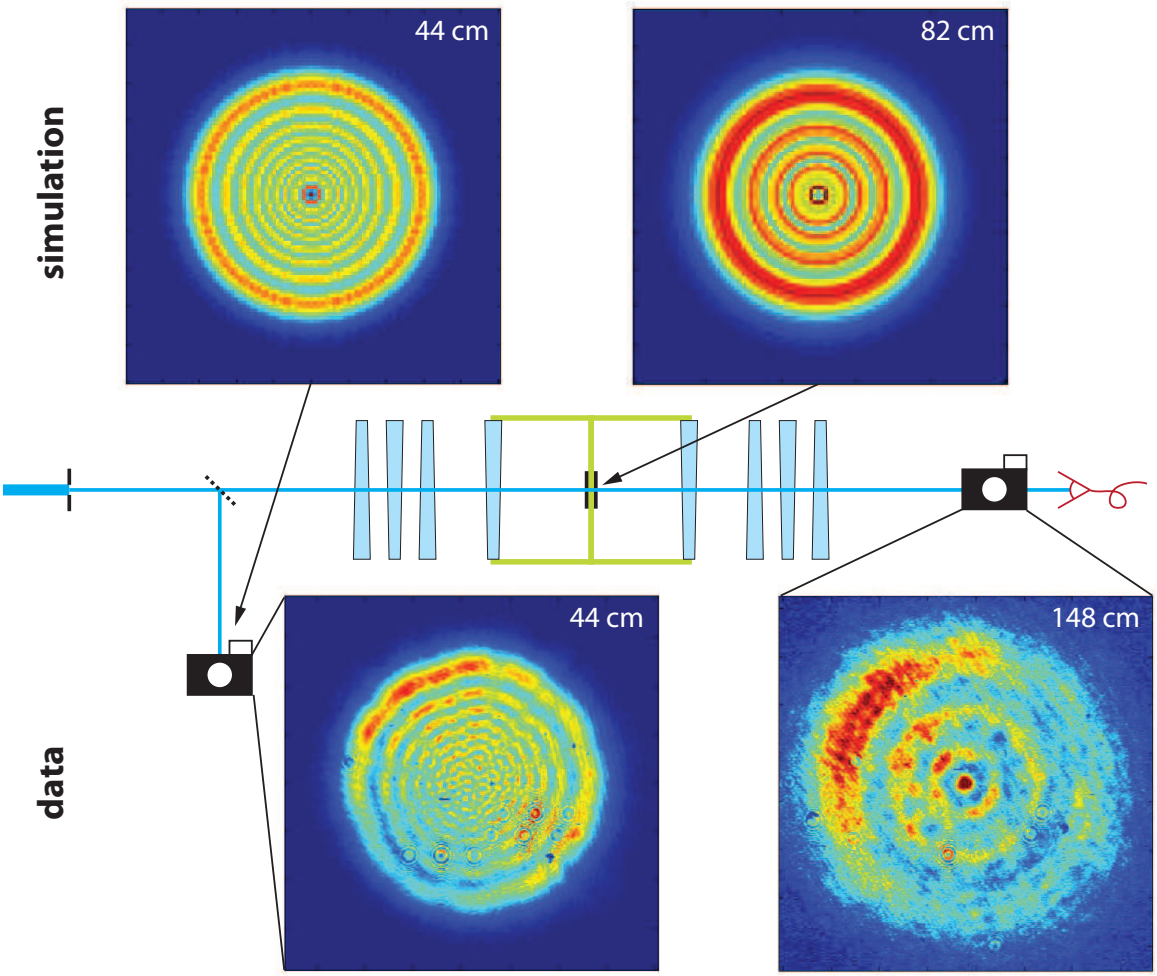

Figure 3.6: Observed and simulated optical pumping beam profiles at different points along the propagation axis. Diffraction from the iris aperture generates radial oscillations in the beam profile downstream. After confirming that the simulations recreate the observed patterns (see $d = 44$ cm images shown), the simulation is used to predict the pattern at the cell mirror, the midpoint of the optical pumping path, where the beam cannot be directly imaged. Additional optics are not shown; the full optics layout is shown in Figure 3.3. The beam used for this diffraction comparison has much greater large-scale intensity variation than that used in the optical pumping experiment.

3.4.3 Pump laser polarization

Each magnetic sublevel of the ground state of aluminum can make a $\Delta m = 0$ transition to the $^2S_{1/2}$ manifold or a transition to the upper state of opposite m_J. The pump laser is parallel

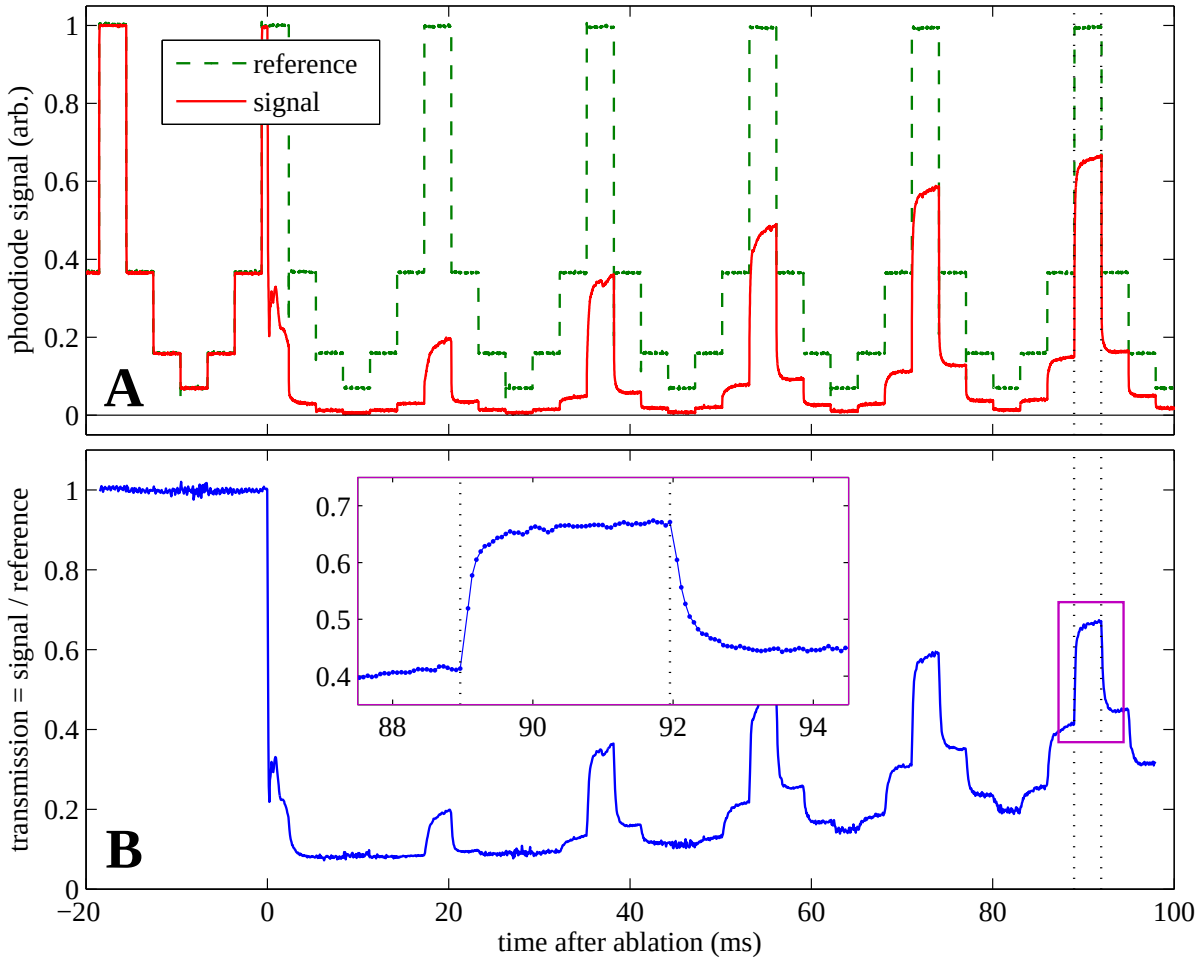

Figure 3.7: (A) Raw photodiode signals, and (B) calculated transmission of probe laser resonant with $|m_J, m_I\rangle = |+1/2, +5/2\rangle$ state of Al, taken with $B = 0.5$ T and $T \approx 800\,mK$. The laser power is AOM-modulated to dwell 3 ms at each of four power levels. The *OD* is reduced at higher power due to faster optical pumping. The inset enlarges the region bounded in purple, which shows the timescale for the transmission to reach steady state after the moment the power is changed (dotted lines).

to the magnetic field, and so cannot have the appropriate π-polarization to drive $\Delta m = 0$ transitions. Therefore there is only one transition option from each sublevel of the ground state: $m_J = \pm 1/2 \rightarrow \mp 1/2$. As the beam propagates parallel to the field, right-circularly-polarized light will be σ_+-polarized; upon reflection from the cell mirror the polarization handedness will invert, so that the beam is then propagating antiparallel to the field and remains σ_+-polarized. Similarly, initially left-circularly-polarized light is σ_--polarized. Thus each ground state sublevel interacts with only one circular polarization.

Engineering the laser polarization to address atoms in the cell is complicated by birefringence in the multiple windows between the atoms and room temperature optics. The four fused silica windows are mounted on the cell, the helium bath, the liquid-nitrogen-cooled radiation shield and the outer dewar, and are referred to as the cell window, 4-K window, 77-K window, and 300-K window, respectively. The cell window[4] is epoxied into a close-fitting G-10 tube; the other three[5] are mounted with clamps. Mechanical stresses due to attachment and thermal contraction are significant, and can cause linear birefringence in excess of the room-temperature unstressed material specifications. In addition, the Faraday effect induces circular birefringence in fused silica in high magnetic fields [99], primarily in the cell window. Measurements of the combined effect are shown in Figure 3.8.

In addition to birefringence in optics, the atomic ensemble itself is birefringent in the magnetic field due to its polarization-sensitive absorption. For very high OD, resonant linearly polarized light will be half absorbed, leaving a single circular polarization. Furthermore, if the light is detuned from resonance then the dispersive ensemble will phase-shift one circular polarization with respect to the other, rotating the linear polarization. This nonresonant effect is especially important when optics between the atoms and detector are polarization

[4]Glass Fab Inc.: UV fused silica, 1° wedge both sides, 0.5 in thick (thin end).

[5]CVI Melles-Griot: UV fused silica, 0.5° wedge one side, 0.5 in thick (thick end).

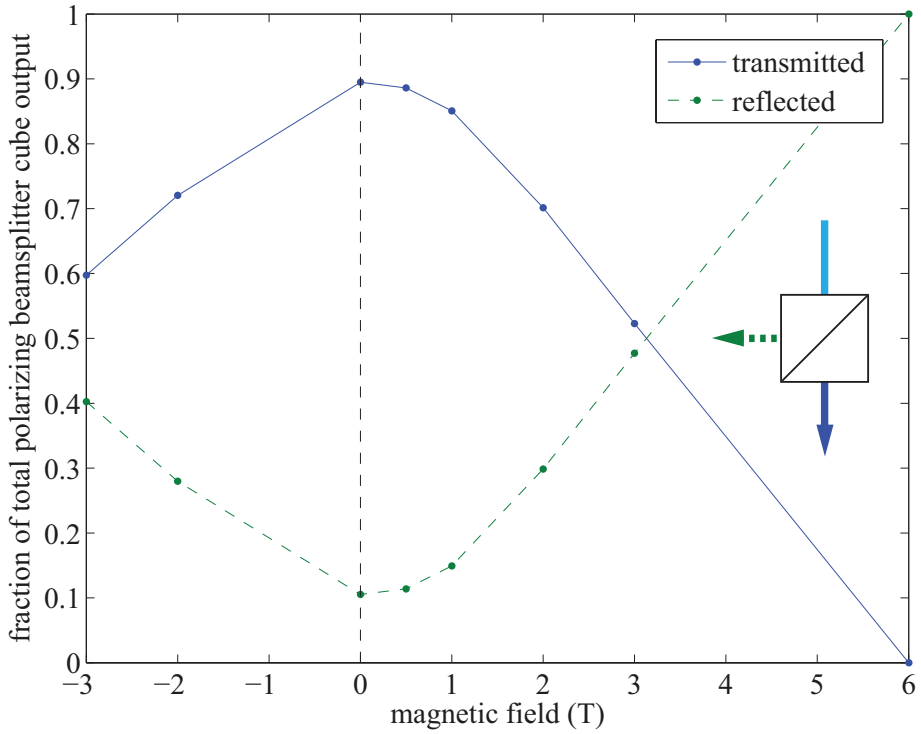

Figure 3.8: Polarization rotation due to linear and magnetic circular birefringence (Faraday effect) in UV fused silica dewar windows. Linearly polarized light is transmitted through a polarizing beamsplitter cube, after which it passes through the 300-K, 77-K, 4-K and cell windows twice each—going in and coming out—and is incident on the same cube. Both polarization outputs are monitored by photodiodes. The magnetic field axis of the plot refers to the maximum Helmholtz field in the cell. The nonzero reflection at zero-field is due to linear birefringence under mechanical and thermal stresses; the field-dependent rotation is the Faraday effect, primarily in the cell window.

sensitive, since rotations can cause more or less light to reach the detector and be mistakenly interpreted as weaker or stronger absorption. It is even possible for such rotations to result in more light reaching the detector than in the case of no atoms in the cell—apparent negative absorption, also referred to as "extra light." This effect is discussed in more detail in Appendix C.

The Faraday effect and the atomic birefringence are the dominant effects. Both are forms of circular birefringence and thus can be mitigated by the use of pure circular pump

laser polarization, so that no differential phase is accumulated. A quarter-wave plate is used for this purpose (see Figure 3.3), converting the linear polarization exiting a polarizing beamsplitter cube into circular polarization and then converting the reflected beam back to the opposite linear polarization. The wave plate is left untouched for observation of both ground state sublevels, but the field direction is reversed between the two so that the polarization remains correct for addressing the atoms. In this configuration, dispersive phase shifts have a minimal impact on the detected intensity. Some effect remains due to the windows' linear birefringence, but the polarization remains >90% pure and the effect on OD is small even for large phase accumulation. As a precaution, however, only data for which resonant $OD < 0.3$ is considered for analysis.

3.4.4 Momentum transfer cross section calibration

In addition to the optical pumping experiment, a comparison was made between diffusion of aluminum and manganese in order to determine $\sigma_{\mathrm{d,Al}}$, similar to the procedure with antimony described in Section 2.3.1. In an improvement over the antimony case, however, the aluminum nitride and manganese targets were simultaneously ablated to ensure an identical buffer gas environment. Alternately, either the aluminum or manganese detection laser was directed through the cell and to the photodiodes. The extracted diffusion times are shown in Figure 3.9 along with exponential decay curves with a shared time constant τ_{b} for decay of the buffer gas density. The resulting exponential amplitudes from the fit are used to determine the thermally averaged cross section ratio $\sigma_{\mathrm{d,Al\text{–}^3He}}/\sigma_{\mathrm{d,Mn\text{–}^3He}}$ using Equation 2.8. This ratio is found to be 1.13(2) at 800 mK, which implies $\sigma_{\mathrm{d,Al}} = 1.1 \times 10^{-14}$ cm^2 [58] and $k_{\mathrm{d}} = 8.8 \times 10^{-11}$ cm^3 s^{-1} at $T = 820$ mK.

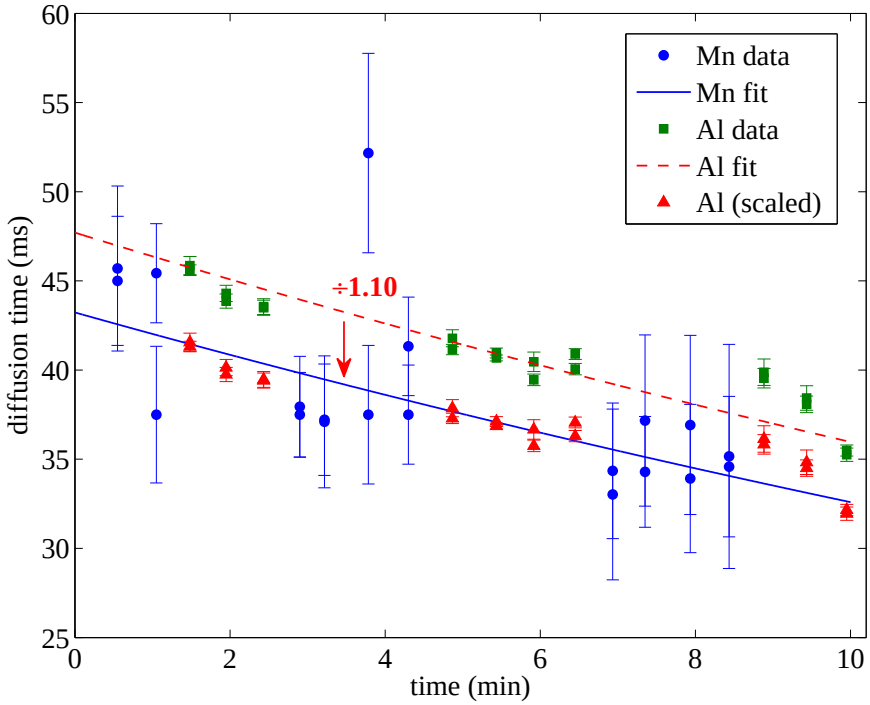

Figure 3.9: Diffusion time comparison of Al and Mn to determine the momentum transfer cross sections ratio $\sigma_{\mathrm{d,Al\text{–}^3He}}/\sigma_{\mathrm{d,Mn\text{–}^3He}}$. The two fits share the same exponential decay time constant. The data are taken with the laser scanning, and the diffusion times plotted are from exponential fits to integrated scans. The two data points at each time are separate analyses considering only one of the two portions of the triangle wave scan—upscans or downscans. Any scan hysteresis is sufficiently small to not affect the integrated spectra.

3.5 Data analysis

3.5.1 Data processing

For each ablation pulse, the photodiodes shown in Figure 3.3 monitor the intensity of both the pump laser exiting the cell (the signal beam) and of a reference beam split from the pump before the dewar. The ratio of the two, normalized to unity in the absence of absorption, is the transmission of the atomic ensemble (Figure 3.7B). The transmission data is collated by power level into four separate data sets, which are individually fit over the same time

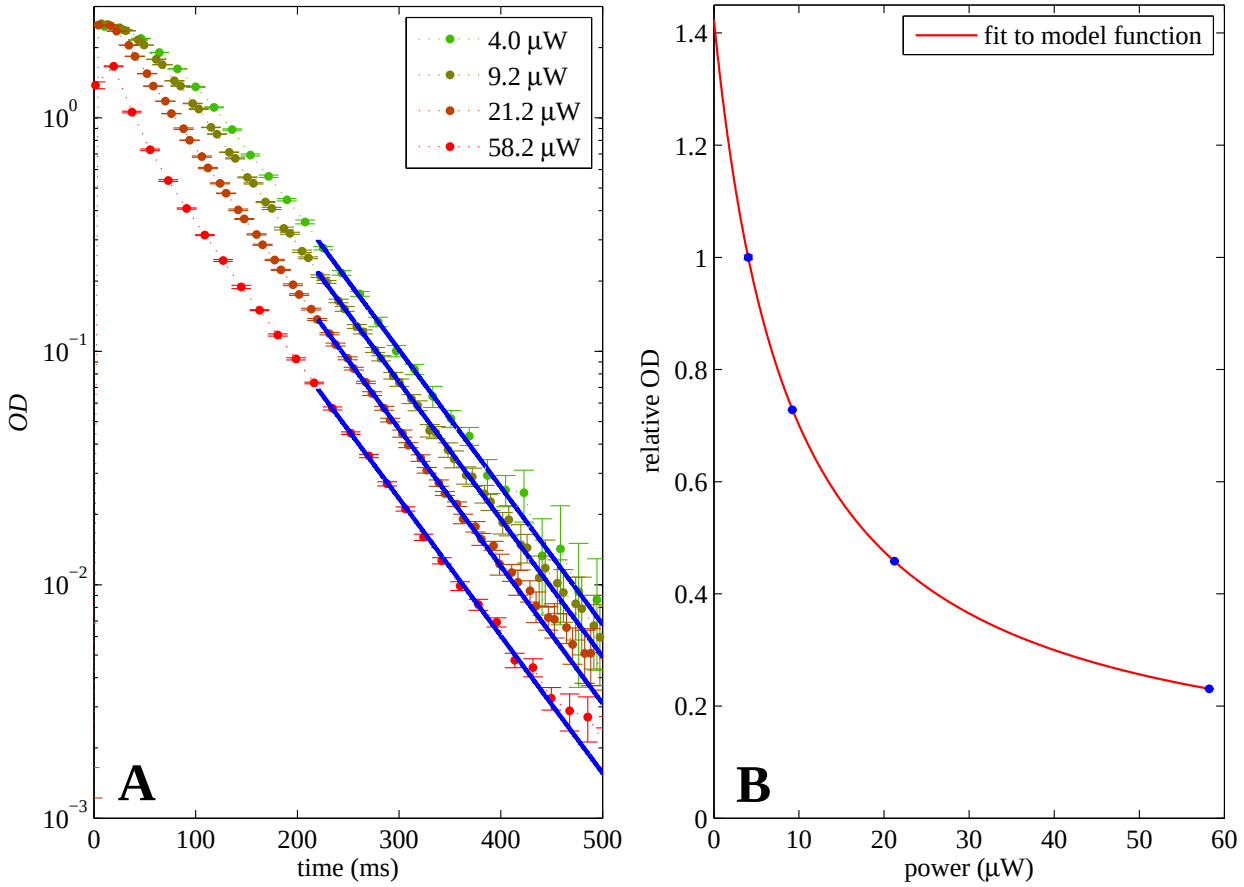

Figure 3.10: Data processing procedure to determine the system's response to optical pumping. (A) Data separated by power level is fit to exponential decay with a shared τ_d, and (B) the OD from these fits is fit to Equation 3.16. Only data with $OD < 0.3$ is used in order to avoid saturation effects.

interval to diffusive exponential decay of the form $OD = OD_0 \exp(-t/\tau_d)$,[6] where OD_0 and τ_d are fitting parameters. A weighted average of the four fitted values of τ_d and associated confidence intervals is then computed to be the diffusion time for the aggregate data set. Finally, the four individual data sets are then simultaneously fit a second time with τ_d fixed at this average value to extract four values of OD_0, the extrapolation of OD at $t = 0$ (Figure 3.10).

[6]more precisely, the transmission is fit to $\exp(-OD) = \exp(-OD_0 \exp(-t/\tau_d))$

To facilitate comparison of the optical pumping response across varying experimental parameters, the four values of OD_0 from each ablation pulse are fit to a model function:

$$OD(P) = a\left(\frac{1-c}{bP+1}+c\right). \tag{3.16}$$

The coefficient a is for normalization and is not relevant to the optical pumping analysis. The model function is a variation of the function in Equation 3.14. The offset c has been added as a fitting parameter to accommodate deviations from the idealized form (such as those caused by Zeeman broadening and by spatial variation of pump laser intensity) in which the system's response is not described by a single parameter b. The parameterization in Equation 3.16 is not unique; however, it provides a good approximation. The resulting fits are generally excellent and give values of $c \lesssim 0.1$. An example fit is shown in Figure 3.10B.

The model function fits are used to predict the ratio $OD(P_{\text{norm}})/OD(P \to 0)$, which gives the OD at a certain normalization power P_{norm} relative to the weak-probe limit. This definition allows for comparison across data sets despite pump power fluctuations. $OD(P \to 0)$ is extrapolated from the fits, and P_{norm} is chosen to be within the range of power levels used in the experiment. The precise value of P_{norm} is not critical; it is chosen such that $OD(P_{\text{norm}})/OD(P \to 0) \approx 0.5$ to maximize sensitivity to changes in the competing rates in Equations 3.8–3.10.

Calculating uncertainties for $OD(P_{\text{norm}})$ and $OD(P \to 0)$ is not trivial due to the transmission noise spectrum. There are significant components to the noise at frequencies $\sim \tau_{\text{d}}^{-1}$ that introduce error in the fit parameters τ_{d} and OD_0. Since these components cannot be sufficiently well-sampled during the decay time of a single data set, uncertainties computed from individual fits systematically underestimate the true uncertainty in these values. Simply put, the fitting procedure will fit noise features with small residuals even if the fit deviates greatly from where the noise-free data would lie. More accurate uncertainties are obtained from the distribution of repeated measurements of the same quantity.

To estimate this distribution, under each set of experimental conditions a null data set is taken without ablation and the Fourier transform of is computed to obtain a noise spectrum. That spectrum is then used to generate artificial noise, with identical frequency component amplitudes to the null data set, but with random phases. The artificial noise is thus a Fourier-transform-equivalent resampling of the original noise. The original fitted values of $\tau_{\rm d}$ and OD_0 are used to generate four noise-free *OD vs. t* curves, which are added to 4×100 independent sets of artificial noise. We fit the resulting simulated data sets in precisely the same manner as the original data (described above). The standard deviation of the 100 sets of fit parameters are taken as representative of the actual uncertainty in the original values. This uncertainty is then propagated for the calculation of $OD(P_{\rm norm})/OD(P \to 0)$ and is used to determine the best-fit parameters for numerical simulation of Equations 3.8–3.10, as described in the next section. An example data set with error bars is shown in Figure 3.11.

3.5.2 Numerical simulation of optical pumping

To interpret the data, Equations 3.8–3.10 are solved numerically to obtain N_+, N_- and $N_{3/2}$ as a function of time and space. Expressed in experimental parameters, the optical pumping rate is

$$\Gamma_{\rm p} = 2\left(\frac{s_0(\boldsymbol{r})A}{2F_{\rm D}}\right), \tag{3.17}$$

where $s_0(\boldsymbol{r}) = I(\boldsymbol{r})/I_{\rm sat}$ is the spatially-varying saturation parameter of the pump beam intensity profile $I(\boldsymbol{r})$, $A = 4.99 \times 10^7$ s^{-1} is the Einstein coefficient for the $^2P_{1/2} \to {}^2S_{1/2}$ transition, and $F_{\rm D}$ is the reduction factor due to Doppler broadening (Section 3.3). The factor of 2 is due to the pump beam passing through the atoms twice. Similarly, using

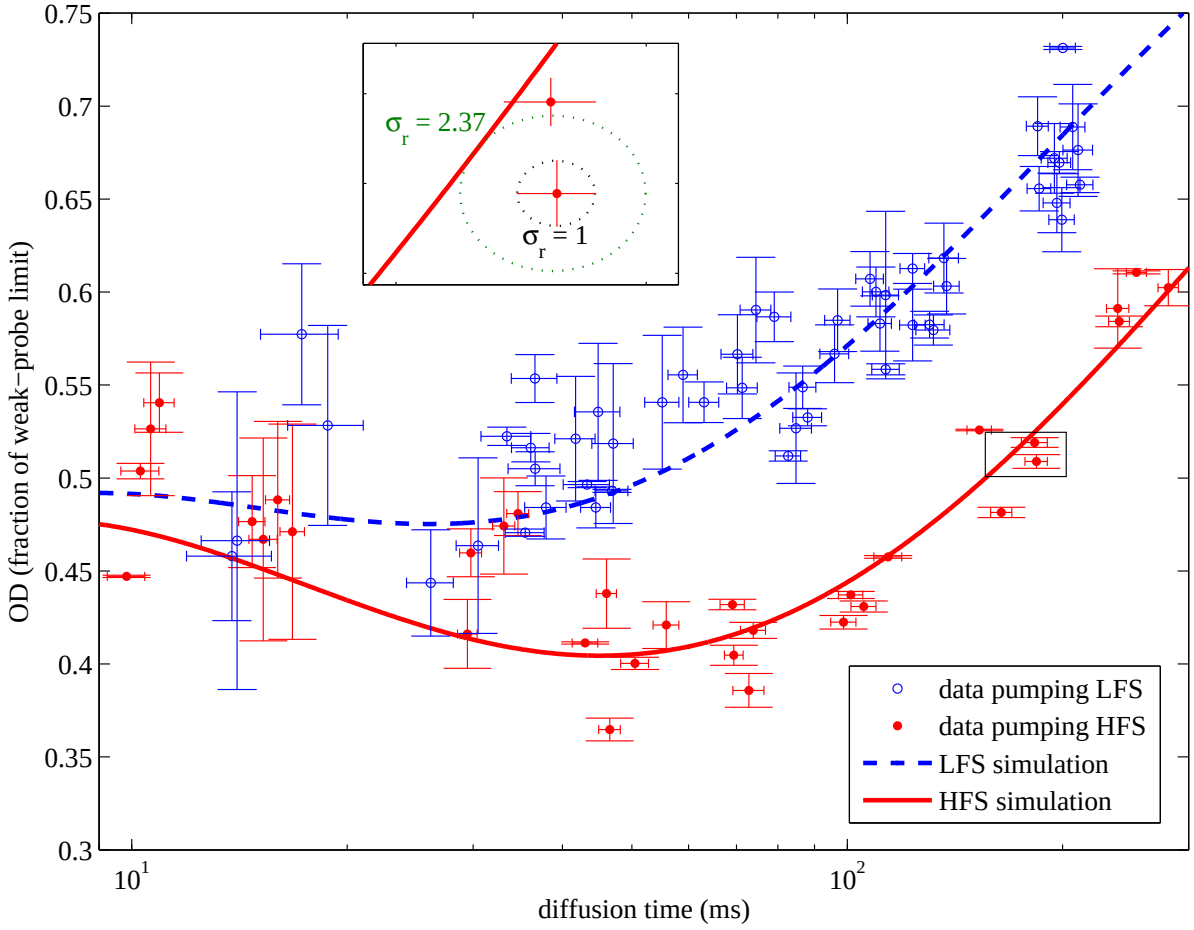

Figure 3.11: Optical pumping data taken at $T = 820$ mK with $B = 4$ T, normalized to $s_0 = 5\times10^{-4}$. Also plotted are predictions simulated for the following parameter values: $\gamma_m =$ 1,099, $\gamma_J = 536$ and $f_+ = 0.69$. A minimum error-normalized residual σ_r is computed for each data point to appropriately account for the 2D error bars. The procedure for each point is as follows. An ellipse with major and minor axes equal to the vertical and horizontal error bars is drawn around the point. The ellipse is expanded until it intersects with the simulated curve, and σ_r is taken to be this expansion factor, which may be less than 1. This procedure for determining the residual gives equal weight to error in both dimensions. The inset enlarges the boxed region to show an example of this procedure.

Equations 1.4 and 2.4 the inelastic collision rates can be expressed as

$$\begin{aligned}\Gamma_m &= n_{\rm b} k_m = \frac{n_{\rm b} k_{\rm d}}{\gamma_m} \\ &= \frac{3\pi}{32}\frac{1}{\gamma_m}\left(\bar{v}^2 G\right)\tau_{\rm d}\end{aligned} \tag{3.18}$$

and

$$\Gamma_J = \frac{3\pi}{32}\frac{1}{\gamma_J}\left(\bar{v}^2 G\right)\tau_{\rm d}, \tag{3.19}$$

where γ_m and γ_J are the ratios of the momentum transfer rate coefficient $k_{\rm d}$ to the inelastic collision rate coefficients k_m and k_J for m_J- and J-changing collisions, respectively.

It is important to note that these two rate coefficients refer to collisions of atoms in different fine-structure states: k_m refers to m_J-changing collisions of $^2P_{1/2}$ atoms and k_m to J-changing collisions of $^2P_{3/2}$ atoms. For purposes of analysis, however, the ratios γ_m and γ_J both express these rate coefficients relative to the same $^2P_{1/2}$ state momentum transfer rate coefficient $k_{\rm d}$. The reason for this is that the experiment has access only to ground state elastic collisions (through the diffusion time $\tau_{\rm d}$) and not those involving $^2P_{3/2}$ atoms. The ratios γ_m and γ_J are the quantities determined by the optical pumping experiment. Calculations of $k_{\rm d}$ for the ground state give a value roughly 40% larger than for the $^2P_{3/2}$ state due to the presence of a collision resonance in the experimental temperature range. Separate measurement of $k_{\rm d} = 8.8 \times 10^{-11}$ cm^3 s^{-1} (Section 3.4.4) allows the rates $k_{\rm m}$ and $k_{\rm J}$ to be determined.

Finally, diffusion is included in the numerical simulation using the cylindrically symmetric diffusion equation [51],

$$D\nabla^2 N(r,t) = D\frac{1}{r}\frac{\partial}{\partial r}\left(r\frac{\partial N(r,t)}{\partial r}\right) = \dot{N}(r,t), \tag{3.20}$$

where the diffusion constant D is given in Equation 2.4. The spatial profiles for all three state populations are evolved forward in time in discrete steps. For each step, the probability

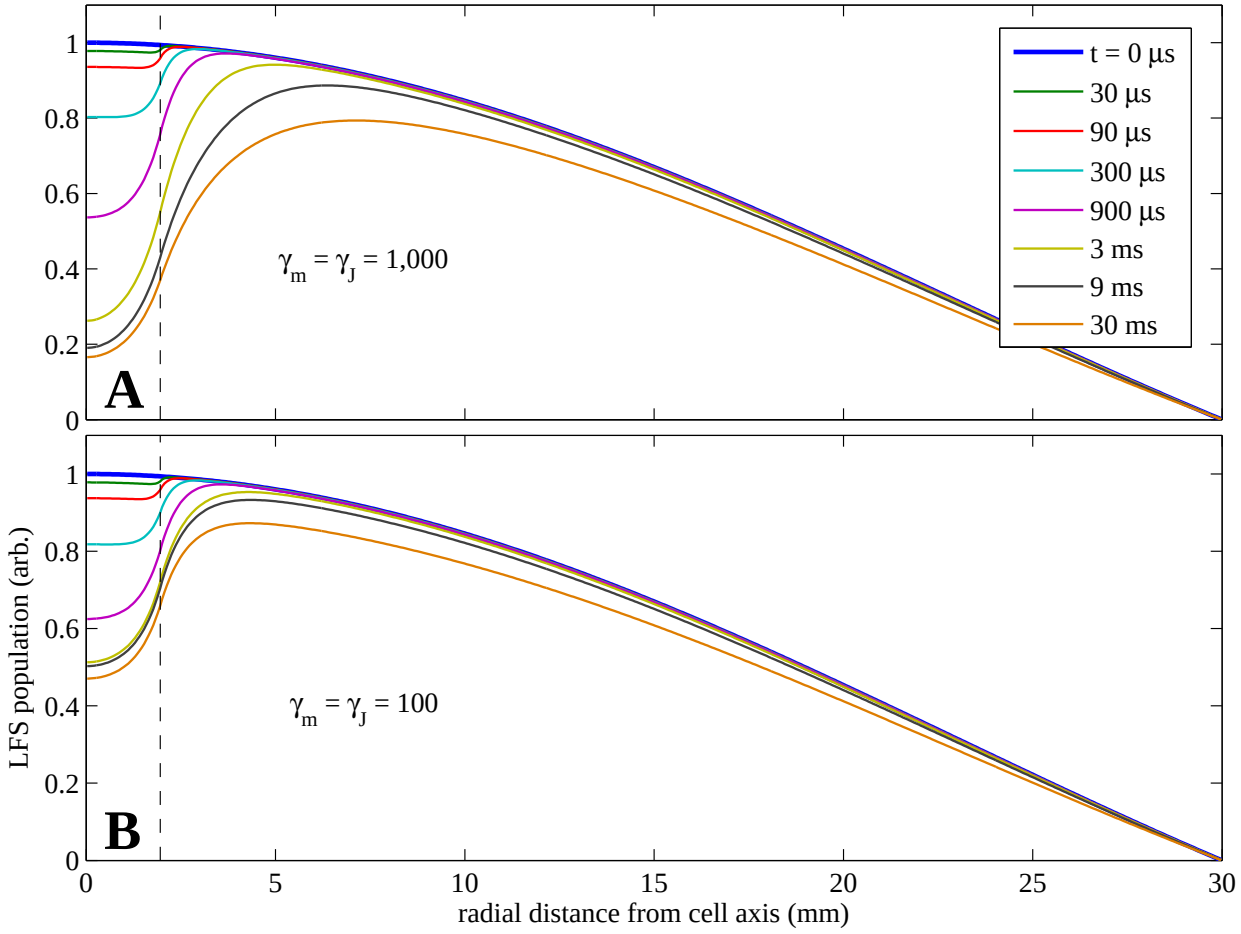

Figure 3.12: Spatial simulation of Al optical pumping, diffusion and Zeeman relaxation. The parameters used are: $T = 820$ mK, $B = 3$ T, $D = 5$ mm^2/ms, $s_0 = 5 \times 10^{-4}$, $f_+ = 0.7$, and a uniform pump beam of diameter 3.9 mm (dashed lines). (A) For slower relaxation, diffusion plays a dominant role, and the region beyond the beam is steadily depleted of LFS atoms; (B) rapid relaxation causes the distribution to reach steady state more rapidly, and with larger LFS population in the beam.

of an atom undergoing an optical or inelastic transition is computed locally. An example of this spatial evolution is shown in Figure 3.12. The *OD* is calculated by integrating the atom density over the beam profile. *OD* is normalized to 1 when optical pumping begins at $t = 0$, at which time the spatial distribution is given by the lowest-order diffusion mode (Equation 2.3).

The simulated *OD vs.* time is integrated over the same interval of $t = 1.5$–2.9 ms that is used for integrating the *OD* observed in the experiment. Since $OD(t = 0) = 1$, this integral is equal to the ratio $OD(P)/OD(P \to 0)$, which is the same quantity extracted from the data. The simulation is repeated for a range of τ_d inclusive of the experimental range. This process is rather computationally intensive, so it would be impractical to employ it in a fitting routine. Instead, a set of simulations is generated over a matrix of values of the parameters γ_m, γ_J and the branching ratio f_+/f_-. For each element of this matrix, a goodness-of-fit criterion is computed by taking the sum of squares of residuals from the simulation curve. To appropriately account for the 2D error bars, minimum 2D error-normalized residuals are computed as shown in Figure 3.11.

One additional free parameter, a scaling factor for the total pump laser power, is included to account for imperfect knowledge of experimental parameters. The numerical solution to Equations 3.8–3.10 is sensitive to: pump beam size, intensity profile and detuning from resonance; Doppler and Zeeman broadening; and absorption and birefringence in optical elements within the cryogenic environment. While each effect is carefully investigated, compounding measurement uncertainties can cause a vertical offset of the simulated curves to the data. The additional free parameter, which is generally $\lesssim$2, accounts for such effects, many of which mimic an adjustment of pump power.

Because there may be several minima of the goodness-of-fit matrix, and since the residuals from this fitting procedure are not normally distributed (because the problem is nonlinear), confidence intervals are computed for the fitting parameters using a bootstrapping procedure. The procedure is as follows: (1) we resample equal-sized data set from the original with replacement (*e.g.*, the data set $\{1, 2, 3, 4, 5\}$ might be resampled as $\{2, 1, 3, 2, 5\}$); (2) we re-compute the goodness-of-fit matrix using the resampled data and find its minimum (best fit); (3) we perform steps (1) and (2) 100 times. We take the median and confidence intervals

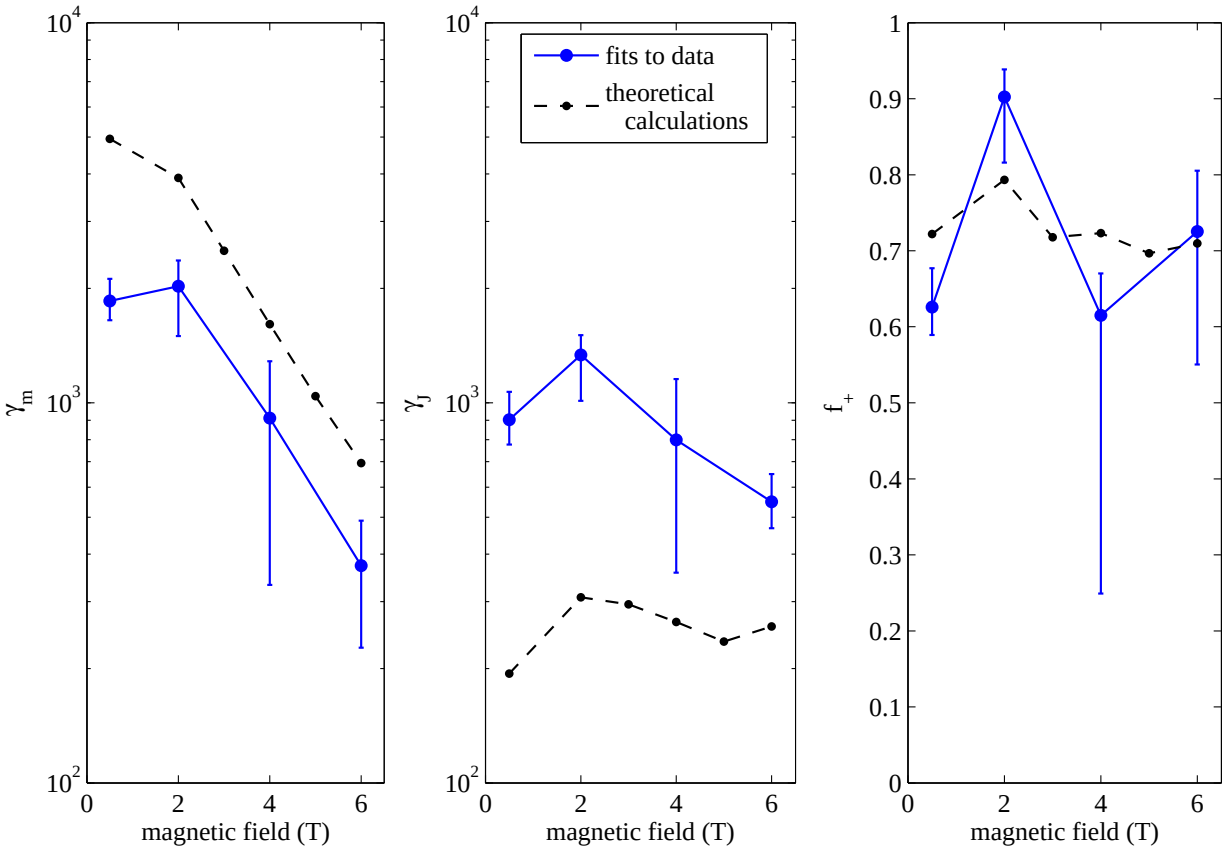

Figure 3.13: Inelastic collision parameters extracted—the m_J-changing collision ratio γ_m, J-changing collision ratio γ_J, and J-changing collision LFS-state branching fraction f_+—from unbounded fitting of optical pumping data to numerical simulation. The parameter f_+ is poorly constrained by the fits, which introduces systematic bias to push γ_m and γ_J toward one another. Also shown are theoretical calculations by Tscherbul (dashed) [95].

of the resulting distribution of 100 best-fit sets of parameter values to be representative of the true best-fit parameters and their statistical uncertainty.

3.5.3 Results from fitting data to simulation

Best-fit parameters for the collision ratios γ_m, γ_J and the branching fraction $f_+ = 1 - f_-$ with bootstrapped confidence intervals are presented in Figure 3.13. It is clear from the large uncertainty in f_+ that this parameter is poorly constrained by the data. This fact

is confirmed by the simulation: if f_+ is set to extremes of 0 or 1, the primary effect is to enhance the distinction between optically pumping the two different ground state sublevels (the solid red and dashed blue curves in Figure 3.11). Otherwise, there is little effect on the functional form of the data as a function of diffusion time. Furthermore, variation in f_+ is mimicked by adjustment of the relative contributions of m_J- *vs.* J-changing collisions (*i.e.*, γ_m *vs.* γ_J). Therefore, allowing f_+ to vary freely in the fit from 0 to 1 confuses these effects in the fitting procedure and introduces a systematic bias forcing γ_m and γ_J toward the same value.

There is, however, *a priori* justification for constraining the value of f_+. The branching fraction is determined by the m_J dependence of the interaction Hamiltonian in Equation 3.3. Specifically, the first 3-j symbol evaluated for $m'_J = \pm 1/2$ gives ratios of $f_+ = 0.8$, 0.6, 0.4 and 0.2 for J-changing transitions from the $m_J = +3/2$, $+1/2$, $-1/2$ and $-3/2$ sublevels of the $^2P_{3/2}$ manifold, respectively. The exact calculation of the scattering matrix, however, will be significantly affected by resonant behavior and higher-order couplings that mix these ratios (to push f_+ toward 0.5, on average). Nevertheless, for decay from the upper $m_J = +3/2$ state, the value of f_+ is expected to be almost 0.8.

This argument is borne out by the calculations of Tscherbul [95]. To test the sensitivity of the theory to error in the potential, calculations were performed three times with the interaction potentials scaled by a factor λ of 1, 1.05 and 0.95, respectively. The resulting values of f_+ for collisions of atoms in the $m_J = -3/2$ sublevel are shown as a function of magnetic field in Figure 3.14. There is no obvious trend with respect to magnetic field or λ. Instead, the values appear more or less randomly distributed around a mean of 0.716, as would be expected from averaging over the contributions from multiple collision resonances. Performing the bootstrapping procedure again with the simulation constrained to this mean value yields the orange points in Figure 3.15, which are in better agreement with

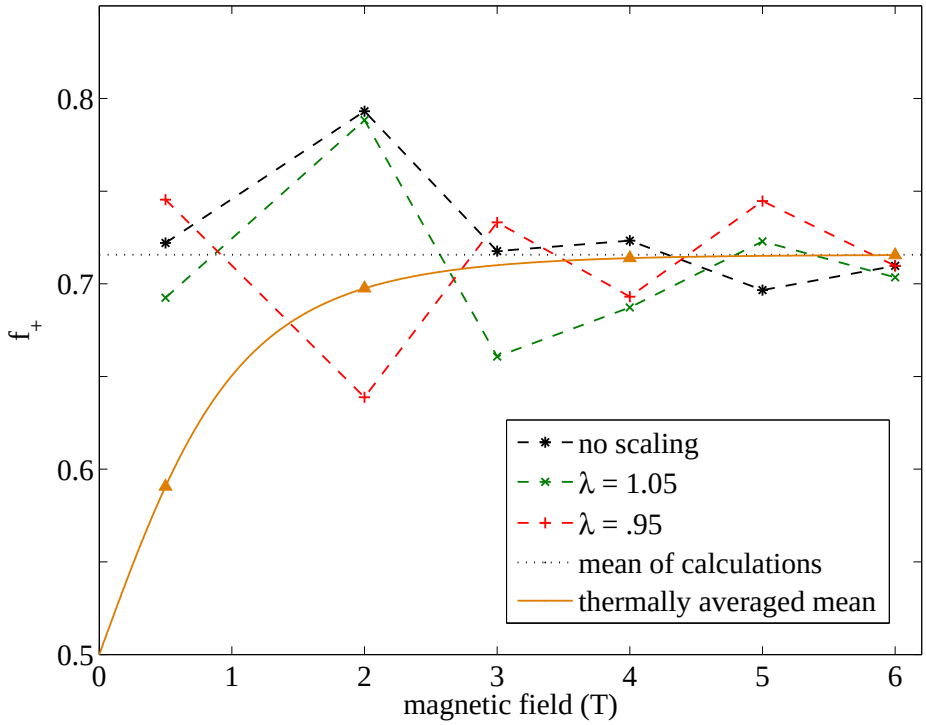

Figure 3.14: Theoretical calculations by Tscherbul [95] of the LFS state branching fraction f_+ for J-changing Al–^{3}He collisions from the $m_J = -3/2$ sublevel of the $^2P_{3/2}$ state. Results are shown for different values of the scaling factor λ. The values appear randomly distributed around a mean of 0.716 (dotted), showing no obvious trend with respect to magnetic field or λ. The solid orange line gives the prediction of the thermally-averaged model given in Equations 3.21 and 3.22.

the calculated values, presumably from removing the systematic bias of the unconstrained fit.

For the lowest fields of the experiment, especially $B = 0.5$ T, there is a nonnegligible thermal population in $m_J > -3/2$ sublevels of the $^2P_{3/2}$ state at the experimental temperature of 820 mK. The branching fraction f_+ should differ for J-changing collisions of atoms in the different sublevels, even if all sublevels are assumed to share the same total J-changing collision rate. At $B = 0.5$ T, where <50% of atoms are in the lowest $^2P_{3/2}$ sublevel, fixing f_+ to 0.716 likely introduces error into the result. To address this, a thermally-averaged value

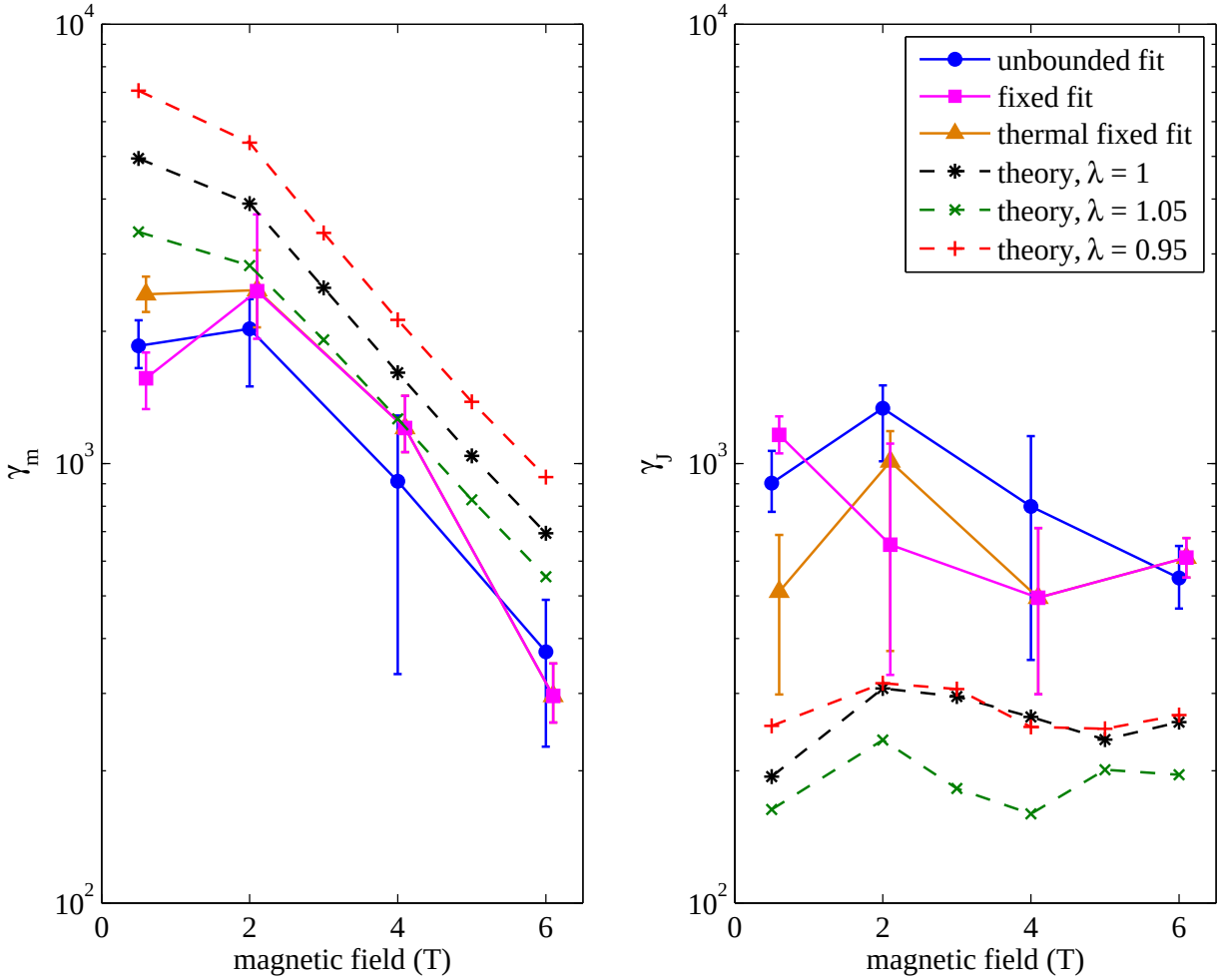

Figure 3.15: Inelastic collision parameters extracted—the m_J-changing collision ratio γ_m and J-changing collision ratio γ_J—from fitting of optical pumping data to numerical simulation with the J-changing branching fraction f_+ unconstrained (blue circles), fixed at $f_+ = 0.716$ (magenta squares), and fixed at $f_+ = \tilde{f}_+$ (orange triangles, Equations 3.21 and 3.22). Theoretical calculations by Tscherbul [95] (dashed lines) are given for Al–^{3}He interaction potential scaling factor $\lambda = 1$, 1.05 and 0.95. Fixing f_+ gives better agreement with theory.

$\tilde{f}_+$ was computed for each field using the function

$$\tilde{f}_+ = 0.5 + \left(\frac{0.716 - 0.5}{0.8 - 0.5}\right) \times (\langle f_+ \rangle_{\text{th}} - 0.5) \tag{3.21}$$

$$\langle f_+ \rangle_{\text{th}} = \sum_{m_J} N_{m_J}(T)\, f_+, \tag{3.22}$$

where f_+ is the branching fraction calculated from the first 3-j symbol in Equation 3.3,

Table 3.3: Thermally-averaged J-changing collision LFS-state branching fractions for $T = 820$ mK used to constrain fitting of optical pumping data to numerical simulations. $\langle f_+ \rangle_{\rm th}$ and $\tilde{f}_+$ are defined in Equations 3.21 and 3.22. $\tilde{f}_+$ is plotted in Figure 3.14.

Magnetic Field (T)	$\langle f_+ \rangle_{\rm th}$	$\tilde{f}_+$
0.5	0.626	0.591
2	0.775	0.698
4	0.797	0.714
6	0.800	0.716

ranging from 0.8 to 0.2, and $N_{m_J}(T)$ is the fractional thermal population at temperature T. This calculation of $\tilde{f}_+$ uses a simple model for the resonance-averaged thermal branching fraction that assumes the result of the $m_J = -3/2$ calculations—namely, the comparison of 0.716 (the mean value of calculations) to 0.8 (the 3-j symbol prediction)—is indicative of how collision resonances push the value of f_+ toward 0.5 for collisions of atoms in any sublevel. The theoretical justification for $\tilde{f}_+$ is weak, but it likely is more accurate than using the resonance-free prediction $\langle f_+ \rangle_{\rm th}$ or the lowest-sublevel-only value of $f_+ = 0.716$. Values of $\tilde{f}_+$ are shown in Figure 3.14 and given in Table 3.3 along with $\langle f_+ \rangle_{\rm th}$. Repeating the bootstrapping procedure using $f_+ = \tilde{f}_+$ yields the orange triangles in Figure 3.15. The parameters using this approach differ beyond the fitting error from the $f_+ = 0.716$ values only for $B = 0.5$ T, for which they give the best agreement with the calculated values. All fitting results are also summarized in Table 3.4.

It is important to consider the possibility that J-changing transitions from thermally populated $m_J > -3/2$ states in the $^2P_{3/2}$ manifold will differ not only in f_+, but also in k_J, the J-changing collision rate coefficient. This would cause the experiments at low field to measure a thermally-averaged contribution of the different values of k_J and confuse the comparison to theory. In the absence of resonances, however, the form of Equation 3.3 implies

Table 3.4: Summary of inelastic parameter fitting results at $T = 820$ mK for the different treatments of f_+ described in the text, with 68% confidence intervals in parentheses.

Magnetic Field (T)	f_+ unconstrained γ_m	γ_J
0.5	1854 (1589, 2059)	903 (736, 1028)
2	2028 (1686, 2557)	1337 (1167, 1662)
4	911 (536, 1491)	799 (443, 1240)
6	373 (256, 519)	549 (449, 630)
Magnetic Field (T)	$f_+ = 0.716$ γ_m	γ_J
0.5	1563 (1337, 1794)	1162 (1043, 1270)
2	2469 (1245, 3015)	654 (198, 978)
4	1204 (983, 1348)	495 (277, 692)
6	296 (241, 334)	611 (545, 672)
Magnetic Field (T)	$f_+ = \tilde{f}_+$ γ_m	γ_J
0.5	2428 (2193, 2643)	511 (334, 724)
2	2482 (1905, 2921)	1011 (836, 1647)

Table 3.5: Summary of theoretical calculations by Tscherbul [95] for $T = 820$ mK with interaction potential depths scaled by λ.

Magnetic Field (T)	γ_m			γ_J		
	$\lambda = 1$	1.05	0.95	$\lambda = 1$	1.05	0.95
0.5	4948	3367	7061	194	163	253
2	3905	2823	5377	308	235	316
3	2512	1913	3351	295	182	307
4	1610	1264	2125	265	159	252
5	1042	827	1383	235	201	249
6	694	552	932	258	196	268

that the inelastic cross section does not vary dramatically between magnetic sublevels. In addition, the thermal average over collision energies performed to obtain k_J and γ_J will blur any resonant behavior.

3.6 Conclusion

3.6.1 Comparison of experiment with theory

Theoretical calculations for the unscaled potential and for ±5% scaling are shown in Figure 3.15 along with the parameters extracted from fitting the data to numerical simulations. The theory values are also summarized in Table 3.5. The calculated magnetic field dependence of both γ_m and γ_J is in good agreement with the data. The $\sim B^{-2}$ dependence of γ_m in the range of $B = 2$–6 T reflects the increased fine-structure state mixing as the magnetic sublevels are Zeeman-shifted toward one another [95]. In the case of γ_J, the J-changing inelastic collisions are a small contribution to the rapid m_J-changing collisions in the $^2P_{3/2}$ state ($\gamma_m < 10$ in this state [1]; see Table 3.1). Therefore, there is no simple field dependence and the form of $\gamma_J(B)$ is more heavily affected by collision resonances that are sensitive to the exact form of the potential. In general, the result is independent of magnetic field in the range calculated.

The magnitudes of the measured values of γ_m and γ_J are in better agreement with theory when the constrained fitting procedure is used. It is likely that the unconstrained fit is systematically biased toward $\gamma_m \sim \gamma_J$. For the constrained-fit data, the magnitude of γ_m agrees very well with theory, especially for $\lambda = 1.05$, however the measured γ_J is a factor of ∼3 larger than the calculated value. It is possible that this reflects residual systematic bias of $\gamma_J \to \gamma_m$. For $\gamma_J \ll \gamma_m$, Equation 3.11 is only weakly dependent on Γ_J (if $\Delta f = f_+ - f_-$ is not near zero), and hence its value is not as tightly constrained by the data in that case.

3.6.2 Implications for future work with ^2P atoms

The comparison of experiment and theory, and specifically the comparison as a function of magnetic field, gives strong evidence that the mechanism of Zeeman relaxation in the $^2P_{1/2}$ system is indeed collisional mixing of the excited fine-structure state. This adds confidence to the predictions of very large values of γ for collisions of gallium and indium (and metastable halogens chlorine, bromine and iodine) with helium, with predictions ranging $\sim 10^4$–10^9. The theoretical picture applies to other S-state atoms, as well (although for collisions with atoms with $L > 0$, Equation 3.3 is modified such that relaxation in the $^2P_{1/2}$ state is not necessarily forbidden at first order). In the cases of indium and thallium, where the ground state is isolated by 2,213 cm^{-1} and 7,793 cm^{-1}, respectively, the Zeeman relaxation suppression may extend to collisions of indium or thallium atoms with trapped ultracold alkali atoms if the strength of the interaction potential does not exceed this splitting. This could allow for sympathetic cooling of these atoms in a magnetic trap.

The large trap depth and volume available with a magnetic trap could translate into many more ultracold atoms available for experiments. Species with poor collision properties have few choices beyond optical dipole traps, which are limited in size and depth by practical and technical limitations on laser power. The ability to laser cool Group 13 atoms has already been demonstrated [27, 79, 80], and trapping is a natural next step. For some of the proposed experiments with these atoms, especially precision measurements [81, 83, 84], large atom numbers are important. The theory developed by Tscherbul *et al.* and confirmed experimentally here and in [1] has provided a potential route to reach that goal. In addition, the discovery that collisions of these ^2P atoms are robustly elastic may inspire future theory and experiment for new uses for these unique systems.

Chapter 4

Rare-earth atom–atom collisions

4.1 Submerged-shell atoms

The previous two chapters gave examples of systems that run counter to the simple principle that S-state atoms should uniquely exhibit robustly elastic collisions. In the case of antimony, a nominally S-state atom was strongly affected by relativistic spin-orbit coupling that rapidly drove inelastic transitions; in the case of aluminum, a P-state atom, such inelastic transitions were suppressed to below the case of antimony.

Another important and widespread exception to the uniqueness of S-state elasticity is the set of so-called "submerged-shell" atoms that account for roughly a third of the periodic table. Due to nonsequential filling of electronic orbitals, these atoms have valence electrons that lie closer to the nucleus than do closed outer electron shells (those with higher principle quantum number) [100]. In many cases, the inner valence electrons are highly anisotropic in the ground state and the total atomic orbital angular momentum is large. During a collision with helium, however, the interaction with the spherical outer electron distribution shields this anisotropy, resulting in a nearly isotropic electrostatic interaction. This shielding was

observed in many transition metal [63] and lanthanide rare-earth (RE) [2] atoms during collisions with helium, demonstrating that electronic anisotropy does not necessarily imply rapid inelastic collisions.

The shielding effect leads to measured values of γ of 10^3–10^5 for many submerged shell atoms [2, 63, 64]. This is in dramatic contrast to the inelasticity for an interaction dominated by anisotropic valence electrons, as calculations predict for the unshielded $^3P_2$ ground state of oxygen [91] and the upper fine-structure state of aluminum described in Chapter 3 [1] (see Table 3.1). The mechanism of submerged-shell anisotropy shielding has also been explored theoretically and shown to indeed arise from the outermost filled s-orbital [3, 101]. Suppression of inelastic collisions in submerged-shell atoms was an exciting development, particularly for the possibility of extending collisional cooling to a wide array of new atoms. Elastic collisions with helium allowed for many new species to be buffer-gas cooled and magnetically trapped [2].

The lanthanide RE atoms, in particular, exhibit very low inelastic collision rates in colliding with helium ($\gamma > 10^4$ [2]) and can be trapped in large numbers. The lanthanide series is of significant technical interest, as well, due to important and sometimes unique attributes such as narrow transition linewidths useful for precision measurement [102, 103] and sub-Doppler cooling [104, 105], and large magnetic moments with strong long-range interactions that can be used to realize unique ultracold states [106–108] or implement quantum computing schemes [109]. The discovery of anisotropy shielding in the RE–helium system laid open the question of whether similar suppression would exist for RE–RE inelasticity, which could allow for efficient evaporative cooling and, for example, the creation of large quantum degenerate ensembles of RE atoms using magnetic traps.

This chapter describes measurements of RE–RE Zeeman relaxation rates in two systems, collisions between erbium atoms and those between thulium atoms. Both erbium and thulium

have highly anisotropic valence electrons (the ground state terms are $[\mathrm{Xe}]4f^{12}6s^2(^3H_6)$ for erbium and $[\mathrm{Xe}]4f^{13}6s^2(^2F_{7/2})$ for thulium [110]) and have magnetic moments of $\mu_{\mathrm{Er}} = 7\ \mu_{\mathrm{B}}$ and $\mu_{\mathrm{Tm}} = 3.5\ \mu_{\mathrm{B}}$. We find that both the erbium–erbium and thulium–thulium relaxation rates are very large ($\gamma \lesssim 10$), in striking contrast to the RE–helium systems, and we see no evidence that electronic interaction anisotropy is suppressed. This discovery helps to draw boundaries on the submerged-shell model of anisotropy shielding, and implies that evaporative cooling is likely impossible for $L \neq 0$ RE atoms in a magnetic trap.

4.2 Experimental design

4.2.1 Apparatus

The experimental cell used to measure RE–RE collisions (Figure 4.1) was originally built for the creation of a buffer-gas cooled Bose-Einstein condensate of metastable helium-4, and is described in detail in the thesis of Charlie Doret [111]. It has several features that are not utilized for trapping RE atoms, including a valve to a pumpout chamber (which is left closed for the experiments described here) and a radiofrequency (RF) discharge coil wound on the outer cell surface. The experimental apparatus is otherwise largely similar to that used in the previous two chapters. Helium-4 buffer gas is added to the cell from the waiting room in the same manner and the same magnet coils surround the cell, except that in this case they are configured in an anti-Helmholtz geometry to produce a quadrupole trapping field.

Detection of ground-state erbium and thulium is accomplished by absorption spectroscopy with diode lasers. The transitions used are $J = 6 \rightarrow 7$ and $J = 6 \rightarrow 5$ for erbium at 400.9 nm and 415.2 nm, respectively, and $J = 7/2 \rightarrow 5/2$ for thulium at 409.5 nm. A probe beams is free-space coupled to the experimental dewar and then split to provide an intensity reference for the absorption measurement. To minimize the noise due to vibration of the cell

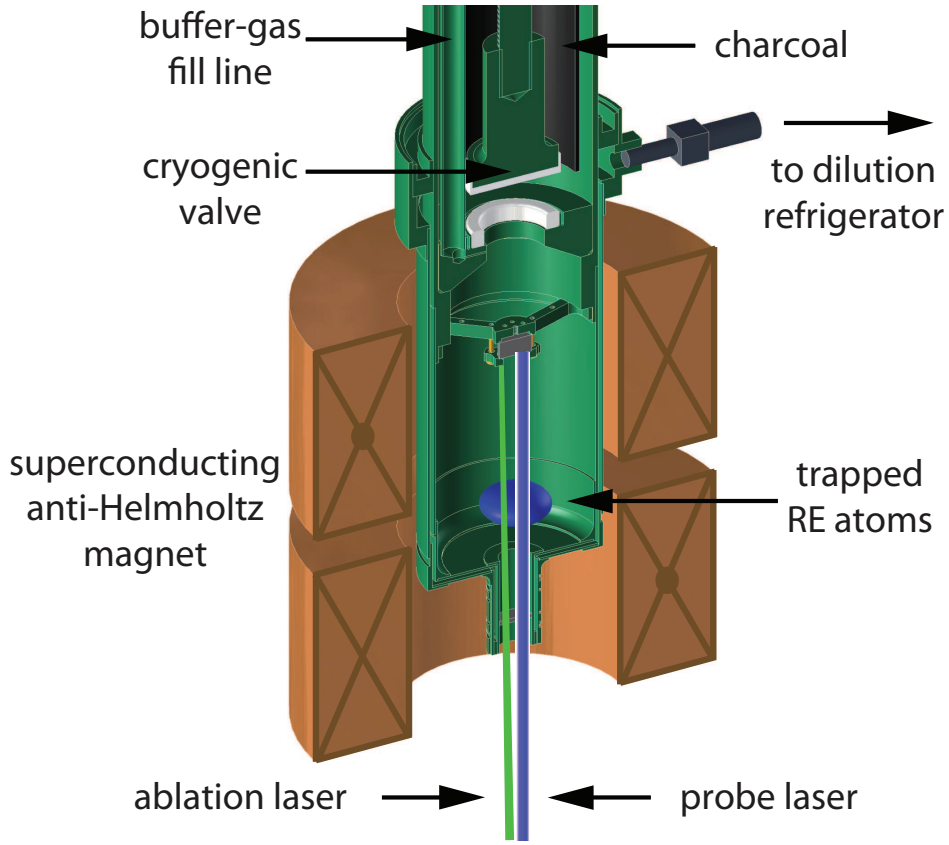

Figure 4.1: Experimental cell used for RE–RE collision measurements. The cell is described in detail in [111].

mirror, a lens outside the dewar focuses the probe beam onto the mirror; upon reflection, the beam is collimated by the same lens and then imaged onto the detector by an additional lens to reduce variation in detected power (see Section 4.2.1 of [111]). The focusing in the cell also ensures a small beam at the trap center, sharpening spectral features to improve fitting precision.

4.2.2 Buffer-gas cold loading of magnetic traps

As was previously demonstrated by Hancox *et al.*, the low inelastic collision rates of erbium and thulium with helium atoms makes it possible to trap these atoms. The previous experi-

ments were performed with helium-3 buffer gas at a density of 8×10^{15} cm^{-3} in a copper cell at ∼800 mK [2]. Under these conditions, the RE–helium collision rate is $\gtrsim 7 \times 10^5$ s^{-1} and lifetimes due to RE–helium Zeeman relaxation are limited to $\lesssim$100 ms, too rapid to observe collisions between the trapped atoms. By using helium-4 buffer gas, the helium density can be reduced after trap loading to achieve thermal isolation. This is done by ablating at high helium density while heating the cell and then allowing the cell to cool to adsorb the buffer gas onto the cell walls, a process that takes about 1 s due to the thermal response time of the heat link to the dilution refrigerator (see Section 2.2.4). This method was applied to trap and thermally isolate dysprosium atoms ($\mu = 9.93\ \mu_B$, $\gamma = 4.5 \times 10^5$), which were observed for up to 20 s in the trap [72]. The loss mechanism for trapped dysprosium after cell cooling was not identified in those experiments, however, and no definite conclusions were drawn regarding collisions between dysprosium atoms.

An additional method called cold loading has been used in several cases to more rapidly reduce the buffer gas density after ablation [30, 70, 112–114]. Cold loading consists simply of ablation (or a YAG pulse in concert with a separate production method [114]) in a cell that is initially cold enough to ensure a very low initial helium density ($n_b \lesssim 10^{13}$ cm^{-3}). Typically, helium-4 is used. The energy of the ablation laser pulse desorbs a sufficient quantity of helium to cool the ablated atoms, and the subsequent cell cooling causes this helium to be readsorbed onto the cell walls. Desorbing with the ablation energy instead of a resistive heater allows for less total energy to be added to the cell, and hence a faster return to pre-ablation temperatures. This method was first used for buffer-gas loading of chromium atoms into a magnetic trap [112], demonstrating significantly less cell heating, but also a reduced trapped atom yield.

There is an important distinction to be made, however, between different regimes of cold loading that employ different loading energies and cell construction. As described below, cold

loading in a copper cell relies on a slow (second-scale) thermal connection to the refrigerator. In contrast, cold loading in superfluid-jacketed G-10 cells can produce a transient buffer gas density with a shorter lifetime (below 100 ms) while retaining a very large cell heat capacity in the superfluid. This extension to the cold loading concept, used in the experiments described here to trap erbium and thulium, is especially suited to moderate-γ species for which minimizing helium collisions is critical for trapping.

We first consider cold loading in a copper cell, which is not likely to be fundamentally different from traditional loading with a heating-cooling cycle, and differs only in the total energy used. Both processes increase the buffer gas density by heating the surfaces to which helium is adsorbed. The deposited heat immediately begins to diffuse into the solid walls of the cell by up to 3 mm on a timescale of $\approx$10 μs (Equation 2.7). This heat diffusion is extremely rapid, far below the 1-ms timescale of ballistic transport across the cell. Hence the cell wall surfaces have equilibrated with a large volume of copper ($\gtrsim$50 cm^3) before the desorbed helium atoms return to the walls. If the ablation energy deposited is small, then the heat capacity of this solid volume will ensure that the cell wall will be cold enough to re-adsorb the helium. In this low-energy situation, buffer-gas cooling is not possible because the necessary helium density [30] cannot develop. In the other regime of large ablation energy, the entire cell will warm significantly within the millisecond-scale thermal diffusion time, and the increased helium density will be temporarily stable. Cooling of the cell must now occur *via* conduction to the refrigerator—a situation not much different from the traditional heating-cooling cycle method of removing buffer gas [97, 112]. Cold loading aims for the ideal intermediate energy, with just enough helium as necessary for buffer-gas cooling. However, the large thermal conductivity of copper ensures that the entire cell must be heated, subsequently requiring $\gtrsim$1 s to cool significantly. The trapped atoms will experience collisions for this duration, which for minimal buffer-gas cooling densities near

$n_b \approx 10^{15}$ cm^{-3} implies more than 5×10^4 collisions (assuming $\sigma_d = 10^{14}$ cm^2). For species with $\gamma \sim 10^4$, this will result in significant losses due to inelastic collisions.

The cold-loading picture is different in a cell constructed from low-thermal-conductivity materials such as G-10, for which the diffusion of heat into the solid is slowed. As described in Section 2.2.4, when the energy of ablation heats G-10 surfaces to desorb helium, the heat will take ≈10 ms to diffuse 1 mm. For ablation energies of 1–10 mJ, the walls will heat significantly and sustain a high buffer gas density long enough for the ablated atoms to reach equilibrium. Unlike copper cells, there can then be an additional heat capacity which provides rapid cooling on the >30-ms time scale, but that does not play a role at shorter times (Figure 2.5). One example of such a heat capacity is the superfluid helium jacket surrounding the inner G-10 wall of the composite cells used in this thesis. The superfluid has a very large heat capacity that exceeds that of the entire mass of G-10, and that of the entire typical copper cell. Hence a modest ablation energy, after first producing a high helium density for ∼10 ms, will subsequently be rapidly absorbed into the cell's heat capacity to ensure a low cell temperature and good vacuum. We refer to this variation on cold loading as *pulsed-density* cold loading.

Pulsed-density cold loading is used here to trap erbium and thulium atoms, which would otherwise leave the trapped state after an average of $\gamma = 4.3 \times 10^4$ and 2.7×10^4 collisions, respectively [2], *i.e.*, within less than 100 ms at a helium density of 10^{16} cm^{-3}, assuming a momentum transfer cross section $\sigma_d = 10^{14}$ cm^2. The cell is held at ≈500 mK before ablation, at which temperature the helium-4 saturated vapor density is $<10^{14}$ cm^{-3} [59] and insufficient for buffer-gas cooling [30]. Erbium or thulium metal is ablated with pulse energy of ≈5 mJ to fill the trap. Figure 4.2 shows trapped spectra for both species, which are compared to simulated spectra to determine the peak density in the trap. RE–RE collisional loss of the trapped atoms is immediately apparent, with no evidence of loss due to RE–helium

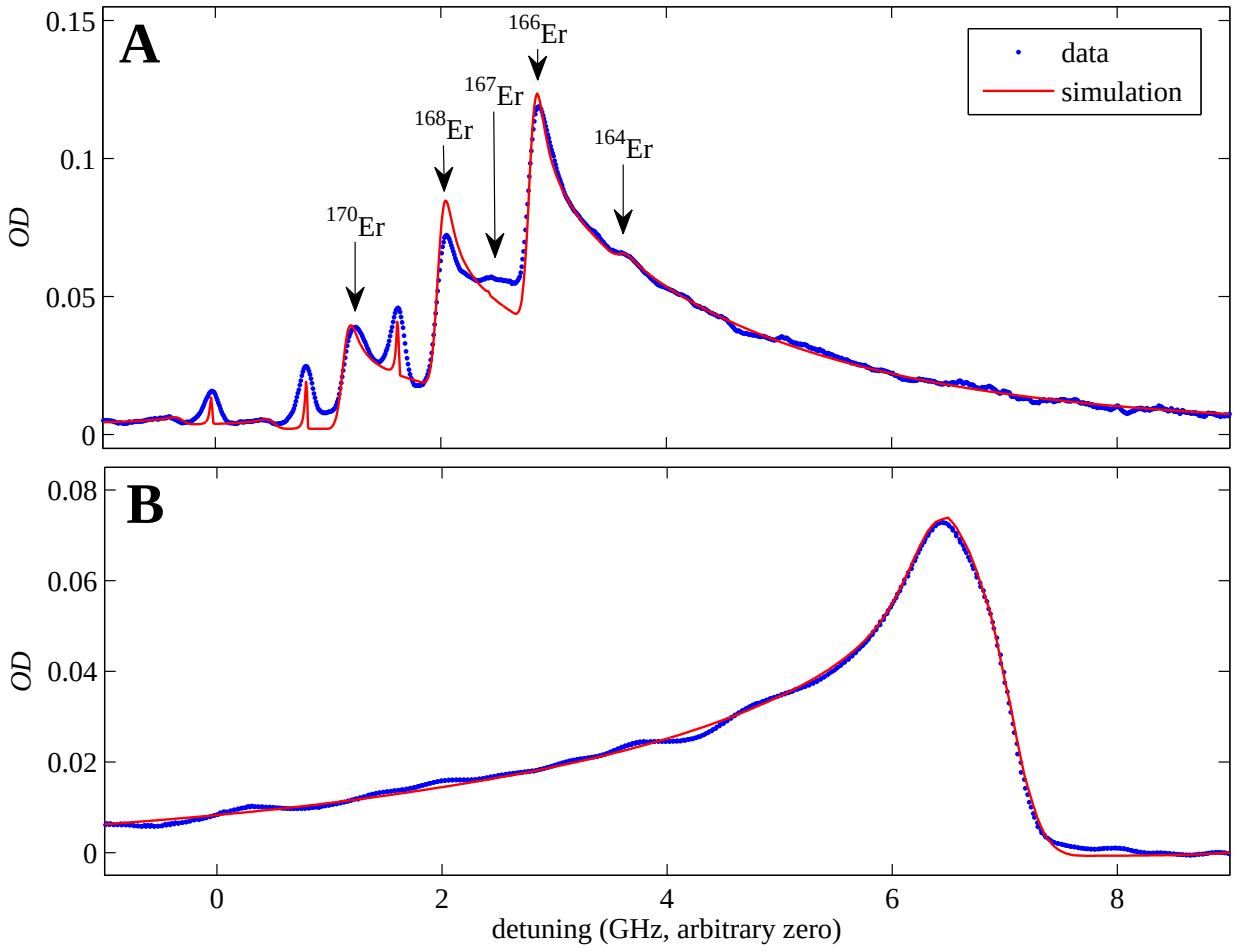

Figure 4.2: (A) Absorption spectrum of Er on the 400.9-nm ($J = 6 \rightarrow 7$) transition in a 0.99-T (4.6 K) deep magnetic trap at 530 mK with a peak density of 4.6×10^{10} cm^{-3}. The $\Delta m_J = +1$ Zeeman broadened peaks of the dominant isotopes are labeled. The sharper peaks are $\Delta m_J = 0$ transitions. Hyperfine constants could not be found for ^{167}Er ($I = 7/2$, 23% abundance), and it is ignored in the spectrum simulation. Due to the substantial Zeeman broadening, this does not significantly affect the implied atom density and temperature. (B) Spectrum of Tm on the 409.5-nm ($J = 7/2 \rightarrow 5/2$) transition in a 3.3-T (8.8 K) deep trap at 500 mK with a peak density of 3.8×10^{11} cm^{-3}. Tm has a single isotope with $I = 1/2$ and known hyperfine splitting [115].

Zeeman relaxation.

4.2.3 Inelastic collisional heating

Once the atoms have been loaded into the magnetic trap and the helium density has returned to low levels ($<10^{12}$ cm^{-3}), the trapped ensemble is thermally isolated from the cell walls with a RE–helium Zeeman relaxation lifetime >100 s. The trapped distribution is now free to evolve on its own *via* RE–RE collisions: elastic collisions thermalize the trapped ensemble and drive evaporation and cooling; and inelastic collisions cause trap loss and heating.[1] Magnetically trapped systems are well-studied and are known to approach an equilibrium temperature determined by the competition of evaporative cooling and inelastic heating [116].

We first consider evaporative cooling, the selective removal of high-energy atoms from an equilibrating distribution. In the RE trapping cell described in Section 4.2.1, the trap depth $U_{\rm trap} = \mu B_{\rm trap} \approx \mu \frac{\partial B}{\partial r} R$ is set by the magnetic field at the inner surface of the cell wall of radius R (the last equality is approximate because the field deviates from a quadrupole near the magnet coils at the trap edges). Trapped atoms in orbits that intersect the wall will freeze there. If the trapping parameter $\eta = \mu B_{\rm trap}/k_{\rm B}T \gg 1$, then these large-orbit atoms will carry away an energy $U_{\rm trap} + E_{\rm K} \gg k_{\rm B}T$ and reduce the average energy of the remaining atoms, where $E_{\rm K} = \frac{3}{2}k_{\rm B}T$ is the average atomic kinetic energy. Elastic collisions[2] continually thermalize the trapped ensemble to repopulate the tail of the Boltzmann distribution that contains these high-energy atoms, providing an evaporative loss rate (in a quadrupole trap)

[1] Three-body collisions may play a role in addition to two-body collisions, but the densities of the experiments described here are low enough that they are not observed.

[2] By convention, the phrase "elastic" is used here instead of "momentum transfer" to match the literature on the subject. In this chapter, elastic collisions refer to those that randomize the velocity of the two atoms.

[116–118] of

$$\Gamma_{\text{evap}} = 4\sqrt{2}\,\eta\, e^{-\eta}\,\Gamma_{\text{el}} \tag{4.1}$$

$$\begin{aligned}\Gamma_{\text{el}} &= \int k_{\text{el}} n(\boldsymbol{r})\; d^3r \\ &= \frac{k_{\text{el}} n_0(\boldsymbol{r})}{8}\end{aligned} \tag{4.2}$$

where k_{el} is the elastic collision rate coefficient, n_0 is the density at the trap center, and Γ_{el} is the trap-averaged elastic collision rate. Equation 4.1 is valid in the limit of $\eta \gg 1$. Evaporation will continue indefinitely to cool the trapped atoms, although the rate of cooling will slow as η increases and it becomes increasingly unlikely for an elastic collision to provide the energy necessary for an atom to leave the trap.

In any realistic system, evaporative cooling will compete with heating processes. Specifically, Zeeman relaxation will cause heating due to the preferential loss of atoms in regions of higher density and therefore lower potential energy. The heating rate can be calculated from the difference between the average potential energy in the trap,

$$\begin{aligned}\bar{U} &= \frac{\int \mu B(\boldsymbol{r}) n(\boldsymbol{r})\; d^3r}{\int n(\boldsymbol{r})\; d^3r} \\ &= \frac{1}{N}\int \mu B_{\text{trap}}\left(\frac{\sqrt{x^2+y^2+4z^2}}{R}\right) n_0\, e^{-\eta\sqrt{x^2+y^2+4z^2}/R}\; d^3r \\ &= 3k_{\text{B}}T,\end{aligned} \tag{4.3}$$

and the average potential energy of atoms undergoing a two-body collision,

$$\begin{aligned}\bar{U}_{\text{coll}} &= \frac{\int \mu B(\boldsymbol{r}) n(\boldsymbol{r})^2\; d^3r}{\int n(\boldsymbol{r})^2\; d^3r} \\ &= \frac{3}{2}\, k_{\text{B}}T,\end{aligned} \tag{4.4}$$

where n_0 is the density at the trap center and the ellipsoidal quadrupole field geometry has been used for both averages. Equations 4.3 and 4.4 show that the inelastically colliding

atoms have on average half the mean potential energy, thus Zeeman relaxation increases the average energy of the atoms that remain. This heating is exacerbated if the Zeeman energy released in the collision is added back to the atomic ensemble. This can occur in two ways: (1) if the cloud is collisionally thick (the mean free path is smaller than the cloud size), such that the relaxed atoms, now in untrapped states, collide again elastically before reaching the cell wall; or (2) if only one colliding partner relaxes and the other remains in the trap, in which case half the energy will remain.

The competition of evaporative cooling and Zeeman relaxation heating will be balanced at a certain cloud temperature $T_{\rm eq}$ where the heating and cooling rates are balanced, corresponding to an equilibrium trapping parameter $\eta_{\rm eq}$. This parameter is calculated by equating the rates of cooling and heating in the trap and assuming a equilibrated trap distribution. The value of $\eta_{\rm eq}$ depends only on the trapping geometry and the elastic-to-inelastic collision ratio γ. This dependence is shown in Figure 4.3, taken from [118]. In general, it will take the cloud a long time to approach $\eta_{\rm eq}$, but the concept is useful for determining which direction the temperature will evolve from a given point.

In the experiments with erbium and thulium, after loading the trap the transient density of buffer gas continues to cool the trapped atoms until thermal isolation is achieved. This leaves the atoms initially at a rather high $\eta \gtrsim 9$. Once thermal contact to the cell is broken, the atom temperature is observed to increase considerably, as shown in Figure 4.4. If the cell is then heated suddenly to desorb helium gas, the atom temperature is observed to *decrease* dramatically, with an associated increase in density. Such behavior implies that without cell heating $T_{\rm eq}$ is well above the cell temperature, and hence $\eta_{\rm eq}$ is quite low.

It is difficult to measure Zeeman relaxation precisely while the cloud temperature and density are evolving. Indeed, when far from equilibrium, Equations 4.3 and 4.4 imply that the cloud temperature roughly doubles in one relaxation time constant $\tau_{\rm R} = \gamma/\Gamma_{\rm el}$. In actuality,

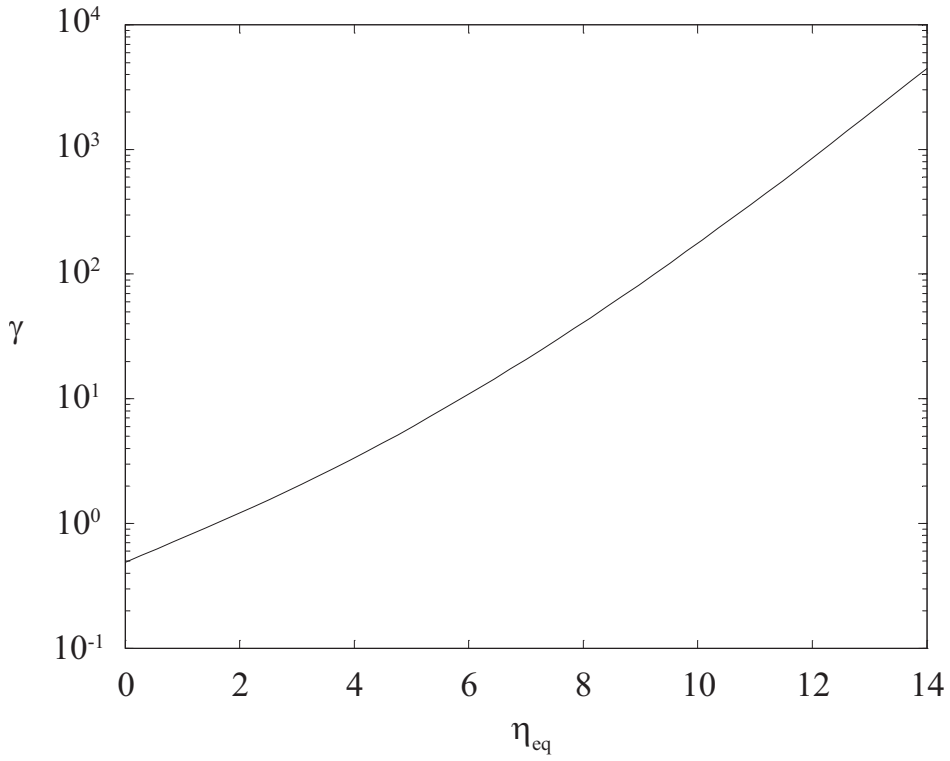

Figure 4.3: Equilibrium trapping parameter η_{eq} as a function of the ratio γ of elastic and inelastic collision cross sections, taken from [118].

however, the density of the warming atom cloud rapidly drops ($n \propto T^{-3}$ in a quadrupole trap), which drives a corresponding drop in the collision rate that stifles inelastic loss and the rate of heating. In order to make an accurate measurement of the inelastic collision rate at a given temperature, it is more straightforward to thermally pin the trapped ensemble to the cell walls. This is accomplished in the experiment by heating the cell to ensure that there are just enough helium collisions to maintain thermal contact without causing significant RE–helium inelastic trap loss. In this ideal helium density range, the observed loss rate follows a stable constant-temperature two-body decay profile. At higher densities, one-body loss due to RE–helium collisions is apparent; at lower densities, the cloud heats and the loss rate stalls. This transition can be seen in the decay profiles of trapped thulium plotted in

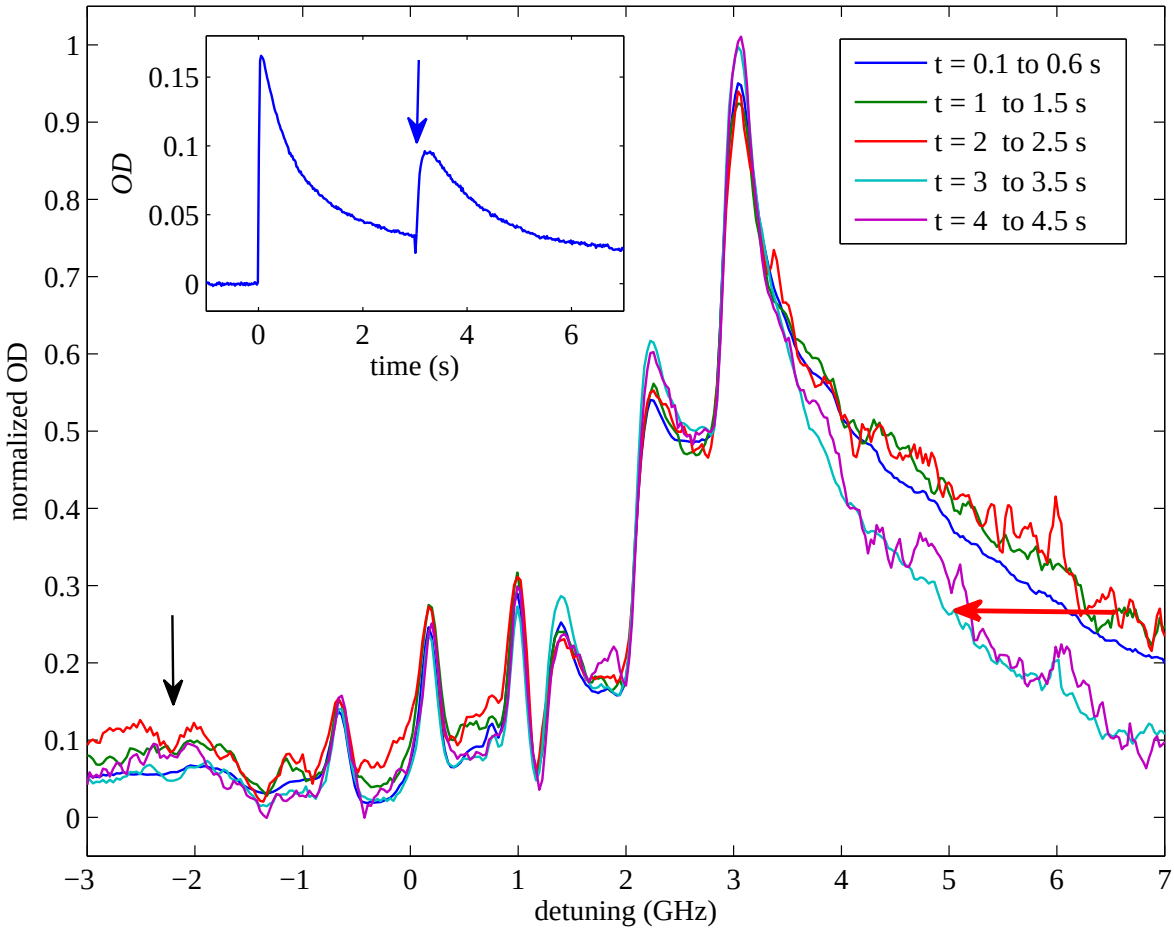

Figure 4.4: Inelastic heating of Er trapped in a 1.65-T deep trap in a ≈ 500 mK cell. Each trace is an average of scans over the time range given in the legend, normalized to peak $OD = 1$. The increasing width of the tall $\Delta m_J = +1$ spectral feature from 0 to 3 s shows the heated atoms moving to higher magnetic field in the trap. At $t = 3$ s, a 3-ms pulse of ≈5-W RF power is sent to a coil surrounding the cell, causing heating that desorbs helium to reestablish thermal contact and cool the trapped atoms (horizontal red arrow). The inset shows data for the same conditions, but with the probe laser frequency held fixed at the spectral peak. The surge in density marked by the blue arrow is due to the rapid cooling of the atoms. The relative strength of the $\Delta m_J = -1$ peak (black arrow) is similar at times just after ablation and just after re-cooling, suggesting similar fractions of atoms with $m_J < J$.

Figure 4.5.

4.3 Results and analysis

4.3.1 Measurement of RE–RE Zeeman relaxation

The density of the trapped atomic ensemble is determined by comparing trapped spectra to simulated spectra. The simulation uses a calculated 3D magnetic field profile and incorporates the effects of probe beam size, polarization and offset from the trap center (the simulation is described in detail in [113]). The spectra are analyzed to ensure that the temperature is stable, under which condition the peak spectral *OD* can be taken as proportional to the atomic density at the trap center. This peak *OD* is monitored over time to determine the density decay profile.

At constant temperature, the trapped atomic density obeys the rate equation

$$\dot{n}(\boldsymbol{r},t) = -[f_{\mathrm{evap}}(\eta)k_{\mathrm{el}} + k_{\mathrm{R}}]\, n(\boldsymbol{r},t)^2, \tag{4.5}$$

where k_{el} and k_{R} are the elastic collision and Zeeman relaxation rate coefficients, respectively, and f_{evap} is the fraction of elastic collisions that drive an atom out of the trap. We maintain T low enough to ensure $f_{\mathrm{evap}} < 1\%$ so that elastic RE–RE collisions do not significantly contribute to atom loss. Ignoring the first term in Equation 4.5, we solve for $n(\boldsymbol{r},t)$, spatially integrate over the quadrupole trap distribution, and take the reciprocal to reach the simple two-body decay result:

$$\frac{1}{n_0(t)} \equiv \frac{1}{n(r=0,t)} = \frac{1}{n_0(t=0)} + \frac{k_{\mathrm{R}}t}{8}. \tag{4.6}$$

Plotting n_0^{-1} versus time yields a straight line of slope $k_{\mathrm{R}}/8$. Data for erbium and thulium decay are plotted in this manner in Figure 4.6 and fit to Equation 4.6. Additionally, com-

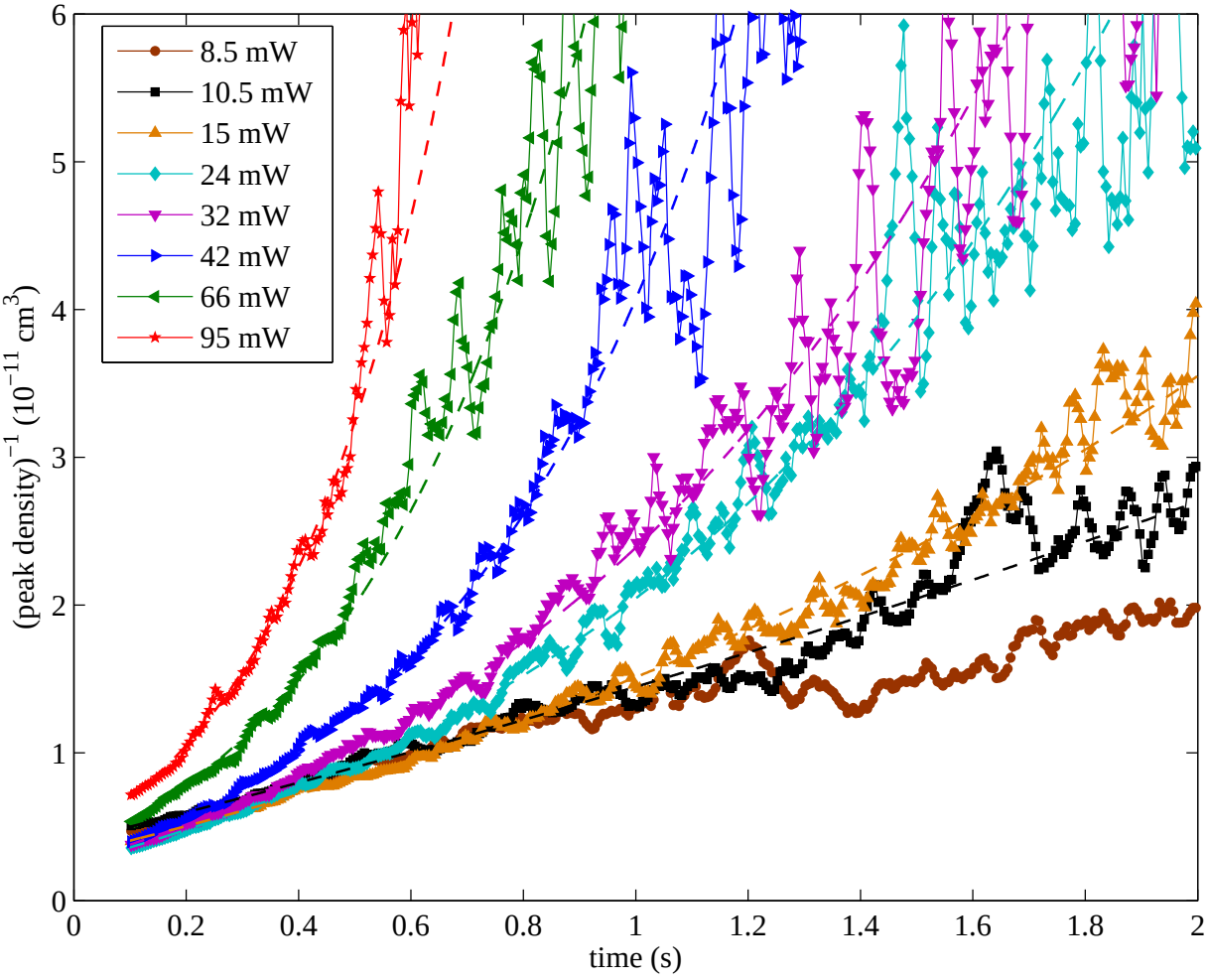

Figure 4.5: Trapped Tm decay (plotted as the reciprocal of the peak trapped atom density) for different levels of constant cell heating. Large applied power generates a high helium density, which results in Tm–He loss that appears as exponential growth on this plot (*e.g.*, red stars). For low applied power, the cooling from elastic Tm–He collisions is insufficient to overcome Tm–Tm inelastic heating, which appears as sublinear behavior on this plot (*e.g.*, brown circles). At 10.5 mW applied power (black squares), the data fit well to Tm–Tm loss at a constant temperature (Equation 4.6, which predicts a straight line). The dashed curves are fits to a combination of Tm–Tm and Tm–He loss processes. The cell temperature remains stable over the duration of the measurement due to the weak dependence on heating in the refrigerator; the cell temperature (in equilibrium) is given by $T \approx (A\dot{Q} + T_{\mathrm{MC}}^4)^{1/4}$, where $\dot{Q}$ is the applied heat, A is a constant, and $T_{\mathrm{MC}} \ll T$ is the mixing chamber temperature (see Section 2.2.1).

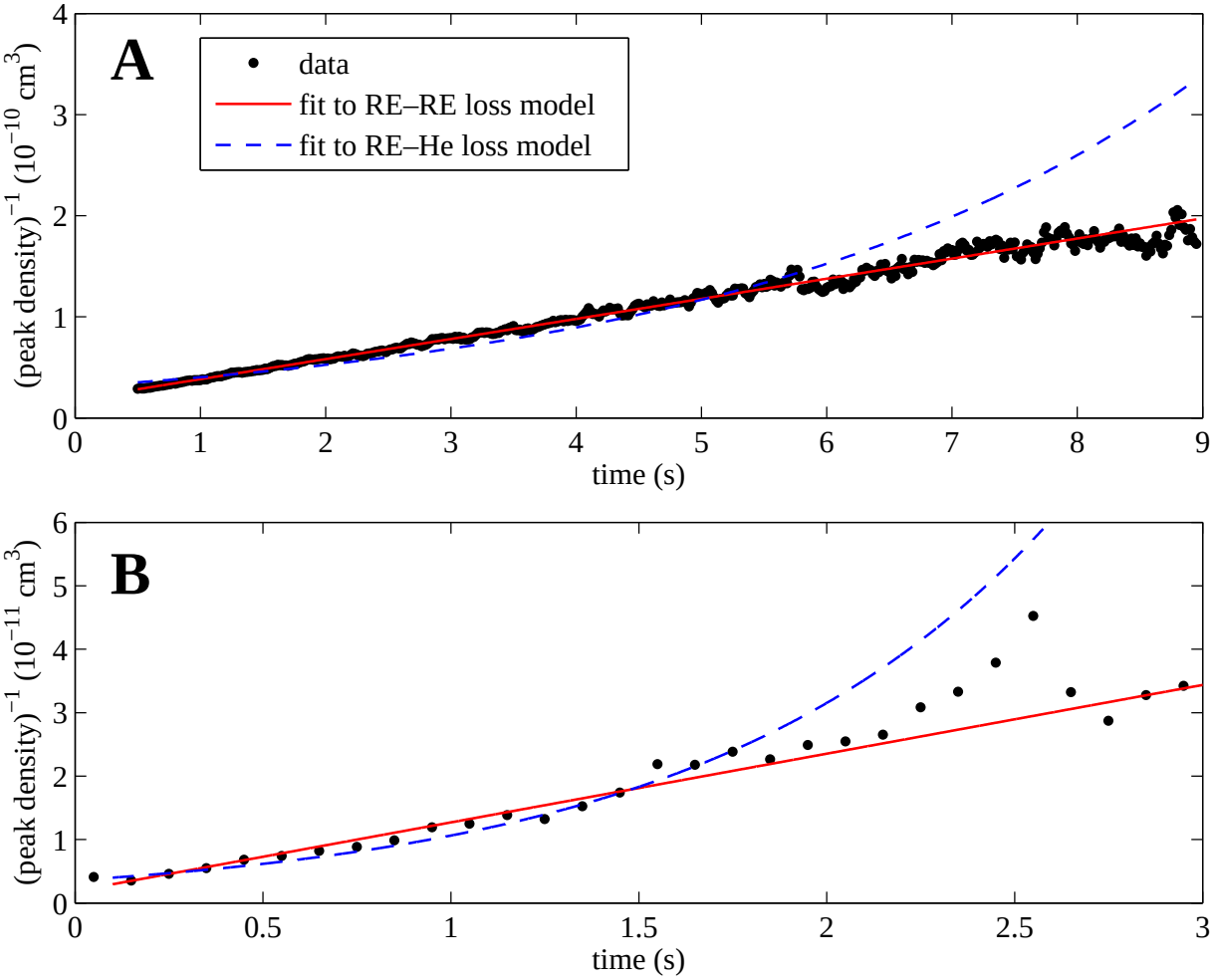

Figure 4.6: Decay of trapped (A) erbium and (B) thulium. The vertical axis is the reciprocal of the peak atom density determined from spectra. The solid red line is a fit to Equation 4.6, for decay only from RE–RE collisions. The dashed blue line is a fit to the exponential decay expected for loss only due to collisions with a constant helium density. The excellent fits to Equation 4.6 indicate that the atom loss is due to RE–RE collisions.

bined fits were made with free parameters for both RE–RE and RE–helium collisional loss processes. These combined fits yielded RE–helium decay rates consistent with zero, confirming that the observed loss is due to Zeeman relaxation collisions between the trapped atoms. The values of k_{R} given by fits to Equation 4.6 are $1.5(0.2) \times 10^{-10}$ cm^3 s^{-1} for erbium and $5.7(1.5) \times 10^{-11}$ cm^3 s^{-1} for thulium, with accuracy limited by the density calibration

determined from spectra.

4.3.2 Discussion of systematic errors

Observed two-body decay rates of trapped atoms can differ from the true Zeeman relaxation rates for several reasons. For example, angular momentum exchange is another inelastic process in addition to Zeeman relaxation that can change the projection of J through a collision. Since the total m_J of the colliding particles is conserved in the exchange collision, this exchange typically proceeds rapidly even in isotropic systems [119]. Since the ground states of both erbium and thulium have $J > 1$, the trapped atom population can be spread over a distribution of $m_J > 0$ states. Observation of $\Delta m_J = 0$ spectral lines using the 415.2-nm ($J = 6 \rightarrow 5$) transition of erbium confirms that a significant fraction of trapped atoms ($> 20\%$) have $m_J < J$ (see Figure 4.7).

Yet while angular momentum exchange collisions likely occur between the RE atoms trapped in these experiments, these collisions cannot cause the observed decay. In the absence of Zeeman relaxation, electronic angular momentum exchange collisions will tend to purify the atomic ensemble towards the stretched $m_J = J$ state as low-m_J collision products leave the trap. The stability of observed spectral features with time implies that this is not the case here. Furthermore, since these collisions conserve the total m_J, they cannot cause loss to untrapped states without also populating more strongly-trapped states. This would cause a net increase in absorption, which also is not observed. Nuclear spin exchange collisions, in contrast, which reduce m_J while increasing m_I, could lead to trap loss. However, the isotopic distribution of erbium gives a majority of $I = 0$ atoms, and the nuclear spin $I = 1/2$ of thulium is insufficient to explain the degree of loss observed. Furthermore, measured nuclear spin exchange rates in other submerged-shell atoms with only $I > 0$ isotopes suggest nuclear spin exchange to be too slow to explain the loss observed here [97, 120]. Therefore,

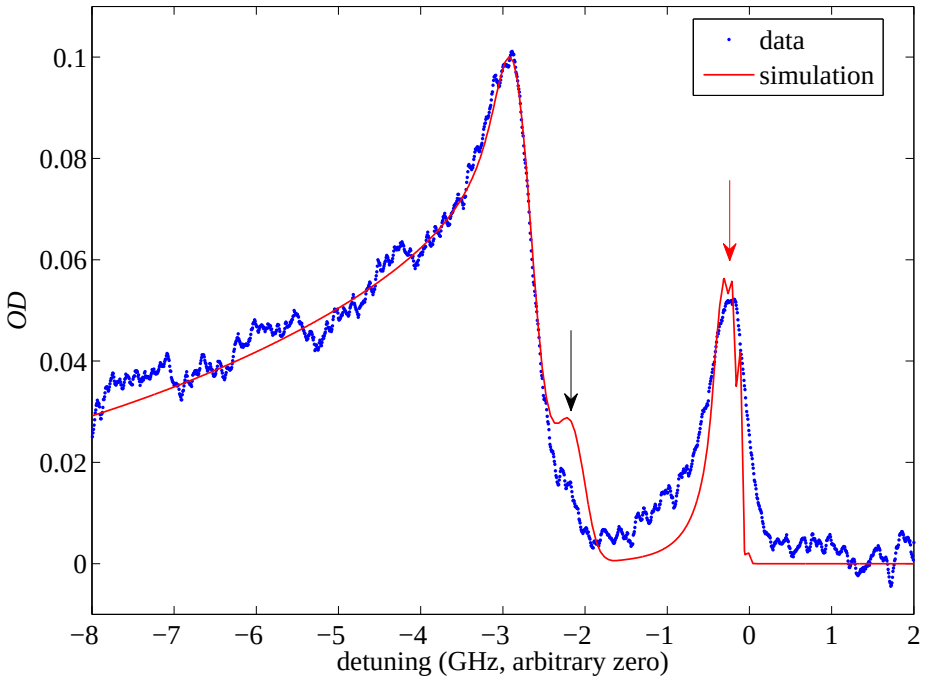

Figure 4.7: Spectrum of Er near 1 K in a 2.64-T deep trap using the 415.2-nm $J \to J-1$ transition. The sharp $\Delta m_J = 0$ peak (red arrow) is evidence of $m_J < J = 6$ state population, as this transition is forbidden for the stretched state. The simulated spectrum is for equal populations of the $m_J = 6$, 5 and 4 states. For computational simplicity, only one hyperfine state of ^{167}Er is included, which enhances the peak marked by the black arrow. Appropriately including all nuclear spin states will reduce its height.

neither electronic nor nuclear angular momentum exchange processes are responsible for the erbium and thulium loss; rather, it is indeed caused by Zeeman relaxation.

Even so, the apparent density decay rate can still underestimate the true Zeeman relaxation rate due to the population in non-stretched states. There is significant uncertainty in how this population is distributed, because the absorption measurement depends only on the sum of all sublevel contributions. This presents a calibration problem for the Zeeman relaxation measurement. Each sublevel population has a unique spatial distribution that depends on the sublevel's magnetic moment $\mu = g_J m_J \mu_B$. Therefore, uncertainty in the state distribution causes uncertainty in the density $n(\boldsymbol{r})$, and in turn, in the spatially-varying Zee-

man relaxation rate $\Gamma_{\mathrm{R}}(\boldsymbol{r}) = k_{\mathrm{R}}\, n(\boldsymbol{r})$. Since the observed trap loss is only the trap-averaged rate, measuring k_{R} requires knowledge of the m_J-state distribution.

This distribution is determined by several factors. Initially, the ablated atoms are equally distributed over all m_J states. Untrapped states with $m_J \leq 0$ are rapidly lost. The states with the lowest positive values of m_J are only weakly trapped ($\eta < 4.5$ at maximum magnetic field) and evaporate quickly, especially in the presence of thermalizing helium collisions. Other states, however, will evaporate slowly enough that they remain in the trap throughout the Zeeman relaxation measurement. Meanwhile, Zeeman relaxation on average causes m_J to decrease for one or both atoms during an inelastic collision, which repopulates states with positive $m_J < J$ as they evaporate. At finite temperature, thermal excitations will also occur, as discussed in Section 2.3.2. Finally, the electronic angular momentum exchange collisions discussed above will cause mixing of the m_J-state distribution and in general speed it toward equilibrium. Lacking a definitive measurement of the state distribution, all these effects combined can introduce significant systematic error to the measurement of k_{R} that comes from simply applying Equation 4.6.

4.3.3 Simulation of trap dynamics

To study the impact of the effects described in the previous section on the measured Zeeman relaxation rates, we perform numerical simulations of the trap dynamics. Population in multiple magnetic sublevels will cause a deviation from Equation 4.6. The three dominant effects are: (1) the spatial integration of Equation 4.5 depends on the cumulative density profile $n(\boldsymbol{r}) = \sum_{m_J} n_{m_J}(\boldsymbol{r})$; (2) thermal excitations occasionally drive relaxation away from equilibrium; and (3) the so-called "Zeeman cascade" of inelastic transitions to still-trapped states will require that more than one collision, on average, is necessary for atoms to leave the trap. The simulation is not intended to be a precise model of these effects—its accuracy

is limited by uncertainty in the state distribution, as well as in the state-specific inelastic collision rates and helium density. Instead, the simulation is constructed to investigate the range of simulated parameters that produce trap decay profiles consistent with the experiment. This range is then used to determine an overall estimate of systematic error in the measurement of k_{R}.

Since there are a large number of particles at high η in the trap, the simulation expresses the density and collision rates as continuous variables in a series of rate equations. Elastic collisions with both helium and other trapped atoms are assumed to be rapid enough to thermalize the distribution, since no significant spectral deformation is observed. Inelastic collisions, both angular momentum exchange and relaxation, are assumed to proceed with the same rate coefficients k_{ex} and k_{R} for all sublevels. These collisions may, however, prudentially cause transitions to certain final states. This is accounted for by including selection rules that vary from 0 (final state not allowed) to 1 (final state maximally allowed). In the case of Zeeman relaxation, we expect that transitions of $|\Delta m_J| \leq 2$ will be favored for the following *a priori* reasons: For relaxation driven by electronic interaction anisotropy, the coupling to more distant m_J states is a higher-order process, as demonstrated theoretically for the thulium–helium and oxygen–helium systems [91, 121]. Similarly, the magnetic dipole-dipole interaction couples states of $\Delta m_J = \pm 1$ to first order [47]. For either mechanism, such selection rules would imply that trapped states of high-J atoms like erbium and thulium will often relax to still-trapped states.

The inelastic collision rates are calculated as follows. First, the rate of electronic angular

momentum exchange, which conserves the total m_J of the colliding partners, is given by

$$(\dot{n}_{m_J})_{\rm ex} = \frac{k_{\rm ex}}{2} \sum_{m'_J} \sum_{m''_J} \sum_{m'''_J} \left[\beta_{|m''_J - m_J|} \delta[(m_J + m'_J) - (m''_J + m'''_J)] \right.$$
$$\left. \times \left(n_{m''_J} n_{m'''_J} - n_{m_J} n_{m'_J}\right)\right], \tag{4.7}$$

where $k_{\rm ex}$ is the exchange rate coefficient, $\delta[x]$ is the Kronecker delta that vanishes for $x \neq 0$ and is otherwise unity, and $\beta_{|\Delta m_J|}$ is the selection rule for exchange that changes the projection of J on the field axis by Δm_J. The factor of 1/2 accounts for double-counting in the summation. Second, the Zeeman relaxation rate is given by

$$(\dot{n}_{m_J})_{\rm R} = k_{\rm R}\, n_{m_J} \left[\sum_{m'_J < m_J} \alpha_{m_J, m'_J} \left(n_{m'_J}\, \exp\left(-\frac{(m_J - m'_J) g_J \mu_{\rm B} B}{k_{\rm B} T}\right) - n_{m_J} \right) \right.$$
$$\left. + \sum_{m'_J > m_J} \alpha_{m_J, m'_J} \left(n_{m'_J} - n_{m_J}\, \exp\left(-\frac{(m'_J - m_J) g_J \mu_{\rm B} B}{k_{\rm B} T}\right)\right)\right], \tag{4.8}$$

where α_{m_J, m'_J} is the selection rule for relaxation $m_J \to m'_J$. Thermal excitations have been included in Equation 4.8. Inelastic RE–helium collisions occur rarely and are ignored in the simulation.

Additionally, the simulation calculates the loss rates for evaporation due to elastic collisions. Equation 4.1 is used to determine the evaporation rate from RE–RE collisions, while RE–helium evaporation is given by

$$\Gamma_{\rm He\ evap} = \Gamma_{\rm RE\text{–}He}\, \epsilon\,(M, m)\, f\,(\eta)\,, \tag{4.9}$$

where $\Gamma_{\rm RE\text{–}He} = n_{\rm b} \sigma_{\rm d} \bar{v}$ is the RE–helium collision rate,

$$\epsilon\,(M, m) = \frac{Mm}{(M+m)^2} \tag{4.10}$$

is the energy transfer efficiency in a collision between two masses M and m [51], and

$$f\,(\eta) \approx \left(\frac{1}{2}\eta^{3/2} + \frac{1}{4}\eta^{5/2}\right) e^{-\eta}, \tag{4.11}$$

is the fraction of thermalized trapped atoms with sufficient energy to leave the trap [113]. This expression for $f(\eta)$ was found by Brahms to be a good approximation at high η of the more precise result that comes from numerical integration of the Boltzmann distribution.

The elastic and inelastic contributions are added and propagated in time to numerically simulate the atomic density distribution and calculate the corresponding *OD* seen by the probe laser. A range of parameter space is explored to identify conditions under which it is possible to reproduce the observed data. One such example is shown in Figure 4.8. As stated above, this process does not provide good constraints to the many underlying parameters; however, it is useful to demonstrate that simple application of Equation 4.6 to the observed *OD* decay—as in Section 4.3.1—will yield a value of k_{R} that underestimates the true Zeeman relaxation rate by a factor of approximately $2.0\ ^{+1.0}_{-0.5}$. With this correction, the rate coefficients k_R are $3.0(0.4) \times 10^{-10}$ cm^3 s^{-1} for erbium and $1.1(0.3) \times 10^{-10}$ cm^3 s^{-1} for thulium.

4.4 Possible mechanisms of RE–RE Zeeman relaxation

4.4.1 Magnetic dipole-dipole interaction

The rates of Zeeman relaxation measured for collisions between erbium and between thulium atoms are significantly higher than inelastic rates observed for other highly magnetic S-state atoms such as chromium [32, 122], europium [97], manganese [120] and molybdenum [33]. The relaxation rate coefficients for these species were measured in similar magnetic traps at similar temperatures and found to be $\lesssim 10^{-12}$ cm^3 s^{-1}. These S-state atom–atom rates are

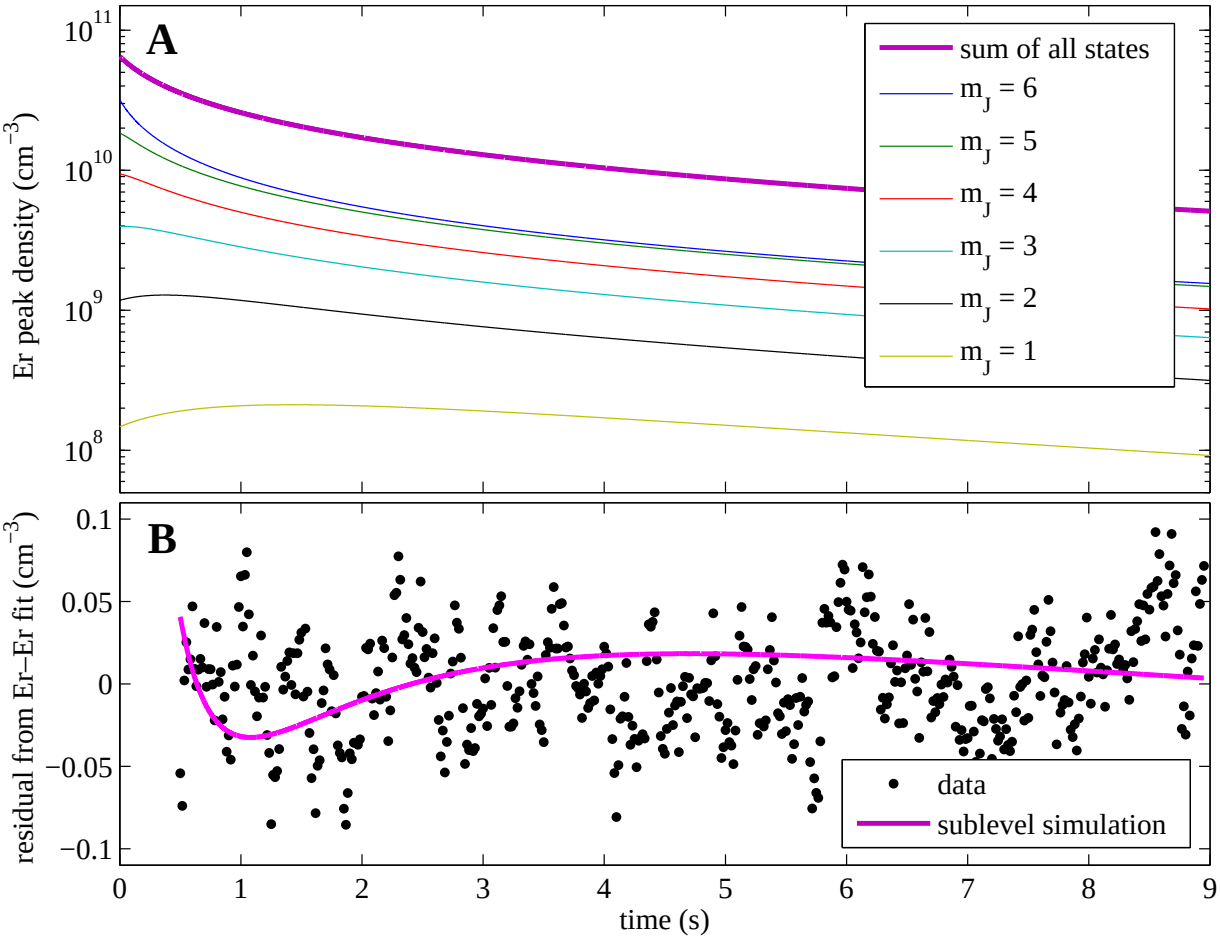

Figure 4.8: (A) Simulation of Er decay under the conditions of Figure 4.6A, including the effects of thermal excitations, Zeeman relaxation selection rules, nearest-state electronic angular momentum exchange, and collisions with the helium buffer gas; (B) residuals from the fit to Equation 4.6 shown in Figure 4.6A for both the measured data and the simulated total density shown in (A). This simulation is for $k_{\mathrm{R}} = 3 \times 10^{-10}$ cm^3 s^{-1}, twice the number extracted from the data. Many simulations are performed to estimate the systematic error caused by simply fitting to Equation 4.6.

consistent with the magnetic dipole-dipole interaction [123–125] described by

$$\hat{V}_{\mathrm{dipole}}(\boldsymbol{r}) = \frac{\mu_0}{4\pi}\frac{\mu^2}{r^3}[(\boldsymbol{J}_1 \cdot \boldsymbol{J}_2) - 3(\boldsymbol{J}_1 \cdot \hat{\boldsymbol{r}})(\boldsymbol{J}_2 \cdot \hat{\boldsymbol{r}})]. \tag{4.12}$$

The Zeeman relaxation rate induced by the operator $\hat{V}_{\mathrm{dipole}}$ is dependent on the specific form of the interatomic potential. However, in the limit of small inelastic transition probability

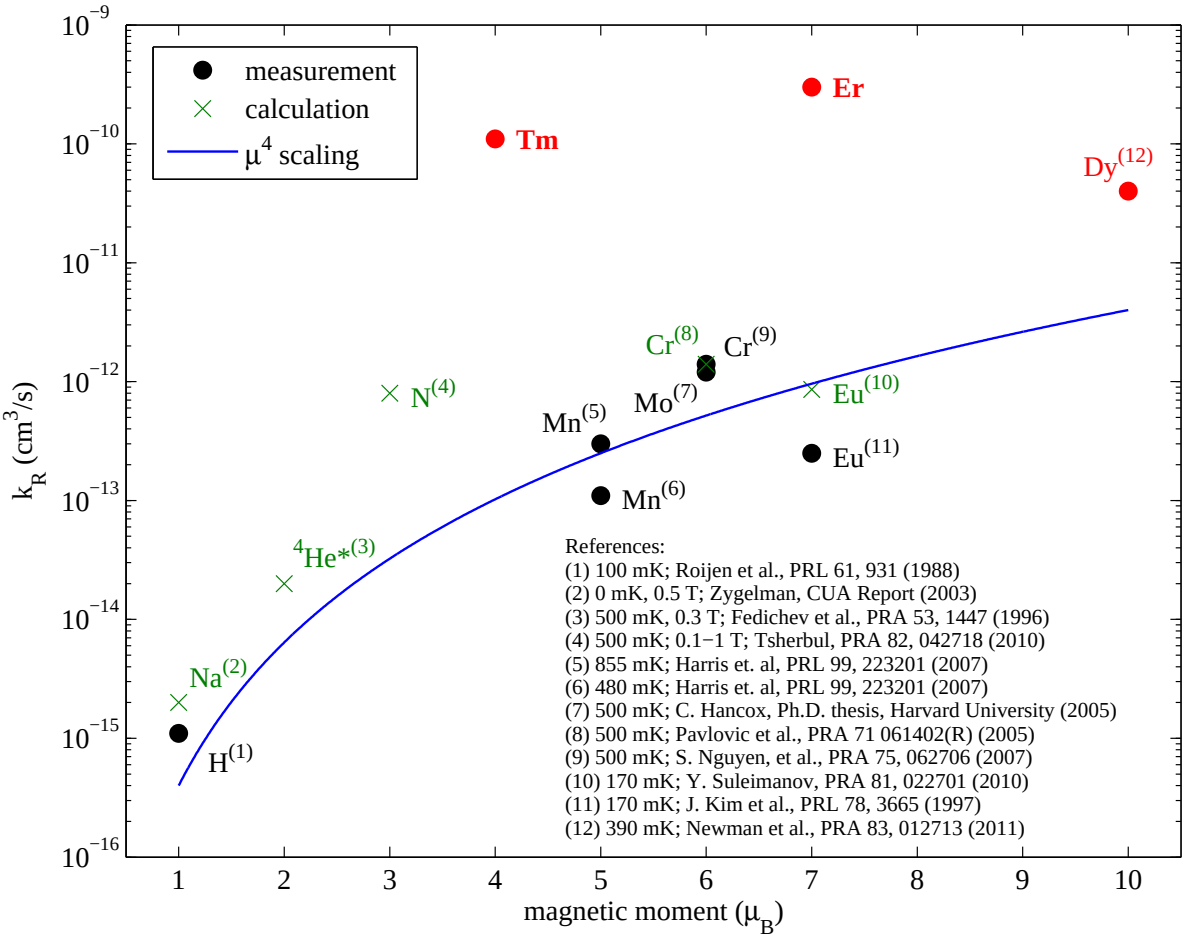

Figure 4.9: Zeeman relaxation rate coefficients measured or calculated for atom–atom collisions near 500 mK in a magnetic trap. The rates for RE atoms with $L \neq 0$ are orders of magnitude faster than the approximate μ^4 scaling predicted from the form of $V_{\rm dipole}$.

Equation 4.12 can be used to construct a simple scaling argument that $k_{\rm R} \propto \hat{V}^2_{\rm dipole} \propto \mu^4$. Figure 4.9 shows experimental and theoretical results for a number of atom–atom collision systems in which the dominant loss mechanism is likely the dipolar interaction.

A rough prediction can be made for magnetic dipole-induced relaxation in erbium and thulium based on the rates observed for europium and manganese. The latter species are $L = 0$ isotropic ground states with large magnetic moments. Like erbium and thulium, they

are also submerged-shell atoms. Scaling the cross sections measured for europium [97] and manganese [33] by μ^4 and averaging yields predictions of $k_{\mathrm{R}} = 3.4 \times 10^{-13}$ cm^3 s^{-1} for erbium and 3.5×10^{-14} cm^3 s^{-1} for thulium. The measured inelastic rate coefficients in our experiments are 2–3 orders of magnitude larger than these scaled dipolar values. We therefore conclude that the measured loss is inconsistent with a purely dipolar model.

4.4.2 Electrostatic quadrupole-quadrupole interaction

Another possible loss mechanism is the electrostatic quadrupole-quadrupole interaction. Like the magnetic dipole-dipole interaction, this interaction is long-range ($\hat{V}_{\mathrm{quad}} \propto r^{-5}$) and thus should not be shielded by outer electrons. The quadrupole moment tensor operator is defined as [126]

$$\hat{Q}_{2q} = \sum_i r_i^2 \sqrt{\frac{4\pi}{5}}\, Y_q^2(\theta_i, \phi_i), \tag{4.13}$$

where r_i is the electronic coordinate, Y_m^ℓ are the spherical harmonics, and the sum is taken over all electrons in the atom. The atomic quadrupole moment refers to the $\hat{\Theta}_{zz}$ component of the expectation value of $\hat{Q}_{2q}$,

$$\hat{\Theta}_{zz} = \langle Lm_L |\, \hat{Q}_{20} \,|\, Lm_L \rangle, \tag{4.14}$$

which by the Wigner-Eckart theorem has only one truly independent component. Hence the quadrupole moment is often written simply as Q and taken to be the $m_L = L$ component of $\hat{\Theta}_{zz}$. The quadrupole-quadrupole interaction operator is then proportional to the product of the quadrupole moments of the colliding partners ($\hat{V}_{\mathrm{quad}} \propto Q^2$ for atom–atom collisions). Since $\langle Lm_L |\, Y_m^2 \,| Lm_L \rangle = 0$ for $L < 1$, this interaction vanishes for collisions of S-state atoms including all collisions with helium; but it is nonzero for nearly all lanthanide RE–RE collisions, including those of erbium and thulium.

There is reason to expect, however, that the quadrupole moments of RE atoms are small. The relativistic collapse of the valence electron shells implies that the electrons are close to the nucleus—the same reason that the anisotropy is submerged—and hence the moment arm (r_i in Equation 4.13) is small. Calculations for the RE atoms thulium [127] and dysprosium [128] give values of $Q < 0.2$ a.u., which corresponds to an interaction energy of $\lesssim$100 mK (in temperature units) at $R = 10$ Bohr radii, approximately the inner turning point of the RE–helium potential. This is similar to the magnetic dipole-dipole interaction energy (at the same R), $\approx$200 and $\approx$50 mK for erbium and thulium, respectively; thus it is unlikely that the electrostatic quadrupole-quadrupole interaction is responsible for the rapid RE–RE relaxation.

4.4.3 Electronic interaction anisotropy

The inelasticity in the anisotropic RE–RE systems studied here is comparable to that observed in anisotropic outer-shell (non-submerged) systems. For example, experiments with metastable $^3P_2$ states of calcium, strontium and ytterbium have observed very rapid inelastic rate coefficients greater than 10^{-11} cm^3 s^{-1} [90, 129, 130]. This comparison suggests that the submerged-shell model of anisotropy shielding that successfully described RE–helium collisions may not be appropriate to RE–RE systems. A stronger RE–RE interaction potential may overcome the shielding effect as the atoms approach each other and experience the valence anisotropy at short range.

In response to recent experiments using laser-cooled dysprosium atoms, Kotochigova and Petrov [128] performed calculations of dysprosium–dysprosium collisions in the ultracold s-wave limit using a universal single-channel loss model. Their calculations yield large inelastic rates at the same order of magnitude as observed experimentally [131], and specifically identify electrostatic interaction anisotropy as the dominant mechanism with a significant addi-

tional contribution from the magnetic dipole-dipole interaction (dysprosium has the largest magnetic moment of any atom, $\mu = 9.93\ \mu_{\mathrm{B}}$). In contrast, the electrostatic quadrupole-quadrupole interaction was shown to be a much weaker effect. Collisions in dysprosium were also experimentally studied at 390 mK by Newman *et al.* [132], finding large relaxation rates similar to those of erbium and thulium. Since these three RE atoms have similarly anisotropic valence shells, there is now strong evidence that the dramatic suppression of electronic interaction anisotropy observed in the RE–helium systems does not exist for collisions between RE atoms.

4.5 Future prospects for RE atoms

An unfortunate consequence of the rapid Zeeman relaxation measured in this experiment is that it is likely that evaporative cooling of these atoms in a magnetic trap is impossible. Evaporative cooling relies on elastic collisions after losing atoms to evaporation in order to thermalize the trapped distribution to a lower temperature, requiring $\gamma \gtrsim 100$ for efficient evaporation [116]. This is not a fundamental limit; cooling can occur for lower values of γ over small temperature ranges, but significantly increased losses will be sustained.

The value of k_{el}, and hence γ, for erbium and thulium is not measured in this experiment, but an estimate can be obtained from the unitarity limit. For collisions at a finite temperature, the total collision cross section σ in the absence of resonances is bounded by [133]

$$\begin{aligned} \sigma &< \sum_{\ell=0}^{\ell_{\max}} \frac{\lambda_{\mathrm{th}}}{\pi}(2\ell+1) \\ &< \frac{2\hbar^2}{\mu k_{\mathrm{B}} T} \sum_{\ell=0}^{\ell_{\max}} (2\ell+1) \end{aligned} \tag{4.15}$$

where $\lambda_{\mathrm{th}} = \sqrt{2\pi\hbar^2/\mu k_{\mathrm{B}} T}$ is the thermal de Broglie wavelength of the colliding system with

reduced mass μ, and $\ell_{\max}$ is the maximum partial wave involved in the collision. $\ell_{\max}$ is found by equating the average collision energy $E_{\mathrm{K}} = 3k_{\mathrm{B}}T/2$ with the centrifugal barrier in the approximate Van der Waals potential

$$\hat{V}(R) = \frac{\hbar^2 \ell^2}{2\mu R^2} - \frac{C_6}{r^6} \tag{4.16}$$

to yield

$$\ell_{\max} = \frac{\sqrt{\mu}}{\hbar} \left[\left(\frac{3}{2}\, k_{\mathrm{B}} T \right) \sqrt{54 C_6} \right]^{1/3} \tag{4.17}$$

The C_6 coefficient has not been calculated for erbium and thulium and must be estimated. With the expectation that other lanthanide RE atoms will have similar isotropic parts of the potential, we take the mean of theoretical calculations for ytterbium [134] and dysprosium [128] to yield $C_6 \approx 1{,}970$ a.u. For erbium and thulium at 500 mK, this corresponds to ≈40 partial waves and a unitarity limit $k_{\mathrm{el}} \approx 8 \times 10^{-10}$ cm^3 s^{-1}. With this limit, $\gamma \lesssim 10$ for both atoms, well below the minimum required for efficient evaporative cooling in a magnetic trap. Since each non-S-state RE atom studied thus far has exhibited similarly rapid relaxation, there is little reason to be optimistic for others in the lanthanide series, with the possible exception of europium ($^8S_{7/2}$).

The inelasticity in these RE–RE systems has been a setback for experimental progress with these atoms. The earlier success in trapping $>10^{11}$ of these highly magnetic and anisotropic atoms held promise that evaporative cooling of buffer-gas trapped RE atoms could provide a route to very large ultracold ensembles. Such techniques have already been demonstrated to achieve Bose-Einstein condensation of metastable helium-4 [31]. Instead, it may be that the RE–helium collisions that allow for buffer-gas trap loading are uniquely insulated from the interactions that cause trap loss. As a result, cooling RE atoms to the ultracold regime requires alternate methods.

Great progress has very recently been made using all-optical methods to cool erbium, thulium and dysprosium. Both dysprosium and erbium atoms have now been laser cooled in

a magneto-optical trap (MOT), loaded directly into an optical dipole trap and evaporatively cooled to quantum degeneracy [11, 135, 136]. Similar work is underway with thulium [137]. The atom numbers are not large, however ($<10^5$ at degeneracy), limited by MOT density and temperature together with the finite optical dipole trap size and depth. The inelastic collision rates are found to be large in the ultracold regime, as well [131], so the short lifetimes of certain states may limit the scope of future experiments. Nevertheless, despite being constrained to different technologies, progress continues with these interesting systems.

Chapter 5

Conclusion

5.1 Summary of collision experiments

We investigate the role of anisotropic interactions in driving inelastic collisions between atoms at low temperatures. We explore how relativistic effects and collisional mixing of energy levels lead to electronic interaction anisotropy that induces Zeeman relaxation. In addition to developing a more complete model of inelastic atomic collisions, these results are technically important to experiments. Buffer-gas loading of magnetic traps requires elastic collisions with helium for cooling, while evaporative cooling requires elastic collisions between trapped atoms. In both cases, relaxation must be sufficiently rare so that the colliding atoms remain in the trapped state.

The experiments presented here explore inelastic atomic collisions arising from three distinct mechanisms. In the first experiment, Zeeman relaxation of antimony occurs in collisions with helium due to distortion of the ground-state wave function induced by the spin-orbit interaction. Couplings to excited states introduce anisotropy into the ground state independent of the collision, so that the interaction with helium is anisotropic. This

fundamentally relativistic effect is a strong function of the nuclear charge and is seen to vary dramatically among the pnictogen atoms, with greatest wave function distortion for the heavy atoms antimony and bismuth. As a result, the excellent collisional properties of nitrogen are likely a special case, and no other pnictogen atom exists that could replace nitrogen in collision experiments while providing more practical detection options.

In the second experiment, inelastic aluminum–helium collisions are suppressed by the spherical symmetry of the ground $^2P_{1/2}$ state. In this case, inelastic transitions occur by a collision-induced admixture of the anisotropic $^2P_{3/2}$ state. The same is true for the other Group 13 atoms gallium, indium and thallium, as well as metastable halogen atoms [1], with the inelastic collision rate suppressed by the fine-structure splitting between the states. For the heavier species with large splitting, the Zeeman relaxation rate is extremely low, with calculated values of γ well over 10^7 for collisions with helium. It may then be possible to sympathetically cool these atoms with other S-state atoms, provided that the interaction strength remains sufficiently weaker than the fine-structure splitting.

In the third experiment, we extend earlier work observing suppressed inelasticity in collisions of anisotropic rare-earth (RE) lanthanide atoms with helium [2] to examine RE–RE collisions, observing no evidence of similar suppression. Indeed, we find inelastic collisions between RE atoms to be just as rapid as those between anisotropic open-shell atoms such as metastable ^3P states of ytterbium [90] and calcium [129], with relaxation rates similar to the elastic collision rates. Thus we demonstrate a fundamental difference between these two systems, along with the limitations of the "submerged-shell" collision model used to describe them. If the interparticle interaction is sufficiently strong, Zeeman relaxation driven by electrostatic interaction anisotropy proceeds rapidly despite the anisotropic valence electrons being submerged below spherical closed electron shells. As a result, evaporative cooling in a magnetic trap is not feasible with these atoms. Instead other technologies, such as optical

dipole traps that can trap the absolute ground state, must be employed, along with their associated disadvantages of low trap depth and size.

5.2 An increasingly complete picture

The three experiments described here join a wealth of previous work in painting an increasingly complete picture of atomic collisions. The variety of interaction mechanisms and collisional processes seen across the periodic table is impressive, and has led to an equal or greater variety of applications for further experiments and technologies. While there remain unanswered questions—and surely surprises—the landscape has now been rather well explored. It is increasingly possible for theoreticians to make accurate predictions about novel systems, and for experimenters to make informed decisions of which collisions to pursue, exploit or avoid.

In particular, it is clear that elasticity in atomic collisions is not the norm. The majority of atoms in the periodic table are not S-states, and as a result Zeeman relaxation induced by collisions between two randomly chosen atoms is likely to be rapid. There are notable exceptions, such as the suppressed relaxation seen in RE–helium systems and in collisions of $^2P_{1/2}$ states with S-states. There are also, however, many S-state atoms that readily undergo inelastic transitions due to relativistic wave function distortion (*i.e.*, antimony) or dipolar relaxation (*i.e.*, chromium). Overall, the number of atoms available for evaporative cooling in magnetic traps is not much more than a dozen, with half being alkali metals. And even when other methods are used—such as evaporation in an optical dipole trap with atoms in the absolute ground state—inelastic transitions can still limit state lifetimes to constrain experiments.

Despite these challenges, there is a wide variety of successful cold atomic physics experi-

ments, both within the limited set of atoms with good collisional properties as well as with other species for which cooling methods are adapted or invented. Looking to the future, the field of cold and ultracold collisions has been increasingly focused on molecules and will likely expand in that direction. Qualitatively more complex than atoms, and with a great deal more species available to explore, molecules bring with them a number of new challenges and opportunities. Only a limited set of molecule–molecule collision experiments exist at very low temperatures, and calculations are significantly more difficult. Nevertheless, the experience of the past two to three decades of studying cold colliding atoms promises another fruitful research effort in the years ahead.

Appendix A

Cryogenic production of NH

A.1 Introduction

A.1.1 Motivations for the study of ultracold polar molecules

There is currently great interest in the production of ultracold ensembles of polar molecules. Unlike atoms, molecules have closely-spaced energy levels of opposite parity, including rotational levels, which can be fully mixed with electric fields available in the laboratory. The resulting dipole moment leads to an electrostatic dipole-dipole interaction between molecules with the same range ($\propto r^{-3}$) as the magnetic dipole-dipole interaction, but stronger by a factor of α^{-2}, where $\alpha \approx 1/136$ is the fine structure constant. Common molecular dipole moments of order 1 Debye interact over 100 times more strongly than even the largest atomic magnetic moments ($\approx$10 μ_{B}), and these interactions can easily dominate other energy scales in ultracold experiments [138].

Such strong, long-range interactions have driven a surge of proposals for ways to use these molecules at low temperatures. These include using polar molecules as qubits to realize a scalable quantum computer [18, 19]; and creating tunable, low-disorder quantum simulators

of condensed matter Hamiltonians [7, 14] to experimentally investigate outstanding problems such as high-temperature superconductivity. Strongly-interacting quantum gases are also predicted to exhibit a range of interesting ultracold phases not yet observed in atomic systems [12, 15, 17]. Other proposed experiments include investigations of controlled cold collisions and chemical reactions [87, 139], in which the applied electric field can be used to align the molecules and tune the interaction strength. Finally, precision measurements using special molecular properties seek to test fundamental symmetries and search for physics beyond the Standard Model. Several experiments are currently hunting for the electric dipole moment of the electron by exploiting the large internal electric fields of polar molecules [20–22, 140, 141]. While these precision studies may not require low temperatures, the enhancement of rotational state purity and interaction time that low temperatures provide can often lead to large improvements in sensitivity.

These many experiments have a variety of needs concerning specific molecular properties. Some demand the largest electric dipole moment available to maximize interaction strength; others need a high-Z constituent atom for relativistic effects; still others require (or cannot tolerate) chemical reaction pathways or collision resonances. As a result, No choice of molecule can satisfy all experimental needs while also being a practical target for cooling. For this reason, and also because many worthy goals likely have not yet been identified, a diverse approach is necessary to provide an array of molecules of varying characteristics.

A.1.2 Direct cooling of molecules

Efforts toward the creation of large ensembles of ultracold polar molecules have so far taken two primary approaches. The first is typically termed the "indirect" approach, and consists of assembly of ultracold molecules from reservoirs of ultracold atoms. This so far is the only approach to yield trapped molecules in their absolute rovibronic (rotational, vibrational and

electronic) and nuclear spin ground states with phase space densities approaching quantum degeneracy [142–144]. The primary downsides to this approach are that: (1) it is limited to diatomic species for which the constituent atoms can be cooled; (2) a practical molecular formation path must exist, typically photoassociation or magnetoassociation with a Feshbach resonance; and (3) the molecules formed may be highly excited, requiring further cooling or state transfer to be experimentally useful.

The second, "direct" cooling approach uses large molecular reservoirs available at higher temperatures as a starting point for cooling directly to ultracold temperatures. One example where recent progress has been made is laser cooling, which has been an enormously useful tool for cooling atoms. Due to the large numbers of rotational and vibrational energy levels between the molecular ground state and electronically excited states, there are many decay paths to dark states, complicating laser cooling. However, molecular systems have been identified in which a manageable number of lasers ($\sim$3, plus modulators) can be used to repump the primary decay paths [35, 36]. In this manner, 10^4–10^5 absorption-emission cooling cycles can be achieved, enough to reach the Doppler limit.

Another direct cooling approach, discussed at length in this thesis, is buffer-gas cooling, a general tool for cooling nearly all internal and external degrees of freedom.[1] Buffer-gas cooling is fundamentally limited by the vapor density of helium, which below $\approx$200 mK is insufficient to cool [28]. For this reason, buffer-gas cooling must be joined with another cooling technique to reach ultracold temperatures. This hybrid approach has already been employed to laser cool a beam of buffer-gas cooled molecules [35, 145]. Buffer-gas cooling can also be useful for systems that do not have level structures suited to laser cooling. In particular, trapped buffer-gas cooled molecules could be sympathetically cooled by atomic

[1]It has been observed that the vibrational degree of freedom of some molecules does not cool readily in the buffer gas [28].

species for which cooling is more straightforward [53, 146, 147]. This final approach has been the goal of the experiments with cold polar NH described in this appendix.

A.1.3 Previous work with cold NH

The imidogen molecule, especially its most common isotopomer NH, is among the best diatomic molecular candidates for combining buffer-gas trap loading with the subsequent thermal isolation required for further cooling in the trap. With a magnetic moment of 2 μ_B, NH is readily trapped at temperatures that allow for the use of helium-4 buffer gas, which can be rapidly removed after cooling and trapping (Section 4.2.2 and [31, 111]).[2] The large rotational splitting of NH prevents the rapid Zeeman relaxation that otherwise can occur when rotational states are thermally populated in collisions with helium [148]. In addition, the spin-spin interaction is weak compared to the rotational splitting, reducing the admixture of the anisotropic $N = 2$ state into the ground state [149]. Finally, NH has accessible laser transitions in the near-UV range, in particular the $A\,^3\Sigma^- \rightarrow X\,^3\Pi_2$ line at 335.9 nm that is accessible with a frequency-doubled dye or solid state laser.

NH molecules were first buffer-gas cooled below 6 K in 2004 at Harvard from a room-temperature beam of radicals created in a glow discharge of ammonia (NH_3) [150]. The experiments that followed with the same apparatus successfully trapped the molecules and measured the elastic and inelastic NH–helium collision rate coefficients [71]. Spin relaxation in this system was experimentally investigated over a range of isotopomers and determined by comparison to theory to be driven by rotational state coupling induced by the spin-spin interaction [151]. In these early experiments NH lifetimes were limited to a maximum of

[2]Thermal isolation has not yet been demonstrated for species buffer-gas loaded with helium-3 buffer gas, due to greater cooling requirements. For a thorough discussion of buffer-gas cooling of 1-μ_B species (for which using helium-3 is generally required) see [113].

≈1 s due to collisions with the buffer gas. Later work extended NH lifetimes to 20 s by implementing a pulsed buffer gas source to minimize collisions after cooling [114]. Unfortunately, the resulting molecule densities were also lower such that no NH–NH collisions were observed. The lifetime remained limited by buffer gas collisions due to the residual helium density created by desorption from helium coating the cell walls.

In 2008 NH molecules and atomic nitrogen ($^4S_{3/2}$, $\mu = 3\ \mu_B$) produced in a glow discharge of a nitrogen-hydrogen gas mixture were simultaneously buffer-gas cooled and co-trapped [54]. This is a critical first step to sympathetic cooling of the molecules to ultracold temperatures. Theoretical calculations show that nitrogen–nitrogen collisions are highly elastic (see Section 2.1) and should allow for efficient evaporative cooling. A later experiment observed NH–nitrogen inelastic collisions at a rate sufficient for sympathetic cooling, finding good agreement with theory that predicts the rate to remain similarly low over the range of 1 K to 1 mK [53, 55], the second criterion for successful sympathetic cooling of NH using trapped nitrogen. However, these experiments were performed in the presence of helium gas, and the NH lifetime was in each case limited by NH–helium collisions. Under such conditions evaporative cooling is not possible, since the trapped ensemble is not thermally isolated from the fixed cell temperature.

In the course of the recent NH experiments described in this appendix, it was discovered that an error was made in the trapped NH density calibration cited in the previous results. A measurement of probe laser absorption by trapped molecules was used to determine the trapped NH density *via* a model using the known experimental conditions and optical transition properties (see Section 5.2 of [152]). Unfortunately, there were two significant errors in the calculation. First, the size of the region of resonant magnetic field used in the calculation was 10 times too large ([152], p. 94). Second, the application of the Landau-Zener model was found to give a different result from Beer's Law, which is incorrect (see Appendix B of

this thesis). Repeating the calculation gives an estimate of the trapped NH density that is larger by a factor of ≈80 than that given in [152]. The corrected calculation gives a lower bound for the density $n_{\mathrm{NH}} > 5.5 \times 10^{10}$ cm^{-3} and a total molecule number $N_{\mathrm{NH}} > 7.3 \times 10^{10}$. This implies that the molecule numbers cited in [53, 54, 71, 114, 153] are too low by about two orders of magnitude.

We describe in this appendix work that advances towards the hybrid approach of buffer-gas cooling and sympathetic cooling of NH. NH has also been studied elsewhere, both theoretically and experimentally, using different techniques. In particular, the NH–NH inelastic collision rates have been the subject of theoretical efforts using at least two distinct approaches [154–156]. Other experiments have used the large dipole moment of NH in the metastable $^1\Delta$ state for Stark deceleration of the molecules [157–159], and cold collisions of NH with several other atoms have been explored theoretically [146, 160–163]. There remain few direct comparisons of theory and experiment with regards to NH collisions, however, primarily due to the experimental challenges. Improved experimental techniques are needed to create large ensembles of cold NH in conditions suitable for a variety of collision experiments.

A.1.4 The need for a better source

Future progress with buffer-gas cooled NH will require a source of molecules that is compatible with the cryogenic conditions necessary for sympathetic cooling. Low cell temperatures after trap loading are required to adsorb residual helium to the cell walls and ensure high vacuum. The previous NH–nitrogen co-trapping experiments used a helium-3 refrigerator to reach a cell temperature near 570 mK with a trap depth of 3.9 T, corresponding to $\eta \approx 9$. Values of η in this range leave little room for heating, and higher cell temperatures resulted in significantly fewer trapped molecules. As a result, the ∼200-mK drop in temperature needed to staunch the desorption of a helium film [60] was not possible. Since all previous

buffer-gas cooling experiments with NH were conducted in copper cells, the pulsed-density cold loading technique described in Section 4.2.2 could not be attempted.

One experimental improvement was identified that would directly benefit these experiments: a dilution refrigerator to reach lower temperatures. Even with such a system, however, due to the heat load associated with the room-temperature molecular beam source, it would be a challenge to reach sufficiently low temperatures ($\lesssim$200 mK) to adequately bind helium-3 to the cell walls. Trap loading with ^{4}He is possible, but the temperature required for adequate vapor pressure sets $\eta \lesssim 7$, for which the NH lifetime is too short ($\lesssim$500 ms) to wait for the copper cell to cool to achieve good vacuum.

Described here is technology that seeks to address both of these issues: (1) the development a pulsed cryogenic source of NH that requires low cell heating (<10 mJ) and is compatible with the low cell temperature (<200 mK) made possible by a dilution refrigerator; and (2) a composite G-10 cell to enable pulsed-density cold loading with helium-4 buffer gas, as well as sympathetic cooling with evaporatively cooled atomic nitrogen. The experiments were conducted in four phases. In Phase I, NH was produced in a cryogenic discharge from a mixture of nitrogen and hydrogen gases, but production was not robust and this method was abandoned. In Phase II, the production method was changed to ablation of nitrogen precursors into a pulsed hydrogen vapor. This was achieved in a copper cell at low temperatures, although trapping was not possible due to the inability to rapidly cool the cell to decrease the helium density after production. In Phase III, the cell was constructed from G-10 composite with a superfluid helium jacket to enable pulsed-discharge cold loading, but production was weaker than in Phase II and no trapped molecules were observed. It was assumed that hydrogen was poorly vaporized due to the specific cell design. Finally, the cell was rebuilt for Phase IV to optimize both production and fluorescence detection. Unfortunately, sensitive fluorescence detection was precluded by large levels of background

fluorescence from unidentified deposits on cold dewar optics, and again no trapping was observed. In summary, a new cryogenic production method was demonstrated for NH, but neither trapping nor sympathetic cooling has yet been demonstrated using this method.

A.2 Phase I: Discharge production

A.2.1 Finding a cryogenic production technique

Experiments with many diatomic radical species are constrained by the challenges of producing large densities of chemically unstable molecules. The ablation technique that has been very successful for a wide range of atomic species has in general produced mixed results for molecular yield and reliability, although some species (such as thorium monoxide [164] and calcium fluoride [165, 166]) give consistently good ablation yield from appropriately prepared ablation targets. Others, such as manganese hydride [167, 168], are stubbornly difficult to produce in this manner. Part of the challenge is surely of fundamental chemical nature and stems from the need for multiple atomic species to not only be present in the target, but also to emerge from the ablation plume in the desired composition. Significant efforts continue towards improving molecular ablation yields, but much is still unknown about ablation production of most species, and finding optimal precursor materials and target preparation methods remains largely an empirical process.

An attempt to identify an ablation precursor target for NH is described in the thesis of Wes Campbell [152]. Briefly, solid targets of urea, ammonium nitrate, ammonium bromide and ammonium chloride were ablated at 4.2 K into helium buffer gas. All these compounds contain both nitrogen and hydrogen and are solid at room temperature. Materials that were obtained in powder form were torch-melted and cooled to form chunks. No absorption signal was detected in the ablation cell, corresponding to a quoted upper limit on the NH density

of 1.8×10^8 cm^{-3}, and the search for an ablation precursor was abandoned.

Due to the success in generating large numbers ($\approx 10^{12}$) of metastable helium (He*) in a pulsed radiofrequency (RF) discharge below 1 K [58], Phase I of a new set of NH cryogenic production experiments attempted to create NH using RF discharge in a nitrogen-hydrogen gas mixture. As demonstrated in the He* experiment, the pulsed discharge reached a saturated He* density within 200 μs at powers below 25 W, meaning that He* discharge production did not require more energy then a standard ablation laser pulse. Furthermore, subsequent evaporative cooling of He* to temperatures of order 1 μK [31] showed that the gas density required to sustain the discharge was compatible with excellent vacuum >10 s later.

Discharge dynamics are a complicated combination of atoms (and/or molecules), ions and electrons colliding in the presence of electromagnetic fields, usually also with spontaneous or collisional state quenching and emission of light. The discharge plasma is often optimized empirically and is highly sensitive to factors such as conductor geometry, gas density and gas impurity concentration. As a result, it is very difficult to predict the equilibrium concentration of a given species in a molecular discharge at any temperature. The cryogenic discharge has the additional complication that both nitrogen and hydrogen have negligible vapor pressure below 1 K [59]. It has been observed, however, that an RF discharge can etch material from surfaces into the discharging plasma despite the surface and neutral gas temperature being too low for equilibrium vapor [169]. It is possible that high-energy electrons or electronically excited atoms and ions collide with the surface and eject material. Such an effect would allow nitrogen and hydrogen to be vaporized for discharge production at temperatures conducive to trapping NH.

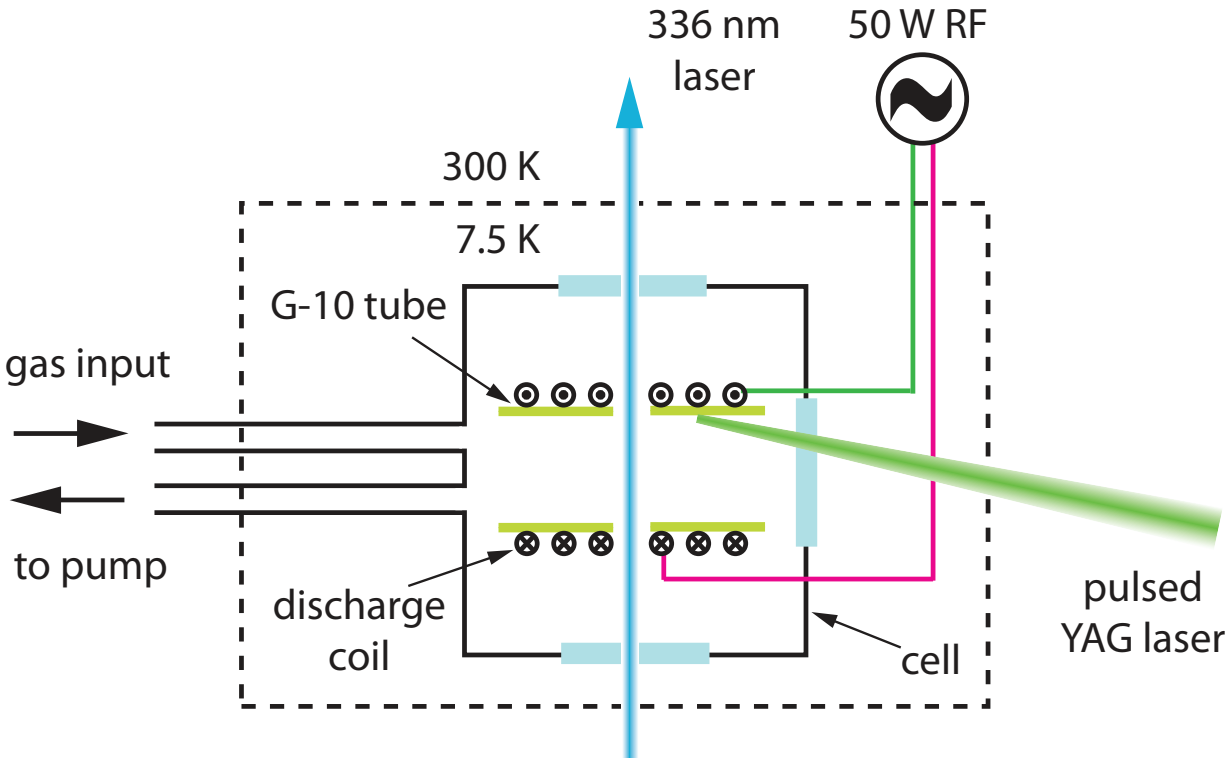

Figure A.1: Phase I test cell schematic.

A.2.2 Production test apparatus

RF discharge production of NH was tested at low temperatures using a small liquid helium dewar[3]. The cryogenic cell (Figure A.1) was constructed from aluminum 6061 alloy with windows on three faces to allow for both absorption and fluorescence spectroscopy. A copper flange mated to the fourth face contained two 1/8" gas input feedthroughs and a hermetic SMA bulkhead connector[4] that remains leak-tight at 4 K. A G-10 support tube waas attached to the inside of this flange with the RF coil wound on the tube. In this manner, the coil

[3]HDL-5, Infrared Laboratories, Inc., Tucson, AZ.

[4]Huber+Suhner #34 SMA-50-0-3/111NE, distributed by Richardson Electronics, Ltd., Chicago, IL

spacing from the inner walls of the cell was more than 1 cm. Transverse holes drilled through the tube allowed for probe laser access.

RF discharge production of NH was first observed at room temperature. The cell was filled with a 1:1 mixture of nitrogen and hydrogen gases, which was kept slowly flowing through the cell to purge contaminants and discharge byproducts. RF current at 168 MHz was chopped at 50-Hz with 50% duty cycle with an RF switch, sent through a 25-W amplifier, and directed to the discharge coil. The coil impedance-matching was poor and the fraction of RF power deposited into the discharge was not measured. At pressures of 300–600 mTorr the discharge glowed brightly, blinking on and off with the RF chop with a lag time of $\lesssim$5 μs.

NH was detected with absorption spectroscopy using the R_1 line of the $A\,^3\Sigma^-(v=0) \rightarrow X\,^3\Pi_2(v=0)$ transition at 335.9 nm from the rovibronic ground state. A 2-μW probe beam was directed through the discharge region and to a photodiode, with a portion of the probe beam diverted before the cell to another photodiode to serve as an intensity reference. The differential photodiode signal was monitored with a lock-in amplifier to extract the signal component at the 50-Hz discharge chopping frequency. The 10 ms that the RF was off in the chop cycle was several times the diffusion lifetime of NH in the cell, so the RF modulation was effectively a modulation of the NH density.

The room-temperature absorption spectrum of NH in the discharge is shown in Figure A.2. The observed Doppler broadening suggests a temperature of 570 K, much hotter than the cell or coil temperature (the cell was not warm to the touch, and internal components would melt or degrade at such a high temperature). It is more likely that the collisional process that produced NH in the discharge occurs at higher temperatures, and the molecules do not have time to cool to the cell temperature before chemically reacting. The NH translational temperature dropped to about 380 K when the experiment was repeated with the cell cooled to 77 K, at which point both nitrogen and hydrogen remain in gas phase. The

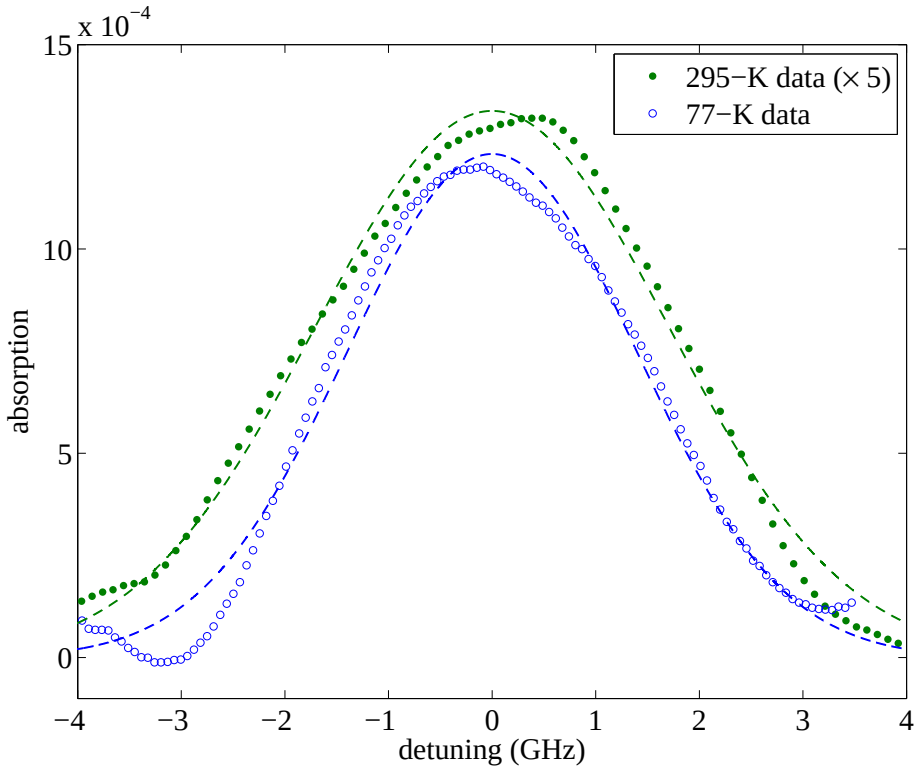

Figure A.2: Absorption spectra of NH produced in an RF discharge of equal parts nitrogen and hydrogen gases. The room temperature and 77 K data are shown with fits (dashed lines) to Doppler temperatures of 570 and 380 K, respectively. The room temperature data has been magnified by a factor of 5 for clarity. If similar production is assumed at the two temperatures, then the increased signal at 77 K suggests that the rotational temperature is close to that of the cell and not in equilibrium with the translational temperature.

population of other rotational levels was not investigated, so it is not known whether the rotational temperature is also much warmer than the cell. Assuming rotational temperatures of 77 K and 300 K, the NH density is calculated to be $\approx 4 \times 10^{10}$ cm^{-3} averaged over the 1 cm diameter of the coil support tube. This corresponds to a fractional NH density of $\sim 10^{-6}$, about an order of magnitude lower than observed for cryogenic He* production [58, 111].

When the cell was cooled to its base temperature of ≈7.5 K, a discharge could still be readily ignited in the cell, suggesting a non-negligible vapor pressure of hydrogen at this temperature. To ensure an effective test of how the production method would fare below

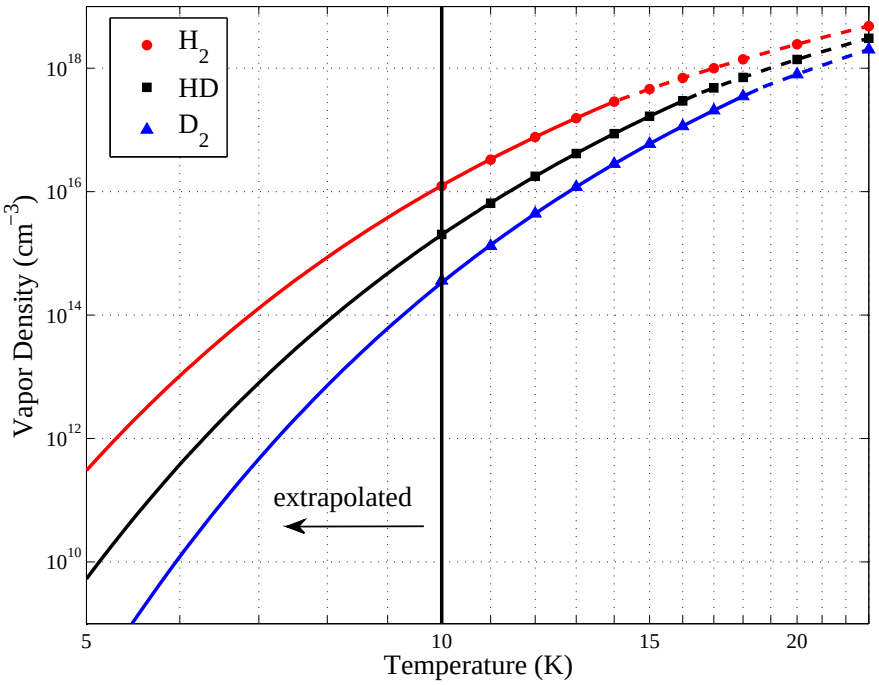

Figure A.3: Saturated vapor density of hydrogen isotopomers [170]. Solid (dashed) lines are for the liquid (solid) phase.

1 K in the absence of thermal vapor, deuterium was used in place of hydrogen to reduce the gas density by more than a factor of 100 (Figure A.3). With deuterium the discharge could not be reliably ignited at 7.5 K, consistent with low density. Higher-temperature $N_2 + D_2$ discharge confirmed the formation of ND, which was observed with the same probe laser detuned by the isotope shift $\nu_{\mathrm{ND–NH}} = -11.70\ \mathrm{cm}^{-1}$ [151].

To create a low-temperature discharge in the cell and to provide cooling after production, helium buffer gas was used. As was observed in the He* experiment, the discharge would not reliably "self-ignite" immediately at low temperatures. In that experiment, a $\lesssim$1-mJ YAG laser pulse focused on a metallic target was sufficient for ignition [58, 111]. In the NH test apparatus here, two methods were tried. First, a high DC voltage of $\approx$900 V was applied to a wire suspended in the cell with the cell walls grounded. The wire was multi-stranded

tinned copper, with the strands pulled apart to form several high-field regions in space near the strand tips. With the ignition voltage applied, the discharge would ignite robustly at low temperatures. At higher voltages arcing was observed to the cell walls spaced ∼1 cm away.

Both nitrogen and deuterium were added to the 7.5-K cell by briefly opening a valve (for ∼0.3 s) to vent gas at approximately 1 bar from a 150-cm^3 volume. The high gas flow ensured poor thermalization in the cryogenic gas lines, so that the precursor molecules entered in gas phase and froze to the inner surface of the coil support tube. After precursor ice was added, however, no ND signal was observed at 7.5 K, suggesting that nitrogen (and possibly also deuterium) was not sufficiently vaporized from the frozen solid. To vaporize the precursor molecules, a 7-mJ unfocused YAG pulse of diameter ≈3 mm was directed onto the inner surface of the coil support tube, where the ice was deposited. This vaporization laser was sufficient to ignite the discharge without the use of the high-voltage ignition wire, and the latter was abandoned.

NH and ND detection at low temperatures differed from the ≥77-K method described above, because the lock-in detection required RF power incompatible with the cryogenic environment. Instead, a single 1-ms RF pulse was used, averaged over several repeated experiments at 1-s intervals. With the vaporization YAG pulse coincident with the start of the discharge pulse, ND could be reliably produced and detected (Figure A.4). The density achieved was significantly lower ($\approx 3 \times 10^9$ cm^{-3}) than that seen in the 77-K discharge, possibly due to reduced precursor gas density. Nevertheless, if similar densities could be achieved over a 100-cm^3 volume in a trapping cell below 1 K, the resulting trapped molecule number would be comparable to that of the previous NH experiments [54, 71].

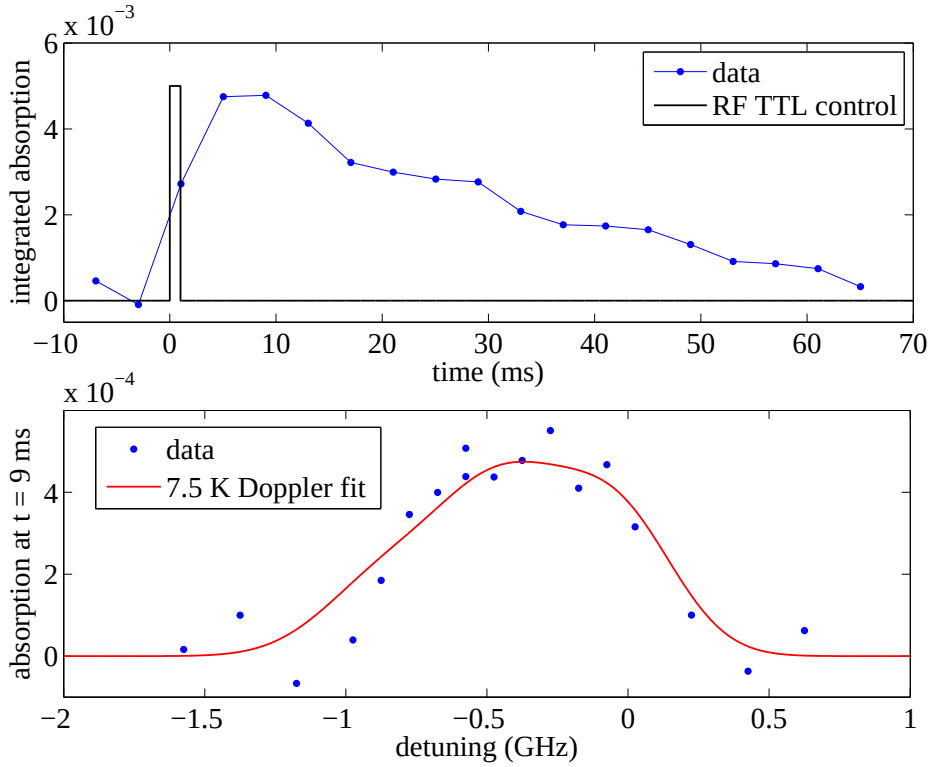

Figure A.4: ND produced in an RF discharge at $T = 7.5$ K from nitrogen and deuterium vaporized into ^{4}He buffer gas by an unfocused YAG laser pulse at $t = 0$. The discharge glow lags the RF pulse by $\lesssim$50 μs. The temperature of the Doppler fit in this range is poorly constrained due to the unresolved hyperfine structure; the actual temperature may be a few kelvin warmer.

A.2.3 G-10 composite trapping cell

The cell built for NH trapping below 1 K was constructed under several design constraints:

1. Discharge production of NH must be possible. This requires a method for delivery of precursor ice to the cell in a manner that does not inhibit transmission of dewar optics. In addition, the ice must be accessible by the vaporization YAG pulse.

2. The cell's heat capacity must be large enough that energy required for NH production does not leave the cell too hot for trapping. In addition, regions of the cell with line-of-sight access to the trap must not take too long to cool, or helium desorbing from

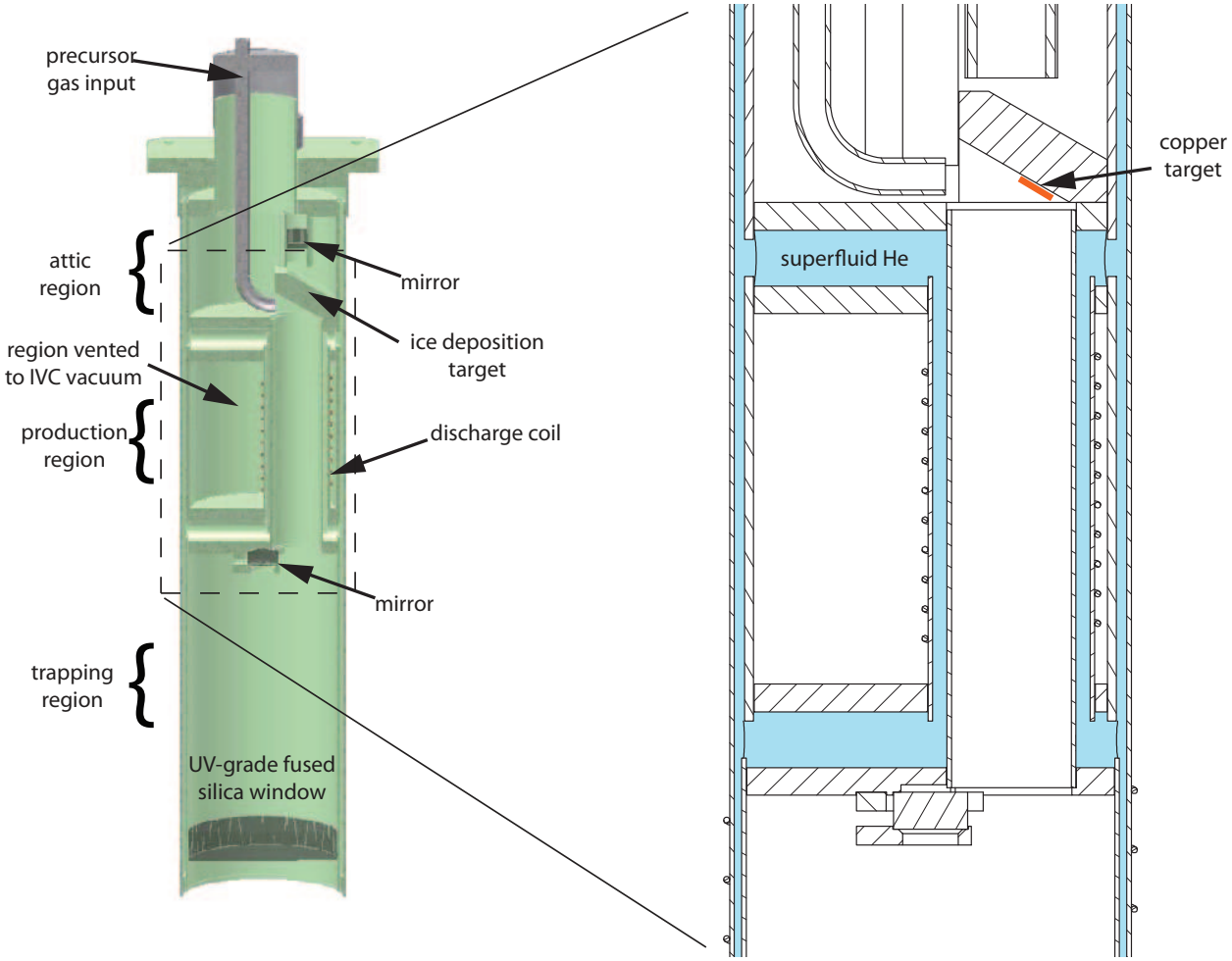

Figure A.5: Phase I G-10 trapping cell schematic.

these places will drive molecules out of the trap.

3. The magnetic field must be ramped for evaporative and sympathetic cooling, which requires a nonmetallic cell to avoid eddy current heating.

With these constraints in mind, we constructed a superfluid-jacketed G-10 composite cell similar to those described in Sections 2.2.1 and 4.2.1.

A schematic of the cell is shown in Figure A.5. The cell is divided into three regions: an "attic" region where gas and precursor ice are introduced; a narrow production region where

the discharge is ignited; and the trapping region where the majority of the exposed surface area is well anchored to the superfluid jacket. A precursor input line deposits ice on an angled target in the attic region to be vaporized into the production region. In order to address the second constraint above, the discharge coil is wrapped around the production region on the outside surface of the superfluid jacket so that the inner cell surface will remain cold after production. This method was successfully used for the He* evaporative cooling cell [58, 111]. It was also hoped that by spatially separating NH production and trapping it might be possible to trap molecules at a higher density than can be achieved in the discharge. Discharge ignition is accomplished by a weak ablation laser pulse targeting a copper foil in the production region. Finally, two separate cell mirrors allow for absorption or fluorescence spectroscopy in both the trapping and production regions.

A.2.4 Phase I failure: No NH nor N_2* detected

Despite the success of the cryogenic test apparatus at 7.5 K, no NH was observed in the trapping cell near 1 K. A range of discharge conditions was tried with a range of vaporization YAG powers, to no avail. Since nitrogen vapor is the most difficult requirement for the success of the discharge production method, it was thought that this was the limiting factor. To investigate the nitrogen gas density, a spectroscopic search was performed for molecular nitrogen in the metastable $A^3\Pi_u$ state (N_2*), which has a radiative lifetime of 1.9 s. The state was probed using the $A^3\Pi_u(v=0) \rightarrow B^3\Pi_g(v=0)$ transition at 1049.6 nm.

Detection of N_2* was first tested in discharges at room temperature and at 70 K.[5] The spectra in Figure A.6 show the observed translational and rotational cooling. The rota-

[5]In addition, N_2* was also detected at room temperature using the $A^3\Pi_u(v=0) \rightarrow B^3\Pi_g(v=3)$ transition at 687.5 nm and the $B^3\Pi_g(v=0) \rightarrow C^3\Pi_u(v=0)$ transition near 337 nm. Inferior signal-to-noise ratios were achieved on these transitions.

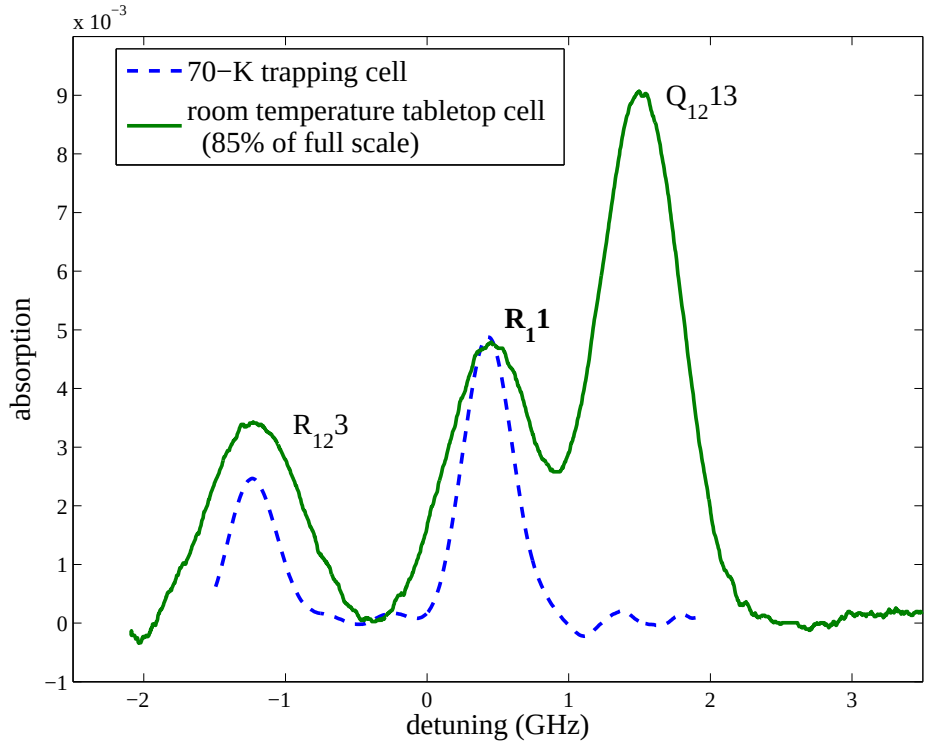

Figure A.6: N_2* $A \rightarrow B$ absorption spectra observed in nitrogen discharge at a detuning near 9,527.13 cm^{-1}. The Doppler widths fit best to 319 and 107 K, however the rotational temperature is consistent with the cell temperature of 295 and 70 K, respectively. The $R_1 1$ line from the ground rotational state is used to search for N_2* near 1 K. Rotational line assignments are based on the (0,0) band analysis in [171].

tional temperatures are more consistent with the cell temperatures than they are with the translational temperatures, suggesting that these degrees of freedom are not equilibrated.

The 70-K spectrum in Figure A.6 implies a N_2* density of $\sim 1 \times 10^{12}$ cm^{-3} in the $v = 0$ vibrational state (the excited state lifetime is 8 μs [172] and the Franck-Condon factor is 0.37 [173]). The nitrogen density is not well known, but is likely to be no more than 10^{16} cm^{-3}, implying a fractional population of N_2* of $\gtrsim 10^{-4}$. Assuming this limit to be the N_2* fraction in the 1-K discharge, as well, and assuming fractional absorption sensitivity of 10^{-4}, this implies sensitivity to molecular nitrogen densities above $\sim 10^{12}$ cm^{-3} at 1 K, and perhaps lower.

Using this spectroscopic tool, no N_2* was observed when the apparatus was cooled to near 1 K. The combination of no signature of molecular nitrogen nor of NH suggests that nitrogen ice is not sufficiently vaporized in the 1-K trapping cell to emulate the performance of the test cell at 7.5 K. It is possible that the geometry of the trapping cell, with the production region significantly larger than that of the test cell, limited the nitrogen density—assuming a similar quantity of molecules vaporized by the YAG laser pulse. It is also possible that the lower temperature affected the N_2* fraction or that the discharge formation of N_2* and NH is significantly altered at 1 K.

Initial tests of fluorescence spectroscopy were performed in the Phase I trapping cell, although no NH fluorescence was observed. Large photon count rates were observed from the cell after the end of a discharge pulse in the helium buffer gas (Figure A.7). This bright source of photons in the first few milliseconds is termed the "discharge flash," and its cause is not understood. The discharge may excite long-lived fluorescence in the G-10 walls surrounding the production region. Alternately, the initial millisecond-scale decay profile is also consistent with the diffusion time of He*, which is produced in densities over 10^{11} cm^{-3}; hence it is possible that the flash is short-lived fluorescence at the wall caused by He* atoms, each depositing 20 eV internal energy. This flash limits the sensitivity to molecule fluorescence at early times. Fluorescence detection is discussed in more detail in Section A.3.7.

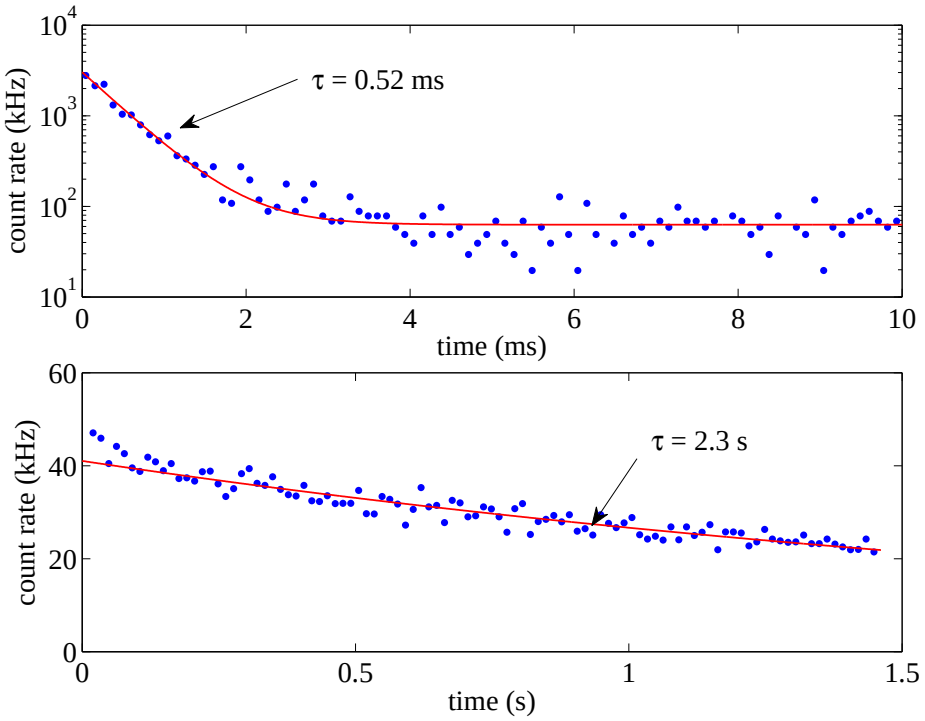

Figure A.7: PMT count rate after a YAG-ignited helium discharge lasting 3 ms in the Phase I G-10 trapping cell near 1 K. This discharge flash displays a bimodal exponential decay with the two time constants shown. The early decay is consistent with the He* diffusion time.

A.3 Phase II: Production by ablation of nitrides into hydrogen

A.3.1 Production test apparatus

After the apparent failure to vaporize molecular nitrogen from solid ice at 1 K, a different process was employed for Phase II of the NH experiment: ablation of ceramic nitrides. The appeal of a solid ablation target is that it can be installed in the cell and trusted not to migrate for the duration of the experiment. In addition, if the target is chemically inert or prepared in a rare gas environment then there is a low probability of target degradation with time, at least for atomic precursors. Aside from the inherent unpredictability of ablation

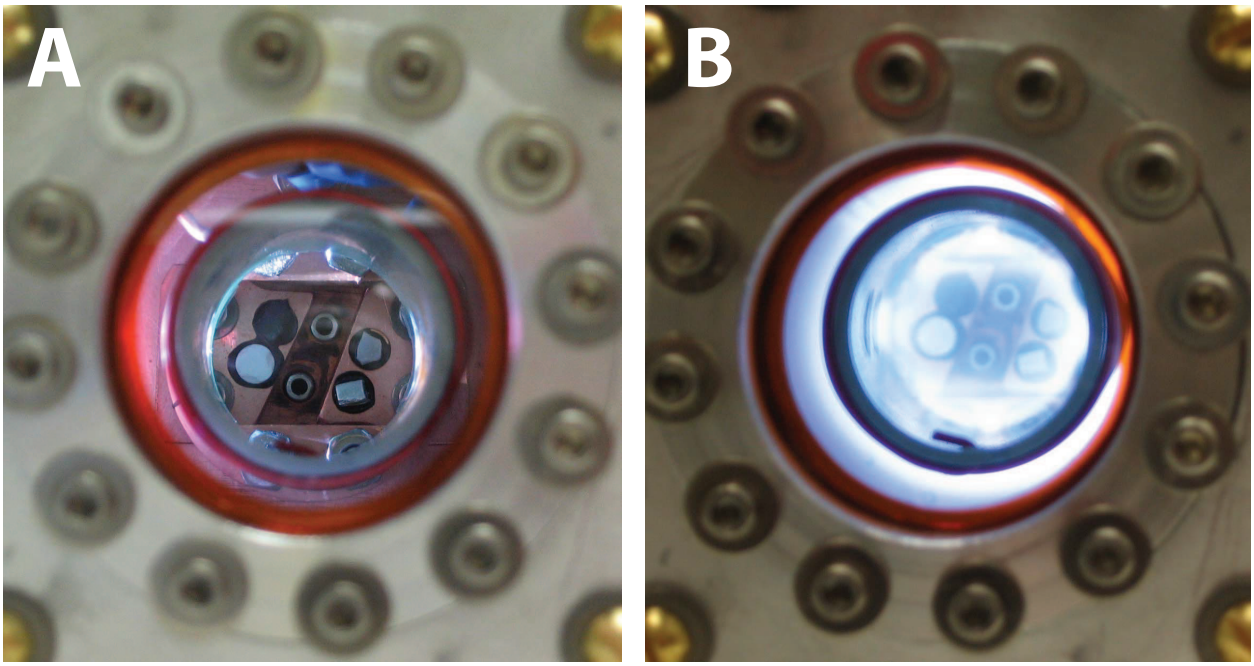

Figure A.8: (A) Phase II test cell looking through the discharge coil to the ablation targets and gas input lines; (B) the cell with a helium discharge ignited.

yield from a given source [28], ablation is an extremely robust production method for atoms.

Ablation of atomic precursors into reactive gases is a common method of generating molecular species, especially radicals that are chemically unstable [22, 50]. Typically, however, the molecular yield from this approach is low, so it is most often used for spectroscopic studies that need only a minimal number of molecules. In the case of NH production, the success in forming NH molecules in a discharge with molecular nitrogen present suggested that ablating atomic nitrogen into a hydrogen discharge could take the place of vaporizing molecular nitrogen.

Testing of the ablation-discharge production concept was first performed in a modified version of the Phase I test cell (Figure A.8). Four ablation targets—boron nitride (BN), aluminum nitride (AlN), silicon nitride (Si_3N_4) and aluminium 6061 alloy (as a negative diagnostic)—were epoxied to a copper mount bolted to the inner cell wall. With the cell

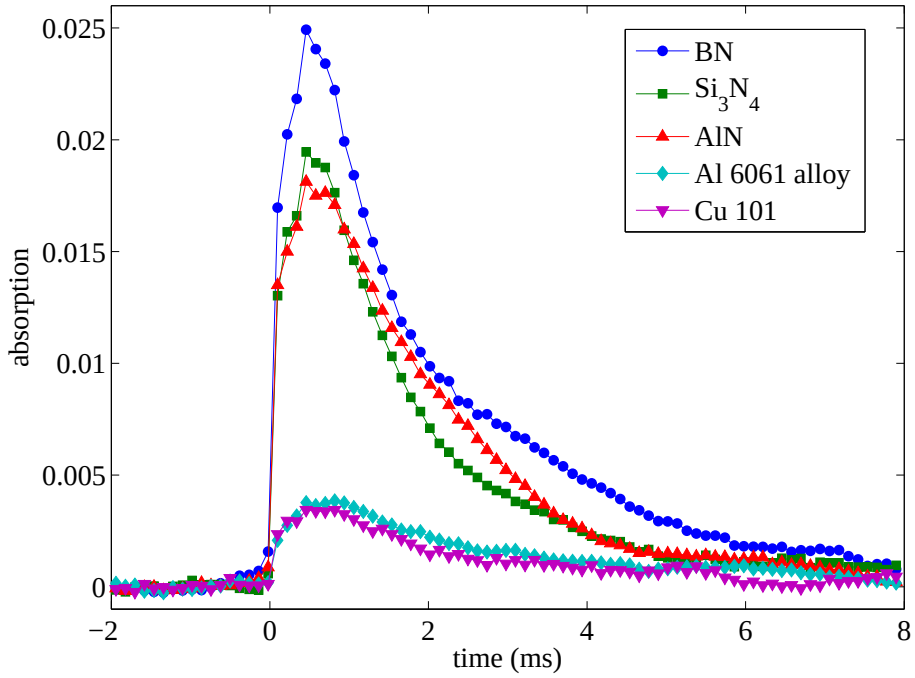

Figure A.9: NH production after ablation of various targets into hydrogen gas in Phase II test cell at 8.5 K, with probe laser parked on resonance at $f = 2 \times 14885.31$ cm^{-1}. The ablation energy is 6.3 mJ and the H_2 pressure, as read with a room-temperature Convectron gauge without correcting for transpiration, is 27 mTorr. The production of NH when ablating non-nitrogenous targets is assumed to make use of nitrogen in cell contaminants, such as air ice.

cooled to 8.5 K, we ablated the targets into hydrogen, which has significant vapor density above 10^{16} cm^{-3} at this temperature. NH was observed when *all* materials were ablated, including the aluminum alloy and the copper target mount (see Figure A.9). Since there is no significant nitrogen content in the latter two materials, it is assumed that NH was formed in these cases with nitrogen deposited from ablation of the nitride targets or from air contamination of the cell while at room temperature. Three rotational lines of NH and one of ND (using deuterium in place of hydrogen in this case) were independently observed to confirm that the apparent NH absorption signal was not a coincidental resonance with another ablation product.

This performance suggests that the chemistry of ablation into hydrogen gas is favorable for NH formation. With ablation energy of 6.3 mJ, an average density of $\approx 3 \times 10^{10}$ cm^{-3} NH molecules was achieved, corresponding to $\gtrsim 10^{11}$ total molecules. Atomic ablation yields are rarely in excess of 10^{14} atoms at these energies [28], which would imply that at least 0.1% of the nitrogen atoms produced in ablation are converted to NH molecules, a significantly higher fraction than that observed in discharge.

The test apparatus was subsequently adapted for lower temperatures and a more open geometry. The G-10 support tube and coil were replaced with a shorter, free-standing coil suspended on two nylon rods, allowing for more open area for gas flow transverse to the coil. The absorption probe laser was directed transverse to the coil just after its end. Better thermal connections allowed the cell to reach 4.5 K, and deuterium was again used in place of hydrogen to further limit the thermal vapor (Figure A.3) to simulate the conditions of a <1 K cell. With deuterium ice added to the cell, we observed ND upon ablation of all nitride targets. The molecule yield steadily decreased with subsequent ablation pulses, but would return when the ablation laser was directed to a fresh target. Refilling the cell with deuterium ice also caused the signal to return. This behavior suggests that ablation alone (without the discharge) is sufficient to vaporize deuterium ice near to the target, but that the ice is rapidly depleted as it migrates elsewhere in the cell. The ND yield was more consistent when a 1-ms discharge was ignited immediately prior to ablation. The discharge likely plays no role in ND formation other than to provide a significant and repeatable deuterium gas density. Roughly 10^{11} ND molecules could be reliably produced at 4.5 K with $\approx$10 mJ of combined ablation and RF energy.

A.3.2 Copper trapping cell

After the Phase I failure to produce NH, the Phase II cell construction was approached with great caution. Rather than construct a new G-10 composite cell, which would be difficult to assemble and even more difficult to modify or to fix in the event of leaks, a copper cell was built. This decision favored a successful test of NH production below 1 K using the technique of nitride ablation into hydrogen vapor, but precluded the possibility of rapid magnetic field changes, including evaporative cooling. A schematic of the copper cell is shown in Figure A.10. The discharge coil sits above the trap center in the cell vacuum, supported on G-10 posts and sufficiently spaced from the grounded cell walls to allow for large electric fields inside the coil. Ablation targets are epoxied in a copper mount above the coil. A 1/4" copper tube for the introduction of hydrogen ice traverses the cell from the top plate to aim at the inner coil surface. The cell window and top plate are affixed with indium seals, and the top plate is thermally anchored to the dilution refrigerator mixing chamber with seven flexible heat links made of braided copper. The bottom of this cell reached a base temperature of about 130 mK.

With the cell cooled to below 1 K, hydrogen was added in a brief pulse from a $\approx$150-cm^3 room temperature volume, in the same manner as described in Section A.2.4. At first, a hydrogen-helium filling mixture was used to ensure that the entrained hydrogen would reach the cell without freezing in the cold fill line. It was discovered, however, that venting a pulse of pure hydrogen with 1 bar backing pressure was adequate and no helium was necessary. This suggests that during the filling procedure the inner surfaces of the gas line warmed momentarily and prevented freezing. Avoiding helium in the fill resulted in a reduced cell heat load and no need to pump on the cell for a long time afterward.

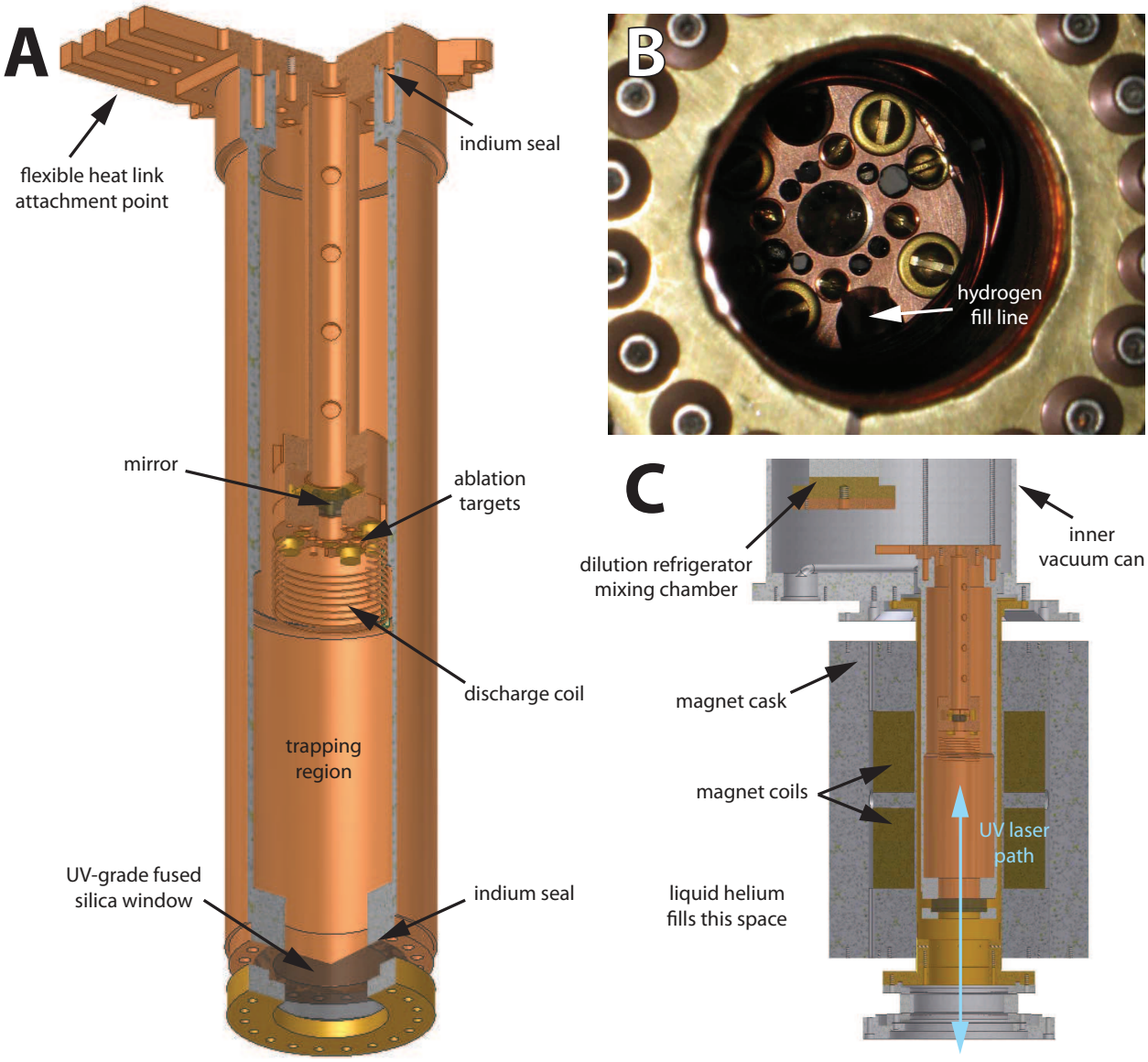

Figure A.10: (A) Phase II trapping cell schematic; (B) view through the cell window; (C) apparatus schematic showing refrigerator, magnet, and vacuum can (flexible copper braid heat links between cell and mixing chamber are not shown).

A.3.3 Observation of cold NH

Despite equivalent performance of the nitride ablation targets in the test apparatus, differences were observed in the trapping cell. Surprisingly, we observed no NH when ablating the silicon nitride target[6]. This target was a fragment of a larger piece, which potentially had different material properties on its outer faces than in the center such that ablation would differ for outer *vs.* cleaved surfaces. Next, the boron nitride target[7] produced a ∼0.5% "absorption" signal independent of probe laser frequency. Since boron nitride is a porous and powdery material, this apparent absorption likely was instead just occlusion of the probe beam by dust particles produced in ablation. The aluminum nitride target[8], however, produced reliable yields of over 10^{11} NH molecules when ablated into a mixture of hydrogen and helium-4 gases with the cell temperature held above 6 K. With the cell cooled to 1 K and no hydrogen in gas phase, the ablation still produced a similar yield, consistent with the observations of the test apparatus. Also consistent with testing, the yield at 1 K steadily decreased with additional ablation pulses, likely due to depletion of hydrogen near the ablation target. NH production consistency was again improved by adding a discharge pulse that ended coincident with ablation. The discharge was usually ignited with a separate, weaker YAG pulse, but this was found to be unnecessary at higher helium densities. It was not known whether the effect of the discharge was to etch hydrogen from cell surfaces or whether it rapidly heated the buffer gas near the coil, which then caused hydrogen to evaporate.

When the cell was cooled below ≈750 mK, NH could no longer be observed. This is likely because the helium-4 density required to sustain the discharge that produces hydrogen was

[6]99.5% purity, Plasmaterials, Inc., Livermore, CA.

[7]Part #44838, 99.5% purity, Alfa Aesar, Ward Hill, MA.

[8]Part #43790, Alfa Aesar, Ward Hill, MA.

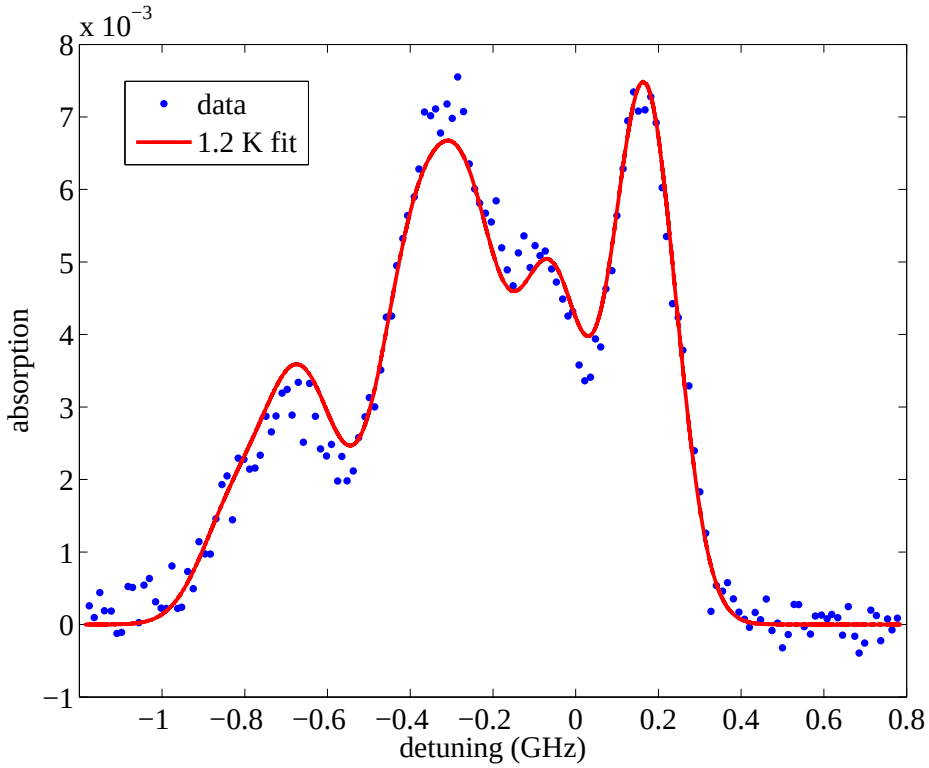

Figure A.11: NH hyperfine spectrum of over 10^{11} molecules at $T = 1.2$ K produced in the Phase II cell by ablation of aluminum nitride into discharge-vaporized hydrogen gas.

at that point vapor-pressure-limited. In addition, the NH signal near 850 mK was largest on the first production attempt, made after adding more helium to the cell. We believe that firing the discharge caused local heating of the discharge coil that evaporated helium there. The helium then migrated to the colder cell walls and was not so easily vaporized on the next attempt. Similar behavior was observed at lower temperatures using helium-3 buffer gas.

NH densities of $\approx 10^{10}$ cm^{-3} were achieved with helium-3 buffer gas in a cell originally held near 300 mK (see Figure A.11). The Doppler temperature obtained from spectra varied with the production energy. Temperatures of ≈900 mK were observed 50 ms after ablation for the lowest production energies of about 10 mJ, consistent with the expected temperature

rise from heating the thermal mass of the cell's ≈300 cm^3 of copper.

A.3.4 Limitations of a copper cell

The inability to produce NH using helium-4 buffer gas at temperatures below 750 mK is consistent with the thermal dynamics of copper described in Section 2.2.4. The high thermal conductivity of the cell walls rapidly diffuses the energy from RF heating and ablation throughout the cell's heat capacity, keeping the walls cool and the helium density too low to ignite a discharge. Without a discharge, the hydrogen density would be limited to what could be vaporized by the ablation pulse, and the low helium density would also likely limit how much of this vaporized hydrogen stayed near to the ablation target.

Unfortunately, the same thermal properties also ensure that the cell temperature, and hence the helium density (of either isotope), will will not drop rapidly after NH production. We estimated the lower limit of helium density necessary for NH production from NH diffusion times and helium vapor pressure curves to be ≈10^{16} cm^{-3}. At this density the NH Zeeman relaxation lifetime is only ∼30 ms [71], which is too short to allow NH produced in a magnetic trapping field to equilibrate to a trapped spatial distribution, and also too short to achieve thermal isolation. NH trapping was not achieved in the Phase II cell.

A.3.5 Limitations of detection

Despite reasonably efficient NH production of over 10^{11} molecules, detection remains a challenge with NH, a challenge that is significantly worsened when trapping is attempted. Due to the long excited state lifetime of 440 μs and the UV wavelength, absorption signals of cold NH were limited to 2% at zero field. In the presence of a trapping field, two competing effects modify the absorption. First, the quadrupole trap compresses the molecular ensemble

to enhance the density from the full trap volume of ≈100 cm^3 to the effective volume

$$V_{\text{eff}} = 4\pi \left(\frac{R}{\eta}\right)^3, \tag{A.1}$$

which is ≈0.5 cm^3 for $R = 3$ cm and $\eta = 9$. This gives a compression factor of about 200 averaged over V_{eff}. Second, however, the large gradient of the trapping field causes significant Zeeman broadening, reducing resonant absorption. For a fixed laser frequency, there is an ellipsoidal shell of constant magnetic field which is resonant. The thickness of this resonant shell, Δz, can be computed from the Doppler width ω_{D}, the Zeeman shift $\partial\omega/\partial B$ of the transition, and the field gradient, giving

$$\Delta z = \sum_i f_i \frac{\Delta\omega_{\text{D}}}{\frac{\partial\omega}{\partial B}\frac{\partial B}{\partial z}}, \tag{A.2}$$

where the sum is taken over all hyperfine transitions with relative transition strengths f_i ($\sum_i f_i = 1$), which overlap in the Zeeman-broadened spectrum. At 0.5 K, $\Delta z \sim 0.5$ mm, which is about 150 times smaller than the effective resonant path length of the spatial molecule distribution at zero-field, as calculated from the lowest-order diffusion mode.

Assuming no change in production yield, the expected trapped absorption can be estimated by combining the ∼200 enhancement in density with ∼150 ÷ 2 decrease in path length, where the factor of two accounts for the interaction of the trap-centered probe laser with both halves of the resonant shell. This factor of ∼3 increase, along with the fact that only a third of the molecules are produced in the $m_J = +1$ trappable state, implies that the observed *OD* will be roughly unchanged with the trap energized *only* if every one of these molecules were trapped. In reality, molecules will evaporate from the trap or relax to untrapped states before coming to equilibrium, thus the *OD* is almost certain to decrease, perhaps dramatically.

Balanced absorption regularly yields a noise floor of 10^{-3} for absorption detection in the experiments with NH, with an additional factor of $\lesssim$10 obtained from averaging. The

limiting factor is differential vibrations between the probe laser and cryogenic apparatus. These are partially compensated by the use of a lens to focus the beam onto the cell mirror (see Section 4.2.1 of [111]). However, residual noise has significant amplitude in the 1–1,000-Hz bandwidth of the experimental dynamics. Rapidly scanning the laser over GHz-scale spectral features cannot be done while maintaining the doubling cavity lock, and so it is difficult to remove this low-frequency noise.

A.3.6 FM spectroscopy of NH

Frequency modulation (FM) spectroscopy is a powerful method for eliminating low-frequency noise sources. A probe laser is frequency modulated to add sidebands before interacting with the molecules. The differential interaction of the sidebands with the molecular spectrum is extracted with a homodyne measurement that includes only the small components of noise at the high modulation frequency. Bjorklund *et al.* [174] calculate the minimum detectable change in the absorption δ in the shot noise limit to be

$$\Delta\delta_{\min} = 2\left[\eta_{\mathrm{e}} M^2 \left(\frac{P}{\hbar\omega_{\mathrm{c}}}\right)\Delta f\right]^{-1/2}, \tag{A.3}$$

where η_{e} is the detector quantum efficiency, M is the modulation index, P and ω_{c} are the laser power and carrier frequency, respectively, and Δf is the measurement bandwidth. The best detection limit is achieved for long wavelengths and high laser power. In addition, the sidebands should be as strong as possible.

Unfortunately, several factors conspire against FM detection of NH in a trap. Foremost, the spectrum is spread over several GHz at temperatures near 0.5 K. Electro-optical modulators (EOMs) in the UV require low-absorption crystals that have high indices of refraction, which makes it more difficult to produce strong modulation at high frequencies in the GHz

range.[9] As a result, both the carrier frequency and sidebands necessarily interact with the molecules. Since the FM signal is proportional to the differential absorption and phase shift between the sidebands, this causes partial common-mode signal rejection. In this regime, the FM signal resembles the derivative of the spectrum rather the spectrum itself. For the largest signal, the experiment should therefore seek to sharpen the spectral features, which can be accomplished by using a small probe beam. On the other hand, the long NH excited state lifetime ensures a low saturation intensity of 3.6 mW/cm^2 and a correspondingly low power limit for a small beam. Taking these limitations and the short wavelength into account, the expected noise floor for trapped NH is only somewhat better than AM spectroscopy can achieve. For a 3-mm beam at saturation intensity and a strong modulation index of 0.3, $\Delta\delta_{\min} \approx 2 \times 10^{-5}$ with 1-kHz bandwidth.

Another technical limit enters when the detector is considered. In practice, the 250-μW beam described above is far in excess of the maximum power observable by the PMTs used for NH detection, which reduces the sensitivity by more than an order of magnitude. This limit can be overcome by using photodiodes, although Johnson noise must be accounted for in this case, since photodiodes have no intrinsic gain. For a room-temperature 50-Ω load, the Johnson noise amplitude is similar to that of shot noise. This permits observation of absorption below 10^{-4} with 1-kHz bandwidth, but only with electronics operating near the

[9]Since the 336-nm probe laser for NH is produced by frequency doubling a 672-nm dye laser, it is possible to modulate the red fundamental wavelength at a higher modulation frequency than is achievable in the UV. The doubling cavity must then be co-resonant for both the carrier and sideband frequencies (which are likely to be spaced at greater than a cavity free spectral range), although this could potentially be avoided by single-pass doubling in a periodically-poled nonlinear crystal [175]. The sidebands and carrier will mix when doubled to produce additional frequency components, with minimum spacing equal to the modulation frequency. Modulation of the fundamental wavelength was not attempted here, but could in principle provide several GHz separation between the UV carrier and nearest sideband frequencies.

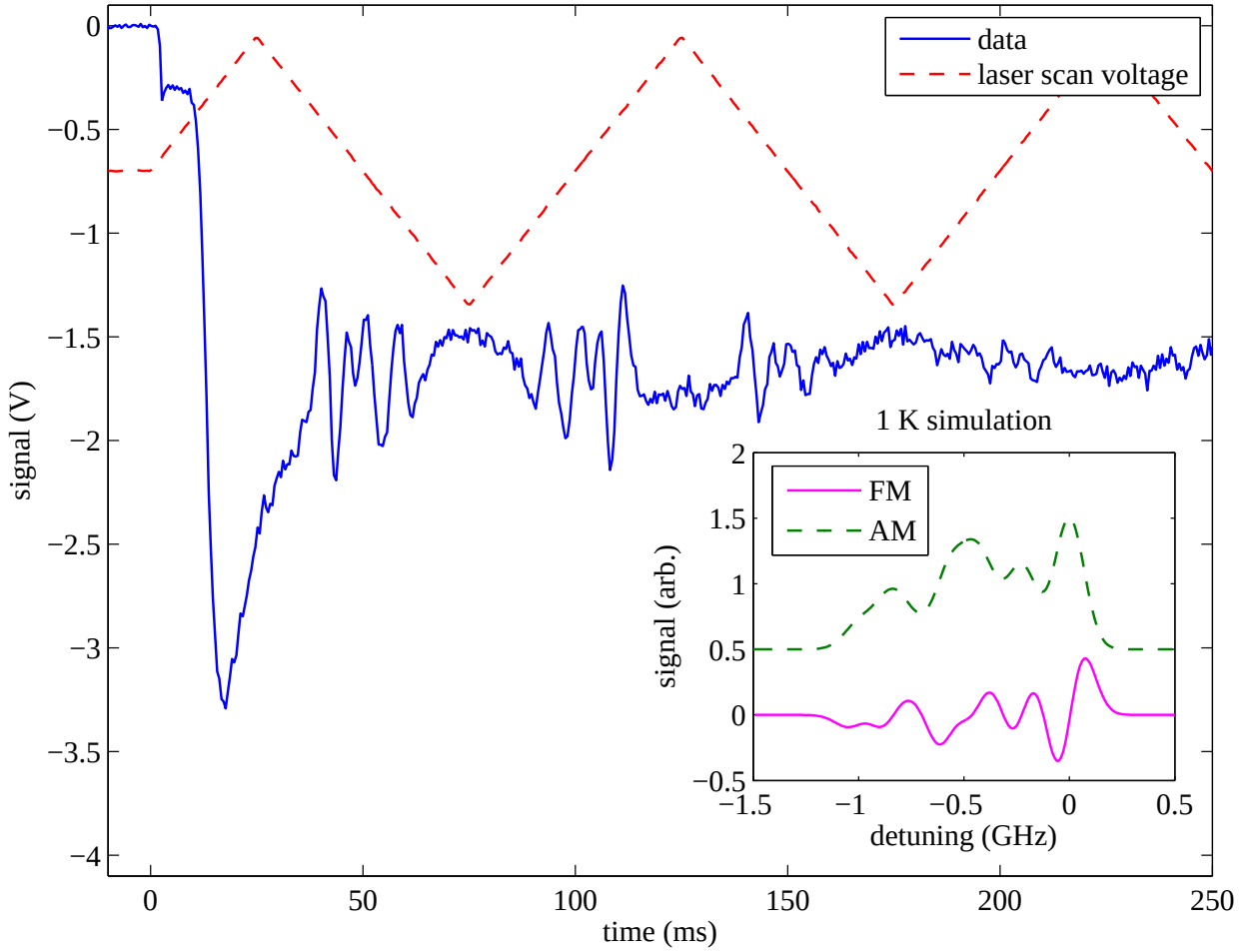

Figure A.12: FM absorption spectrum of NH near 1 K taken with 50 MHz modulation frequency. The PMT is protectively gated off until 2 ms after the ablation pulse to allow for decay of the ablation plume. The large initial spike at $t \sim 15$ ms is a recovery artifact due to the fact that the PMT is operating near its maximum output current. The inset shows simulated AM and FM spectra.

Johnson noise limit. It is also important to note that a 250-μW probe beam will cause significant optical pumping of the trapped ensemble, which limits observation time.

For narrow zero-field spectra, the constraints are relaxed somewhat. Figure A.12 shows a zero-field hyperfine spectrum obtained with FM spectroscopy. The EOM used to produce

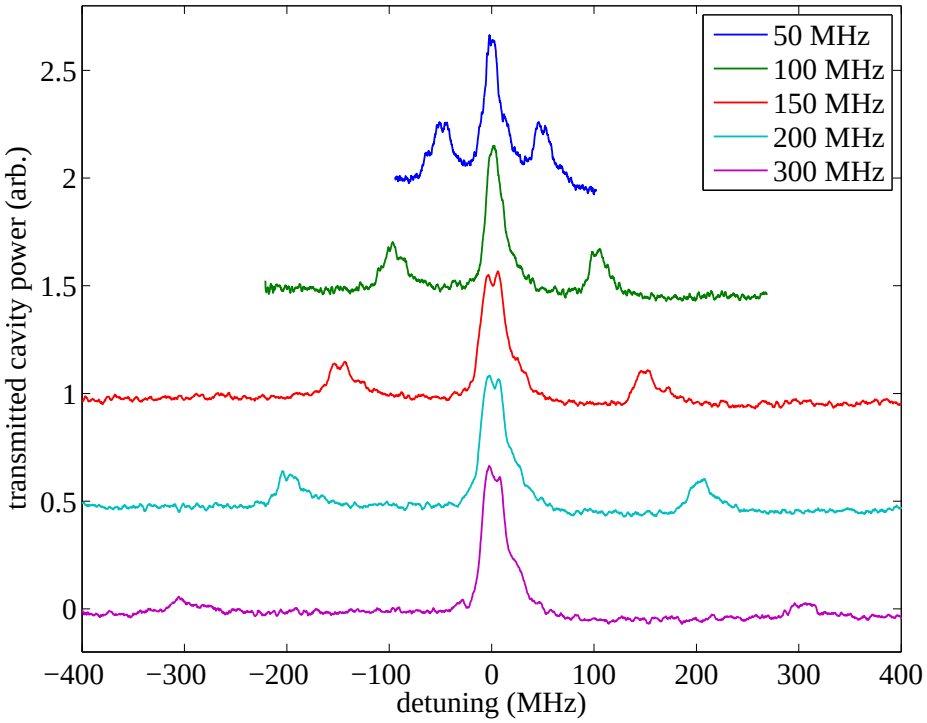

Figure A.13: Sidebands of 336-nm NH probe beam at different modulation frequencies, as measured by transmission of a 8-cm confocal cavity, for use in FM absorption spectroscopy. The EOM is non-resonantly driven with RF signal power of 10 dBm × 45 dB amplification. The individual cavity scans are offset vertically for clarity.

the sidebands[10] is broadband to allow for tuning of the modulation frequency, although the modulation index is stronger at lower frequencies (Figure A.13). The downside of a nonresonant EOM is that the necessary RF drive power is large (≈300 W is used here[11]) and the radiated drive signal is picked up by detection electronics to cause additional noise. For this technical reason and the fundamental limitations noted above regarding in-trap detection, FM spectroscopy of NH was abandoned.

[10]Model 350-50-UV-Phase EOM with potassium dideuterium phosphate (KD*P) crystal, Conoptics, Inc., Danbury, CT.

[11]Model 550 amplifier, 50–500 MHz, Conoptics, Inc., Danbury, CT.

A.3.7 Challenges of fluorescence detection with limited optical access

The dilution refrigerator and magnet used in these experiments were both designed to be fully or partially immersed in liquid helium for normal operation. Retrofitting the apparatus to run with these components in vacuum (and using, for example, a pulse tube cooler to provide cooling to 4 K) would be an extremely expensive and formidable engineering effort. The alternative—the constraint of maintaining a liquid helium reservoir surrounding the experiment—makes it very difficult to optically access the trapped ensemble through the midplane of the magnet. Doing so would require creating several additional cryogenic seals to provide beam access through the liquid reservoir, magnet, and inner vacuum can. These seals would complicate the mechanical constraints and assembly procedures of the apparatus. In addition, the interface with the vacuum can, in particular, would likely require a reduction in trap depth. Finally, providing superfluid leak-tight optical access through the side of the superfluid jacket surrounding the cell is an especially complex task.

For these reasons, the experiments in this apparatus have made exclusive use of optical access *via* downward-facing windows and a cell mirror. Imaging or fluorescence detection must therefore collect photons from the same window as lasers used for optical pumping and ablation, reducing available solid angle. Even worse, unavoidable scatter from these lasers into collection optics can swamp low signal levels. This is especially true for diagonal fluorescence spectroscopy, in which the emitted photons are the same wavelength as the pump photons and scatter cannot be spectrally filtered from the signal.

Diagonal fluorescence detection can still be achieved by temporally filtering the signal photons from the scattered pump light. As described in Section 2.3.2 of the thesis of Matthew Hummon [168], the 440-ns excited state lifetime allows enough time to turn off the pump beam and collect fluorescence light in the absence of scatter. The process is repeated with a

1-MHz square-wave chop of the pump beam. This temporal filtering reduces the signal level by about a factor of 6 (including the ≈100-ns dead time to wait for the pump shutoff) while fully eliminating pump scatter as a source of noise.

Unfortunately, secondary effects of the pump light cause noise that is not eliminated using this technique. First, fluorescence in cold solid materials may take longer to decay than the excited molecules, and hence cannot be removed with the pump laser chop. Second, a high rate of scattered pump photons incident on the detection PMT in the bright phase of the chop cycle can cause spurious delayed noise pulses called "afterpulses" when the pump laser is off [176]. Such afterpulsing is sometimes seen when the PMT vacuum becomes contaminated with helium gas. With the pump laser off the PMT used for these experiments[12] generated afterpulses at a rate of approximately 1% the pump-on count rate (Figure A.14), with a decay time of roughly 300 ns.[13] The afterpulsing can be eliminated by gating the PMT off when the pump laser is on. However, the repetition rate of the gate is limited to 10 kHz (due to capacitance in the gating circuit that provides rapid gate speed—higher duty cycle may be possible with slower gate speed), hence this solution sacrifices two orders of magnitude in signal photons.

Another detection option is off-diagonal fluorescence using the (0,1) vibrational transition at 375 nm. The fractional decay to the $v = 1$ state is only 0.6% [152], hence about 150 photons must be scattered on the (0,0) transition for every 375-nm photon. The bright pump light can be spectrally filtered, but fluorescence in other materials may be spectrally

[12]Model H10304 PMT module with gate function, Hamamatsu Corporation, Bridgewater, NJ.

[13]The afterpulsing of the PMT used for the previous NH work (Model P25A-02, Electron Tubes Limited, now defunct) was also measured and found to be about a factor of 2 worse, although this behavior may have worsened in the intervening months. This suggests that afterpulsing may be the limiting noise source for the previous chopped-pump experiments of Hummon *et al.*, rather than imperfect AOM extinction, as was thought at the time [168].

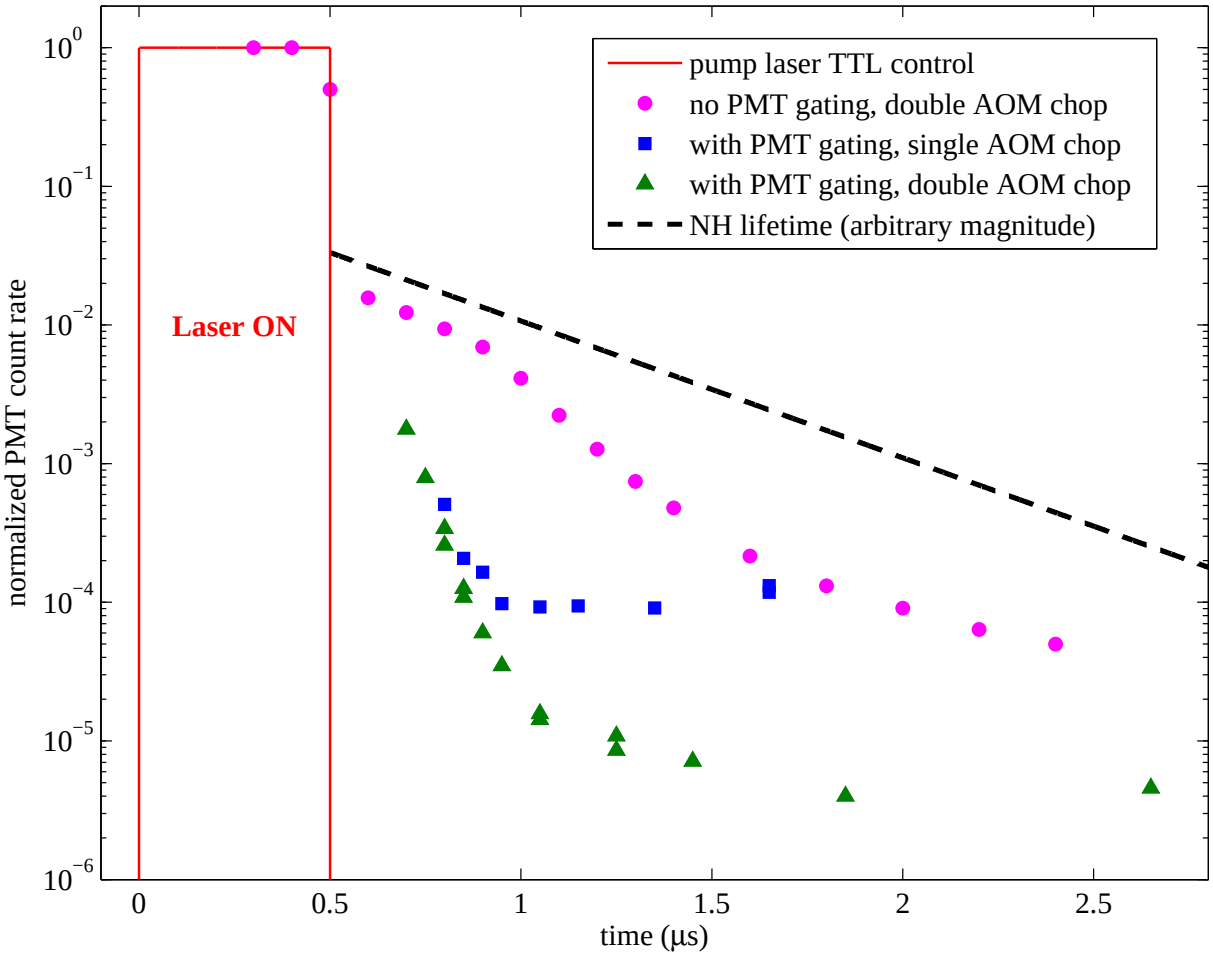

Figure A.14: PMT count rate with 0.5-μs pump laser pulse, normalized by the rate observed when the pump laser is on (dominated by scattered pump light). When the PMT is not gated off during the pump pulse, the count rate drops only to ≈1% when the pump laser is extinguished and decays on a time scale similar to the NH natural lifetime. If the PMT is gated off (by reverse-biasing the photocathode) during the pump pulse, the count rate drops much faster. A single AOM is found to provide an extinction ratio of about 10^4. When gating, the count rate in the first 400 μs after extinguishing the pump laser may be due to the finite AOM extinction time, materials fluorescence, or a combination of both.

broad and have a significant component in the detection band, especially when that band is at a longer wavelength than the excitation. The opposite pumping scheme, in which $v = 1$ molecules are pumped on the (0,1) line and 336-nm photons are collected, reverses the wavelength order to reduce materials fluorescence. In this scheme, however, the experiment will be limited by the 37-ms lifetime of the $v = 1$ state [153].

Off-diagonal fluorescence detection was attempted in the copper cell by pumping from the ground (0,0) state and looking for 375-nm photons. With an observed 0.7% pump laser absorption, no fluorescence signal above background was observed. Based on the measured fluorescence rate and estimated detection efficiency, a signal-to-noise ratio of $\sim$8 was expected. It is difficult to align the fluorescence collection optics to an unobserved signal, however, and imperfect alignment may be to blame.

A.4 Phase III: Modification of G-10 cell from Phase I

A.4.1 No NH production enhancement with discharge

After the success of producing NH in the copper Phase II cell using ablation of aluminum nitride into discharge-vaporized hydrogen gas, the Phase I G-10 cell was modified to insert ablation targets. The cell walls were cut with a Dremel tool fitted with an abrasive cutting wheel, with care taken to minimize dust contamination of the interior cell space. With new ablation targets in place, a new cell window and superfluid jacket patch were epoxied to the remaining cell wall.

When the modified cell was cooled below 1 K and filled with precursor hydrogen ice, NH was observed from ablation of aluminum nitride in the production region of the cell.

Unfortunately, the density was about an order of magnitude lower than that observed in Phase II. More significantly, while a discharge pulse had served to enhance the hydrogen density in the copper cell, the discharge had no positive effect on the signal in the G-10 cell. The maximum NH density was the same as that achieved purely with ablation. As was seen in the previous cell, the production steadily decreased with repeated ablation pulses after filling the cell once with hydrogen, and would be replenished upon subsequent filling. Unlike the previous cell, the discharge appeared to accelerate the production decrease.

One potentially significant difference between the cells is that the Phase III cell had the discharge coil wrapped external to the superfluid jacket (see Figure A.5), whereas the Phase II cell coil was in contact with the buffer gas and hydrogen. It is possible that the dramatic difference in production between the two cells is due to the necessary hydrogen vaporization being primarily a thermal process: the coil surface heats during the discharge pulse to evaporate hydrogen. This heating could be caused by resistive heating in the copper wire or by dissipation of energy into the plasma in the regions of high electric field near the wire. On the other hand, in contrast to this thermal vaporization, hydrogen could be vaporized in a process of etching from cold ice by energetic particles produced in the discharge [169]. The etching process would likely be less dependent on the surface temperature than the evaporative process, and should not depend strongly on whether or not the coil is in contact with the hydrogen ice. The contrasting behavior of the Phase II and III cells is evidence in support of the thermal process being dominant.

A second performance difference between the cells is that the discharge in the Phase III cell was weaker and less repeatable, due primarily to the twisted-pair cabling leading to the coil from outside of the cell. The heating observed from the discharge was roughly a factor of 2 lower than observed in previous cells at similar RF power input, suggesting that power was being reflected from the coil due to poor coupling.

A.4.2 Detection limited by fluorescence of G-10

Since off-diagonal fluorescence detection of NH had failed in the copper cell with a clear simultaneous NH absorption signal, a test experiment was performed to observe (0,1) fluorescence at room temperature. Boron nitride was ablated into hydrogen gas and illuminated with a 50-μW pump beam resonant with the (0,0) line. Fluorescence was observed separately at both 336 nm and 375 nm, with a ratio consistent with previous measurements [152]. The observed collection efficiency was ≈7 times weaker than estimated, which may expose an flaw in the calculated spatial distribution of fluorescence, and may be related to the failure to see fluorescence in Phase II. Nevertheless, this observation confirmed the feasibility of detecting NH using off-diagonal fluorescence.

Due to the weak off-diagonal fluorescence rate, excellent rejection of pump light is necessary. To this end, the PMT aperture was covered by a stack of four filters in the following order of incidence, as seen by arriving photons: (1) a 6-nm bandwidth interference filter centered at 375 nm[14]; (2) a colored glass filter passing 375 nm but not 336 nm[15]; (3) an identical copy of (1); and (4) a colored glass filter that passes both 336 and 375 nm[16]. The stack is oriented in this way to minimize laser-induced fluorescence in the filters themselves. The effective rejection factor of this filter stack for the 336-nm pump photons is measured to be 3×10^8.[17] When looking for (0,1) fluorescence in the G-10 Phase III cell, a large noise background was observed. The noise was correlated with the (0,0) pump laser, but was in-

[14]Model LD01-37516, Semrock, Inc., Rochester, NY.

[15]Model B-440, Edmund Optics, Inc., Barrington, NJ.

[16]Model FGUV11, Thorlabs, Newton, NJ.

[17]It is not known whether the $(3 \times 10^8)^{-1}$ photons detected for each 336-nm photon incident on the filter stack is a transmitted photon or whether it is produced by laser-induced fluorescence in the filters. Transmission data the individual filters suggest that the filter stack transmission should be lower than this value.

dependent of the pump laser frequency, suggesting that the source was either pump scatter or unwanted fluorescence in the apparatus. The former was ruled out by the measured filter stack rejection factor. Visual inspection of the cell revealed visibly fluorescing spots where stray pump reflections struck G-10, which implied bright, broadband sources of unwanted light. When the fluorescence detection system was aligned to one of these spots, the noise level grew dramatically.

Stray reflections are a particular challenge in this apparatus due to the four uncoated UV fused silica windows between the laser system and molecular ensemble. Each window surface produces a 3.7% Fresnel reflection of the pump beam. The windows are wedged to eliminate etalon effects that convert frequency shifts into amplitude noise, and so these stray reflections propagate in many directions. In principle, the NH experiment could have used antireflection window coatings for wavelengths of 336 nm, 375 nm and 532 nm to accomodate the pump, fluorescence and ablation light, respectively. However, other wavelengths are also often used for diagnostic purposes, especially when other experiments share the apparatus on the same experimental run. Moreover, the coating is not perfect and the reflections that remain are still significant.

On the way into the cell, the pump beam produces 8 primary reflections of $\approx$3.7% power (some are somewhat weaker due to prior attenuation of the pump beam), and another 8 on the way out. These primary reflections produce 56 secondary reflections at $\approx$0.14%, and 240 tertiary reflections. Controlling the directions of all of these reflections is not feasible, although alignment of the window wedge angles can allow for all the reflections to be contained in a single plane for spatial filtering. Half of these reflections enter the cell, where many strike a G-10 surface to cause fluorescence. This background light prevented observation of NH (0,1) fluorescence in the Phase III cell, since even the secondary reflections cause an unacceptable noise level. Without fluorescence detection, the weaker NH production en-

sured that no trapped signal could be observed. It was clear from Phase III that fluorescence detection had to be improved.

A.5 Phase IV: Design for maximized production and fluorescence sensitivity

A.5.1 Building a new cell

We come now to the final phase of the NH cryogenic production experiments. The Phase IV cell, a schematic of which is shown in Figure A.15, was designed as the best effort for trapping, cooling and detection of NH within the constraints of the current apparatus. The primary improvements are in production and detection. First, in an attempt to recreate the good production of the Phase II copper cell in a manner consistent with trapping and further cooling, the discharge coil for the Phase IV cell was anchored to the internal surface of the cell wall. The calculated time constant necessary to cool this coil after production is similar to the time for cooling the wall surface itself, consistent with the need to rapidly decrease the helium density after trap loading. Whether the Phase II cell discharge vaporized hydrogen by evaporation or by etching, the Phase IV cell mimicked that design for similar results.

Second, to improve the fluorescence detection sensitivity, the cell was engineered to be dramatically less fluorescent. Rather than the back surface of the cell that is exposed to stray pump beam reflections being composed entirely of fluorescent G-10, it was covered by a beam reflector created from polished single-crystal silicon (Figure A.15B). The two halves of the beam reflector were cut with a waterjet cutter[18] from silicon wafer, sandwiching the wafer between two sheets of 5-mil Kapton and then two 1/4" thick Teflon plates. Piercing

[18]OMAX Corporation, Kent, WA.

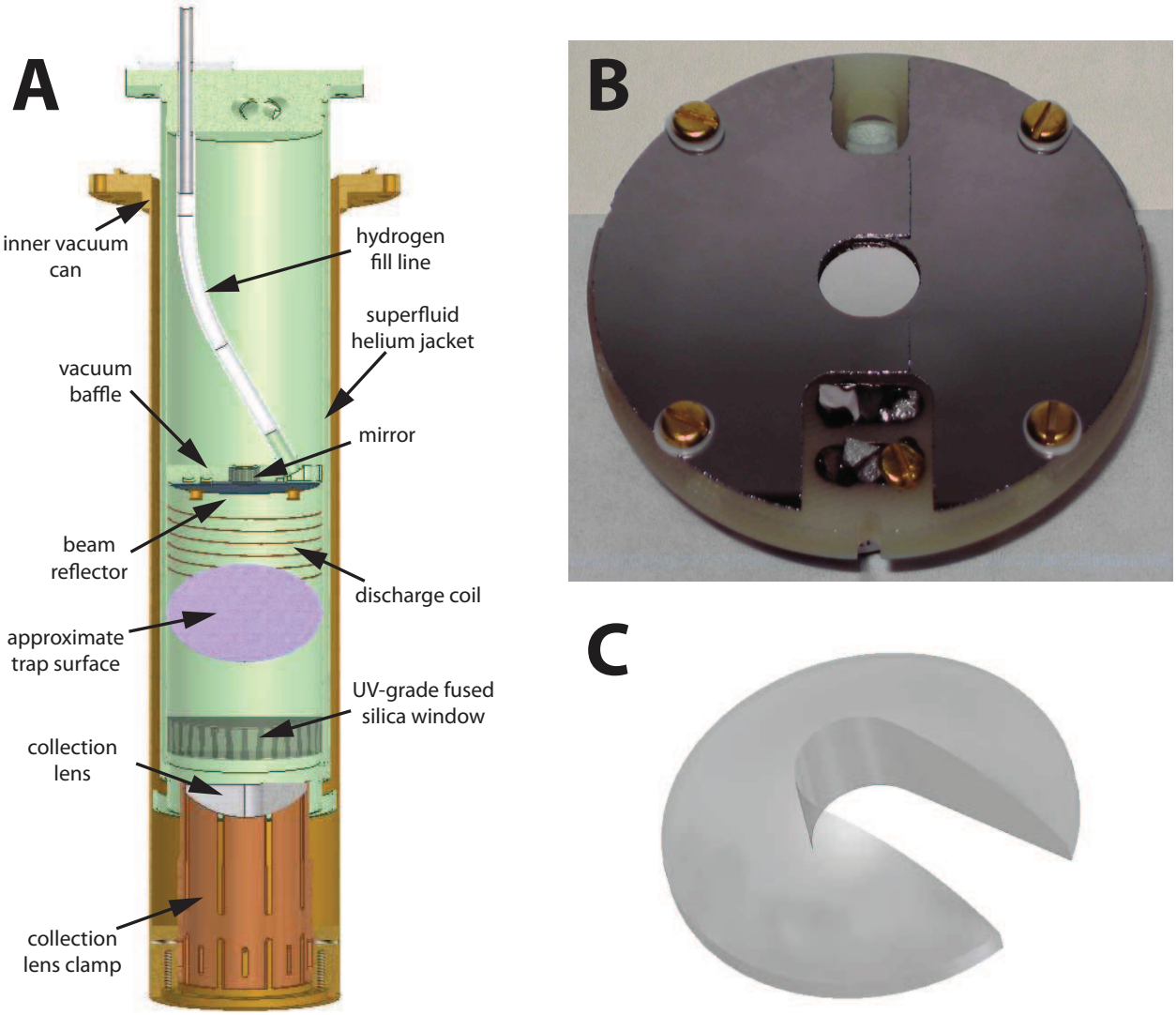

Figure A.15: (A) Phase IV trapping cell shown with lower portion of inner vacuum can and fluorescence collection lens; (B) single-crystal silicon beam reflector before installation in the Phase IV trapping cell; (C) schematic of fluorescence collection lens design. Both the beam reflector and collection lens were fabricated using a waterjet cutter.

wafers with the jet causes them to fracture, due to the large force generated when the jet scatters from the surface. However, wafers can be successfully cut from an edge where the jet can be minimally deflected by the cutting process. In addition, using the low-pressure cutting mode results in a reduced failure rate. The roughness of the edges cut with the water jet in the wafer is sub-millimeter scale. The beam reflector, with measured reflectance of ≈50% at 336 nm and no detected fluorescence, was mounted to the mirror so that reflections of the pump beam would strike the silicon and exit through the cell windows. Cutouts in the beam reflector accommodate ablation targets and the hydrogen fill line, and the window wedge alignment was chosen such that all pump reflections would be contained in a plane that does not intersect these cutouts.

In addition to these changes in cell design, additional apparatus changes were made to improve fluorescence detection. The "UV grade synthetic fused silica" dewar windows used in Phase III[19] were observed to fluoresce *visibly* under excitation at 336 nm, despite the manufacturer's literature stating that the material "does not fluoresce in respond to wavelengths longer than 290 nm" [177]. Before choosing windows for the Phase IV apparatus, room-temperature tests were performed with several UV fused silica windows from several manufacturers. The results of this testing are shown in Table A.1. While the magnesium fluoride (MgF_2) windows exhibit the least fluorescence, the transmission of infrared wavelengths for this material is such that it provides a less reliable barrier against heating due to blackbody radiation. Suprasil 1, essentially high-purity UV fused silica, is another low-fluorescence material, but it is very expensive and could not be available soon enough to be used in Phase IV. Instead, the UV fused silica windows from Optosigma were used.

The final major change to the fluorescence collection apparatus was the incorporation of a

[19]Model IF-3050-UV, CVI Melles Griot, Albuquerque, NM.

Table A.1: Fluorescence in UV windows under 336-nm excitation. Fluorescence rates are given as number of photons fluoresced per 1 cm of material into the 6-nm detection band centered at 375 nm divided by the total number of incident photons.

Material	Vendor	Part Number	Fluorescence Fraction ($\times 10^{-9}$ cm^{-1})
UVFS	CVI Melles Griot	IF-3050-UV	9
UVFS	Laser Components	PL2-24850UV-S	6
UVFS	Optosigma	CI# 100205RT01[a]	5
UVFS[b]	Thorlabs	LA4984-UV	80
MgF_2	CVI Melles Griot	PWI-2019-MF	1.5
Suprasil 1	CVI Melles Griot	IF-2037-SS	1.5

[a]Custom-ordered optic: ⌀3" × 0.5" with 2° wedge

[b]This optic had a antireflective UV coating which may contribute additional fluorescence.

high numerical aperture lens[20] directly outside of the cell within the inner vacuum can. This lens was designed to collimate light emitted from the trap center to enhance the fraction of fluorescence that exits the dewar. The collimation also allowed for spatial filtering to reduce the collection of unwanted downstream window fluorescence. To allow for pump and ablation laser propagation, the lens was cut with a waterjet cutter to form a 1.5-cm wide notch from the lens center to its edge (Figure A.15C). Simulations of fluorescence collection demonstrated collection efficiency of approximately 1% for photons emitted from a 5-mm diameter volume surrounding the trap center. The lens had spherical curvature; however, the ability to focus fluorescence on the detector surface was limited not by spherical aberration, but by the finite size of the emitter. The lens was held in place by a copper tube bolted to the 4.2-K inner vacuum can, with eight long slits cut in the tube to provide greater flexibility so that the lens would not crack under the stress of thermal contraction.

[20]Model LA-4078, ⌀2", $f = 7.5$ cm, Thorlabs, Newton, NJ.

A.5.2 Leaky G-10 tubing

After the Phase IV cell was constructed, a very large leak was discovered (>1 sccm at 1 bar differential pressure) between the cell space and superfluid jacket. Leaks in G-10 trapping cells are not uncommon, and will readily occur due to design errors. Leaks at joints due to differential thermal contraction, in particular, are more difficult to prevent with G-10 due to the fact that contraction is anisotropic in the composite [178]. Surprisingly, the leak in the Phase IV cell was not at a joint. With the jacket space filled with water and the cell pressurized with 1–2 psig, a stream of bubbles poured from a pinhole defect in the G-10 tube[21] forming the inner jacket wall.

A 1 cm × 2 cm section of the outer jacket wall was removed with a Dremel tool to expose the area, but there was no obvious defect visible in the inner wall tube. The exposed region was painted with a thin coating of Stycast 1266 epoxy to seal the leak. After the epoxy had cured, however, multiple other, smaller pinholes were found within 1 cm of the same area. The outer jacket wall cutout was enlarged and these areas were also painted. After this, no leak was detected. Next a 77-K leak test was conducted by immersing a vacuum can containing the cell into liquid nitrogen. Another large leak was measured, presumably having opened as a result of thermal stress. The leak remained when the cell was returned to room temperature.

When the jacket space was again filled with water, a new point defect was discovered. Again, a section of the outer wall was removed and the defect was painted. Unfortunately, upon cooling to 77 K, yet another, smaller leak appeared ($\approx 10^{-4}$ mbar l/s at 1 bar). To avoid an endless game of "G-10 Leak Whack-a-Mole," the entire outer jacket wall was removed and the entire outer surface of the inner jacket wall was painted with a more liberal coating of Stycast 1266 (enough to ensure that the epoxy layer continuously coated the surface,

[21]Spaulding Composites, Inc., Rochester, NH

although the layer was still thinner than 1 mm). A new section of G-10 tube from the same stock was then attached. Before this was done, the new outer wall tube stock was separately cooled to 77 K, warmed back to room temperature, and leak tested. For the new tube attachment, each joint was made with the standard 0.25" of overlap between the two parts, one or both of which was 1/32" in thickness. Thankfully, this time the cell had no leak at 77 K above 2×10^{-9} mbar l/s, and it was subsequently used for Phase IV of the NH experiment, as well as for the experiments with antimony and aluminum described in Chapters 2 and 3.

Pinhole leaks in G-10 are not unheard of (see Section 5.5 of [70]). To avoid them, the inner jacket wall of the Phase IV cell had originally been painted with a very light coating of Stycast 1266 to avoid such leaks. This coating was apparently either patchy or too thin to fix the defects in the tubing, but a more aggressive coating appeared sufficient. Much worse leak behavior was observed in poor-quality G-10 that was not constructed with very finely-woven fiberglass fabric, or which had significant defects in the fabric. The quality of the weave can be investigated by soaking a portion of the tube stock in an epoxy stripping agent such as MS-111.[22] An example of particularly poor-quality G-10 fabric (unknown origin) exposed in this manner is shown in Figure A.16.

A.5.3 Production performance

As was seen in the Phase II and III cells, NH could be successfully produced in the Phase IV cell purely by ablation of aluminum nitride after adding hydrogen ice to the cell. The density produced was larger and more stable than the Phase III cell, possibly due to the larger volume reducing diffusive loss to the cell walls. Unfortunately, a brief discharge pulse using 25 W of RF power seemed to provide little signal enhancement, as was observed in

[22]Miller-Stephenson Chemical Company, Inc., Danbury, CT.

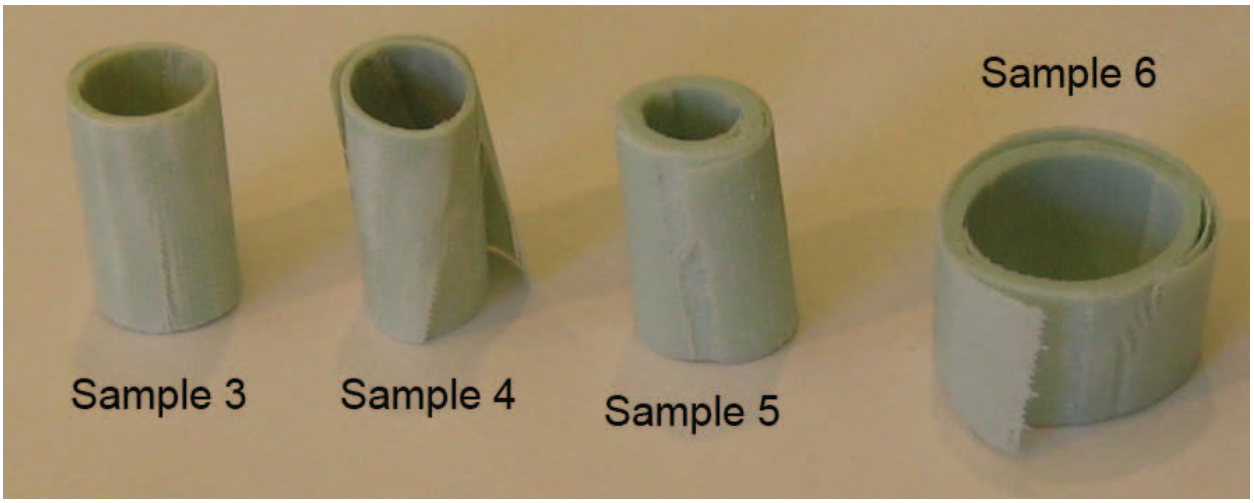

Figure A.16: Defects in the fiberglass fabric of poor-quality G-10 tubes (unknown origin) exposed by soaking the tubes in MS-111 epoxy stripping agent. A section of tube stock similar to this was found to leak longitudinally through the wall from one end of the tube to the other, without penetrating either the inner or outer surface.

the Phase III cell. Somewhat longer discharge pulses (with energy ~ 10 mJ) were observed to *decrease* the observed OD, possibly due to increased Doppler broadening. Finally, with very large discharge energies of $\gtrsim$100 mJ the signal increased to several times larger than the ablation-only production. This is likely due to warming of the internal surfaces of the cell above 5 K, forming a dense hydrogen vapor. However, this energy is far in excess of what can be used in conjunction with trapping.

The inability to recreate the Phase II production yield in a G-10 cell leads to some disheartening conclusions. The most significant difference between the cells may be that the Phase II discharge coil is effectively thermally disconnected from the cell on short timescales below 100 ms. This is because the only significant cooling processes are conductive cooling along the $\approx$1 m coil length and energy transfer to the buffer gas. This thermal disconnect and the small heat capacity of the coil imply that a few-mJ discharge pulse will heat the coil to temperatures where the hydrogen vapor density is above 10^{17} cm^{-3}. While this is excellent for NH production, this thermal disconnect is in conflict with the need for the coil

to cool rapidly after production to allow for trapping and thermal isolation. The experience of Phase III and IV seems to imply that these conflicting requirements cannot be reconciled to achieve the simultaneous goals of large production yield, trapping, and thermal isolation.

A.5.4 Detection performance

Before the Phase IV cooldown, the room-temperature noise background of unwanted fluorescence in the new cell was tested in a tabletop apparatus where full optics positioning control is possible. These tests confirmed a dramatically reduced fluorescence rate compared to the Phase III cell, with fluorescence noise at a similarly low level as that caused by pump beam reflections striking the PMT filter stack. With the pump beam deliberately aligned poorly to strike the G-10 hydrogen fill line, a somewhat larger, but still acceptable, noise level was measured, demonstrating the effective spatial filtering of the fluorescence collection lens. The total noise level with a 50-μW pump beam was measured to be less than 10 kHz, where a signal of over 1 MHz would be expected for 0.01% of the pump being absorbed and fluoresced in the collection region.[23]

Phase IV of the NH experiment was conducted in the cold apparatus after the antimony–helium collision experiment described in Chapter 2. In the 3–4 weeks of discharge and production tests after ending the antimony experiment, a film of unknown composition was deposited on the outer surface of the 77-K window. This film was found to be opaque to the 207-nm laser used to detect antimony, and hence it cannot have been present for that experiment. When fluorescence detection of NH was attempted, the film glowed brightly under excitation with the 336-nm pump beam, with correspondingly terrible background

[23]This region is about 10% the length of the cell and is overlapped with the trap. Therefore this 10^{-4} local fluorescence level would be equal to the in-trap OD, or 10% of the zero field OD.

noise levels at the 375-nm detection band. This background prevented fluorescence detection of NH in Phase IV, and further testing of the detection improvements could not be performed.

A.6 Summary and future prospects

A.6.1 Successful cryogenic production

The experiments described here demonstrated production of 10^{11} NH molecules at temperatures below 1 K (in the copper Phase II cell) and over 10^{10} molecules under conditions compatible with trapping (low production energy in a G-10 cell). The production method is relatively straightforward to implement, involving only an aluminum nitride target, a gas line to deposit hydrogen ice, and an ablation laser. This yield is approximately an order of magnitude smaller than the previous room-temperature discharge source [150], but can be implemented with under 10 mJ of energy and no additional heat load, such as that associated with open apertures that pass room-temperature blackbody radiation. Cryogenic discharge production of NH from nitrogen and hydrogen vapor was also achieved at 7.5 K, but this could not be replicated in a trapping cell.

Despite this success in production, none of the four phases of the NH work described here demonstrated NH trapping. The fundamental barrier is poor detection, since a large number of molecules are produced. As a result, future work with NH could benefit from adopting the cryogenic production described here in an apparatus better suited to low-background fluorescence spectroscopy.

A.6.2 Proposed improvements for improved detection sensitivity

The apparatus used for this work struggles against a single design constraint: both optical pumping and fluorescence detection share the same optical path into the cell. Especially because of the UV wavelengths needed for NH detection, the inevitable scatter and fluorescence due to the pump beam cannot be adequately filtered from the signal photons. The task of retrofitting the current experiment for perpendicular optical access would be prohibitively expensive and difficult, and future experiments would do better to construct a new apparatus that allows the magnet, refrigerator and cell to occupy the same vacuum space.

Even with perpendicular access, care must still be taken to minimize stray window reflections and fluorescence of materials. If pump laser scatter can be adequately reduced, then diagonal detection is preferable due to the much higher fluorescence rate. Chopping the pump beam improves the signal-to-noise by a factor of about 12, limited by PMT afterpulsing. Afterpulses are not intrinsic to detection with PMTs, so the effect likely can be greatly reduced if extreme care is taken to avoid helium contamination.[24] Alternatively, a gated detector can be used to remain insensitive to the bright pump, but the gate repetition rate must be close to 1 MHz to preserve the high signal rate. Likewise, off-diagonal detection with a perpendicular pump beam could achieve extremely low background noise with appropriate elimination of line-of-sight between the detector and fluorescing materials along the pump beam path. Off-diagonal sensitivity would then likely be shot-noise limited due to the weak Franck-Condon factor.

[24]Reasonable care was taken with the PMTs used for this work, and the previous NH work. The PMTs were kept in enclosures either pumped to vacuum or continuously purged with nitrogen gas. Nevertheless, both PMTs show similar afterpulsing behavior.

A.6.3 Prospects for sympathetic cooling

Based on the work outlined in this appendix, one can make modestly optimistic assumptions about the ability to produce and cool NH in a future G-10 cell. With 10^{10} molecules produced under trappable conditions at 0.5 K and a reasonable 10% trapping efficiency, an maximum initial density of 2×10^{11} cm^{-3} would be achieved. A significant number of these molecules would likely undergo spin relaxation in the initial ∼30 ms during which the helium-4 density drops and thermal isolation is achieved.

Nitrogen is not directly observed in the experiments described here, but the rather efficient NH production from ablation of aluminum nitride into hydrogen suggests a large nitrogen yield. Based on previous measurements and calculations of the nitrogen–helium system, it is safe to assume that nitrogen will be efficiently buffer-gas cooled and trapped after production and will likely be present in much greater numbers than NH in the trap. The resulting nitrogen–nitrogen collision rate will be more than rapid enough to proceed with evaporative cooling.

Sympathetic cooling of NH with evaporatively cooled nitrogen is hampered by the mismatched magnetic moments of the two species. The 3-μ_B nitrogen atoms will form a dense cloud at the trap center with a more diffuse surrounding cloud of 2-μ_B NH, precisely the wrong ordering for efficient sympathetic cooling with the large nitrogen reservoir. As cooling continues, NH will be consistently at a value of η that is 2/3 that of nitrogen, and thus NH will be preferentially evaporated. The sympathetic cooling of NH is therefore necessarily less efficient than evaporative cooling of nitrogen, even neglecting NH–nitrogen inelastic losses.

Evaporative cooling of buffer-gas cooled nitrogen will follow similar constraints as those outlined in the thesis of Charlie Doret [111] in reference to cooling metastable helium, including the rather slow rate at which current can be removed from the superconducting magnet coils to reduce the trap depth. For this technical reason, and because the values of γ for ni-

trogen and ^{4}He* are similarly high [52, 179], we take the demonstrated evaporation of ^{4}He* in that experiment as an efficiency benchmark for predicting the behavior with nitrogen. Specifically, the two orders of magnitude of atom loss required to reduce the temperature by two orders of magnitude [180] is a reasonable expectation. As this atom loss would stem largely from evaporative losses at $\eta_N < 8$, the NH loss is likely to be at least an additional order of magnitude worse (Equation 4.1). Finally, it is important to consider the inelastic NH–nitrogen losses that will be sustained in addition to this evaporative loss. If ramping the magnet takes the ∼100 s necessary for the ^{4}He* work, inelastic losses could be significant even with the interspecies γ being greater than 100. Also, the inelasticity of the interspecies collisions is calculated to increase at lower temperatures [53]. It will be thus be critical for the sympathetic cooling experiment not to "waste" any collisions with a suboptimal evaporation trajectory. Finally, a large initial molecule reservoir will be necessary—a condition satisfied by the cryogenic production method described here.

Appendix B

Calculating absorption for trapped molecules in motion

B.1 Reconciling Beer's Law with the Landau-Zener model

Molecules (or atoms) in a magnetic trap will have a distribution of Zeeman shifts corresponding to their spatial distribution superimposed on the trapping field. For a fixed probe laser frequency, only a certain shell of constant magnetic field will be in resonance. For a spherical quadrupole field with field along the z-axis given by $\boldsymbol{B} = B_0'\boldsymbol{z}$, the thickness Δz of this shell is given by

$$\Delta z = \frac{\Gamma_{\rm nat}}{\frac{\partial\omega}{\partial B}B_0'} = \frac{1}{\tau_{\rm nat}\frac{\partial\omega}{\partial B}B_0'}, \tag{B.1}$$

where $\Gamma_{\rm nat}$ and $\tau_{\rm nat}$ are the natural linewidth and lifetime, respectively, and $\partial\omega/\partial B$ is the differential magnetic moment between the ground and excited states. For $B_0' \sim 1$ T/cm, $\partial\omega/\partial B \sim \mu_{\rm B}$, and $\tau_{\rm nat} \sim 100$ ns, this resonant shell has $\Delta z \sim 1$ μm, much smaller than the trap size. The absorption of the probe laser with initial intensity I_0 at the intersection of

this shell can be calculated from Beer's Law,

$$1 - \frac{I}{I_0} = 1 - e^{-OD} \tag{B.2}$$

$$OD = \int n(z)\,\sigma(z)\,dz \tag{B.3}$$

where $n(z)$ is the molecule density distribution averaged over the laser beam cross section and σ is the optical cross section.

At temperatures near 500 mK, the molecules are moving at a mean velocity of $\bar{v}_z \sim 1$–2×10^3 cm/s. Doppler broadening inhomogeneously thickens the resonant shell, however each individual molecule sees the same $\Delta z \sim 1$ μm at a Doppler-shifted location. The molecules traverse Δz on average in a time $\Delta t < 100$ ns (for transitions with longer excited state lifetimes, transit time broadening will increase Δz and Δt). Even for short lifetimes of 10 ns, the molecules will still cross the resonant shell slower than the mean time to excitation (assuming saturation $s_0 < 1\%$, as is typically used to avoid optical pumping out of the trap).

It is then reasonable to ask whether the fact that the molecules are in resonance for a very brief time affects the absorption rate of photons from the laser beam. Going further, if we assume a mean collision time longer than Δt, the molecules will maintain a constant velocity as they pass through resonance, and hence will experience a linearly-varying detuning

$$\delta = \frac{\partial \omega}{\partial B} B_0' z = \frac{\partial \omega}{\partial B} B_0' v_z t. \tag{B.4}$$

This linear sweep through a resonant interaction is reminiscent of the classic Landau-Zener treatment of an avoided crossing. It is not obvious that the result of Beer's Law, obtained from integrating over a stationary distribution in space, will be the same as that obtained from applying the Landau-Zener method to each passing molecule. However, through a series of cases, we show in this appendix that the two approaches are indeed equivalent in the limit of weak laser power.

B.1.1 Case 1: Stationary atoms

For the purposes of all four cases considered here, we will consider a uniform density n of two-level atoms with excited state lifetime $\tau_{\rm nat} = \Gamma_{\rm nat}^{-1}$. The atoms are moving with constant uniform velocity $\boldsymbol{v} = v_z\,\hat{\boldsymbol{z}}$ in a constant-gradient magnetic field $\boldsymbol{B} = B_0'\boldsymbol{z}$. We will first consider the stationary case of $v_z = 0$. When illuminated with laser light with frequency ω and saturation parameter s_0, the scattering rate of the atoms will be

$$\begin{aligned}\Gamma_{\rm sc} &= \frac{1}{2\tau_{\rm nat}}\left[\frac{s_0}{1+s_0+(2\delta/\Gamma_{\rm nat})^2}\right] \\ &= \frac{s_0}{2\tau_{\rm nat}}\left[\frac{1}{1+(2\delta\tau_{\rm nat})^2}\right],\end{aligned} \tag{B.5}$$

where the second equality has used $s_0 \ll 1$. The total fluorescence rate is given by integrating Equation B.5 over all space,

$$\begin{aligned}\Gamma_{\rm f} &= \int n\,\Gamma_{\rm sc}\,d^3r \\ &= \frac{s_0 nA}{2\tau_{\rm nat}}\int\frac{dz}{1+(2\tau_{\rm nat}\delta(z))^2} \\ &= \frac{\pi s_0 nA}{4\tau_{\rm nat}^2\frac{\partial\omega}{\partial B}B_0'},\end{aligned} \tag{B.6}$$

where A is the cross sectional area of the laser beam.

B.1.2 Case 2: Arbitrarily slow atoms

Next we calculate $\Gamma_{\rm f}$ for the case in which the atoms are moving at a constant, very slow velocity that satisfies $v_z/\Delta z \ll \Gamma_{\rm sc} \ll \Gamma_{\rm nat}$, *i.e.*, the timescale for crossing the resonance is the slowest in the problem. Each atom will now see a linearly-changing detuning (Equation B.4), which moves through resonance as t goes from $-\infty \to \infty$. Ignoring the excited state decay, this is the standard Landau-Zener case. The probability of each atom being found in the

excited state after passage is given by [181]

$$P = 1 - \exp\left(-2\pi\frac{\Omega^2}{\alpha}\right). \tag{B.7}$$

where $\alpha = \partial\delta/\partial t$ is the detuning sweep rate and $\hbar\Omega$ the interaction matrix element. It is important to note the relationship between Ω and the Rabi frequency $\Omega_{\mathrm{R}} = -(eE_0/\hbar)\langle e|(\boldsymbol{r}\cdot\boldsymbol{\varepsilon})|g\rangle$ that results from the interaction of the two-level atomic dipole, $\boldsymbol{d} = -e\,\boldsymbol{r}$, with the electric field, $E(t) = E_0\boldsymbol{\varepsilon}\cos(kz - \omega t)$, of the laser (with wavevector $\boldsymbol{k}$ and frequency ω). In the rotating wave approximation, only half of the electric field magnitude drives the transition with the correct frequency, giving $\Omega^2 = (\Omega_{\mathrm{R}}/2)^2 = s_0/8\tau_{\mathrm{nat}}^2$ [181, 182].

Akulin and Schleich have analyzed the Landau-Zener problem when excited state decay is taken into account [183]. They find that the number of photons emitted by each atom passing through resonance is given by

$$N_{\mathrm{ph}} = 2\pi\frac{\Omega^2}{\alpha}\,e^{-\pi\Omega^2/\alpha}\left|W_{i\Omega^2/\alpha,-1/2}\left(-\frac{i\Gamma_{\mathrm{nat}}^2}{\alpha}\right)\right|^2, \tag{B.8}$$

where $W_{k,m}(z)$ is the Whittaker function [184]. This result is nontrivial and rather opaque, but useful asymptotic limits are presented in [183]. In the slow-sweep limit considered in this case ($\Omega^2\Gamma_{\mathrm{nat}}^2/\alpha^2 \gg 1$), Equation B.8 simplifies to

$$N_{\mathrm{ph}} = 2\pi\frac{\Omega^2}{\alpha}. \tag{B.9}$$

We then must only multiply by the rate that atoms pass through the resonance to determine the fluorescence rate

$$\begin{aligned}\Gamma_{\mathrm{f}} &= (nv_zA)\left[2\pi\frac{\Omega^2}{\alpha}\right] \\ &= (nv_zA)\left[2\pi\frac{\frac{s_0}{8\tau_{\mathrm{nat}}^2}}{\frac{\partial\omega}{\partial B}B_0'v_z}\right] \\ &= \frac{\pi s_0 nA}{4\tau_{\mathrm{nat}}^2\frac{\partial\omega}{\partial B}B_0'},\end{aligned} \tag{B.10}$$

where we have used $\Omega^2 = s_0/8\tau_{\rm nat}^2$. Comparison of Equations B.6 and B.10 shows no difference between the stationary case and the arbitrarily-slow case, which is comforting.

B.1.3 Case 3: Rapid atoms

Next, we consider the case where atoms cross the resonance quickly ($v_z/\Delta z \gg \Gamma_{\rm nat} \gg \Omega$). Akulin and Schleich also consider this limit ($\alpha \gg \Gamma_{\rm nat}^2$), finding that the number of photons scattered per atom is given by [183]

$$N_{\rm ph} = 1 - \exp\left(-2\pi\frac{\Omega^2}{\alpha}\right). \tag{B.11}$$

Note that this is the same as the result that ignores decay (Equation B.7). This makes sense, since in the case of slow decay the number of photons emitted per atom is at most one and equal to the probability of reaching the excited state during the crossing. For the weak-probe limit ($s_0 \ll 1$), Equation B.11 reduces to Equation B.9 and the fluorescence rate is the same as in Case 2 (Equation B.10).

B.1.4 Case 4: Intermediate-speed atoms

Finally, we consider the case in which the atoms are moving at a speed such that $\Omega \ll v_z/\Delta z \ll \Gamma_{\rm nat}$. This is the case in which the atoms cross the resonance much slower than the excited state decay, but much faster than the mean time to excitation—so most atoms cross without scattering a photon. This case ($\Omega^2/\alpha \ll \Omega/\Gamma_{\rm nat} \ll 1$ and $\Gamma_{\rm nat}^2 \gg \alpha$) is not specifically addressed in [183]. In this limit, Equation B.8 reduces to

$$\begin{aligned} N_{\rm ph} &= \lim_{\Gamma_{\rm nat}^2/\alpha \to \infty} 2\pi\frac{\Omega^2}{\alpha}\, e^{-\pi\Omega^2/\alpha} \left| W_{i\Omega^2/\alpha,-1/2}\left(-\frac{i\Gamma_{\rm nat}^2}{\alpha}\right)\right|^2 \\ &= 2\pi\frac{\Omega^2}{\alpha}\, e^{-\pi\Omega^2/\alpha}\, e^{\pi\Omega^2/\alpha} \\ &= 2\pi\frac{\Omega^2}{\alpha}, \end{aligned} \tag{B.12}$$

which is the same result as found in Case 2. Hence the fluorescence rate is again the same as Equation B.10.

B.1.5 Conclusions from the comparison

Using the appropriate asymptotic limits of the Landau-Zener problem with decay, comparison of Cases 2–4 gives the same result in all velocity limits, (assuming laser intensity well below saturation). This shared result is also the same as that of Case 1, the stationary case. Therefore, we conclude that there is no difference between calculating the fluorescence rate as a Landau-Zener level crossing or by integrating over a spatially-extended resonance with a stationary atom distribution. It is safe to assume the atoms to be stationary for the calculation (except in regards to Doppler shifts), which is a more straightforward calculation.

To determine the *OD* from the fluorescence rate $\Gamma_{\rm f}$, we normalize by the incident photon flux $\Gamma_{\rm ph}$ to yield the absorption:

$$\begin{aligned}\Gamma_{\rm f}/\Gamma_{\rm ph} &= \left[\frac{\pi s_0 n A}{4\tau_{\rm nat}^2 \frac{\partial\omega}{\partial B} B_0'}\right]\left[\frac{s_0 I_{\rm sat} A}{\hbar\omega}\right]^{-1} \\ &= \frac{\pi}{2} n\sigma \left(\frac{1}{\tau_{\rm nat}\frac{\partial\omega}{\partial B} B_0'}\right) \\ &= \frac{\pi}{2} n\sigma\Delta z, \end{aligned} \tag{B.13}$$

where we have used Equation B.1 and the definition of the saturation intensity,

$$I_{\rm sat} = \frac{\hbar\omega}{2\sigma_0\tau_{\rm nat}}. \tag{B.14}$$

where σ_0 is the resonant optical cross section. We have already made the assumption in Equation B.5 that absorption of photons does not affect the fluorescence rate (*i.e.*, $\Gamma_{\rm f} \ll \Gamma_{\rm ph}$) and so $OD \ll 1$ and we can equate it with absorption,

$$OD = \frac{\pi}{2}\, n\sigma_0\Delta z. \tag{B.15}$$

As a final check, it is simple to show that Equation B.15 is the same as the result of using Beer's Law (Equation B.3):

$$\begin{aligned} OD &= \int n(z)\,\sigma(z)\,dz \\ &= n\sigma_0 \int \frac{dz}{1+(2\delta(z)\tau_{\mathrm{nat}})^2} \qquad \text{(B.16)} \\ &= \frac{\pi}{2}\, n\sigma_0 \Delta z, \qquad \text{(B.17)} \end{aligned}$$

where again we have used Equation B.1 and assumed $s_0 \ll 1$.

When the problem is generalized to more complicated situations, the equivalence between Beer's Law and the Landau-Zener approach holds. To start, we can replace the two-level atoms with multi-level molecules. Also, Doppler broadening leads to a velocity-dependent shift of the resonant region in space, but the same result is obtained for each 3D velocity component of the distribution; and similarly, the magnetic field gradient can have a complicated form without effect, as long as the curvature remains small on the scale of Δz. Lastly, the polarization of the laser beam will introduce a numerical factor that depends on the angle between the polarization and the local magnetic field (see Section A.2.2 of [113]). All of these effects can be included in the optical cross section when performing the integration in Equation B.16, including the addition of a second integration over the 2D beam profile.

B.2 Implications for simulations of trapped spectra

The equivalence of the Beer's Law and Landau-Zener approaches implies that one is free to choose whichever method is more straightforward for calculation of trapped absorption in a given circumstance. The trapped spectrum simulations described in the theses of Jonathan Weinstein and Nathan Brahms [70, 113] use Beer's law with the stationary assumption.

These simulations also go much further than this discussion to appropriately account for the Zeeman effect in multi-level systems, the finite extent and offset of the beam, and the spatial integration through the actual trapping geometry.

The thesis of Wes Campbell includes a separate calculation of the fluorescence rate using the Landau-Zener approach (see Section 5.2 of [152]). He finds a discrepancy compared with the Beer's Law result, but this is due to an error in the calculation. The correct result for trapped absorption is that shown in Equation B.17, along with appropriate consideration of polarization and spatial integration in the trap.

Appendix C

Polarization-sensitive absorption spectroscopy and "extra light"

C.1 Observations of "extra light"

Appendix C of the thesis of Cindy Hancox [72] details observations of a confusing phenomenon in which the presence of atoms in a buffer-gas cell led to *more* light reaching the signal photodetector, rather than less. This effect gives the impression of negative absorption and was dubbed "extra light." Hancox gives her expression for calculating the absorption A as

$$A(t) = 1 - \frac{D(t)}{D_{\text{baseline}}} \tag{C.1}$$

$$D(t) = \frac{V_{\text{signal}}(t)}{V_{\text{reference}}(t)}, \tag{C.2}$$

where the ratio $D(t)$ of voltages from photodetectors monitoring signal and reference beams is called the "divide," and D_{baseline} is the divide measured with no atoms in the cell. The extra light effect was observed purely as an increase in the V_{signal}, with no unusual behavior in $V_{\text{reference}}$. Examples of extra light given by Hancox in her thesis are reproduced in Figures C.1,

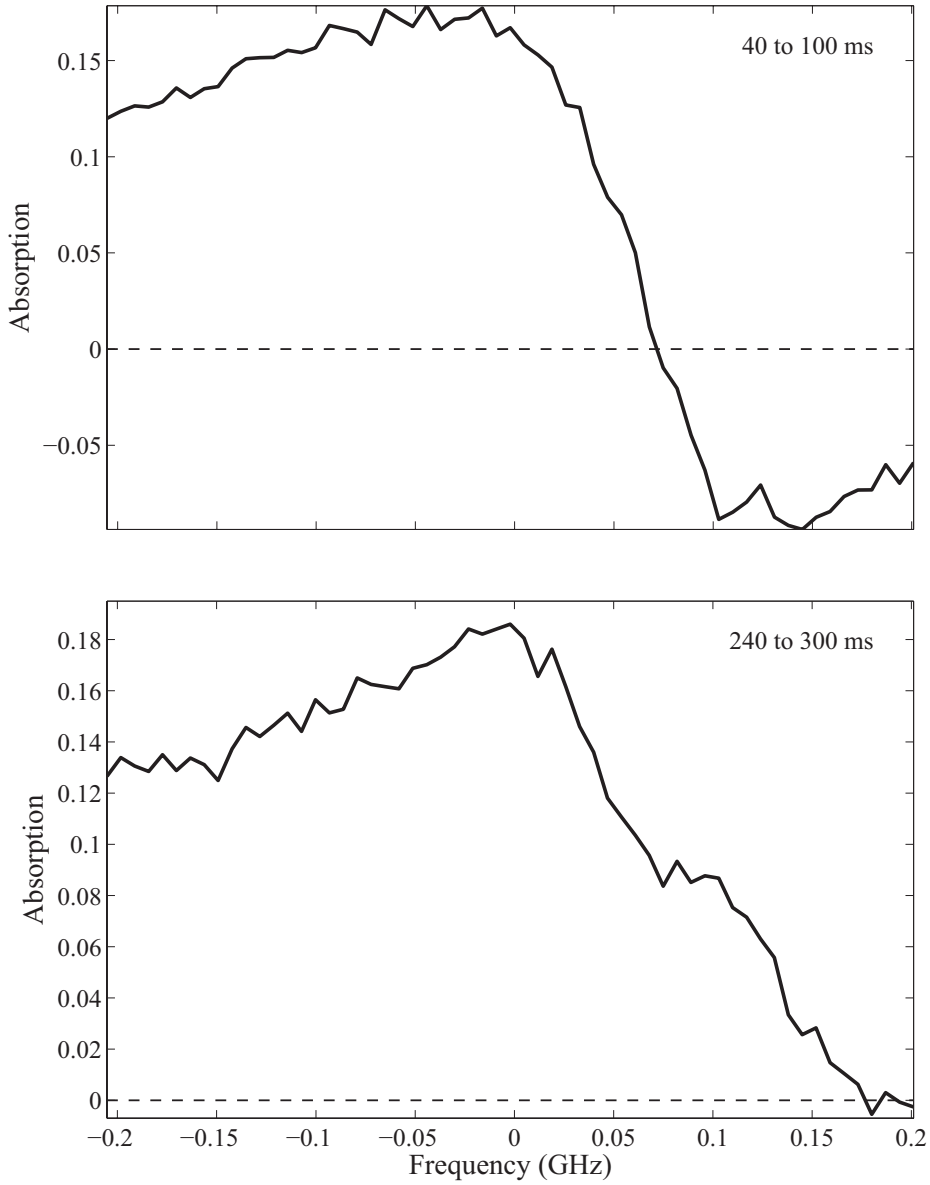

Figure C.1: Negative absorption observed by Hancox *et al.* in the spectrum of HFS states of Ti at the saddle points of an anti-Helmholtz field. Figure taken from [72].

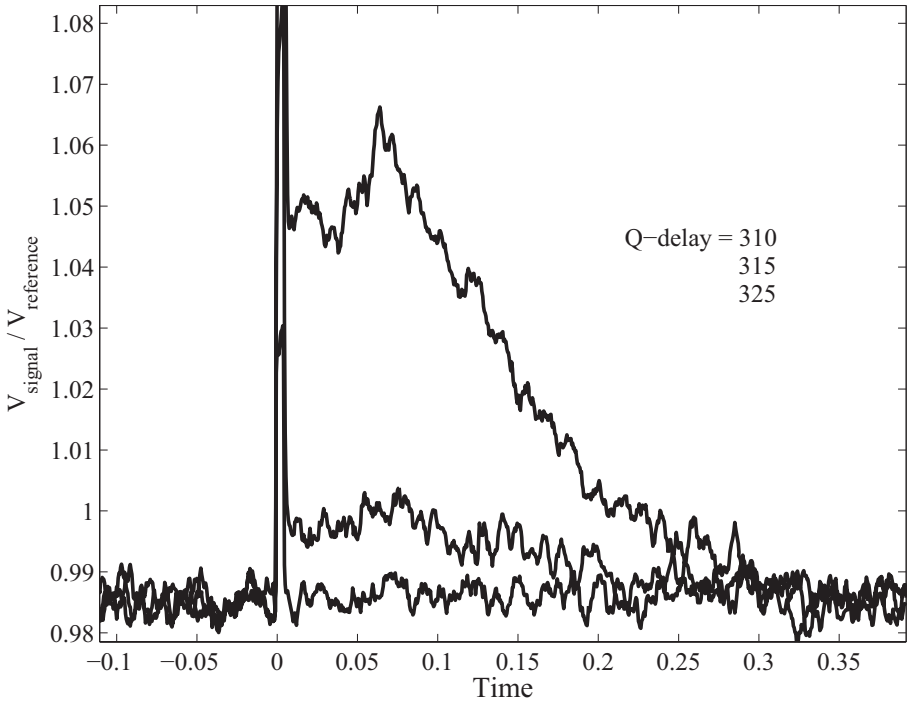

Figure C.2: Negative absorption observed by Hancox *et al.* with laser frequency parked near a HFS line of Ti at the saddle points of an anti-Helmholtz field. Different traces are for different ablation energies. The legend gives the YAG laser Q-delay for each trace, with lower Q-delay corresponding to higher energy. Figure taken from [72].

C.2, and C.3.

While she did not offer any physical explanation for the effect, Hancox catalogued its observed properties. These include:

1. The extra light is coherent and does not decrease if the beam exits the cell through an iris or the PMT detector is moved across the room.

2. The amount of extra light observed is linear in laser intensity.

3. Extra light is only observed with atoms in a magnetic field, and it is observed in both Helmholtz and anti-Helmholtz field configurations.

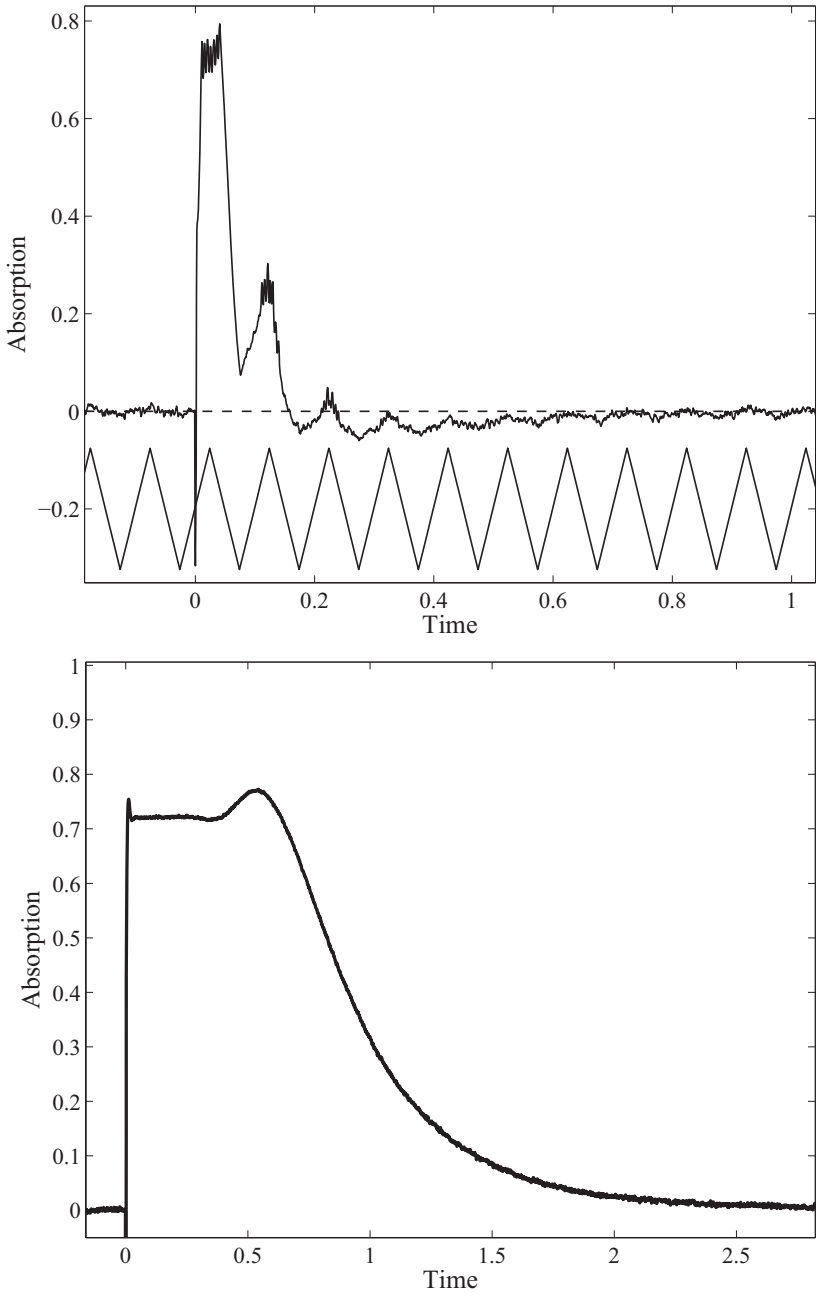

Figure C.3: Negative absorption observed by Hancox *et al.* in the spectrum of LFS (top) and HFS (bottom) states of Dy in a Helmholtz field. The bottom figure is taken with laser frequency parked on the HFS peak. The stable portion from ≈50–300 ms was believed to be 100% absorption, but with extra light causing it to appear lower. Figure taken from [72].

4. The effect is frequency dependent and strongest near strong spectral features associated with both low- and high-field-seeking (LFS and HFS) states.

5. The effect is most pronounced at high buffer gas densities.

6. Extra light was observed in experiments with both titanium and dysprosium. No other species were investigated for the effect.

Since the extra light effect did not interfere with the measurements of Hancox *et al.*, it was not investigated further. The effect was limited to $\lesssim$5% of V_{signal}.

Negative absorption was also observed in the experiments with aluminum described in Chapter 3 of this thesis. In that case, the effect was much more dramatic (Figure C.4), with V_{signal} increasing by up to 40% when the laser was tuned near resonance at high aluminum density. In addition, a >10% effect was observed with metastable helium-4 (Figure C.5) in the same experimental run as the rare-earth atom experiments described in Chapter 4. At this level, the effect is no longer a small perturbation to the measurement and becomes a significant concern. This appendix presents a model of apparent negative absorption caused by the combination of atomic birefringence and polarization-sensitive optical detection.

C.2 Absorption spectroscopy with polarization-dependent optics

The premise of absorption spectroscopy is straightforward: one laser beam passes through and interacts with the atomic cloud while a reference beam monitors the laser intensity. Both beams strike (ideally) matched photodetectors and the ratio of the two signals, normalized to unity for zero absorption, provides the transmission of the cloud independent of laser intensity fluctuations to first order. In practice, however, more optics are involved. At minimum,

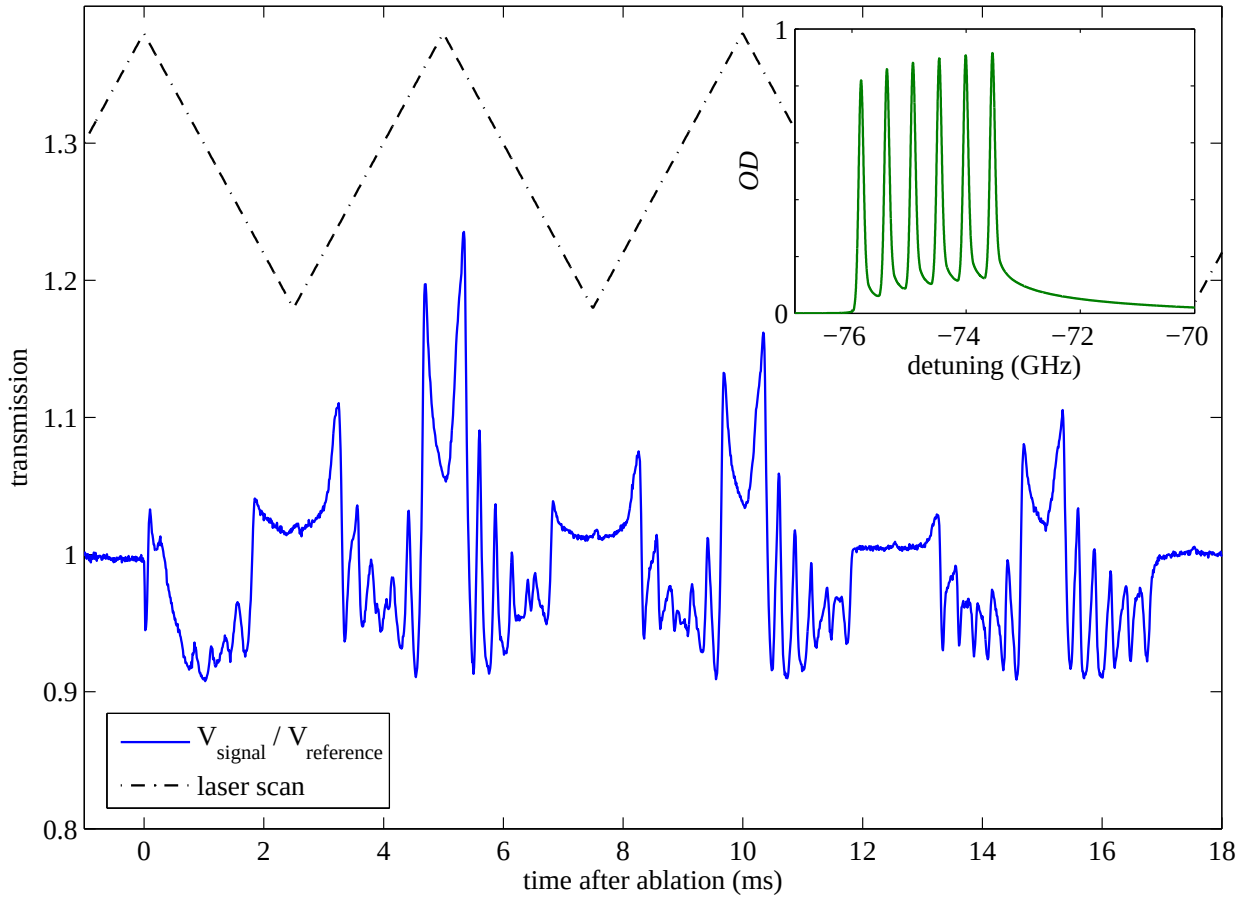

Figure C.4: Negative absorption observed in the scanned spectrum of LFS states of Al in a 0.5-T Helmholtz magnetic field with $T \approx 850$ mK. The inset shows the simulated hyperfine spectrum with asymmetric Helmholtz lineshape (see Figure 2.3).

there are almost always windows on the experimental chamber, and often in multiple layers. Usually there is also a beamsplitter to separate the signal and reference beams, and mirrors to steer the beams onto the detectors. The optics schematic for the experiments of Hancox *et al.* [72] is shown in Figure C.6. Most buffer-gas trapping experiments with a single half-axis of optical access have similar layouts (see also Figures 2.7 and 3.3). After the beamsplitter, the probe beam is overlapped with its reflection from the cell mirror. This overlap ensures that both beams sample the same region of the cell, simplifying data analysis and minimizing error. The return beam strikes the same beamsplitter and is partially transmitted to the

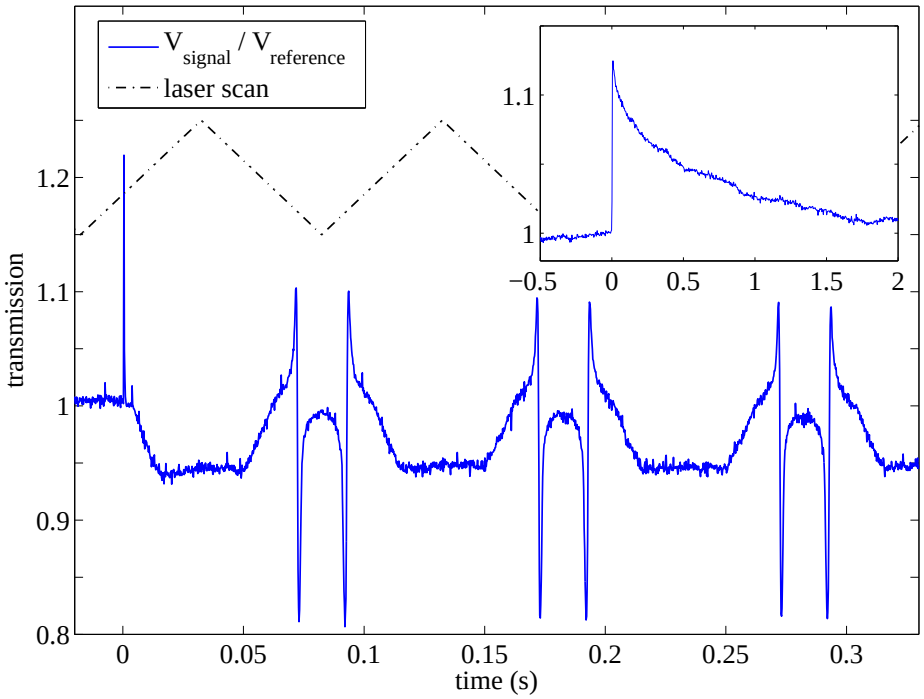

Figure C.5: Negative absorption observed in spectrum of trapped He*. The sharp feature is the $\Delta m = 0$ transition on top of the broader $\Delta m = +1$ feature (see Figure 4.3 of [111] for an undistorted spectrum). The inset (same axis units) shows the signal obtained by holding the laser frequency constant where the transmission is maximized.

signal detector.

In the optics layout described above, only a fraction of the laser power exiting the cell is incident on the signal detector, due to the second pass through the beamsplitter. The reflected component retraces the beam path back toward the laser and is not monitored. If some process acts to change the splitting fraction, then more or less light will be seen by the signal detector, with a corresponding change in V_{signal}. An example of such a process is a polarization rotation. Unless optimized to avoid it, most beamsplitters are polarization sensitive at 45° incidence, especially beamsplitters with dielectric coatings. Therefore birefringence in the dewar optics or cell can alter the splitting fraction. An extreme example of this is given in Figure 3.8, which shows the exiting beam polarization rotating as the mag-

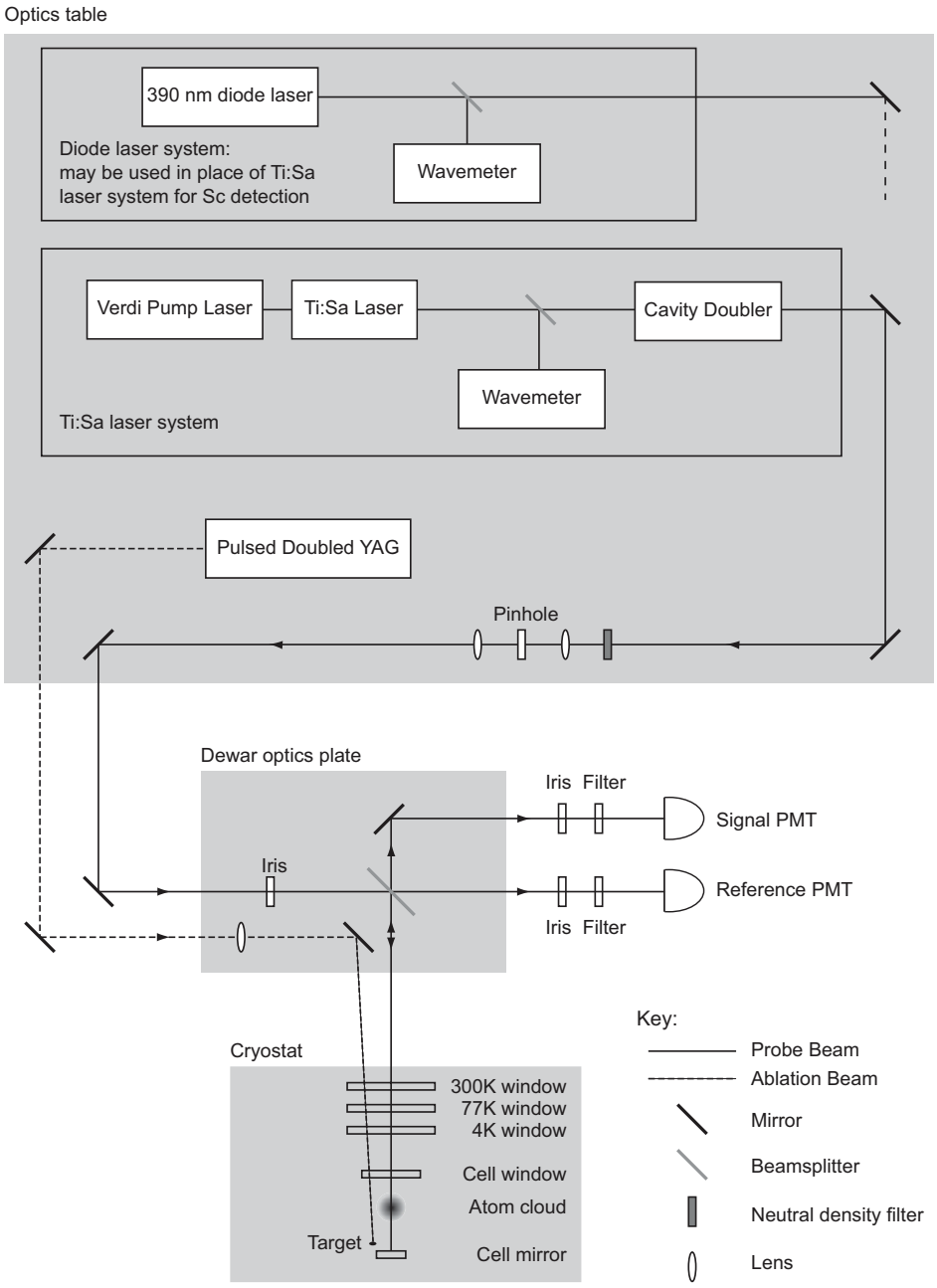

Figure C.6: Optics schematic for the experiments by Hancox *et al.* with Ti and Dy, taken from [72].

netic field is changed, due to the Faraday effect. In that case, the beamsplitter is a polarizing beamsplitter cube, and so the splitting fraction is maximally polarization sensitive.

It is easy to see how an atomic cloud in a magnetic field can give rise to frequency- and atom-density-dependent birefringence. Consider a cell filled with buffer-gas cooled aluminum atoms at 1 K in a constant magnetic field of 1 T parallel to the laser propagation direction. From the $m_J = +1/2$ sublevel of the $^2P_{1/2}$ ground state, there is only one option for excitation to the $^2S_{1/2}$ state: absorbtion of a σ_--polarized photon for a $\Delta m_J = -1$ transition to the excited state $m_J = -1/2$ sublevel (the aluminum level diagram is shown in Figure 3.2). $\Delta m = 0$ transitions are forbidden, as they would require polarization along the propagation direction. Therefore, the atoms only absorb right-circularly polarized light. Upon reflection from the cell mirror, the beam propagates antiparallel to the field such that σ_--polarization is equivalent to left-circular polarization. The handedness of the probe light also inverts upon reflection, and so the interaction is unchanged for the second pass through the atom cloud. In summary, right-circularly polarized light entering the cell can be entirely absorbed, while left-circularly polarized light cannot be absorbed at all. If linearly polarized light enters the cell, half of it will interact and the other half will not, leaving the beam polarization elliptical.

C.2.1 Quantitative model

It is still not obvious from the argument above why the signal detector should see more light due to absorption of one circular component. After all, the total beam power is definitely reduced. For a full picture, it is important to consider both absorption and dispersion caused by the atomic cloud. When the laser with electric field E_0 passes through the atoms, it is attenuated and phase shifted to yield $E = tE_0\, e^{i\phi}$. The attenuation coefficient t and phase

shift ϕ are given by

$$t = \exp\left(-\frac{OD_0}{2}\,\frac{1}{1+\delta^2}\right) \tag{C.3}$$

$$\phi = -\frac{OD_0}{2}\,\frac{\delta}{1+\delta^2}, \tag{C.4}$$

where OD_0 is the resonant optical density and $\delta = \frac{\omega-\omega_0}{\Gamma/2}$ is the detuning in half-linewidths.

To compute the effect of atomic birefringence on the probe laser intensity at the signal photodetector, we use the Jones matrix representation [185, 186]. We assume linear x-polarization initially, in which case the complex amplitude of the electric field can be written as

$$\tilde{E}_0 = \begin{bmatrix} 1 \\ 0 \end{bmatrix} = \frac{1}{2}\left(\begin{bmatrix} 1 \\ -i \end{bmatrix} + \begin{bmatrix} 1 \\ i \end{bmatrix}\right), \tag{C.5}$$

where the second equality has expressed the polarization in terms of right- and left-circularly polarized components. The atomic interaction interacts solely with one component to yield

$$\tilde{E} = \frac{1}{2}\left(te^{i\phi}\begin{bmatrix} 1 \\ -i \end{bmatrix} + \begin{bmatrix} 1 \\ i \end{bmatrix}\right). \tag{C.6}$$

At the cell mirror, the phase inverts. On the return trip through the atoms, they interact with the opposite circular polarization. The exiting beam polarization is then given by

$$\tilde{E} = \frac{1}{2}\left(t^2e^{2i\phi}\begin{bmatrix} 1 \\ i \end{bmatrix} + \begin{bmatrix} 1 \\ -i \end{bmatrix}\right). \tag{C.7}$$

Finally, the beam is incident on the beamsplitter, which has splitting fractions f_x and f_y for the x and y components of the polarization. The beamsplitter transmission is given by the Jones matrix

$$M_{\mathrm{BS}} = \begin{bmatrix} \sqrt{f_x} & 0 \\ 0 & \sqrt{f_y} \end{bmatrix}. \tag{C.8}$$

Multiplying by M_{BS} gives the final beam polarization at the signal detector,

$$\tilde{E} = \frac{1}{2}\left(t^2 e^{2i\phi} \begin{bmatrix} \sqrt{f_x} \\ i\sqrt{f_y} \end{bmatrix} + \begin{bmatrix} \sqrt{f_x} \\ -i\sqrt{f_y} \end{bmatrix} \right). \tag{C.9}$$

The signal voltage is proportional to the sum of the intensities of the two polarization components,

$$\begin{aligned} I &= \left|\tilde{E}_x\right|^2 + \left|\tilde{E}_y\right|^2 \\ &= \frac{1}{4}\left[(f_x + f_y)(1+t^4) + 2t^2(f_x - f_y)\,\cos(2\phi)\right]. \end{aligned} \tag{C.10}$$

Equation C.10 reduces to $I = f_x\,(1+t^4)/2$ in the case of a polarization insensitive beamsplitter ($f_x = f_y$). This is precisely the expression expected for absorption of only one circular component after double-passing the atoms (for that component, $t^4 = e^{-OD}$).

Simulated spectra calculated from Equation C.10 are shown in Figure C.7. The simulation reproduces the effect seen in the data quite well. We therefore conclude that the "extra light" seen in the aluminum experiment is light that is normally discarded, but which reaches the detector when atomic birefringence rotates the probe beam polarization. In regard to the other experiments that observed negative absorption, it also seems likely that polarization rotation is the cause. While the experimental conditions were not completely recorded, based on the description of those cases the model described here is sufficient to explain the observations. The case of dysprosium described by Hancox, in particular, matches very closely to the aluminum case. The simulations clearly predict incomplete absorption such as that shown in Figure C.3.

The cases of titanium and metastable helium are less clear because the observations were made with the atoms in an anti-Helmholtz field geometry. At first glance, it would appear that any phase shift accumulated in the first half of the cell would be cancelled by an opposite shift from the second half, where the quadrupole field has reversed direction. This picture

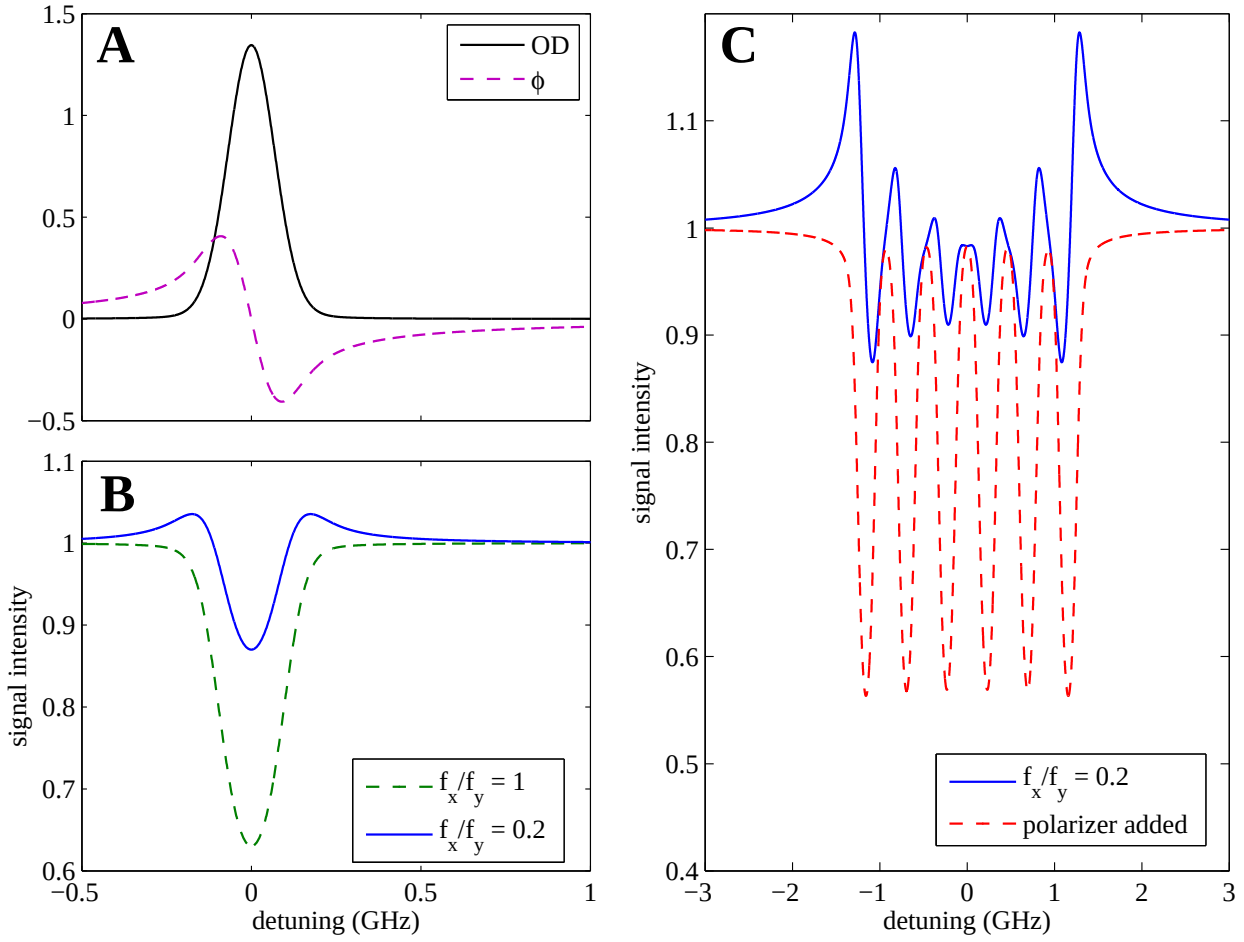

Figure C.7: Simulation of Al absorption spectrum in a Helmholtz field with polarization-sensitive detection. (A) *OD* and phase of a 1-K Doppler broadened line with the wavelength (394.5 nm) and natural linewidth (11.8 MHz) of the Al $^2P_{1/2} \rightarrow {}^2S_{1/2}$ transition, with unbroadened resonant $OD = 13$; (B) result using Equation C.10 for the apparent transmission of the line shown in (A); (C) result using Equation C.10 for 6 of the lines shown in (A) with spacing to match the Al hyperfine spectrum at 0.5 T. Also shown in (C) is the simulated effect of inserting a linear polarizer between the beamsplitter and dewar. The distorted lineshapes in (B) and (C) may appear asymmetric if there is polarization rotation unrelated to the atoms (such as that due to linear birefringence in windows), or if the lineshape is asymmetric. The value of $f_x/f_y = 0.2$ is similar to that of the beamsplitter used in the experiment.

is incomplete, however. When probing high-field-seeking atoms in the saddle points of the field, the cancellation argument relies on identical densities in the two trap saddles, which is unlikely to be the case. On the other hand, for low-field-seeking atoms in the trap—the case of the metastable helium experiment—this cancellation can be very good because the trapped distribution will rapidly equilibrate.

Cancellation is *not* expected, however, for polarization rotation caused by absorption of the π-polarized light that drives $\Delta m = 0$ transitions. The negative absorption seen in the helium experiment was observed near resonance with such a transition (Figure C.5). This can be shown quantitatively using the Jones matrices. We assume an infinitesimally-sized beam. The beam will intersect a resonant ellipsoidal shell in the trap where the magnetic field has projections on the x- and y-axes of B_x and B_y, respectively. Only the component of polarization parallel to the field (π-polarization) will drive the transition. The values of B_x and B_y will be the same for the intersection on both sides of the resonant shell (and for the return pass), so each will constructively add a factor of $te^{i\phi}$ to the appropriate polarization component of the electric field. The resulting light-atom interaction can be expressed by rotating the polarization by an angle $\alpha = -\tan^{-1}(B_y/B_x)$ before and by $-\alpha$ after the interaction,

$$\tilde{E} = M_{\mathrm{BS}}\, R(-\alpha) \begin{bmatrix} t^4 e^{4i\phi} & 0 \\ 0 & 1 \end{bmatrix} R(\alpha) \begin{bmatrix} 1 \\ 0 \end{bmatrix}. \tag{C.11}$$

The resulting intensity at the detector is then found to be

$$\begin{aligned} I = f_x \left[\sin^4(\alpha) + t^8 \cos^4(\alpha)\right] + f_y \sin^2(\alpha)\cos^2(\alpha)\left(1 + t^8\right) \\ + 2\left(f_x - f_y\right) t^4 \sin^2(\alpha)\cos(4\phi). \end{aligned} \tag{C.12}$$

The first two terms are well-behaved partial absorption ($t^8 = e^{-OD}$) for a given value of α. The third term represents the nonlinear effect, and is zero if α, ϕ, or $(f_x - f_y)$ are zero. This term can cause apparent negative absorption if the total phase accumulation 4ϕ is greater

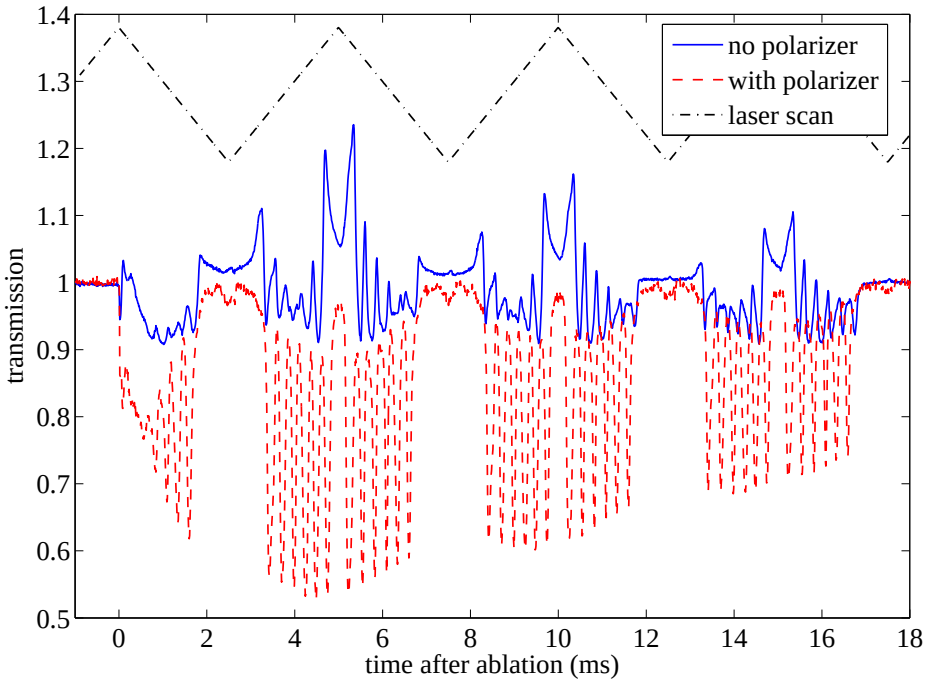

Figure C.8: Negative absorption in the Al spectrum eliminated by inserting a polarizer between the dewar and polarization-sensitive beamsplitter. The solid blue trace (no polarizer) is the same as that shown in Figure C.4. Both traces are well reproduced by the simulation shown in Figure C.7, aside from the neglected asymmetry due to the Helmholtz lineshape.

than $\pi/2$. The result for a beam of finite size can be constructed from a sum of Equation C.12 over many infinitesimal beams.

C.2.2 Mitigating the problem

This polarization rotation can be mitigated in several ways. Initially, it was thought that a polarizer between the beamsplitter and cell would be sufficient, such that any polarization component differing from the initial state would be discarded rather than distort the signal. The polarizer does indeed improve detection (Figure C.8), increasing the signal contrast (*i.e.*, the apparent absorption) and reducing the nonlinearity of V_{signal} with respect to atom density. However, the fact that the detection system is still polarization-sensitive (now

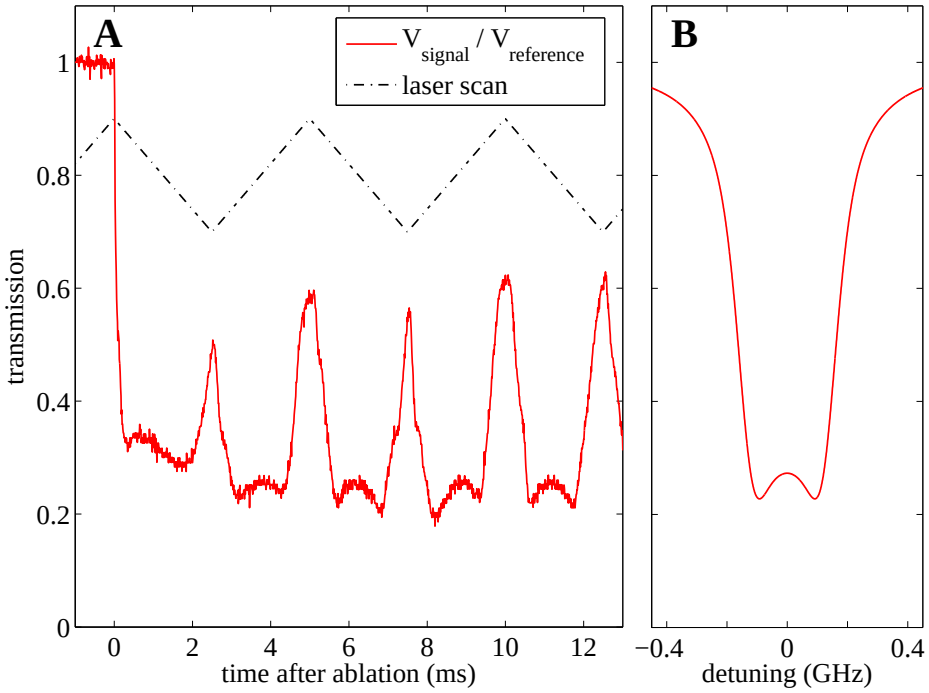

Figure C.9: Nonlinear effects of polarization rotation on Al lineshape seen at high OD with a polarizer between the dewar and beamsplitter. The doubled-peak distortion is seen both in (A) the data and (B) the simulation, for unbroadened resonant $OD = 60$.

due to the polarizer) necessarily implies that distorting effects remain. Figure C.9 gives a comparison between measured and simulated spectra in a case of high OD. The quantitative effect of the polarizer is to alter the intensity calculation in Equation C.10 to eliminate the y-polarized contribution, giving $I = \left|\tilde{E}_x\right|^2$.

A better way to mitigate the rotation effect is to simply avoid polarization-sensitive optics downstream of the cell. This can be impractical, however. Even with a minimally sensitive beamsplitter, attention must be paid to the polarization dependence of other downstream optics, such as dielectric mirrors. An alternative approach is to use a quarter-wave plate between the beamsplitter and dewar (see Figure 3.3) so that the probe beam is circularly polarized and thus unaffected by circular birefringence. This also avoids complications from circular birefringence in cell and dewar optics due to the Faraday effect (see Section 3.4.3

and [99]). Unfortunately, this also is an imperfect solution, since linear birefringence in dewar optics will alter the polarization and re-introduce some level of sensitivity to atomic birefringence.

In practice, the effect can simply be ignored in the many experimental cases in which it is tolerable for the transmission to deviate from $-\log\left[\int \sigma(z)n(z)\,dz\right]$, where $\sigma(z)$ and $n(z)$ are the optical cross section and beam-averaged atomic density, respectively. Nonlinearities in OD can be minimized by working at low OD, so that the interaction and hence the phase are weak. Often, other experimental factors will limit the accuracy of the measurement before polarization rotation issues become significant.

C.2.3 Extensions to the model

The matrix treatment of polarization above allows for straightforward inclusion of other optical elements or other processes that affect the polarization. Some common examples are given here. Jones matrices are not unique, and their definitions may differ between authors up to an arbitrary phase.

Phase retarder

Wave plates use linear birefringence to retard the phase of one linear polarization relative to the other. Unwanted linear birefringence can also be observed in other optics, especially thick windows under mechanical and thermal stress. The Jones matrix for a retarder with differential phase shift $\delta = \delta_y - \delta_x$ and fast axis at an angle θ with respect to the x-axis is given by

$$M_{\text{retarder}} = \begin{bmatrix} \cos^2(\theta) + e^{i\delta}\,\sin^2(\theta) & (1-e^{i\delta})\,\cos(\theta)\,\sin(\theta) \\ (1-e^{i\delta})\,\cos(\theta)\,\sin(\theta) & e^{i\delta}\,\cos^2(\theta) + \sin^2(\theta) \end{bmatrix}, \tag{C.13}$$

For the case of a half-wave plate ($\delta = \pi$), this reduces to

$$M_{\lambda/2} = \begin{bmatrix} \cos(2\theta) & \sin(2\theta) \\ \sin(2\theta) & -\cos(2\theta) \end{bmatrix}, \tag{C.14}$$

For the case of a quarter-wave plate ($\delta = \pi/2$), it reduces instead to

$$M_{\lambda/4} = \begin{bmatrix} 1 & 0 \\ 0 & i \end{bmatrix} \tag{C.15}$$

for fast axis along $\hat{\boldsymbol{x}}$ ($\theta = 0$) and

$$M_{\lambda/4} = \begin{bmatrix} 1 & 0 \\ 0 & -i \end{bmatrix} \tag{C.16}$$

for fast axis along $\hat{\boldsymbol{y}}$ ($\theta = 90°$).

Rotator

Rotation of the polarization axis by an angle β is given by

$$R(\beta) = \begin{bmatrix} \cos(\beta) & -\sin(\beta) \\ \sin(\beta) & \cos(\beta) \end{bmatrix}. \tag{C.17}$$

Circular birefringence is also a rotation of the linear polarization, by an angle $\beta = \phi/2$, where ϕ is the differential phase shift between circular polarization components.

Linear polarizer

The Jones matrix for a linear polarizer with angle θ between the transmission axis and x-axis is given by

$$M_{\text{polarizer}} = \begin{bmatrix} \cos^2(\theta) & \cos(\theta)\,\sin(\theta) \\ \cos(\theta)\,\sin(\theta) & \sin^2(\theta) \end{bmatrix}. \tag{C.18}$$

Mirror

A mirror inverts the parity of the coordinate system, which is expressed as

$$M_{\text{mirror}} = \begin{bmatrix} 1 & 0 \\ 0 & -1 \end{bmatrix}. \tag{C.19}$$

Bibliography

[1] T. V. Tscherbul, A. A. Buchachenko, A. Dalgarno, M.-J. Lu, and J. D. Weinstein. Suppression of Zeeman relaxation in cold collisions of $^2P_{1/2}$ atoms. *Phys. Rev. A* **80**, 040701 (2009).

[2] C. I. Hancox, S. C. Doret, M. T. Hummon, L. Luo, and J. M. Doyle. Magnetic trapping of rare-earth atoms at millikelvin temperatures. *Nature* **431**, 281–284 (2004).

[3] R. V. Krems and A. A. Buchachenko. Electronic interaction anisotropy between open-shell lanthanide atoms and helium from cold collision experiment. *J. Chem. Phys.* **123**, 101101 (2005).

[4] Colin B. Connolly, Yat Shan Au, S. Charles Doret, Wolfgang Ketterle, and John M. Doyle. Large spin relaxation rates in trapped submerged-shell atoms. *Phys. Rev. A* **81**, 010702 (2010).

[5] K. M. R. van der Stam, E. D. van Ooijen, R. Meppelink, J. M. Vogels, and P. van der Straten. Large atom number Bose-Einstein condensate of sodium. *Rev. Sci. Instrum.* **78**, 013102 (2007).

[6] Patrick Medley, David M. Weld, Hirokazu Miyake, David E. Pritchard, and Wolfgang Ketterle. Spin gradient demagnetization cooling of ultracold atoms. *Phys. Rev. Lett.* **106**, 195301 (2011).

[7] Jonathan Simon, Waseem S. Bakr, Ruichao Ma, M. Eric Tai, Philipp M. Preiss, and Markus Greiner. Quantum simulation of antiferromagnetic spin chains in an optical lattice. *Nature* **472**, 307–312 (2011).

[8] S. Weyers, V. Gerginov, N. Nemitz, R. Li, and K. Gibble. Distributed cavity phase frequency shifts of the caesium fountain PTB-CSF2. *Metrologia* **49**, 82 (2012).

[9] Jun Ye, H. J. Kimble, and Hidetoshi Katori. Quantum state engineering and precision metrology using state-insensitive light traps. *Science* **320**, 1734–1738 (2008).

[10] Thierry Lahaye, Tobias Koch, Bernd Fröhlich, Marco Fattori, Jonas Metz, Axel Griesmaier, Stefano Giovanazzi, and Tilman Pfau. Strong dipolar effects in a quantum ferrofluid. *Nature* **448**, 672–675 (2007).

[11] Mingwu Lu, Nathaniel Q. Burdick, Seo Ho Youn, and Benjamin L. Lev. Strongly dipolar Bose-Einstein condensate of dysprosium. *Phys. Rev. Lett.* **107**, 190401 (2011).

[12] Haiqing Wei, Rushan Han, and Xiuqing Wei. Quantum phase of induced dipoles moving in a magnetic field. *Phys. Rev. Lett.* **75**, 2071–2073 (1995).

[13] B. Damski, L. Santos, E. Tiemann, M. Lewenstein, S. Kotochigova, P. Julienne, and P. Zoller. Creation of a dipolar superfluid in optical lattices. *Phys. Rev. Lett.* **90**, 110401 (2003).

[14] A. Micheli, G. K. Brennen, and P. Zoller. A toolbox for lattice-spin models with polar molecules. *Nat. Phys.* **2**, 341–347 (2006).

[15] H. P. Büchler, E. Demler, M. Lukin, A. Micheli, N. Prokof'ev, G. Pupillo, and P. Zoller. Strongly correlated 2D quantum phases with cold polar molecules: Controlling the shape of the interaction potential. *Phys. Rev. Lett.* **98**, 060404 (2007).

[16] Charlotte Gils, Simon Trebst, Alexei Kitaev, Andreas W. W. Ludwig, Matthias Troyer, and Zhenghan Wang. Topology-driven quantum phase transitions in time-reversal-invariant anyonic quantum liquids. *Nat. Phys.* **5**, 834–839 (2009).

[17] B. Capogrosso-Sansone, C. Trefzger, M. Lewenstein, P. Zoller, and G. Pupillo. Quantum phases of cold polar molecules in 2D optical lattices. *Phys. Rev. Lett.* **104**, 125301 (2010).

[18] D. DeMille. Quantum computation with trapped polar molecules. *Phys. Rev. Lett.* **88**, 067901 (2002).

[19] Chaohong Lee and Elena A. Ostrovskaya. Quantum computation with diatomic bits in optical lattices. *Phys. Rev. A* **72**, 062321 (2005).

[20] J. Lee, E. R. Meyer, R. Paudel, J. L. Bohn, and A. E. Leanhardt. An electron electric dipole moment search in the $X\ ^3\Delta_1$ ground state of tungsten carbide molecules. *J. Mod. Opt.* **56**, 2005–2012 (2009).

[21] A. C. Vutha, W. C. Campbell, Y. V. Gurevich, N. R. Hutzler, M. Parsons, D. Patterson, E. Petrik, B. Spaun, J. M. Doyle, G. Gabrielse, and D. DeMille. Search for the electric dipole moment of the electron with thorium monoxide. *J. Phys. B* **43**, 074007 (2010).

[22] J. J. Hudson, D. M. Kara, I. J. Smallman, B. E. Sauer, M. R. Tarbutt, and E. A. Hinds. Improved measurement of the shape of the electron. *Nature* **473**, 493–496 (2011).

[23] Edmund R. Meyer and John L. Bohn. Electron electric-dipole-moment searches based on alkali-metal- or alkaline-earth-metal-bearing molecules. *Phys. Rev. A* **80**, 042508 (2009).

[24] Lasse Kragh Sørensen, Stefan Knecht, Timo Fleig, and Christel M. Marian. Four-component relativistic coupled cluster and configuration interaction calculations on the ground and excited states of the RbYb molecule. *J. Phys. Chem. A* **113**, 12607–12614 (2009).

[25] Hideaki Hara, Yosuke Takasu, Yoshifumi Yamaoka, John M. Doyle, and Yoshiro Takahashi. Quantum degenerate mixtures of alkali and alkaline-earth-like atoms. *Phys. Rev. Lett.* **106**, 205304 (2011).

[26] Tino Weber, Jens Herbig, Michael Mark, Hanns-Christoph Ngerl, and Rudolf Grimm. Bose-Einstein condensation of cesium. *Science* **299**, 232–235 (2003).

[27] B. Klöter, C. Weber, D. Haubrich, D. Meschede, and H. Metcalf. Laser cooling of an indium atomic beam enabled by magnetic fields. *Phys. Rev. A* **77**, 033402 (2008).

[28] Wesley C. Campbell and John M. Doyle. *Cold Polar Molecules: Creation and Applications*, Chapter 13: Cooling, trap loading, and beam production using a cryogenic helium buffer gas, 473–508. CRC, Boca Raton, FL, 2009.

[29] David Patterson, Edem Tsikata, and John M. D. Cooling and collisions of large gas phase molecules. *Phys. Chem. Chem. Phys.* **12**, 9736–9741 (2010).

[30] Robert deCarvalho, John M. Doyle, Bretislav Friedrich, Jinha Kim Thierry Guillet, David Patterson, and Jonathan D. Weinstein. Buffer-gas loaded magnetic traps for atoms and molecules: a primer. *Eur. Phys. J. D* **7**, 289–309 (1999).

[31] S. Charles Doret, Colin B. Connolly, Wolfgang Ketterle, and John M. Doyle. Buffer-gas cooled Bose-Einstein condensate. *Phys. Rev. Lett.* **103**, 103005 (2009).

[32] J. D. Weinstein, R. deCarvalho, C. I. Hancox, and J. M. Doyle. Evaporative cooling of atomic chromium. *Phys. Rev. A* **65**, 021604(R) (2002).

[33] C. I. Hancox, M. T. Hummon, S. V. Nguyen, and J. M. Doyle. Evaporative cooling of magnetically trapped atomic molybdenum. *Phys. Rev. A* **71**, 031402(R) (2005).

[34] Bonna K. Newman. *Trapped Atom collisions and Evaporative Cooling of non-S State Atoms*. PhD thesis, Massachusetts Institute of Technology, September 2008.

[35] E. S. Shuman, J. F. Barry, and D. DeMille. Laser cooling of a diatomic molecule. *Nature* **467**, 820–823 (2010).

[36] M. D. Di Rosa. Laser-cooling molecules. *Eur. Phys. J. D* **31**, 395–402 (2004).

[37] Benjamin K. Stuhl, Brian C. Sawyer, Dajun Wang, and Jun Ye. Magneto-optical trap for polar molecules. *Phys. Rev. Lett.* **101**, 243002 (2008).

[38] A. Robert, O. Sirjean, A. Browaeys, J. Poupard, S. Nowak, D. Boiron, C. I. Westbrook, and A. Aspect. A Bose-Einstein condensate of metastable atoms. *Science* **292**, 461–464 (2001).

[39] F. Pereira Dos Santos, J. Léonard, Junmin Wang, C. J. Barrelet, F. Perales, E. Rasel, C. S. Unnikrishnan, M. Leduc, and C. Cohen-Tannoudji. Bose-Einstein condensation of metastable helium. *Phys. Rev. Lett.* **86**, 3459–3462 (2001).

[40] Axel Griesmaier, Jörg Werner, Sven Hensler, Jürgen Stuhler, and Tilman Pfau. Bose-Einstein condensation of chromium. *Phys. Rev. Lett.* **94**, 160401 (2005).

[41] Simon Stellmer, Meng Khoon Tey, Bo Huang, Rudolf Grimm, and Florian Schreck. Bose-Einstein condensation of strontium. *Phys. Rev. Lett.* **103**, 200401 (2009).

[42] William H. Wing. On neutral particle trapping in quasistatic electromagnetic fields. *Prog. Quantum Electron.* **8**, 181–199 (1984).

[43] H. M. J. M. Boesten, C. C. Tsai, J. R. Gardner, D. J. Heinzen, and B. J. Verhaar. Observation of a shape resonance in the collision of two cold ^{87}Rb atoms. *Phys. Rev. A* **55**, 636–640 (1997).

[44] S. Inouye, M. R. Andrews, J. Stenger, H.-J. Miesner, D. M. Stamper-Kurn, and W. Ketterle. Observation of Feshbach resonances in a Bose-Einstein condensate. *Nature* **392**, 151–154 (1998).

[45] Ph. Courteille, R. S. Freeland, D. J. Heinzen, F. A. van Abeelen, and B. J. Verhaar. Observation of a Feshbach resonance in cold atom scattering. *Phys. Rev. Lett.* **81**, 69–72 (1998).

[46] K.-K. Ni, S. Ospelkaus, D. Wang, G. Quemener, B. Neyenhuis, M. H. G. de Miranda, J. L. Bohn, J. Ye, and D. S. Jin. Dipolar collisions of polar molecules in the quantum regime. *Nature* **464**, 1324–1328 (2010).

[47] S. Hensler, J. Werner, A. Griesmaier, P. O. Schmidt, A. Görlitz, T. Pfau, S. Giovanazzi, and K. Rzążewski. Dipolar relaxation in an ultra-cold gas of magnetically trapped chromium atoms. *Appl. Phys. B* **77**, 765–772 (2003).

[48] Joop J. Gilijamse, Steven Hoekstra, Sebastiaan Y. T. van de Meerakker, Gerrit C. Groenenboom, and Gerard Meijer. Near-threshold inelastic collisions using molecular beams with a tunable velocity. *Science* **313**, 1617–1620 (2006).

[49] Ellison H. Taylor and Sheldon Datz. Study of chemical reaction mechanisms with molecular beams. The reaction of K with HBr. *J. Chem. Phys.* **23**, 1711–1718 (1955).

[50] Giacinto Scoles. *Atomic and molecular beam methods*. Oxford University Press, New York, 1988.

[51] J. B. Hasted. *Physics of atomic collisions*. American Elsevier, New York, 1972.

[52] T. V. Tscherbul, J. Kłos, A. Dalgarno, B. Zygelman, Z. Pavlovic, M. T. Hummon, H.-I. Lu, E. Tsikata, and J. M. Doyle. Collisional properties of cold spin-polarized nitrogen gas: Theory, experiment, and prospects as a sympathetic coolant for trapped atoms and molecules. *Phys. Rev. A* **82**, 042718 (2010).

[53] Matthew T. Hummon, Timur V. Tscherbul, Jacek Kłos, Hsin-I Lu, Edem Tsikata, Wesley C. Campbell, Alexander Dalgarno, and John M. Doyle. Cold N + NH collisions in a magnetic trap. *Phys. Rev. Lett.* **106**, 053201 (2011).

[54] Matthew T. Hummon, Wesley C. Campbell, Hsin-I Lu, Edem Tsikata, Yihua Wang, and John M. Doyle. Magnetic trapping of atomic nitrogen (^{14}N) and cotrapping of NH ($X\,^3\Sigma^-$). *Phys. Rev. A* **78**, 050702 (2008).

[55] Piotr S. Zuchowski and Jeremy M. Hutson. Cold collisions of N (^4S) atoms and NH ($^3\Sigma$) molecules in magnetic fields. *Phys. Chem. Chem. Phys.* **13**, 3669–3680 (2011).

[56] J. E. Sansonetti and W. C. Martin. Handbook of basic atomic spectroscopic data. *J. Phys. Chem. Ref. Data* **34**, 1559–2259 (2005).

[57] S. E. Maxwell, M. T. Hummon, Y. Wang, A. A. Buchachenko, R. V. Krems, and J. M. Doyle. Spin-orbit interaction and large inelastic rates in bismuth–helium collisions. *Phys. Rev. A* **78**, 042706 (2008).

[58] Scott Vinh Nguyen. *Buffer gas loading and evaporative cooling in the multi-partial-wave regime*. PhD thesis, Harvard University, May 2006.

[59] Frank Pobell. *Matter and Methods at Low Temperatures*. 2nd edition. Springer, 1996.

[60] Robert Michniak. *Enhanced buffer gas loading: cooling and trapping of atoms with low effective magnetic moments*. PhD thesis, Harvard University, May 2004.

[61] J. G. E. Harris, R. A. Michniak, S. V. Nguyen, W. C. Campbell, D. Egorov, S. E. Maxwell, L. D. van Buuren, and J. M. Doyle. Deep superconducting magnetic traps for neutral atoms and molecules. *Rev. Sci. Instrum.* **75**, 17–23 (2004).

[62] B. N. Chichkov, C. Momma, S. Nolte, F. von Alvensleben, and A. Tünnermann. Femtosecond, picosecond and nanosecond laser ablation of solids. *Appl. Phys. A* **63**, 109–115 (1996).

[63] C. I. Hancox, S. C. Doret, M. T. Hummon, R. V. Krems, and J. M. Doyle. Suppression of angular momentum transfer in cold collisions of transition metal atoms in ground states with nonzero orbital angular momentum. *Phys. Rev. Lett.* **94**, 013201 (2005).

[64] Cort Johnson, Bonna Newman, Nathan Brahms, John M. Doyle, Daniel Kleppner, and Thomas J. Greytak. Zeeman relaxation of cold atomic iron and nickel in collisions with ^{3}He. *Phys. Rev. A* **81**, 062706 (2010).

[65] H. S. Carslaw and J. C. Jaeger. *Conduction of Heat in Solids*. 2nd edition. Oxford, 1959. p. 104.

[66] D. N. Nikogosyan. Beta barium borate (BBO): A review of its properties and applications. *App. Phys. A* **52**, 359–368 (1991).

[67] Chuangtian Chen, Siyang Luo, Xiaoyang Wang, Guiling Wang, Xiaohong Wen, Huaxing Wu, Xin Zhang, and Zuyan Xu. Deep UV nonlinear optical crystal: $RbBe_2(BO_3)F_2$. *J. Opt. Soc. Am. B* **26**, 1519–1525 (2009).

[68] C. Chen, G. Wang, X. Wang, and Z. Xu. Deep-UV nonlinear optical crystal $KBe_2BO_3F_2$—discovery, growth, optical properties and applications. *Appl. Phys. B* **97**, 9–25 (2009).

[69] H. Jones-Bey. Deep-UV applications await improved nonlinear optics. *Laser Focus World* , 127133 (1998).

[70] Jonathan D. Weinstein. *Magnetic trapping of atomic chromium and molecular calcium monohydride*. PhD thesis, Harvard University, December 2001.

[71] Wesley C. Campbell, Edem Tsikata, Hsin-I Lu, Laurens D. van Buuren, and John M. Doyle. Magnetic trapping and Zeeman relaxation of NH ($X\,^3\Sigma^-$). *Phys. Rev. Lett.* **98**, 213001 (2007).

[72] C. I. Hancox. *Magnetic trapping of transition-metal and rare-earth atoms using buffer-gas loading*. PhD thesis, Harvard University, 2005.

[73] Nathan Brahms, Timur V. Tscherbul, Peng Zhang, Jacek Kłos, Robert C. Forrey, Yat Shan Au, H. R. Sadeghpour, A. Dalgarno, John M. Doyle, and Thad G. Walker. Formation and dynamics of van der Waals molecules in buffer-gas traps. *Phys. Chem. Chem. Phys.* **13**, 19125–19141 (2011).

[74] Alexei A. Buchachenko, 2011. Private communication.

[75] Alexei A. Buchachenko, 2012. Private communication.

[76] Timur V. Tscherbul, 2011. Private communication.

[77] Alexei A. Buchachenko. Anisotropy of the static dipole polarizability induced by the spin-orbit interaction: the S-state atoms N–Bi, Cr, Mo and Re. *Proc. Roy. Soc. A* **467**, 1310–1328 (2011).

[78] T. V. Tscherbul, P. Zhang, H. R. Sadeghpour, A. Dalgarno, N. Brahms, Y. S. Au, and J. M. Doyle. Collision-induced spin depolarization of alkali-metal atoms in cold ^{3}He gas. *Phys. Rev. A* **78**, 060703 (2008).

[79] Roger W. McGowan, David M. Giltner, and Siu Au Lee. Light force cooling, focusing, and nanometer-scale deposition of aluminum atoms. *Opt. Lett.* **20**, 2535–2537 (1995).

[80] Steven J. Rehse, Karen M. Bockel, and Siu Au Lee. Laser collimation of an atomic gallium beam. *Phys. Rev. A* **69**, 063404 (2004).

[81] Isaac Fan, Tzu-Ling Chen, Yu-Sheng Liu, Yu-Hung Lien, Jow-Tsong Shy, and Yi-Wei Liu. Prospects of laser cooling in atomic thallium. *Phys. Rev. A* **84**, 042504 (2011).

[82] Th. Schulze, T. Muther, D. Jurgens, B. Brezger, M. K. Oberthaler, T. Pfau, and J. Mlynek. Structured doping with light forces. *Appl. Phys. Lett.* **78**, 1781–1783 (2001).

[83] K. Beloy, A. Derevianko, V. A. Dzuba, and V. V. Flambaum. Micromagic clock: Microwave clock based on atoms in an engineered optical lattice. *Phys. Rev. Lett.* **102**, 120801 (2009).

[84] B. K. Sahoo, R. Pandey, and B. P. Das. Search for a permanent electric-dipole moment using atomic indium. *Phys. Rev. A* **84**, 030502 (2011).

[85] B. C. Regan, Eugene D. Commins, Christian J. Schmidt, and David DeMille. New limit on the electron electric dipole moment. *Phys. Rev. Lett.* **88**, 071805 (2002).

[86] Eugene D. Commins. Berry's geometric phase and motional fields. *Am. J. Phys.* **59**, 1077–1080 (1991).

[87] R. V. Krems. Cold controlled chemistry. *Phys. Chem. Chem. Phys.* **10**, 4079–4092 (2008).

[88] R. V. Krems, G. C. Groenenboom, and A. Dalgarno. Electronic interaction anisotropy between atoms in arbitrary angular momentum states. *J. Phys. Chem. A* **108**, 8941–8948 (2004).

[89] Nathan Brahms, Bonna Newman, Cort Johnson, Tom Greytak, Daniel Kleppner, and John Doyle. Magnetic trapping of silver and copper, and anomalous spin relaxation in the Ag–He system. *Phys. Rev. Lett.* **101**, 103002 (2008).

[90] A. Yamaguchi, S. Uetake, D. Hashimoto, J. M. Doyle, and Y. Takahashi. Inelastic collisions in optically trapped ultracold metastable ytterbium. *Phys. Rev. Lett.* **101**, 233002 (2008).

[91] R. V. Krems and A. Dalgarno. Disalignment transitions in cold collisions of ^3P atoms with structureless targets in a magnetic field. *Phys. Rev. A* **68**, 013406 (2003).

[92] Mei-Ju Lu, Kyle S. Hardman, Jonathan D. Weinstein, and Bernard Zygelman. Fine-structure-changing collisions in atomic titanium. *Phys. Rev. A* **77**, 060701 (2008).

[93] Bernard Zygelman and Jonathan D. Weinstein. Theoretical and laboratory study of suppression effects in fine-structure-changing collisions of Ti with He. *Phys. Rev. A* **78**, 012705 (2008).

[94] Harry Partridge, James R. Stallcop, and Eugene Levin. Potential energy curves and transport properties for the interaction of He with other ground-state atoms. *J. Chem. Phys.* **115**, 6471–6488 (2001).

[95] Timur V. Tscherbul, 2012. Private communication.

[96] D. E. Kelleher and L. I. Podobedova. Atomic transition probabilities of aluminum. a critical compilation. *J. Phys. Chem. Ref. Data* **37**, 709–911 (2008).

[97] J. Kim, B. Friedrich, D. P. Katz, D. Patterson, J. D. Weinstein, R. deCarvalho, and J. M. Doyle. Buffer-gas loading and magnetic trapping of atomic europium. *Phys. Rev. Lett.* **78**, 3665–3668 (1997).

[98] Edward S. Chang. Energy levels of atomic aluminum with hyperfine structure. *J. Phys. Chem. Ref. Data* **19**, 119–125 (1990).

[99] E. Munin, J. A. Roversi, and A. Balbin Villaverde. Faraday effect and energy gap in optical materials. *J. Phys. D* **25**, 1635 (1992).

[100] Donald C. Griffin, Kenneth L. Andrew, and Robert D. Cowan. Theoretical calculations of the d-, f-, and g-electron transition series. *Phys. Rev.* **177**, 62–71 (1969).

[101] R. V. Krems, J. Kłos, M. F. Rode, M. M. Szczęśniak, G. Chałasiński, and A. Dalgarno. Suppression of angular forces in collisions of non-S-state transition metal atoms. *Phys. Rev. Lett.* **94**, 013202 (2005).

[102] J. L. Hall, M. Zhu, and P. Buch. Prospects for using laser-prepared atomic fountains for optical frequency standards applications. *J. Opt. Soc. Am. B* **6**, 2194 (1989).

[103] K. Chebakov, A. Sokolov, A. Akimov, D. Sukachev, S. Kanorsky, N. Kolachevsky, and V. Sorokin. Zeeman slowing of thulium atoms. *Opt. Lett.* **34**, 2955–2957 (2009).

[104] Andrew J. Berglund, James L. Hanssen, and Jabez J. McClelland. Narrow-line magneto-optical cooling and trapping of strongly magnetic atoms. *Phys. Rev. Lett.* **100**, 113002 (2008).

[105] D. Sukachev, A. Sokolov, K. Chebakov, A. Akimov, N. Kolachevsky, and V. Sorokin. Sub-Doppler laser cooling of thulium atoms in a magneto-optical trap. *JETP Lett.* **92**, 703706 (2010).

[106] M. A. Baranov. Theoretical progress in many-body physics with ultracold dipolar gases. *Physics Reports* **464**, 71–111 (2008).

[107] T. Lahaye, C. Menotti, L. Santos, M. Lewenstein, and T. Pfau. The physics of dipolar bosonic quantum gases. *Rep. Prog. Phys.* **72**, 126401 (2009).

[108] Benjamin M. Fregoso, Kai Sun, Eduardo Fradkin, and Benjamin L. Lev. Biaxial nematic phases in ultracold dipolar Fermi gases. *New J. of Phys.* **11**, 103003 (2009).

[109] M. Saffman and K. Mølmer. Scaling the neutral-atom Rydberg gate quantum computer by collective encoding in holmium atoms. *Phys. Rev. A* **78**, 012336 (2008).

[110] W. C. Martin, R. Zalubas, and L. Hagan. Atomic energy levels—The rare-earth elements. Technical report, National Bureau of Standards, 1978. in *Nat. Stand. Ref. Data Ser., NSRDS-NBS 60*, 422 pp.

[111] Stephen Charles Doret. *A buffer-gas cooled Bose-Einstein condensate*. PhD thesis, Harvard University, October 2009.

[112] Jonathan D. Weinstein, Robert deCarvalho, Jinha Kim, David Patterson, Bretislav Friedrich, and John M. Doyle. Magnetic trapping of atomic chromium. *Phys. Rev. A* **57**, R3173–R3175 (1998).

[113] Nathaniel Charles Brahms. *Trapping of 1 μ_B atoms using buffer gas loading*. PhD thesis, Harvard University, May 2008.

[114] E. Tsikata, W. C. Campbell, M. T. Hummon, H.-I. Lu, and J. M. Doyle. Magnetic trapping of NH molecules with 20 s lifetimes. *New J. of Phys.* **12**, 065028 (2010).

[115] A. V. Akimov, K. Yu. Chebakov, I. Yu. Tolstikhina, A. V. Sokolov, P. B. Rodionov, S. I. Kanorsky, V. N. Sorokin, and N. N. Kolachevsky. Study of transitions in thulium atoms in the 410–420-nm range for laser cooling. *Quantum Electron.* **38**, 961–968 (2008).

[116] W. Ketterle and N. J. van Druten. Evaporative cooling. *Adv. At. Mol. Opt. Phys.* **37**, 181–236 (1996).

[117] O. J. Luiten, M. W. Reynolds, and J. T. M. Walraven. Kinetic theory of the evaporative cooling of a trapped gas. *Phys. Rev. A* **53**, 381–389 (1996).

[118] Robert deCarvalho and John Doyle. Evaporative cooling at low trap depth. *Phys. Rev. A* **70**, 053409 (2004).

[119] John L. Bohn, James P. Burke, Chris H. Greene, H. Wang, P. L. Gould, and W. C. Stwalley. Collisional properties of ultracold potassium: Consequences for degenerate Bose and Fermi gases. *Phys. Rev. A* **59**, 3660–3664 (1999).

[120] J. G. E. Harris, S. V. Nguyen, S. C. Doret, W. Ketterle, and J. M. Doyle. Spin-exchange collisions of submerged shell atoms below 1 kelvin. *Phys. Rev. Lett.* **99**, 223201 (2007).

[121] A. A. Buchachenko, G. Chałasiński, M. M. Szczęśniak, and R. V. Krems. *Ab initio* study of Tm–He interactions and dynamics in a magnetic trap. *Phys. Rev. A* **74**, 022705 (2006).

[122] S. V. Nguyen, R. deCarvalho, and J. M. Doyle. Cold ^{52}Cr elastic and inelastic collision-rate determination using evaporative cooling analysis. *Phys. Rev. A* **75**, 062706 (2007).

[123] Z. Pavlović, R. V. Krems, R. Côté, and H. R. Sadeghpour. Magnetic Feshbach resonances and Zeeman relaxation in bosonic chromium gas with anisotropic interaction. *Phys. Rev. A* **71**, 061402(R) (2005).

[124] A. A. Buchachenko, Y. V. Suleimanov, G. Chałasiński, and M. M. Szczęśniak. Interactions and collisions of cold metal atoms in magnetic traps. *Phys. Scr.* **80**, 048109 (2009).

[125] Yury V. Suleimanov. Zeeman relaxation of magnetically trapped Eu atoms. *Phys. Rev. A* **81**, 022701 (2010).

[126] Anthony J. Stone. *The Theory of Intermolecular Forces*, Volume 32. Clarendon Press, Oxford, 1996.

[127] Alexei A. Buchachenko, 2009. Private communication.

[128] Svetlana Kotochigova and Alexander Petrov. Anisotropy in the interaction of ultracold dysprosium. *Phys. Chem. Chem. Phys.* **13**, 19165–19170 (2011).

[129] D. Hansen and A. Hemmerich. Observation of multichannel collisions of cold metastable calcium atoms. *Phys. Rev. Lett.* **96**, 073003 (2006).

[130] A. Traverso, R. Chakraborty, Y. N. Martinez de Escobar, P. G. Mickelson, S. B. Nagel, M. Yan, and T. C. Killian. Inelastic and elastic collision rates for triplet states of ultracold strontium. *Phys. Rev. A* **79**, 060702 (2009).

[131] Mingwu Lu, Seo Ho Youn, and Benjamin L. Lev. Trapping ultracold dysprosium: A highly magnetic gas for dipolar physics. *Phys. Rev. Lett.* **104**, 063001 (2010).

[132] Bonna K. Newman, Nathan Brahms, Yat Shan Au, Cort Johnson, Colin B. Connolly, John M. Doyle, Daniel Kleppner, and Thomas J. Greytak. Magnetic relaxation in dysprosium–dysprosium collisions. *Phys. Rev. A* **83**, 012713 (2011).

[133] R. Shankar. *Principles of Quantum Mechanics*. 2nd edition. Plenum Press, 1994. p. 548.

[134] P. Zhang and A. Dalgarno. Static dipole polarizability of ytterbium. *J. Phys. Chem. A* **111**, 12471–12476 (2007).

[135] Mingwu Lu, Nathaniel Q. Burdick, and Benjamin L. Lev. Quantum degenerate dipolar Fermi gas. *Phys. Rev. Lett.* **108**, 215301 (2012).

[136] K. Aikawa, A. Frisch, M. Mark, S. Baier, A. Rietzler, R. Grimm, and F. Ferlaino. Bose-Einstein condensation of erbium. *Phys. Rev. Lett.* **108**, 210401 (2012).

[137] D. Sukachev, A. Sokolov, K. Chebakov, A. Akimov, S. Kanorsky, N. Kolachevsky, and V. Sorokin. Magneto-optical trap for thulium atoms. *Phys. Rev. A* **82**, 011405 (2010).

[138] S. Ospelkaus, K.-K. Ni, D. Wang, M. H. G. de Miranda, B. Neyenhuis, G. Qumner, P. S. Julienne, J. L. Bohn, D. S. Jin, and J. Ye. Quantum-state controlled chemical reactions of ultracold potassium-rubidium molecules. *Science* **327**, 853–857 (2010).

[139] Brian C. Sawyer, Benjamin K. Stuhl, Mark Yeo, Timur V. Tscherbul, Matthew T. Hummon, Yong Xia, Jacek Kłos, David Patterson, John M. Doyle, and Jun Ye. Cold heteromolecular dipolar collisions. *Phys. Chem. Chem. Phys.* **13**, 19059–19066 (2011).

[140] M G Kozlov and L N Labzowsky. Parity violation effects in diatomics. *J. Phys. B* **28**, 1933 (1995).

[141] A. E. Leanhardt, J. L. Bohn, H. Loh, P. Maletinsky, E. R. Meyer, L. C. Sinclair, R. P. Stutz, and E. A. Cornell. High-resolution spectroscopy on trapped molecular ions in rotating electric fields: A new approach for measuring the electron electric dipole moment. *J. Mol. Spectrosc.* **270**, 1–25 (2011).

[142] K.-K. Ni, S. Ospelkaus, M. H. G. de Miranda, A. Pe'er, B. Neyenhuis, J. J. Zirbel, S. Kotochigova, P. S. Julienne, D. S. Jin, and J. Ye. A high phase-space-density gas of polar molecules. *Science* **322**, 231–235 (2008).

[143] J. Deiglmayr, A. Grochola, M. Repp, K. Mörtlbauer, C. Glück, J. Lange, O. Dulieu, R. Wester, and M. Weidemüller. Formation of ultracold polar molecules in the rovibrational ground state. *Phys. Rev. Lett.* **101**, 133004 (2008).

[144] David DeMille. Ultracold molecules: Production techniques and scientific applications. In *Quantum Electronics and Laser Science Conference*, QWB1. Optical Society of America, 2011.

[145] Matthew Hummon, Mark Yeo, Benjamin Stuhl, Yong Xia, and Jun Ye. Direct laser cooling of yttrium monoxide. In *43rd Annual Meeting of the APS Division of Atomic, Molecular and Optical Physics*, Volume 57. American Physical Society, June 2012.

[146] Pavel Soldán, Piotr S. Zuchowski, and Jeremy M. Hutson. Prospects for sympathetic cooling of polar molecules: NH with alkali-metal and alkaline-earth atoms—a new hope. *Faraday Discuss.* **142**, 191–201 (2009).

[147] T. V. Tscherbul, J. Kłos, and A. A. Buchachenko. Ultracold spin-polarized mixtures of $^2\Sigma$ molecules with S-state atoms: Collisional stability and implications for sympathetic cooling. *Phys. Rev. A* **84**, 040701 (2011).

[148] Vijay Singh, Mei-Ju Lu, Kyle Hardman, Muir Morrision, and Jonathan Weinstein. Inelastic collisions of CaH molecules at cryogenic temperatures. In *41st Annual Meeting of the APS Division of Atomic, Molecular and Optical Physics*, Volume 55. American Physical Society, May 2010.

[149] R. V. Krems, H. R. Sadeghpour, A. Dalgarno, D. Zgid, J. Kłos, and G. Chałasiński. Low-temperature collisions of NH($X^3\Sigma^-$) molecules with He atoms in a magnetic field: An *ab initio* study. *Phys. Rev. A* **68**, 051401 (2003).

[150] D. Egorov, W. C. Campbell, B. Friedrich, S. E. Maxwell, E. Tsikata, L. D. van Buuren, and J. M. Doyle. Buffer-gas cooling of NH via the beam loaded buffer-gas method. *Eur. Phys. J. D* **31**, 307–311 (2004).

[151] Wesley C. Campbell, Timur V. Tscherbul, Hsin-I Lu, Edem Tsikata, Roman V. Krems, and John M. Doyle. Mechanism of collisional spin relaxation in $^3\Sigma$ molecules. *Phys. Rev. Lett.* **102**, 013003 (2009).

[152] Wesley C. Campbell. *Magnetic trapping of imidogen molecules.* PhD thesis, Harvard University, February 2008.

[153] Wesley C. Campbell, Gerrit C. Groenenboom, Hsin-I Lu, Edem Tsikata, and John M. Doyle. Time-domain measurement of spontaneous vibrational decay of magnetically trapped NH. *Phys. Rev. Lett.* **100**, 083003 (2008).

[154] Liesbeth M. C. Janssen, Piotr S. Żuchowski, Ad van der Avoird, Gerrit C. Groenenboom, and Jeremy M. Hutson. Cold and ultracold NH–NH collisions in magnetic fields. *Phys. Rev. A* **83**, 022713 (2011).

[155] Liesbeth M. C. Janssen, Piotr S. Zuchowski, Ad van der Avoird, Jeremy M. Hutson, and Gerrit C. Groenenboom. Cold and ultracold NH–NH collisions: The field-free case. *J. Chem. Phys.* **134**, 124309 (2011).

[156] Y. V. Suleimanov, T. V. Tscherbul, and R. V. Krems. Efficient method for quantum calculations of molecule–molecule scattering properties in a magnetic field. Submitted (arXiv:1202.0597).

[157] Sebastiaan Y. T. van de Meerakker, Irena Labazan, Steven Hoekstra, Jochen K upper, and Gerard Meijer. Production and deceleration of a pulsed beam of metastable NH ($a^1\Delta$) radicals. *J. Phys. B* **39**, S1077 (2006).

[158] Heather Lewandowski, L. Paul. Parazzoli, and Daniel Lobser. Cold free-radical NH molecules. In *Frontiers in Optics*. Optical Society of America, 2006.

[159] Steven Hoekstra, Markus Metsälä, Peter C. Zieger, Ludwig Scharfenberg, Joop J. Gilijamse, Gerard Meijer, and Sebastiaan Y. T. van de Meerakker. Electrostatic trapping of metastable NH molecules. *Phys. Rev. A* **76**, 063408 (2007).

[160] Pavel Soldán and Jeremy M. Hutson. Interaction of NH($X\,^3\Sigma^-$) molecules with rubidium atoms: Implications for sympathetic cooling and the formation of extremely polar molecules. *Phys. Rev. Lett.* **92**, 163202 (2004).

[161] Daniel J. Haxton, Steven A. Wrathmall, H. J. Lewandowski, and Chris H. Greene. Theoretical study of the quenching of NH ($^1\Delta$) molecules via collisions with Rb atoms. *Phys. Rev. A* **80**, 022708 (2009).

[162] Alisdair O. G. Wallis and Jeremy M. Hutson. Production of ultracold NH molecules by sympathetic cooling with Mg. *Phys. Rev. Lett.* **103**, 183201 (2009).

[163] Alisdair Wallis, Edward Longdon, Piotr Żuchowski, and Jeremy Hutson. The prospects of sympathetic cooling of NH molecules with Li atoms. *Eur. Phys. J. D* **65**, 151–160 (2011).

[164] Nicholas R. Hutzler, Maxwell F. Parsons, Yulia V. Gurevich, Paul W. Hess, Elizabeth Petrik, Ben Spaun, Amar C. Vutha, David DeMille, Gerald Gabrielse, and John M. Doyle. A cryogenic beam of refractory, chemically reactive molecules with expansion cooling. *Phys. Chem. Chem. Phys.* **13**, 18976–18985 (2011).

[165] Dimitri Michael Egorov. *Buffer-gas cooling of diatomic molecules*. PhD thesis, Harvard University, August 2004.

[166] Kenneth Maussang, Dima Egorov, Joel S. Helton, Scott V. Nguyen, and John M. Doyle. Zeeman relaxation of CaF in low-temperature collisions with helium. *Phys. Rev. Lett.* **94**, 123002 (2005).

[167] Michael Stoll, Joost M. Bakker, Timothy C. Steimle, Gerard Meijer, and Achim Peters. Cryogenic buffer-gas loading and magnetic trapping of CrH and MnH molecules. *Phys. Rev. A* **78**, 032707 (2008).

[168] Matthew Taylor Hummon. *Magnetic trapping of atomic nitrogen and cotrapping of NH*. PhD thesis, Harvard University, March 2010.

[169] J. Helffrich, M. Maley, M. Krusius, and J. C. Wheatley. Hydrogen dissociation below 1 K. *J. Low Temp. Phys.* **66**, 277–304 (1987).

[170] Russell B. Scott. *Cryogenic Engineering*. Van Nostrand, Princeton, NJ, 1959.

[171] C. Effantin, C. Amiot, and J. Verges. Analysis of the (0-0), (1-0), and (2-0) bands of the $B^3\Pi_g \rightarrow A^3\Sigma_u^+$ system of $^{14}N_2$ and $^{15}N_2$. *J. Mol. Spectrosc.* **76**, 221–265 (1979).

[172] Thomas A Carlson, Nada Duric, Peter Erman, and Mats Larsson. Collisional transfer to the B state in N_2. *Phys. Scr.* **19**, 25 (1979).

[173] F. Roux, F. Michaud, and J. Verges. High-resolution Fourier spectrometry of $^{14}N_2$ infrared emission spectrum: Extensive analysis of the $B^3\Pi_g$–$A^3\Sigma_u^+$ system. *J. Mol. Spectrosc.* **97**, 253–265 (1983).

[174] G. C. Bjorklund, M. D. Levenson, W. Lenth, and C. Ortiz. Frequency modulation (FM) spectroscopy. *Appl. Phys. B* **32**, 145–152 (1983).

[175] M. M. Fejer, G. A. Magel, D. H. Jundt, and R. L. Byer. Quasi-phase-matched second harmonic generation: Tuning and tolerances. *IEEE J. of Quantum Electron.* **28**, 2631 –2654 (1992).

[176] Editorial Committee Hamamatsu Photonics K. K. *Photomultiplier Tubes: Basics and Applications*. 3rd edition. Hamamatsu Photonics K. K., Electron Tube Division, February 2006.

[177] CVI Melles Griot. Materials properties. http://www.cvimellesgriot.com, 2009.

[178] L. F. Goodrich, S. L. Bray, and T. C. Stauffer. Nb_3Sn critical-current measurements using tubular fiberglass-epoxy mandrels. *IEEE Trans. on Magn.* **25**, 2375 –2378 (1989).

[179] P. O. Fedichev, M. W. Reynolds, U. M. Rahmanov, and G. V. Shlyapnikov. Inelastic decay processes in a gas of spin-polarized triplet helium. *Phys. Rev. A* **53**, 1447–1453 (1996).

[180] Scott V. Nguyen, S. Charles Doret, Colin B. Connolly, Robert A. Michniak, Wolfgang Ketterle, and John M. Doyle. Evaporative cooling of metastable helium in the multi-partial-wave regime. *Phys. Rev. A* **72**, 060703 (2005).

[181] Jan R. Rubbmark, Michael M. Kash, Michael G. Littman, and Daniel Kleppner. Dynamical effects at avoided level crossings: A study of the Landau-Zener effect using Rydberg atoms. *Phys. Rev. A* **23**, 3107–3117 (1981).

[182] Harold Metcalf and Peter van der Straten. *Laser Cooling and Trapping*. Springer, New York, 1999.

[183] V. M. Akulin and W. P. Schleich. Landau-Zener transition to a decaying level. *Phys. Rev. A* **46**, 4110–4113 (1992).

[184] G. N. Watson E. T. Whittaker. *A Course of Modern Analysis*. Fourth edition. Cambridge University Press, Cambridge, 1996.

[185] R. Clark Jones. A new calculus for the treatment of optical systems. *J. Opt. Soc. Am.* **31**, 488–493 (1941).

[186] Frank L. Pedrotti, Leno Matthew. Pedrotti, and Leno S. Pedrotti. *Introduction to Optics*. Third edition. Pearson Prentice Hall, Upper Saddle River, N.J., 2007. Chapter 14.